

MATER. TEHNOL.	LETNIK VOLUME	46	ŠTEV. NO.	5	STR. P.	429–554	LJUBLJANA SLOVENIJA	SEP.–OCT. 2012
-------------------	------------------	----	--------------	---	------------	---------	------------------------	-------------------

## VSEBINA – CONTENTS

## IZVIRNI ZNANSTVENI ČLANKI – ORIGINAL SCIENTIFIC ARTICLES

**Identification of the material parameters of a unidirectional fiber composite using a micromodel**

Identifikacija parametrov materiala enosmernega kompozita z uporabo mikromodela

H. Srbová, T. Kroupa, R. Zemčík ..... 431

**Microstructure and mechanical properties of carbon/carbon-silicon carbide composites prepared by sol-gel processing**

Mikrostruktura in mehanske lastnosti kompozitov ogljik/ogljik-silicijev karbid, pripravljenih po sol-gel metodi

K. Krnel, Z. Stadler, T. Kosmač ..... 435

**Study of the microstructure and oxidation behavior of YSZ and YSZ/Al<sub>2</sub>O<sub>3</sub> TBCs with HVOF bond coatings**Študij mikrostrukture in vedenja pri oksidaciji YSZ in YSZ/Al<sub>2</sub>O<sub>3</sub> TBC z HVOF naneseeno zaščitno prevleko

A. C. Karaoglanlı, G. Erdoğan, Y. Kahraman, A. Türk, F. Üstel, İ. Özdemir ..... 439

**Microstructure development of the Ni-GDC anode material for IT-SOFC**

Razvoj mikrostrukture Ni-GDC anodnega materiala za srednjetermperaturne SOFC

K. Zupan, M. Marinšek ..... 445

**Modeling of PM10 emission with genetic programming**

Modeliranje emisije PM10 z genetskim programiranjem

M. Kovačič, S. Senčič ..... 453

**Effect of tempering on the room-temperature mechanical properties of X20CrMoV121 and P91 steels**

Vpliv popuščanja na mehanske lastnosti jekel X20CrMoV121 in P91 pri sobni temperaturi

F. Kafexhiu, F. Vodopivec, J. Vojvodič Tuma ..... 459

**Structure and properties of AlMgSi alloys after ECAP and POST-ECAP ageing**

Struktura in lastnosti zlitin AlMgSi, staranih pred ECAP in po njem

M. Fujda, M. Matvija, T. Kvačkaj, O. Milkovič, P. Zubko, K. Nagyová ..... 465

**Application of a Taguchi-based neural network for forecasting and optimization of the surface roughness in a wire-electrical-discharge machining process**

Uporaba Taguchijeve nevronske mreže za napovedovanje in optimiranje površinske hrapavosti pri postopku žične erozije

Y. Kazancoglu, U. Esme, M. K. Kulekci, F. Kahraman, R. Samur, A. Akkurt, M. P. Ipekci ..... 471

**Prediction of the thermodynamic properties for liquid Al-Mg-Zn alloys**

Napovedovanje termodinamičnih lastnosti tekoče zlitine Al-Mg-Zn

D. Živković, Y. Du, Lj. Balanović, D. Manasijević, D. Minić, N. Talijan ..... 477

**Friction-stir welding of aluminium alloy 5083**

Varjenje s trenjem in mešanjem aluminijeve zlitine 5083

D. Klobčar, L. Kosec, A. Pietras, A. Smolej ..... 483

**Influence of segregations on the fracture toughness  $K_{Ic}$  of high-strength spring steel**Vpliv izcejev na lomno žilavost  $K_{Ic}$  visokotrnostnega vzmetnega jekla

B. Senčič, V. Leskovšek ..... 489

**Mechanical and tribological characteristics of stir-cast Al-Si10Mg and self-lubricating Al-Si10Mg/MoS<sub>2</sub> composites**Mehanske in tribološke lastnosti z mešanjem ulitih kompozitov Al-Si10Mg in samomazalnih kompozitov Al-Si10Mg/MoS<sub>2</sub>

K. Somasundara Vinoth, R. Subramanian, S. Dharmalingam, B. Anandavel ..... 497

**Computer-aided modeling of the rubber-pad forming process**

Računalniško modeliranje preoblikovalnega procesa z vmesnikom iz gume

M. Benisa, B. Babic, A. Grbovic, Z. Stefanovic ..... 503

## STROKOVNI ČLANKI – PROFESSIONAL ARTICLES

**Effect of fly-ash amount and cement type on the corrosion performance of the steel embedded in concrete**

Učinek količine letečega pepela in vrste cementa na korozijo jekla v betonu

A. R. Boğa, İ. B. Topçu, M. Öztürk ..... 511

**Effect of the delta-ferrite content on the tensile properties in Nitronic 60 steel at room temperature and 750 °C**

Vpliv vsebnosti delta ferita na natezne lastnosti jekla Nitronic 60 pri sobni temperaturi in pri 750 °C

A. Gigović-Gekić, M. Oruč, S. Muhamedagić ..... 519

**Physical regularities in the cracking of nanocoatings and a method for an automated determination of the crack-network parameters**

Fizikalne zakonitosti pokanja nanoprevlek in metoda za avtomatsko določevanje parametrov mreže razpok

P. Maruschak, V. Gliha, I. Konovalenko, T. Vuherer, S. Panin ..... 525

**Laboratory assessment of micro-encapsulated phase-change materials**

Laboratorijska ocena mikroenkapsuliranih materialov s fazno premeno

M. Ostrý, R. Přikryl, P. Charvát, T. Mlčoch, B. Bakajová. .... 531

**Content of Cr and Cr (VI) in a welding fume by different Cr content in an experimental coating of a Cr-Ni rutile electrode**

Vsebnost Cr in Cr (VI) v varilnem dimu pri različni vsebnosti Cr v plašču rutilne elektrode Cr-Ni

R. Begić, M. Jenko, M. Godec, Č. Donik. .... 535

**Use of a two-dimensional pseudo-homogeneous model for the study of temperature and conversion profiles during a polymerization reaction in a tubular chemical reactor**

Uporaba dvodimenzionalnega psevdohomogenega modela za študij temperature in profila pretvorbe med reakcijo polimerizacije v cevastem kemijskem reaktorju

M. Marghsi, D. Benachour ..... 539

**Theoretical and experimental estimation of the working life of machine parts hard faced with austenite-manganese electrodes**

Teoretično in eksperimentalno ugotavljanje zdržljivosti strojnih delov, oplášenih s trdimi avstenitno-manganskimi elektrodami

V. Lazić, A. Sedmak, D. Milosavljević, I. Nikolić, S. Aleksandrović, R. Nikolić, M. Mutavdžić ..... 547

# IDENTIFICATION OF THE MATERIAL PARAMETERS OF A UNIDIRECTIONAL FIBER COMPOSITE USING A MICROMODEL

## IDENTIFIKACIJA PARAMETROV MATERIALA ENOSMERNEGA KOMPOZITA Z UPORABO MIKROMODELA

**Hana Srbová, Tomáš Kroupa, Robert Zemčík**

University of West Bohemia in Pilsen, Department of Mechanics, Univerzitní 22, 306 14 Plzeň, Czech Republic  
hsrbova@kme.zcu.cz

*Prejem rokopisa – received: 2011-10-20; sprejem za objavo – accepted for publication: 2012-02-14*

The paper is focused on the identification of material parameters of the constituents of an unidirectional carbon-epoxy long-fiber-reinforced composite. Simple tensile tests using thin coupons with various fiber orientations were performed and force-displacement diagrams were obtained. A model of a unit cell is created in MSC.Marc. Fibers are considered to form a non-linear, elastic, transversely isotropic material and the matrix is considered to be an elasto-plastic isotropic material. The unit cell is loaded by a uniaxial stress up to the same level of loadings as the experimental samples. The sum of the squared differences of displacements between the numerically and experimentally obtained force-displacement diagrams is minimized within an identification process. The parameters of the linear relation between the Young's modulus of fibers and strain in the fiber-axis direction, and three shape coefficients of the matrix work-hardening function are searched. The identification process is performed using the MSC.Marc, OptiSlang optimization software and Matlab.

**Keywords:** unidirectional fiber composite, non-linear behavior, optimization, identification, matrix work-hardening function, representative volume element, unit cell, micromodel

Cilj dela je bila identifikacija parametrov materiala za nadomestek pri enosmernem ogljik-epoksi dolgovlaknatem ojačenem kompozitu. Enostavni raztržni preizkusi z uporabo odrezkov z različno orientacijo vlaken so bili izvršeni in dobljeni so bili diagrami sila – pomik. Model z enotno celico je bil ustvarjen v MSC.Marc. Vlakna so bila upoštevana kot nelinearen elastičen, prečno izotropen material, matica pa je bila upoštevana kot elastoplastičen izotropen material. Vsota kvadratov razlik v pomiku med numerično in eksperimentalno doseženimi diagrami sila – deformacija je bila minimalizirana z identifikacijskim procesom. Iskani so bili parametri linearne odvisnosti med Young modulom vlaken in deformacijo v smeri osi vlaken ter trije oblikovni koeficienti za deformacijsko utrditev matice. Proces identifikacije je bil izvršen z uporabo MSC.Marc, OptiSlang-sofтверa za optimizacijo in Matlaba.

**Ključne besede:** enosmerni vlaknati kompozit, nelinearno vedenje, optimizacija, identifikacija, funkcija deformacijske utrditve matice, reprezentativni element volumna, celica enote, mikromodel

## 1 INTRODUCTION

Composite materials are widely used in all fields of industry such as aerospace, sport, automotive and transportation. Frequently used composites are based on a carbon-fibers and epoxy matrix for its high specific strength and stiffness. The knowledge of the material characteristics is crucial for the accuracy of the numerical models used in a designing process. The above type of composite shows a significant non-linear behavior. Therefore, complex non-linear material models must be used in order to achieve a good agreement with the experimental data even for the simple tensile tests. The modeling of large structures requires the use of macromodels, i.e., homogenized material models. The parameters of a macromodel can be assessed either by using a combination of a finite-element model with the mathematical optimization technique and experimental data or by using a micromodel of a unit-cell element, which is a periodically repeated volume fraction, with the knowledge of mechanical properties of all the constituents. A micromodel of the composite material

can be advantageous for deeper analyses of the phenomena such as the influence of heterogeneities or microdamage mechanisms, etc.

## 2 EXPERIMENT

Tensile tests of the thin coupons made of unidirectional long-fiber carbon-epoxy composite SE84LV-HSC-450-400-35 were performed on the testing machine ZWICK/ROELL Z050. The coupons were cut by a water jet from one large plate.

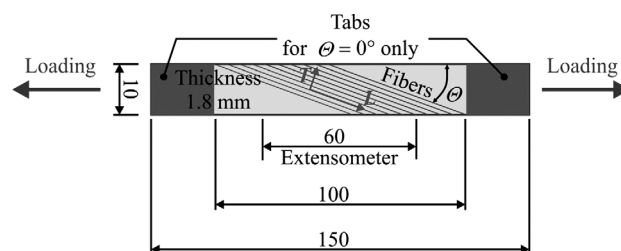


**Figure 1:** Geometry of composite coupons (mm) <sup>1</sup>

**Slika 1:** Geometrija odrezkov kompozita (mm) <sup>1</sup>

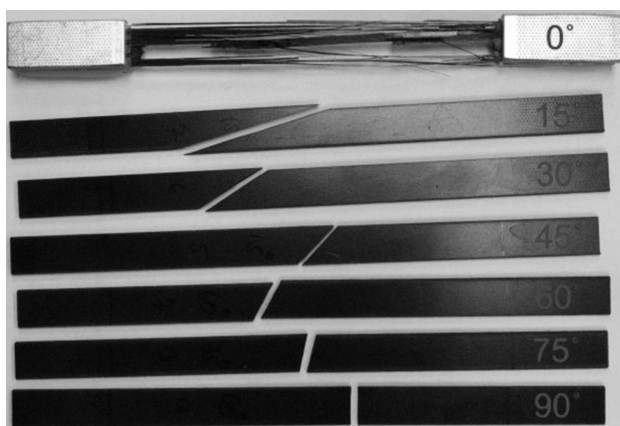


**Figure 2:** Cracked specimens with aluminum tabs<sup>1</sup>

**Slika 2:** Razpokani vzorci z aluminijevo podlago<sup>1</sup>

The fiber direction forms the angles of 0°, 15°, 30°, 45°, 60°, 75° and 90° with the direction of the loading force (**Figure 1**). There were 10 specimens tested for each angle. Cracked specimens<sup>1</sup> are shown in **Figure 2**. The specimens loaded along the fiber direction are fractured due to a fiber failure. All the specimens loaded at a different angle are fractured due to a matrix failure.

The resulting force-displacement diagrams are shown in **Figure 3**.

## 2.1 Micromodel

A finite-element model (micromodel) of a periodically repeated volume (unitcell, **Figure 4**) of the unidirectional composite material was created in the finite-element system MSC.Marc<sup>2</sup>. A perfect honeycomb distribution of the fibers and a fiber-volume ratio of 55% were assumed (**Table 1**).

**Table 1:** Geometry ratios of a unit cell

**Tabela 1:** Geometrična razmerja enotne celice

Fiber radius	$r$
Short side length	$1.28 r$
Long side length	$2.22 r$

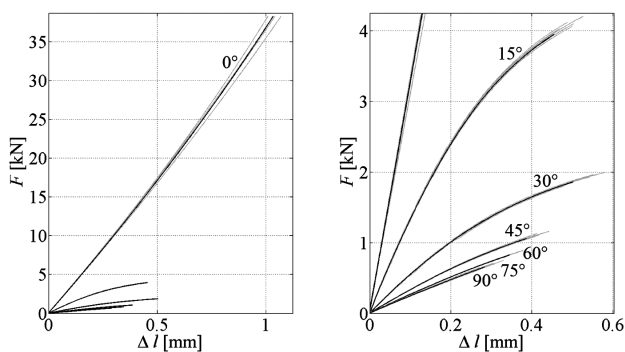


**Figure 3:** Measured force-displacement diagrams (grey) for each fiber angle and the corresponding averaged values (black)

**Slika 3:** Izmerjeni diagrami sila – pomik (sivo) za vsak kot vlakna in ustrezne povprečne vrednosti (črno)

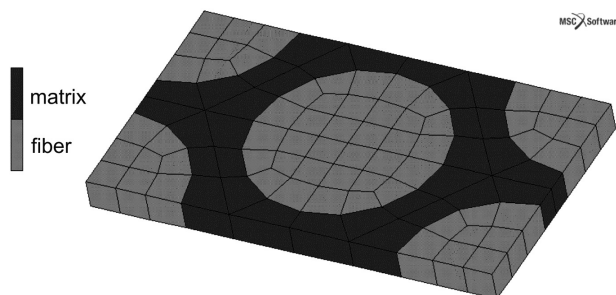


**Figure 4:** Three-dimensional mesh of a unit cell

**Slika 4:** Tridimenzionalna mreža enotne celice

Assuming the uniaxial stress across the whole specimen, the behavior of the material can be simulated by loading the unit cell with the normal stress  $\sigma$  corresponding to the external force  $F$ :

$$\sigma = \frac{F}{A} \quad (1)$$

where  $A$  is a cross-section of the specimen.

The global coordinate system ( $xyz$ ) is given with the force direction ( $x$ ) and the direction perpendicular to the composite surface ( $z$ ). The local coordinate system (123) is defined with the unit-cell edges, where the axis directions correspond to the fiber direction (1) and the directions perpendicular to it (**Figure 5**).

The loading force is transformed to the local coordinate system using the transformation:

$$\begin{bmatrix} \sigma_1 \\ \sigma_2 \\ \tau_{12} \end{bmatrix} = \begin{bmatrix} \cos^2 \varphi & \sin^2 \varphi & 2 \sin \varphi \cos \varphi \\ \sin^2 \varphi & \cos^2 \varphi & -2 \sin \varphi \cos \varphi \\ -\sin \varphi \cos \varphi & \sin \varphi \cos \varphi & \cos^2 \varphi \end{bmatrix} \begin{bmatrix} \sigma_1 \\ 0 \\ 0 \end{bmatrix} \quad (2)$$

where  $\varphi$  is the angle of rotation between the local and the global coordinate systems<sup>3</sup>.

The results from the finite-element analysis (strains) are transformed back to the global coordinate system using the transformation<sup>4</sup>:

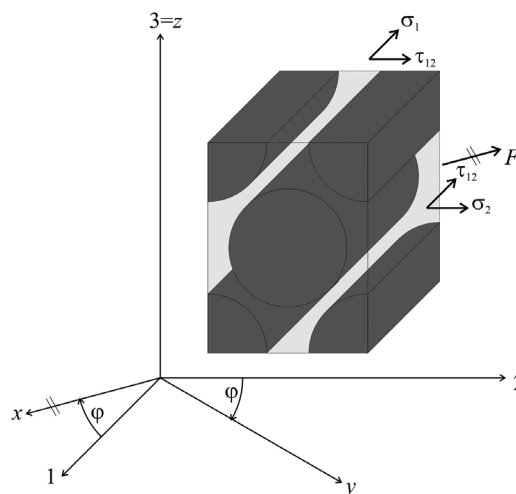


**Figure 5:** Rotated coordinate systems

**Slika 5:** Rotirani koordinatni sistem



$$\begin{bmatrix} \varepsilon_x \\ \varepsilon_y \\ \gamma_{xy} \end{bmatrix} = \begin{bmatrix} \cos^2 \varphi & \sin^2 \varphi & -\sin \varphi \cos \varphi \\ \sin^2 \varphi & \cos^2 \varphi & \sin \varphi \cos \varphi \\ 2 \sin \varphi \cos \varphi & -2 \sin \varphi \cos \varphi & \cos^2 \varphi - \sin^2 \varphi \end{bmatrix} \begin{bmatrix} \varepsilon_1 \\ \varepsilon_2 \\ \gamma_{12} \end{bmatrix} \quad (3)$$

The unit cell must also respect the periodical boundary conditions (shown schematically in **Figure 6**):

$$\begin{aligned} \Delta u &= u_B - u_A \\ \Delta v &= v_B - v_A \\ \Delta w &= w_B - w_A \end{aligned} \quad (4)$$

where  $\Delta u$ ,  $\Delta v$  and  $\Delta w$  are the translation differences of a pair of opposing nodes in directions 1, 2 and 3, respectively. These differences must remain constant for all the pairs of the corresponding nodes on the opposite sides<sup>3</sup>.

In MSC.Marc, the periodical boundary conditions were implemented using a combination of links defined in the Fortran subroutine and springs.

## 2.2 Material models

The experimental results from the tensile tests show a non-linear behavior of the composite even when loaded in the fiber direction (**Figure 1**). In order to capture this phenomenon a non-Hookean material model was considered for the fibers. The dependence of the longitudinal Young's modulus of fibers on strain is:

$$E_{11}(\varepsilon_{11}) = E_{11}^0 (1 + g\varepsilon_{11}) \quad (5)$$

where  $g$  is the coefficient describing the measure of non-linearity and  $E_{11}^0$  is the initial Young's modulus of fibers in the longitudinal direction<sup>5</sup>.

The fiber is modeled as a transversely isotropic material<sup>6,7</sup>. The standard material constants given by the manufacturer are in **Table 2**.

**Table 2:** Material parameters of the fiber given by the manufacturer  
**Tabela 2:** Parametri materiala vlakna, dobijeni od proizvajalca

$E_{11}^0$	(GPa)	230.00
$E_{22} = E_{33}$	(GPa)	15.00
$G_{12} = G_{23} = G_{31}$	(GPa)	50.00
$\nu_{12} = \nu$	(-)	0.30
$\nu_{31}$	(-)	0.02
$V_f$	(-)	0.55

The work-hardening function which respects a non-linear behavior of the matrix was proposed in the following form:

$$\sigma = \frac{E^m \varepsilon_p}{\left[ 1 + \left( \frac{E^m \varepsilon_p}{\sigma_0} \right)^n \right]^{\frac{1}{n}}} \quad (6)$$

where  $\varepsilon_p$  is an equivalent plastic deformation<sup>1</sup>. The matrix material was modeled to be isotropic having a Poisson's ratio of  $\nu^m = 0.3$  (given by the manufacturer).

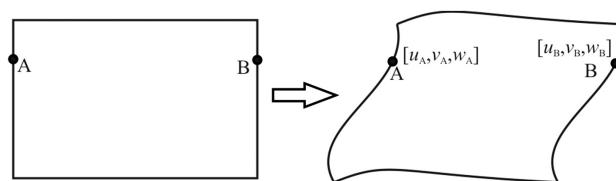


**Figure 6:** Equivalently deformed opposite boundaries of a heterogeneous unit cell

**Slika 6:** Ekvivalentno deformirane nasprotne meje heterogene enotne celice

**Table 3:** Identified material parameters

**Tabela 3:** Identificirani parametri materiala

$g$	(-)	23.23
$E_{11}^0$	(GPa)	189.93
$E^m$	(GPa)	7.17
$\sigma_0$	(kPa)	88.15
$n$	(-)	1.56
$\Delta\varphi$	(°)	-0.36

## 2.3 Identification process

The average curve for the experimentally obtained force-displacement diagrams was calculated for each angle of the fiber direction. These averaged diagrams are considered as target curves for the further analysis.

Hereafter, the unit cell was loaded with the stress components corresponding with the uniaxial loading of the samples (2). The unit cell is loaded up to the range corresponding to the maximum value of the loading force in the target curve. The displacement dependence on the axial force is obtained by transforming the unit-cell strains back to the global coordinate system (3).

The numerically obtained force-displacement diagrams are subsequently compared with the target force-displacement curves.

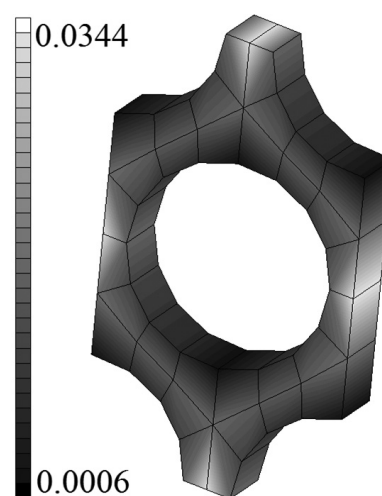


**Figure 7:** Equivalent plastic-strain contours in the matrix for  $\varphi = 30^\circ$  at the maximum load

**Slika 7:** Ekvivalenten kontur plastične deformacije matice za  $\varphi = 30^\circ$  pri največji obremenitvi

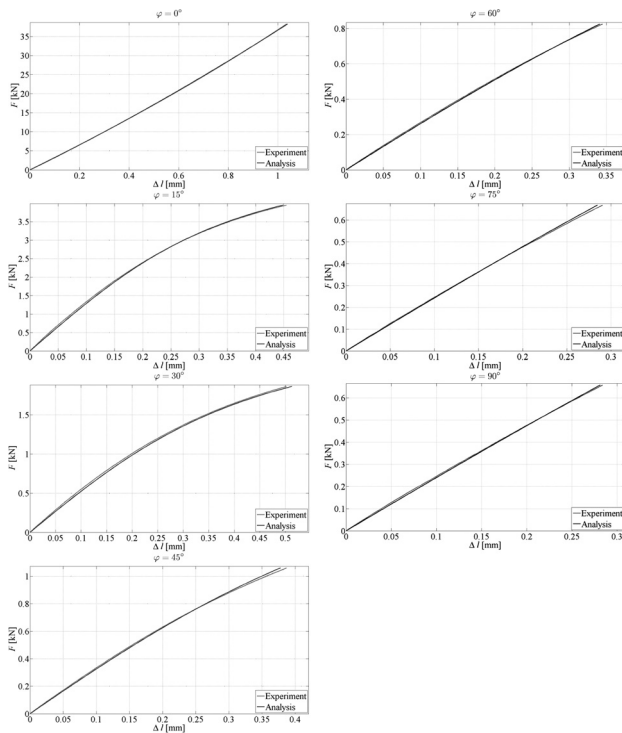


**Figure 8:** Comparison of the experimental and numerical force-displacement diagrams for all the angles  $\varphi$

**Slika 8:** Primerjava eksperimentalnih in numeričnih diagramov sila – pomik za vse kote  $\varphi$

An optimization process was performed using Matlab, the optimization system OptiSlang and MSC.Marc. The goal was to find the best combination of all material coefficients by minimizing the sum of the squared differences of the numerical and experimental displacements  $\Delta l$  calculated as:

$$e = \sum_{\varphi} e_{\varphi} = \sum_{\varphi} \sum_{i=1}^N \left[ \frac{(\Delta l_i^{\text{EXP}} - \Delta l_i^{\text{FEA}})^2}{\Delta l_N^{\text{EXP}}} \right] \quad (7)$$

Besides the material parameters from relations (5) and (6) an inaccuracy of the cutting of the samples was taken into account. This inaccuracy  $\Delta\varphi$  was attributed to the angle  $\varphi$  (**Figure 5**).

The identified material parameters are summarized in **Table 3**, an example of the plastic strain in the matrix is shown in **Figure 7**, and the resulting force-displacement diagrams are compared in **Figure 8**.

### 3 CONCLUSION

The tensile tests of the unidirectional fiber-reinforced carbon-epoxy composite coupons were performed for different angles of the fibers. A micromodel of the composite material was created. Parameters of the non-linear material models of both constituents (matrix and fibers) were identified in the optimization process. The parameters were identified by minimizing the error between numerically and experimentally obtained force-displacement diagrams. Moreover, a manufacturing inaccuracy during the specimen cutting was taken into account in the optimization.

Future research will be aimed at the effects of the material imperfections, such as fiber undulation or inclusions in the matrix, and the modeling of the material-failure processes.

### Acknowledgement

The work has been supported by the projects GA P101/11/0288 and the European project NTIS – New Technologies for Information Society No. CZ.1.05/1.1.00/02.0090.

### 4 REFERENCES

- <sup>1</sup> T. Kroupa, V. Laš, R. Zemčík, Improved Non-Linear Stress–Strain Relation for Carbon–Epoxy Composites and Identification of Material Parameters, *Journal of Composite Materials*, 45 (2011) 9, 1045–1057
- <sup>2</sup> MSC.Software Corporation: MSC.Marc User's Guide, 2000
- <sup>3</sup> H. Srbová, Analysis of fiber composite from micromechanics point of view (in Czech), Diploma thesis, University of West Bohemia, Plzeň
- <sup>4</sup> D. Roylance, Transformation of Stresses and Strains, Department of Materials Science and Engineering, Massachusetts Institute of Technology, Cambridge 2001
- <sup>5</sup> I. M. Djordjević, D. R. Sekulić, M. M. Stevanović, Non-Linear Elastic Behavior of Carbon Fibres of Different Structural and Mechanical Characteristic, *Journal of the Serbian Chemical Society*, 72 (2007) 5, 513–521
- <sup>6</sup> P. P. Camanho, C. G. Dávila, S. T. Pinho, J. J. C. Remmers, *Mechanical Response of Composites*, Springer – Verlag, 2008
- <sup>7</sup> V. Laš, *Mechanics of Composite Materials* (in Czech), University of West Bohemia, Plzeň

# MICROSTRUCTURE AND MECHANICAL PROPERTIES OF CARBON/CARBON-SILICON CARBIDE COMPOSITES PREPARED BY SOL-GEL PROCESSING

## MIKROSTRUKTURA IN MEHANSKE LASTNOSTI KOMPOZITOV OGLJIK/OGLJIK-SILICIJEV KARBID, PRIPRAVLJENIH PO SOL-GEL METODI

Kristoffer Krnel<sup>1</sup>, Zmago Stadler<sup>2</sup>, Tomaž Kosmač<sup>1</sup>

<sup>1</sup>Engineering Ceramics Department, Jožef Stefan Institute, Jamova 39, 1000 Ljubljana, Slovenia

<sup>2</sup>MS Production, Pot na Lisice 17, 4260 Bled, Slovenia  
kristof.krnel@ijs.si

*Prejem rokopisa – received: 2011-10-23; sprejem za objavo – accepted for publication: 2012-05-24*

In this work the preparation of a C/C composite with SiC precipitates in the matrix was studied. The formation of SiC particles in the matrix was achieved by substituting the phenolic resin used for the preparation of the composites with a phenolic resin-silica precursor prepared with the sol-gel method. The change of the matrix-phase composition resulted in improved mechanical properties of the composites which was attributed to the change in the interface between the matrix and the fibres. The silicon-carbide particles precipitating from the silicon containing a matrix are present directly at the interface increasing the bonding strength between the matrix and the fibres.

Keywords: ceramic-matrix composites, carbon fibres, silicon carbide, sol-gel methods, mechanical properties

V delu smo raziskovali pripravo C/C-kompozitov z izločki SiC v matrični fazi. SiC-delce smo pripravili z zamenjavo dela fenolne smole, ki se uporablja za pripravo kompozitov, s prekurzorjem fenolna smola-SiO<sub>2</sub>, ki smo ga pripravili po sol-gel metodi. Zaradi spremembe matrične faze so se izboljšale mehanske lastnosti materiala, kar smo pripisali spremembi na fazni meji med vlaknom in matrično fazo. Delci silicijevega karbida so se namreč izločali na površini vlaken in s tem povečali trdnost spoja med matrico in vlaknom.

Ključne besede: kompoziti s keramično matrico, ogljikova vlakna, silicijev karbid, sol-gel, mehanske lastnosti

## 1 INTRODUCTION

Non-oxide composites with a ceramic matrix (C/C, C/SiC and SiC/SiC) have aroused great interest in the past years as a high-temperature structural material for use as a construction material in modern engines, braking systems, gas turbines and heat exchangers.<sup>1,2</sup> On the one hand, we have C/C composites, which are, compared with the ceramic materials, relatively tough and elastic, but have low corrosion and wear resistance and lower thermal conductivity, and, on the other hand, there are C/SiC and SiC/SiC composites with good corrosion and wear resistance and higher thermal conductivity, but they are more rigid and brittle. Recently, new types of C/C-SiC composites were developed, which combine the good properties of all the above-mentioned systems.<sup>3</sup> These materials preserve the structure of a C/C composite in the core, which gives the material the required toughness and elasticity; however, on the surface there is a layer of a C/SiC composite with good corrosion and wear resistance, which makes it ideal for use in the advanced braking systems. The weakness of these materials is a thermal-expansion mismatch between C/C in the core and C/SiC on the surface leading to an intensive cracking of the surface layer, which is amplified also

because of the low thermal conductivity of the C/C core perpendicular to the carbon fibres leading to high-temperature differences between the surface and the core.<sup>4</sup>

The aim of this work was to prepare a C/C composite with SiC precipitates in the matrix since such precipitates can improve the mechanical properties and possibly improve the thermal conductivity of the matrix phase. The formation of SiC particles in the matrix was studied by substituting the phenolic resin used for the preparation of the composites with a phenolic-resin-silica precursor (a ceramic-forming polymer) prepared by the sol-gel method.<sup>5,6</sup> The microstructure and its influence on the mechanical properties of such composites were also investigated.

## 2 EXPERIMENTAL

The materials used in this study were as follows: for the preparation of all composites staple fibre fabrics (SGL Technik, Germany) were used. The samples of ceramic-matrix composites (CMCs) were prepared by impregnating the fabrics with a precursor produced via the sol-gel procedure from a phenolic resin (resolic type; Fenolit, Slovenia), TEOS (Acros Organic, USA), absolute ethanol (Carlo Erba Reagenti, Italy) and deionised



water with an addition of the mass fraction of concentrated HCl (37 %; Merck, Germany) used as a catalyst. 35.5 % of water was mixed with 33 % of ethanol and 1.5 % of HCl. 30 % of TEOS was added and the solution was mixed for 5 min to obtain a stable sol which was mixed with the phenolic resin for another 10 min in various ratios. The name of the samples, e.g. 50/50, denotes the mass ratio between the phenolic resin and the silica gel used for the preparation of the creamer to be 50 % phenolic resin and 50 % silica gel. All the samples were prepared with a polymer infiltration and pyrolysis process (PIP) with 5 subsequent impregnations and pyrolysis cycles. The carbonisation conditions were as follows: 950 °C, 2 h, a heating rate of 2 °C/min in Ar gas. An additional heat treatment at 1600 °C for 2 h in the flowing argon with a heating rate of 20 °C/min was conducted to allow the matrix phase to crystallise. All the samples were characterised by XRD (D4 Endeavor, Bruker AXS, Germany), scanning (JSM-5800, JEOL, Japan) and a transmission electron microscope (JEM-2000 FX, JEOL, Japan). The flexural strength was measured with a 3-point bending test with a span length of 80 mm (1362, Instron, UK).

### 3 RESULTS AND DISCUSSION

**Figure 1** shows the microstructures of the samples prepared from the precursor synthesised using the sol-gel procedure after the last cycle of the PIP process. In all

the figures the carbon fibres are surrounded by a brighter matrix phase that is rich in silicon. The presence of the silicon was confirmed using an EDXS analysis shown in **Figure 2**. In all the samples the presence of some porosity and inhomogeneity can be seen; there is almost no brighter, silicon-rich phase present in between the fibres in the fabric. The reason for this is a relatively high viscosity of the phenolic-resin-silica ceramer used for the impregnation of the fabrics and the spaces between the fibres, which are not well filled. They are only filled later, during the re-impregnation of the composite with a pure phenolic resin. The variation of the SiO<sub>2</sub>-gel/phenolic-resin ratio does not have any influence on the microstructures of the composites after the PIP process.

The microstructures of the samples after the crystallisation heat treatment at 1600 °C are shown in **Figure 3**. At this temperature the precipitation of small nanometric particles can be observed in the matrix phase, preferentially around the carbon fibres. There is also a relatively large amount of free carbon present. After the thermal treatment the influence of the SiO<sub>2</sub>-gel/phenolic-resin ratio can be observed, and with an increased amount of SiO<sub>2</sub> gel the number of SiC precipitates increases as well. The precipitates shown in **Figure 4** were analysed using transmission electron microscopy. The results are presented in **Figure 5**. Electron diffraction patterns of the nanocrystalline material, consisting of a few broadened rings and many scattered spots could not be easily analyzed, thus simulated electron-diffraction patterns of

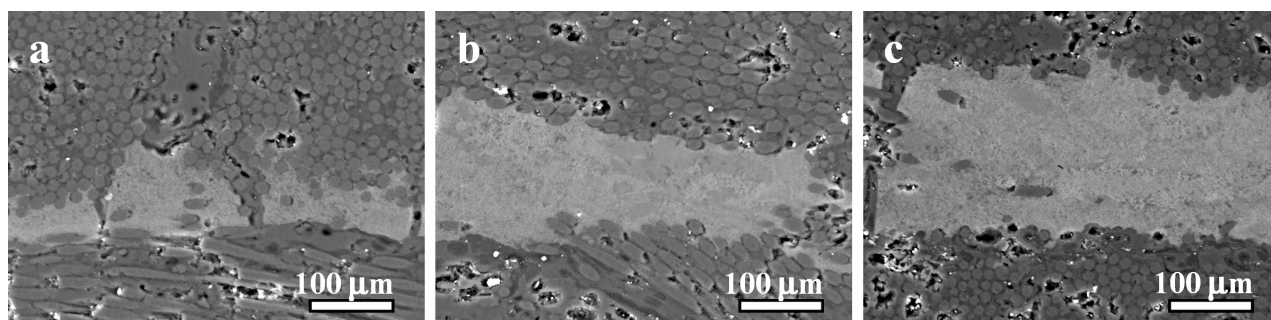


**Figure 1:** SEM microstructures of the samples prepared from a sol-gel precursor after PIP: a) sample CMC 70/30, b) sample CMC 60/40 and c) sample CMC 50/50

**Slika 1:** Mikrostruktura vzorca, pripravljenega iz sol-gel prekurzorja po PIP: a) vzorec CMC 70/30, b) vzorec CMC 60/40 in c) vzorec CMC 50/50

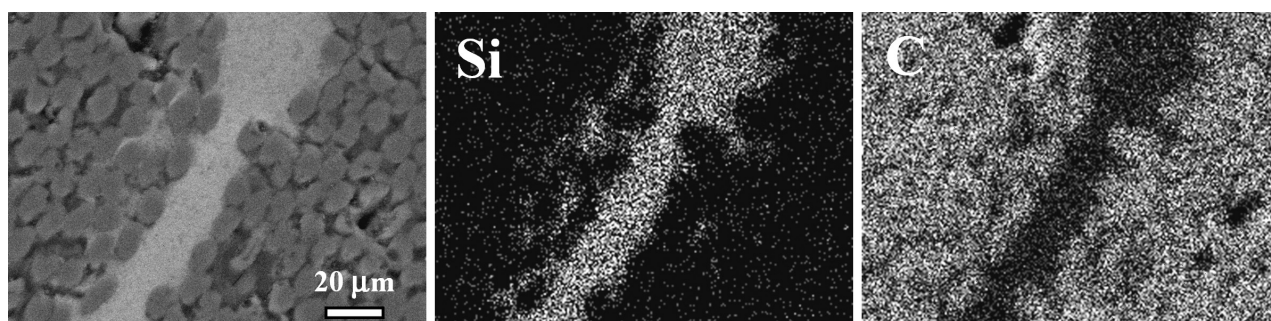


**Figure 2:** SEM microstructures and an EDX analysis of the CMC 50/50 sample after PIP

**Slika 2:** Mikrostruktura in EDS-analiza vzorca CMC 50/50 po PIP

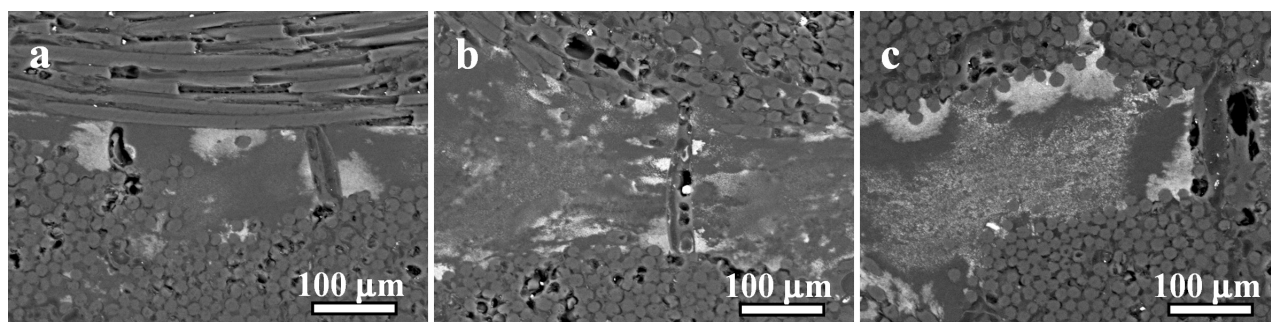


**Figure 3:** SEM microstructures of the samples prepared from a sol-gel precursor after crystallisation thermal treatment: a) sample CMC 70/30, b) sample CMC 60/40 and c) sample CMC 50/50

**Slika 3:** SEM-posnetek vzorcev, pripravljenih s sol-gel prekurzorjem po termični obdelavi: a) vzorec CMC 70/30, b) vzorec CMC 60/40 in c) vzorec CMC 50/50

possible candidates were calculated and compared to the experimental diffraction patterns. Based on these calculations it was concluded that nanocrystals have a structure of hexagonal (6H) silicon carbide that are embedded in an amorphous carbon matrix. The comparison of the experimental results with the calculated data for the nanocrystalline material is presented in **Figure 2b**.

In our first attempts the flexural strength of the samples prepared by using the phenolic-resin-silica ceramer was approximately the same as the flexural strength of C/C composites prepared by using only phenolic resin and the values were around 60 MPa.<sup>4</sup> However, the microstructure analysis showed that the samples prepared by using the phenolic-resin-silica precursor were more porous and contained larger amounts of inhomogenities. For that reason the new set of samples was prepared with more attention paid to the preparation step. The results of the flexural-strength measurements of the new, more homogenous samples, before and after the crystallisation thermal treatment, are presented in **Table 1**.

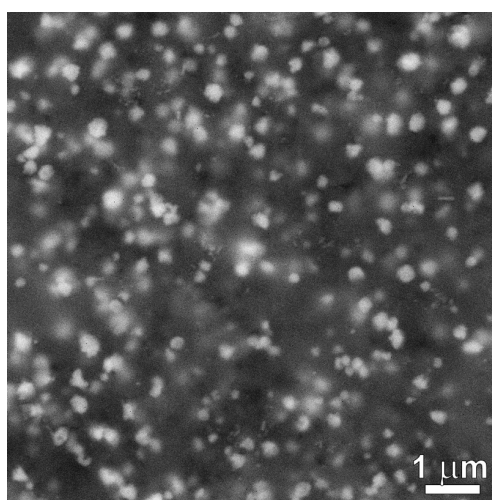


**Figure 4:** SEM microstructure of a carbon matrix showing nanosized precipitates

**Slika 4:** Mikrostruktura matrične faze, v kateri so vidni nanometrski izločki

The flexural strength of the samples prepared from the phenolic-resin-silica precursor is somewhat higher than that of the carbon-carbon composite prepared by using just a phenolic resin (sample CMC 100/0). These results are somewhat in contrast with the results of a similar study by Chen-Chi et al.<sup>7</sup> The presence of the silicon in the amorphous matrix changes the structure of the carbon-fibre-matrix interface and influences the strength. From the results it can also be seen that the crystallisation heat treatment further improves the strength of the composites prepared with the ceramer. The reasons for that are most probably the increased strength of the matrix phase as well as the increased strength of the interface between the fibres and the

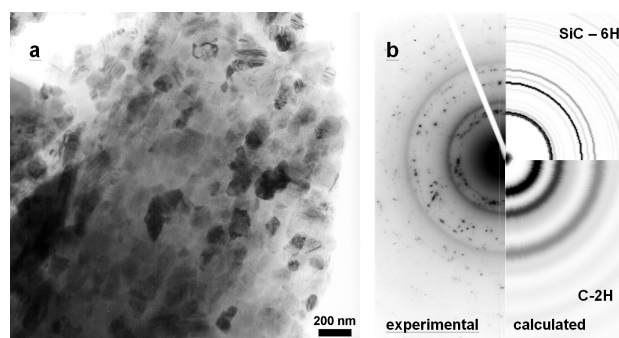


**Figure 5:** a) TEM microstructure showing nano-precipitates in the carbon matrix, b) experimental and calculated electron-diffraction patterns

**Slika 5:** a) TEM-posnetek, ki prikazuje nanoprecipitate v ogljikovi matrici, b) eksperimentalna ter izračunana elektronska difrakcija

**Table 1:** Flexural strength of the samples (SD) after their preparation via PIP and after additional heat treatment at 1600 °C for 2h in the flowing Ar

**Tabela 1:** Upogibne trdnosti vzorcev (in standardna deviacija) po pripravi preko PIP in dodatni termični obdelavi pri 1600 °C 2h v pretoku Ar

	CMC 100/0	CMC 70/30	CMC 60/40	CMC 50/50
Flexural strength after PIP (SD), MPa	59 (4)	62 (5)	67 (5)	69 (6)
Flexural strength after heat treatment (SD), MPa	58 (3)	68 (5)	72 (6)	73 (4)



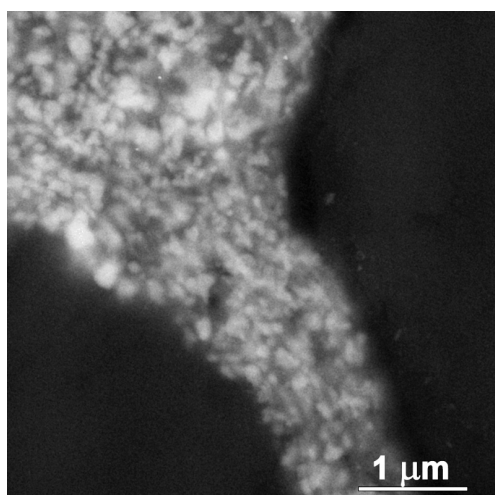


**Figure 6:** SEM microstructure of the carbon fibre/matrix interface  
**Slika 6:** Mikrostruktura fazne meje matrica/vlakno

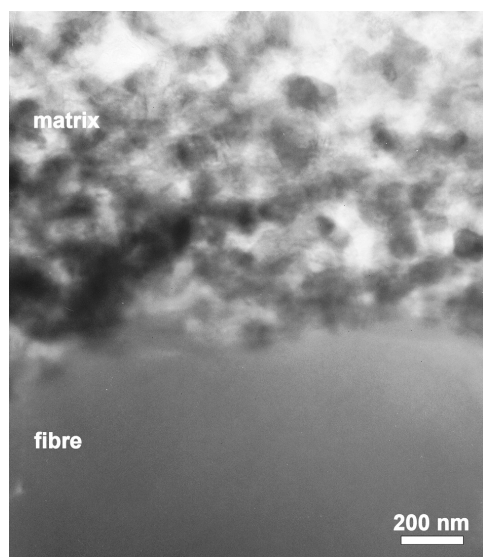


**Figure 7:** TEM microstructure of the carbon fibre/matrix interface  
**Slika 7:** TEM-posnetek fazne meje matrica/vlakno

matrix, resulting from the precipitation of the silicon-carbide particles around the fibres. In **Figure 6** the fibre/matrix interface of the CMC 50/50 sample is shown. The interface of the sample containing silicon carbide shows the presence of the SiC particles at the matrix-fibre interface that is influencing the strength of the interface resulting in a higher strength of the composite. The interface was analysed using also the trans-

mission electron microscope to verify the presence of the SiC particles at the interface. The micrograph of the interface between the fibre and the SiC particles containing the matrix is presented in **Figure 7**. It can be seen that the SiC particles are precipitating at the interface without any phase visible in between. Obviously, the interface between the matrix and the fibres is changed, which is affecting the mechanical properties of the composite. The bonding is stronger, but not too strong, so the pull-out of the fibres is still visible on the fracture surfaces of the samples. This effect is also the reason for high strength and toughness of these composite materials.

#### 4 CONCLUSIONS

The preparation of the C/C-SiC composites is possible by replacing the phenolic resin with a phenolic-resin-silica ceramer. In the case of the phenolic-resin-silica ceramer the matrix phase contained nanoprecipitates of SiC after the crystallisation heat treatment at 1600 °C in an inert atmosphere. The changing of the matrix phase improved the mechanical properties of the composites, which was attributed to the change in the interface between the matrix and the fibres. The silicon-carbide particles precipitating from the silicon containing a matrix are present directly at the interface increasing the bonding strength between the matrix and the fibres. The presence of the SiC particles on the interface was also confirmed by the TEM microscopy.

#### 5 REFERENCES

- <sup>1</sup> R. Naslain, Design, preparation and properties of non-oxide CMCs for application in engines and nuclear reactors: an overview, *Comp Sci Tech.*, 64 (2004), 155–170
- <sup>2</sup> W. J. Sherwood, CMCs Come Down to Earth, *Am Ceram Soc Bull.*, 82 (2003), 25–27
- <sup>3</sup> M. Zornik, EP 0 818 636 B1, Fahrzeugbrems- bzw. Fahrzeug-Kupplungsscheibe aus mit SiC beschichtetem C-C Werkstoff, 1997
- <sup>4</sup> K. Krnel, Z. Stadler, T. Kosmač, Preparation and properties of C/C-SiC nano-composites, *J Eur Ceram Soc.*, 27 (2007), 1211–1216
- <sup>5</sup> J. W. Li, J. M. Tian, L. M. Dong, Synthesis of SiC precursors by a two-step sol-gel process and their conversion to SiC powders, *J Eur Ceram Soc.*, 77 (2000), 1853–1857
- <sup>6</sup> J. M. Tian, J. W. Li, L. M. Dong, Synthesis of SiC precursors by sol-gel process, *J Inorg Mat.*, 14 (1999), 297–301
- <sup>7</sup> C. C. M. Ma, J. M. Lin, W. C. Chang, T. H. Ko, Carbon/carbon nanocomposites derived from phenolic resin – silica hybrid ceramers: microstructure, physical and morphological properties, *Carbon*, 40 (2002) 7, 977–984



## STUDY OF THE MICROSTRUCTURE AND OXIDATION BEHAVIOR OF YSZ AND YSZ/Al<sub>2</sub>O<sub>3</sub> TBCs WITH HVOF BOND COATINGS

### ŠTUDIJA MIKROSTRUKTURE IN VEDENJA PRI OKSIDACIJI YSZ IN YSZ/Al<sub>2</sub>O<sub>3</sub> TBC Z HVOF NANESENO ZAŠČITNO PREVLEKO

Abdullah Cahit Karaoglanlı<sup>1</sup>, Garip Erdoğan<sup>2</sup>, Yaşar Kahraman<sup>3</sup>, Ahmet Türk<sup>2</sup>,  
Fatih Üstel<sup>2</sup>, İsmail Özdemir<sup>1</sup>

<sup>1</sup>Department of Metallurgical and Materials Engineering, Bartın University, 74100 Bartın, Turkey

<sup>2</sup>Department of Metallurgical and Materials Engineering, Sakarya University, 54187 Sakarya, Turkey

<sup>3</sup>Department of Mechanical Engineering, Sakarya University, 54187 Sakarya, Turkey  
cahitkaraoglanli@gmail.com, karaoglanli@bartin.edu.tr

*Prejem rokopisa – received: 2011-11-11; sprejem za objavo – accepted for publication: 2012-03-27*

A significant improvement in efficiency has been achieved by using thermal barrier coatings (TBCs) in gas turbines and diesel engines. A typical TBC is a multilayered coating system that comprises an oxidation-resistant metallic bond coating (BC) and a thermally insulating ceramic top coating (TC). Under service conditions an Al<sub>2</sub>O<sub>3</sub> inter-layer, the thermally grown oxide (TGO), forms in the interface between the bond and the top coating, by a chemical reaction between the metallic aluminum from the BC material and the oxygen that comes from the environment through the pore channels of the TC. The aim of the present study is to describe the TGO formation on metallic bond coats deposited using the high-velocity oxygen fuel (HVOF) spraying technique. Therefore, TBCs that consist of a YSZ top (ZrO<sub>2</sub> + 8 % Y<sub>2</sub>O<sub>3</sub>) and YSZ-Al<sub>2</sub>O<sub>3</sub> double-layer systems with CoNiCrAlY bond coats were deposited on Inconel 718 super-alloy substrates. The bond coats were applied via HVOF, with the ceramic top coats being applied by atmospheric plasma spraying (APS) as well. The oxidation behaviors of the TBC systems were investigated. The oxidation tests were performed at 1000 °C in an air atmosphere for (8, 24, 50) h. The formation and growth of the TGO layers and the microstructural changes during the oxidation tests were scrutinized systematically. The results indicate that the TBC coating with the YSZ-Al<sub>2</sub>O<sub>3</sub> double layer had a higher oxidation resistance and a lower TGO layer growth than that of the traditional TBC system. Likewise, the initial state of the porosity plays a critical role in enhancing or limiting the growth of the TGO scale in the TBC.

**Keywords:** thermal barrier coatings (TBCs), oxidation behavior, thermally grown oxide (TGO), high-velocity oxygen fuel (HVOF), atmospheric plasma spraying (APS)

Doseženo je bilo občutno izboljšanje učinkovitosti plinskih turbin in dieselskih motorjev z uporabo toplotnih zaščitnih prevlek (TBC). Značilni TBC je večslojni varovalni sistem, ki vključuje prevleko, odporno proti oksidaciji, s kovinsko vezjo (BC) in toplotno izolativno keramično vrhno plastjo (TC). Pri obratovalnih razmerah vmesni sloj Al<sub>2</sub>O<sub>3</sub> omogoča nastanek oksidov (TGO) na stiku med vezivnim in vrhnjim slojem, s kemijsko reakcijo kovinskega aluminija iz BC-materiala in kisika, ki iz okolice prodira skozi pore TC. Namen te študije je opisati nastanek TGO na kovinskem vezivu, nanesenem z nabrizgavanjem s kisikovim plamenom z veliko hitrostjo (HVOF). TBC, ki sestoji na vrhu iz YSZ (ZrO<sub>2</sub> + 8 % Y<sub>2</sub>O<sub>3</sub>) ter z dvoslojnim sistemom YSZ-Al<sub>2</sub>O<sub>3</sub> z vezivno plastjo CoNiCrAlY so bili naneseni na podlago iz superzlitine Inconel 718. Vezivna plast je bila nanesena z HVOF, keramični vrhnji sloj pa z atmosfersko plazmo (APS). Preiskovane so bile značilnosti oksidacije TBC-sistema. Preizkusi oksidacije so bili izvršeni na zraku pri 1000 °C, za (8, 24 in 50) h. Med preizkusi oksidacije so bili sistematično preiskovani nastanek in rast TGO-plasti ter spremembe v mikrostrukturi. Rezultati kažejo, da ima TBC-prevleka YSZ-Al<sub>2</sub>O<sub>3</sub> z dvojnimi slojem boljšo odpornost proti oksidaciji in manjšo rast TGO-plasti v primerjavi z navadnim TBC-sistemom. Videti je, da ima začetna poroznost ključno vlogo pri pospeševanju ali zaviranju rasti TGO-plasti na TBC.

**Ključne besede:** termični varovalni sloj (TBC), vedenje pri oksidaciji, termična rast oksida (TGO), kisikov plamen z veliko hitrostjo (HVOF), atmosfersko plazemsko nabrizgavanje (APS)

## 1 INTRODUCTION

Many attempts have been made to understand the role of TGO, formed at the interface between the bond coat and the top coat during elevated-temperature service conditions, which strictly governs the lifetime of the TBC. The thickness, the roughness of the TGO, the adherence quality of the bond coat to the substrate, the type and shape of the oxides present in the vicinity of the TGO during oxidation are the main issues in controlling the degradation of the TBC<sup>1-4</sup>. Likewise, the oxidation behavior of the TBC is strongly linked to the bond coat properties, which affect the durability of the TBC. The

bond coat is deposited conventionally by LPPS, HVOF, plasma and also cold gas dynamic spray: a method recently preferred to avoid complex oxide formation as well<sup>5-8</sup>.

Generally, the forming of a dense, homogeneous,  $\alpha$ -Al<sub>2</sub>O<sub>3</sub> oxide scale is preferred as it is relatively stable, chemically and thermally, which means the degradation of the  $\alpha$ -Al<sub>2</sub>O<sub>3</sub> is negligible and also has a low ion diffusivity, which causes a slow growth rate and prevents further oxidation<sup>9-11</sup>. Oxidation-based damage, which is the result of stresses developed at the interface of the top coat and the bond coat during TGO growth, is a common failure of TBC since these stresses result in the

spallation-induced failure of the topcoat. In order to retard or avoid such a failure in the TBC, i.e., better oxidation resistance, any methods employed should facilitate the slow growth of the TGO scale, which favors good adherence of the TGO<sup>12–14</sup>. To achieve this, apart from employing several kinds of methods to deposit the bond coat, a thermal barrier thin film deposited by EB-PVD, CVD, etc. was employed over the bond coat in order to inhibit the formation of undesirable mixed oxides as they have a fast growth rate leading to accelerated TBC failure<sup>15–17</sup>.

In addition, the introduction of alumina powders to the YSZ might possibly reduce the inward diffusion of oxygen from the topcoat and thus make it difficult to have rapid growth of the TGO. It was claimed in studies that Al<sub>2</sub>O<sub>3</sub> present in the topcoat exhibited better oxidation resistance compared to the YSZ without Al<sub>2</sub>O<sub>3</sub> powders<sup>18,19</sup>. In this work, the YSZ topcoat with a conventional composition and with YSZ/Al<sub>2</sub>O<sub>3</sub> double-layer systems were applied on Inconel 718 super-alloy substrates to investigate and compare their oxidation behaviors. The oxidation results for the traditional TBC that has the YSZ system was compared with the YSZ/Al<sub>2</sub>O<sub>3</sub> double-layer TBC system. The microstructural differences and the formation and growth of the TGO layers in the isothermal oxidation resistance of these TBC systems are discussed.

## 2 EXPERIMENTAL METHODS

### 2.1 Materials and coating-deposition methods

The Inconel 718 Ni-based super-alloy, in disc-shaped coupons, was used as the substrate. Co<sub>38</sub>Ni<sub>32.5</sub>Cr<sub>21</sub>Al<sub>8</sub>Y<sub>0.5</sub>, ZrO<sub>2</sub>-8 % Y<sub>2</sub>O<sub>3</sub> and Al<sub>2</sub>O<sub>3</sub> powder were used as the starting materials. A Microtrack S3500 laser particle-size analyzer was used to determine the powder size distribution. The mean diameters were determined to be

$d_{50} = 33 \mu\text{m}$ ,  $38.52 \mu\text{m}$ ,  $33.36 \mu\text{m}$  for the CoNiCrAlY, ZrO<sub>2</sub>-8 % Y<sub>2</sub>O<sub>3</sub>, and Al<sub>2</sub>O<sub>3</sub> powders, respectively. Half of the TBC samples consisted of a CoNiCrAlY BC and a ZrO<sub>2</sub>-8 % Y<sub>2</sub>O<sub>3</sub> TC and the other half of the TBC samples were composed of a CoNiCrAlY BC, a ZrO<sub>2</sub>-8 % Y<sub>2</sub>O<sub>3</sub> TC and an Al<sub>2</sub>O<sub>3</sub> top coat over the YSZ. The HVOF technique was used to produce bond coats and the ceramic top coatings were produced by the APS method using a fully automated MultiCoat System from Sulzer Metco. All the spraying parameters are shown in **Table 1**.

### 2.2 Microstructural Characterization

The microstructures of the TBC systems were investigated by scanning electron microscopy (SEM, Tescan VEGA II, SBU Bruker EDX, Czech Republic). The porosity of the bond coatings was measured using optical image-analysis software (Olympus a4i). The coating microhardness (HV<sub>0.3</sub>) was determined using a microhardness tester (Shimadzu, Japan) with a load of 300 g for 15 s from the bond coats and the top coats. The oxidation tests of the TBC system produced were conducted by means of a high-temperature furnace (Nabertherm, Germany) with an air atmosphere.

## 3 RESULTS AND DISCUSSION

### 3.1 Microstructure of the powders and the coatings

Two types of TBC were prepared using the HVOF method to produce bond coats that included CoNiCrAlY. The APS method was used to produce ceramic top coats, which included traditional YSZ and a double layer of YSZ and Al<sub>2</sub>O<sub>3</sub> in which the Al<sub>2</sub>O<sub>3</sub> was a top coat over the YSZ in a second system. The thickness of the bond and the top coats of both systems were about 100  $\mu\text{m}$  and 300  $\mu\text{m}$ , respectively. The YSZ top coat used in the first system was 300  $\mu\text{m}$ . The YSZ and Al<sub>2</sub>O<sub>3</sub> ceramic top coatings used in the second system were both 150  $\mu\text{m}$ . The type, components, thicknesses and spray systems of the coating layers are shown in **Table 2**.

**Table 1:** Spraying parameters for deposition of the coatings

**Tabela 1:** Parametri nabrizgavanja pri nanašanju prevlek

HVOF CoNiCrAlY Bond Coatings	APS YSZ Top Coatings	APS Al <sub>2</sub> O <sub>3</sub> Over Top Coatings
Combustion medium	Voltage (Plasma)	Voltage (Plasma)
O <sub>2</sub> (880 L/min) and kerosene (25 L/h)	70 V	70 V
Powder Carrier Gas	Current (Plasma)	Current (Plasma)
Argon (15 L/min)	650 A	600 A
Powder Feed Rate	Carrier Gas	Carrier Gas
50 g/min	3 nlpm	2.5 nlpm
Powder feed gas flow	H <sub>2</sub> (Plasma)	H <sub>2</sub> (Plasma)
12 L/min	13 L/min	13 L/min
Stand-off distance	Argon (Plasma)	Argon (Plasma)
330 mm	45 L/min	45 L/min
	Spraying Distance	Spraying Distance
	100 mm	120 mm
	Traverse Speed	Traverse Speed
	300 mm/s	300 mm/s

**Table 2:** Type, components, thicknesses and spray systems of the coating layers

**Tabela 2:** Vrsta, komponente, deblina in sistem za nanašanje prevlek

Type of TBC system	Component	Thickness of layers, $\mu\text{m}$	Spray system
1	CoNiCrAlY	100	HVOF
	YSZ	300	APS
2	CoNiCrAlY	100	HVOF
	YSZ	150	APS
	Al <sub>2</sub> O <sub>3</sub>	150	APS

**Figure 1** shows the morphology of the as-received ZrO<sub>2</sub>+Y<sub>2</sub>O<sub>3</sub>, Al<sub>2</sub>O<sub>3</sub> and CoNiCrAlY powders. As can be seen from this figure, the CoNiCrAlY powder has a spherical morphology, while the Al<sub>2</sub>O<sub>3</sub> is angular. **Figures 2a** and **b** show the cross-sectional microstructure of

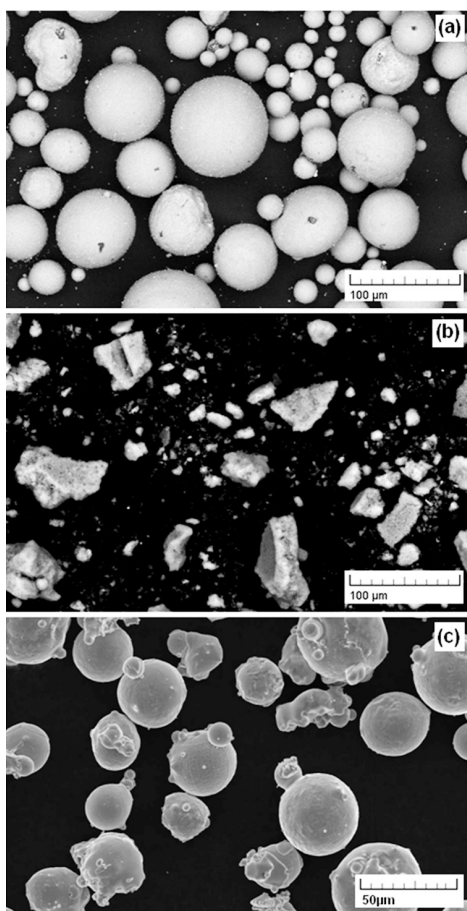


**Figure 1:** SEM micrographs of the morphology of: a)  $\text{ZrO}_2$ -8 %  $\text{Y}_2\text{O}_3$ , b)  $\text{Al}_2\text{O}_3$  and c) CoNiCrAlY powders

**Slika 1:** SEM-posnetek morfologije: a)  $\text{ZrO}_2$ -8 %  $\text{Y}_2\text{O}_3$ , b)  $\text{Al}_2\text{O}_3$  in c) CoNiCrAlY-prahov

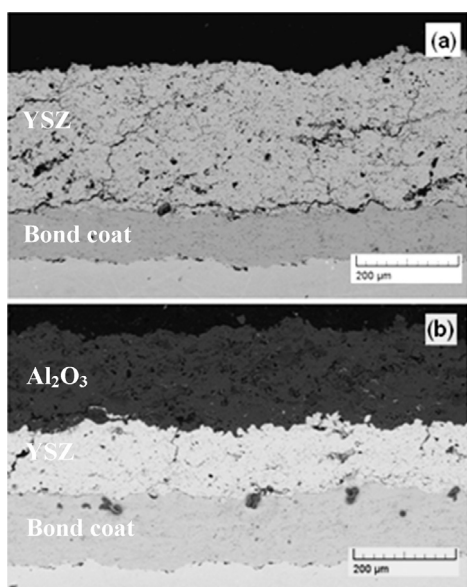


**Figure 2:** SEM micrographs of as-sprayed thermal barrier coatings: a) APS YSZ with HVOF bond coat and b) YSZ/ $\text{Al}_2\text{O}_3$  with HVOF bond coat system

**Slika 2:** SEM-posnetek nabriganega sloja toplotne prevleke: a) APS YSZ z HVOF vezivno plastjo in b) YSZ/ $\text{Al}_2\text{O}_3$  z HVOF vezivno plastjo

traditional TBC and  $\text{Al}_2\text{O}_3$ -YSZ gradient double layer TBC system. The HVOF-CoNiCrAlY bond coats have relatively less porosity and cracks in the TBCs.

The ceramic top coats contain porosity and some crack-like discontinuities during the spraying process. A smaller amount of porosity for the BC of both TBC systems was measured to be approximately 1.0 %. On the other hand, like for the top coat the porosity values were not significantly different from each other. The porosity level of the top coat was found to be approximately 5.0 % in both TBC systems. But as is clear from **Figure 2**, the size and distribution of the porosity in the TC of the two-layer YSZ/ $\text{Al}_2\text{O}_3$  TBC are quite different from the traditional values.

### 3.2 Oxidation tests

The TBC specimens were subjected to oxidation tests. These oxidation tests were carried out in an air atmosphere at 1000 °C for (8, 24 and 50) h. Typical SEM microstructures of the whole TBC-systems are shown in **Figures 3 and 4**.

As shown in these figures, the TGO was formed at the ceramic/bond-coat interface due to oxygen penetration through the ceramic layer. Various formations of

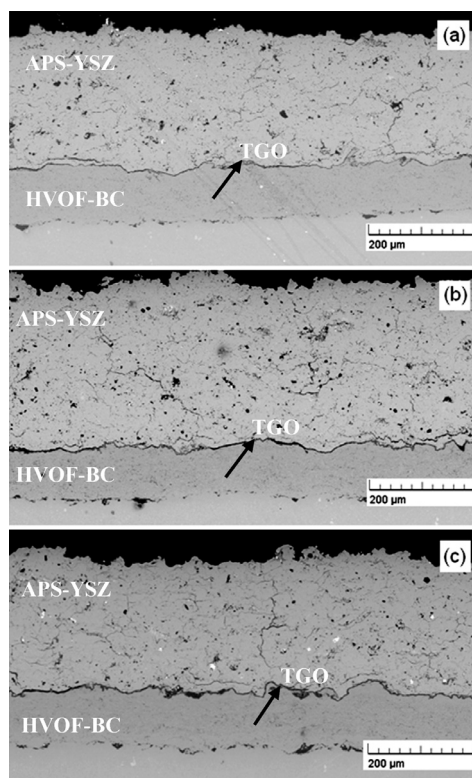


**Figure 3:** Cross-sectional microstructures at the bond coat/ceramic layer interface for YSZ top coats with CoNiCrAlY coatings after oxidation at 1000 °C for (8, 24, 50) h

**Slika 3:** Mikrostruktura prereza vezivne plasti/keramične plasti z vrhno plastjo YSZ za CoNiCrAlY-prevleko po oksidaciji (8, 24 in 50) h na 1000 °C



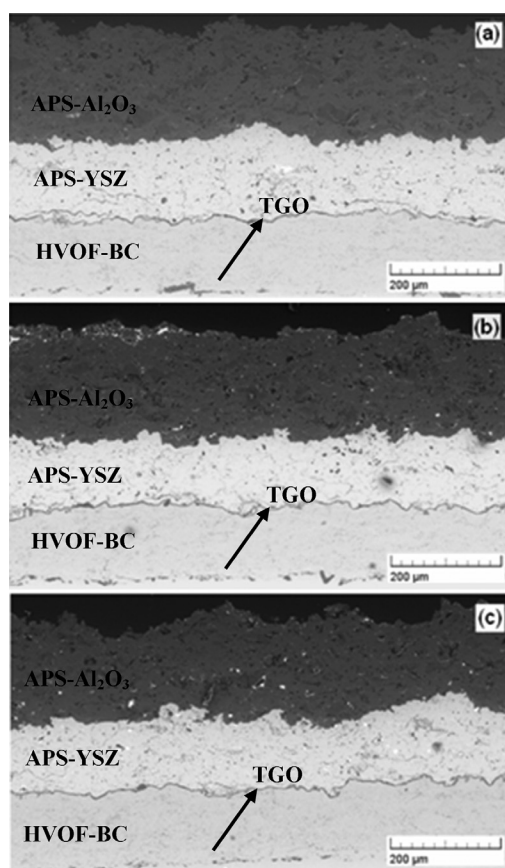


**Figure 4:** Cross-sectional microstructures at the bond coat/ceramic layer interface for YSZ/Al<sub>2</sub>O<sub>3</sub> top coats with CoNiCrAlY coatings after oxidation at 1000 °C for (8, 24, 50) h

**Slika 4:** Mikrostruktura prereza vezivne plasti/keramične plasti z vrhnjo plastjo YSZ/Al<sub>2</sub>O<sub>3</sub> za CoNiCrAlY-prevleko po oksidaciji (8, 24 in 50) h na 1000 °C

discontinuities between the bond layer and the ceramic top layer can be clearly seen in **Figures 3 and 4**.

When the oxidation properties of the two different TBC systems are compared, it was clear that the oxidation in the conventional TBC system (CoNiCrAlY bond layer with YSZ top coat) developed faster than that of the YSZ/Al<sub>2</sub>O<sub>3</sub> double-layer TBC system, and the TGO growth rate in the former system was found to be higher. As seen from the interface microstructures given in **Figure 5**, the TGO structure in the YSZ/Al<sub>2</sub>O<sub>3</sub> double-layer TBC system is more uniform and is mainly composed of Al<sub>2</sub>O<sub>3</sub>, which was confirmed by an EDX analysis. In the conventional YSZ system, due to the increasing oxidation process, complex oxides developed in the TGO layer and affected the growth behaviors of the TGO. This was caused by the prevention of the oxygen penetration to the bond coat from the surface due to the Al<sub>2</sub>O<sub>3</sub> layer and hence a slowing down of the oxygen attack in YSZ/Al<sub>2</sub>O<sub>3</sub> coating systems. As a result, the decrease of the Al<sub>2</sub>O<sub>3</sub> content in the TGO layer caused by bond-coat oxidation is delayed, the degradation of the uniform structure is retarded and in this way an increase in the volume of the TGO occurs at

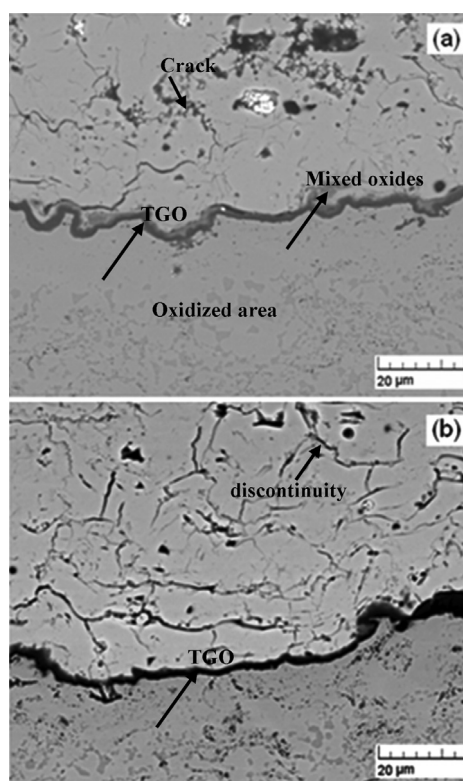


**Figure 5:** Microstructures at the bond coat/ceramic-layer interface after oxidation at 1000 °C for 50 h; a) TGO in traditional YSZ coating; b) TGO in YSZ/Al<sub>2</sub>O<sub>3</sub> coating

**Slika 5:** Mikrostruktura stika vezivne plasti/keramične plasti po oksidaciji 50 h na 1000 °C; a) TGO in navadna YSZ-plast; b) TGO in YSZ/Al<sub>2</sub>O<sub>3</sub>-plast

a lower rate. Similar results showing an increase in the oxidation resistance of the coatings due to the Al<sub>2</sub>O<sub>3</sub> layer depending on the temperature and the time exist in the literature<sup>18,20–25</sup>.

**Figure 6** indicates that the thickness of the TGO layer increased with increasing exposure time for both

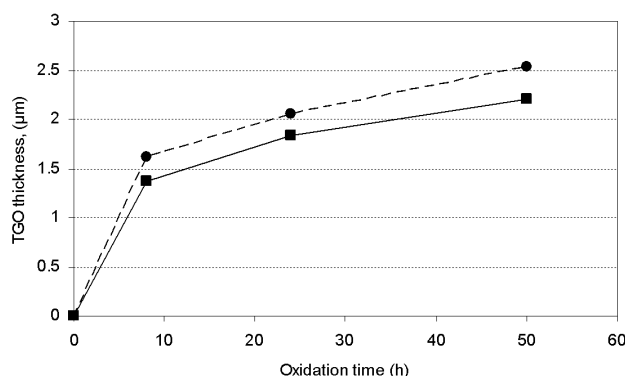


**Figure 6:** TGO thickness measurements as a function of oxidation time at 1000 °C, respectively (● YSZ top coatings with CoNiCrAlY bond coatings, ■ YSZ/Al<sub>2</sub>O<sub>3</sub> top coatings with CoNiCrAlY bond coatings)

**Slika 6:** Debelina TGO v odvisnosti od časa oksidacije pri 1000 °C (● vrhnja plast YSZ z vezivno plastjo CoNiCrAlY, ■ vrhnja plast YSZ/Al<sub>2</sub>O<sub>3</sub> z vezivno plastjo CoNiCrAlY)

kinds of TBC specimens. The specimens with the YSZ top coatings with CoNiCrAlY bond coatings show a higher rate of TGO thickness growth than the samples with YSZ/Al<sub>2</sub>O<sub>3</sub> top coatings with CoNiCrAlY bond coatings. This difference could be attributed to the initial porosity state of the as-sprayed TBC samples and/or the Al<sub>2</sub>O<sub>3</sub> layer acting as a diffusion barrier due to its low diffusion coefficient for oxygen ions. This effect has been observed in many other studies<sup>20–25</sup>.

Therefore, the greater the increase of the TGO thickness of the specimen with traditional YSZ top coatings with CoNiCrAlY bond coatings at the same exposure time compared to the specimen YSZ/Al<sub>2</sub>O<sub>3</sub> top coatings with HVOF-BC could be attributed to this mechanism. After increasing the exposure time the TGO layer thickness increased to higher values.

### 3.3 Mechanical properties

The microhardness value for the bond and top coats were taken from the average value of all the measurement points. **Figures 7 and 8** present the Vickers microhardness measurements before and after the oxidation tests for the bond and the top layers. The bottom and top limit lines in the graph show the maximum and minimum hardness values. The microhardness of the substrate Inconel 718 super-alloy was in the range 310–340 HV.

The mean values of the bond and top-coat microhardness changed before and after the oxidation tests with increasing time. The microhardness of the bond coats decreased with increasing time at 1000 °C for traditional and two-layered coatings. The decline in microhardness of the bond coatings was possibly linked to the decrease in the density of the bond coats. The

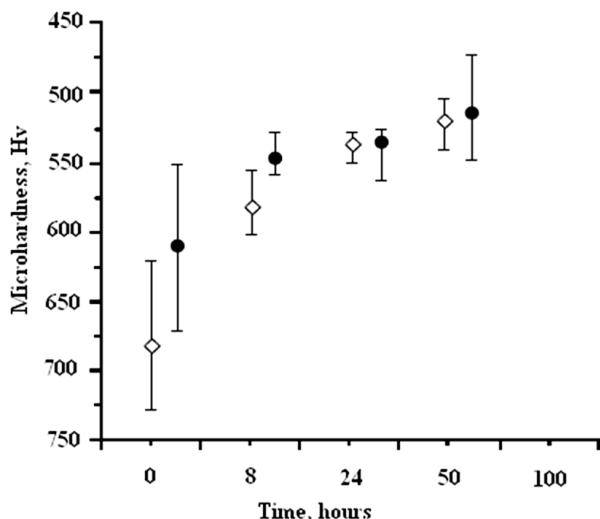


**Figure 7:** Microhardness values of bond coats for two kinds of TBCs, respectively (◇ CoNiCrAlY bond coats with YSZ top layer, ● CoNiCrAlY bond coats with YSZ/Al<sub>2</sub>O<sub>3</sub> top layer)

**Slika 7:** Vrednosti mikrotvrdoće vezivnih plasti za dve vrste TBC, (◇ vezivna plast CoNiCrAlY z vrhnjo plastjo YSZ, ● vezivna plast CoNiCrAlY z vrhnjo plastjo YSZ/Al<sub>2</sub>O<sub>3</sub>)

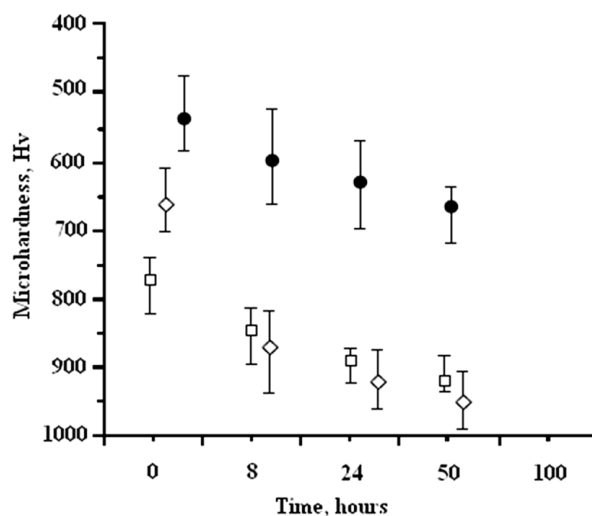


**Figure 8:** Microhardness values of top coats for two kinds of TBCs, respectively (□ YSZ top coats with CoNiCrAlY bond layer, ● YSZ top coats with YSZ/Al<sub>2</sub>O<sub>3</sub> top layer and CoNiCrAlY bond layer, ◇ Al<sub>2</sub>O<sub>3</sub> top coats with YSZ/Al<sub>2</sub>O<sub>3</sub> top layer and CoNiCrAlY bond layer)

**Slika 8:** Vrednosti mikrotvrdoće za dve vrste TBC, (□ vrhnja plast YSZ z vezivno plastjo CoNiCrAlY, ● vrhnja plast YSZ z vrhnjo plastjo YSZ/Al<sub>2</sub>O<sub>3</sub> in vezivno plastjo CoNiCrAlY, ◇ vrhnja plast Al<sub>2</sub>O<sub>3</sub> z vrhnjo plastjo YSZ/Al<sub>2</sub>O<sub>3</sub> in vezivno plastjo CoNiCrAlY)

decrease of the microhardness in the HVOF bond coats is related to the thermal relaxation of the residual stress present in the as-sprayed coating due to the high temperature. The fact that the decrease in microhardness after 8 h is higher while the decrease after 24 h is lower and no change is observed after 50 h should support this theory, i.e., thermal relaxation occurs very quickly, and since almost no change in microhardness is observed after 8 h it can be concluded that this initial change is due to thermal relaxation.

The microhardness of the top coats increased with increasing time at 1000 °C for the traditional and two-layered ceramic coatings. According to the literature, the situation mentioned above is caused by the decreasing density of the porosity and the increasing density of the ceramic top coating depending on increasing time<sup>26</sup>.

## 4 CONCLUSIONS

Traditional YSZ and YSZ/ Al<sub>2</sub>O<sub>3</sub> double-layer TBCs were produced using the APS technique and bond coats were deposited using the HVOF spraying technique. The following results were obtained:

During oxidation of the TBCs, the TGO layer was formed along the interface of the BC/TC layer. The thickness of the TGO in the traditional YSZ coating is higher in comparison with the YSZ/Al<sub>2</sub>O<sub>3</sub> coating after oxidation at 1000 °C for different oxidation times. According to the TGO growth in both TBC systems, the TGO thickening became steady state in the YSZ/Al<sub>2</sub>O<sub>3</sub> two-layer system and, on the other hand, the TGO

thickness in the traditional TBC system was still increasing.

The different formations of the discontinuities between the bond and the ceramic top layers were observed. The ceramic top coats contained porosity and some crack-like discontinuities for both kinds of TBC. After a prolonged oxidation time the number of cracks was much larger in the traditional YSZ ceramic top coat with the CoNiCrAlY bond coating system. The initial porosity state of the as-sprayed TBC samples and/or the acting of the  $\text{Al}_2\text{O}_3$  layer as a diffusion barrier at high temperatures have a great influence on determining the TGO growth, since they change the penetration behavior of the oxygen from the surface. In the conventional YSZ system, due to the increasing oxidation process, complex oxides developed in the TGO layer and affected the growth behaviors of the TGO. The mean values of the bond and top-coat microhardnesses changed before and after the oxidation tests with increasing time. The microhardness of the bond coats decreased and that of the top coats increased with increasing time at 1000 °C for the traditional and two-layered coatings.

## 5 REFERENCES

- A. G. Evans, D. R. Mumma, J. W. Hutchinson, G. H. Meier, F. S. Pettit, Mechanisms controlling the durability of thermal barrier coatings, *Progress in Materials Science*, 46 (2001) 5, 505–553
- Y. Li, C. J. Li, Q. Zhang, G. J. Yang, C. X. Li, Influence of TGO Composition on the Thermal Shock Lifetime of Thermal Barrier Coatings with Cold-sprayed MCrAlY Bond Coat, *Journal of Thermal Spray Technology*, 19 (2010) 1–2, 168–177
- W. R. Chen, R. Archer, X. Huang, B. R. Marple, TGO Growth and Crack Propagation in a Thermal Barrier Coating, *Journal of Thermal Spray Technology*, 17 (2008) 5–6, 858–864
- L. Swadźba, G. Moskal, B. Mendala, T. Gancarczyk, Characterisation of air plasma sprayed TBC coating during isothermal oxidation at 1100 °C, *Journal of Achievements in Materials and Manufacturing Engineering*, 21 (2007) 2, 81–84
- W. J. Brindley, Properties of Plasma-Sprayed Bond Coats, *Journal of Thermal Spray Technology*, 6 (1997) 1, 85–90
- Y. Li, C. J. Li, G. J. Yang, L. K. Xing, Thermal fatigue behavior of thermal barrier coatings with the MCrAlY bond coats by cold spraying and low-pressure plasma spraying, *Surface and Coatings Technology*, 205 (2010), 2225–2233
- W. O. Soboyejo, P. Mensah, R. Diwan, J. Crowe, S. Akwabo, High temperature oxidation interfacial growth kinetics in YSZ thermal barrier coatings with bond coatings of NiCoCrAlY with 0.25 % Hf, *Materials Science and Engineering A*, 528 (2011), 2223–2230
- S. Saeidi, K. T. Voisey, D. G. McCartney, The Effect of Heat Treatment on the Oxidation Behavior of HVOF and VPS CoNiCrAlY Coatings, *Journal of Thermal Spray Technology*, 18 (2009) 2, 209–216
- N. Mu, T. Izumi, L. Zhang, B. Gleeson, Compositional Factors Affecting the Oxidation Behavior of Pt-Modified  $\gamma$ -Ni+ $\gamma'$ -Ni<sub>3</sub>Al-Based Alloys and Coatings, *Materials Science Forum*, 239 (2008) 595–598, 239–247
- P. Richer, M. Yandouzi, L. Beauvais, B. Jodoin, Oxidation behaviour of CoNiCrAlY bond coats produced by plasma, HVOF and cold gas dynamic spraying, *Surface and Coatings Technology*, 204 (2010), 3962–3974
- Q. Zhang, C. J. Li, C. X. Li, G. J. Yang, S. C. Lui, Study of oxidation behavior of nanostructured NiCrAlY bond coatings deposited by cold spraying, *Surface and Coatings Technology*, 202 (2008), 3378–3384
- J. A. Thompson, T. W. Clyne, The effect of heat treatment on the stiffness of zirconia top coats in-plasma sprayed TBCs, *Acta Mater.*, 49 (2001), 1565–1575
- J. A. Haynes, M. K. Ferber, W. D. Porter, Thermal Cycling Behavior of Plasma-Sprayed Thermal Barrier Coatings with Various MCrAlX Bond Coats, *Journal of Thermal Spray Technology*, 9 (2000) 1, 38–48
- F. H. Yuan, Z. X. Chen, Z. W. Huang, Z. G. Wang, S. J. Zhu, Oxidation behavior of thermal barrier coatings with HVOF and detonation-sprayed NiCrAlY bond coats, *Corrosion Science*, 50 (2008), 1608–1617
- J. R. V. Garcia, T. Goto, Thermal barrier coatings produced by chemical vapor deposition, *Science and Technology of Advanced Materials*, 4 (2003), 397–402
- F. Pedraza, C. Tuohy, L. Whelan, A. D. Kennedy, High Quality Aluminide and Thermal Barrier Coatings Deposition for New and Service Exposed Parts by CVD Techniques, *Materials Science Forum*, 461–464 (2004), 305–312
- M. H. Li, X. F. Sun, S. K. Gong, Z. Y. Zhang, H. R. Guan, Z. Q. Hu, Phase transformation and bond coat oxidation behavior of EB-PVD thermal barrier coating, *Surface and Coatings Technology*, 176 (2004), 209–214
- M. Saremi, A. Afrasiabi, A. Kobayashi, Microstructural analysis of YSZ and YSZ/ $\text{Al}_2\text{O}_3$  plasma sprayed thermal barrier coatings after high temperature oxidation, *Surface and Coatings Technology*, 202 (2008), 3233–3238
- Q. Yu, A. Rauf, C. Zhou, Microstructure and Thermal Properties of Nanostructured 4 %  $\text{Al}_2\text{O}_3$ -YSZ Coatings Produced by Atmospheric Plasma Spraying, *Journal of Thermal Spray Technology*, 19 (2010) 6, 1294–1300
- Kh. G. S. Thomas, U. Dietl, Thermal barrier coatings with improved oxidation resistance, *Surface and Coatings Technology*, 68/69 (1994), 113–115
- Q. Yu, A. Rauf, C. Zhou, Microstructure and Thermal Properties of Nanostructured 4 %  $\text{Al}_2\text{O}_3$ -YSZ Coatings Produced by Atmospheric Plasma Spraying, *Journal of Thermal Spray Technology*, 19 (2010) 6, 1294–1300
- C. Ren, Y. D. He, D. R. Wan, Fabrication and Characteristics of YSZ-YSZ/ $\text{Al}_2\text{O}_3$  Double-Layer TBC, *Oxidation of Metals*, 75 (2011), 325–335
- J. Müller, M. Schierling, E. Zimmermann, D. Neuschütz, Chemical vapor deposition of smooth  $\alpha$ - $\text{Al}_2\text{O}_3$  films on nickel base superalloys as diffusion barriers, *Surface and Coatings Technology*, 120–121 (1999), 16–21
- H. Bolta, F. Koch, J. L. Rodet, D. Karpov, S. Menzel,  $\text{Al}_2\text{O}_3$  coatings deposited by filtered vacuum arc-characterization of high temperature properties, *Surface and Coatings Technology*, 116–119 (1999), 956–962
- A. C. Karaoglanli, E. Altuncu, I. Ozdemir, A. Turk, F. Ustel, Structure and durability evaluation of YSZ +  $\text{Al}_2\text{O}_3$  composite TBCs with APS and HVOF bond coats under thermal cycling conditions, *Surface and Coatings Technology*, 205 (2011) 2, 369–S373
- H. Guo, X. Bi, S. Gong, H. Xu, Microstructure Investigation On Gradient Porous Thermal Barrier Coating Prepared By EB-PVD, *Scripta Mater.*, 44 (2001), 683–687



## MICROSTRUCTURE DEVELOPMENT OF THE Ni-GDC ANODE MATERIAL FOR IT-SOFC

### RAZVOJ MIKROSTRUKTURE Ni-GDC ANODNEGA MATERIALA ZA SREDNJETEMPERATURNE SOFC

Klementina Zupan, Marjan Marinšek

Faculty of Chemistry and Chemical Technology, University of Ljubljana, Aškerčeva 5, 1000 Ljubljana, Slovenia  
klementina.zupan@fkkt.uni-lj.si

*Prejem rokopisa – received: 2011-12-02; sprejem za objavo – accepted for publication: 2012-03-02*

The NiO-GDC-based material is a potential candidate for an anode material for the low-temperature SOFCs. In this work a modified combustion synthesis was used for the preparation of NiO-GDC. The main advantage of the preparation method employed was that after the synthesis both phases, NiO and GDC, in the ash product were randomly distributed on a nanometre scale. The citrate-nitrate ( $c/n$ ) ratios in the combustion-reaction mixtures varied from 0.15 to 0.18. The prepared powders were isostatically pressed into pellets, sintered at 1200 °C, 1250 °C, 1300 °C, 1350 °C or 1400 °C, reduced and subsequently submitted to a microstructure analysis. The crystallite sizes of both phases in the as-prepared powders, as well as the grain sizes of nickel in the final reduced samples greatly depended on the slight variation of the  $c/n$  ratio in the starting reaction gel mixture. In the as-synthesized samples, crystallite sizes were calculated to be 4.3 nm or 40.0 nm for the GDC phase and 7.6 nm or 48.0 nm for the NiO phase for the samples with the  $c/n$  ratios of 0.15 or 0.18, respectively. After sintering under different conditions and reductions, the final average particle size of Ni varied from 71 nm to 146 nm or from 143 nm to 254 nm, while the average size of GDC grains ranged from 84 nm to 193 nm or from 96 nm to 247 nm for the samples with the  $c/n$  ratios of 0.15 or 0.18, respectively. The temperatures from 1200 °C to 1250 °C were recognized as the most appropriate temperature interval that provided good connectivity between the grains and the smallest one-phase regions in the final Ni-GDC cermets with an average Ni-particle diameter of around 70 nm.

**Keywords:** combustion synthesis, nanocomposites, microstructure, fuel cells, Ni-GDC

Materiali na osnovi NiO-GDC spadajo med potencialne kandidate za izdelavo anod v srednjetermperaturnih SOFC. NiO-GDC smo pripravili z modificirano zgorevalno sintezo. Največja prednost metode je ta, da sta po sintezi obe fazi NiO in GDC naključno porazdeljeni na nanometrijskem nivoju. Citratno-nitratno razmerje  $c/n$  v reakcijskih zmesih je bilo 0,15 in 0,18. Pripravljeni prah smo po sintezi izostatsko stisnili v tablete, jih sintrali pri temperaturah 1200 °C, 1250 °C, 1300 °C, 1350 °C in 1400 °C, reducirali ter izvedli kvantitativno analizo mikrostruktur. Razmerje  $c/n$  v začetni raztopini močno vpliva na velikost kristalinitov faz (NiO in GDC) v vzorcu po sintezi, kot tudi na velikost zrn faz v sintranih in reduciranih vzorcih. Najmanjša nikljeva zrna (povprečna velikost okoli 70 nm) v končnem Ni-GDC-kompozitu keramika-kovina so nastala po sintranju in kasnejši redukciji v temperaturnem intervalu med 1200 °C in 1250 °C.

**Gljučne besede:** zgorevalna sinteza, nanokompoziti, mikrostruktura, gorivne celice, Ni-GDC

## 1 INTRODUCTION

Fuel cells are environmentally friendly energy converters that can transform chemical energy directly to electricity, resulting in high-energy conversion efficiencies. Solid-oxide fuel cells (SOFCs) have several advantages over the other types of fuel cells, including flexibility of the fuels used, high-reaction kinetics due to high-temperature operation and relatively inexpensive materials formed in thin layers. However, the high-temperature operation results in a number of inherent challenges, such as mechanical stress, electrode sintering and low start-up time. First, it is difficult to obtain gas-tight seal between the chambers. Moreover, an addition of a large amount of steam to hydrocarbon fuels is required to avoid carbon deposition on the anode, resulting in a complicated water management in the SOFC systems.<sup>1,2</sup>

One approach to overcoming the above challenges is to reduce the operating temperatures of SOFCs to 800 °C or less to enable the metal materials (stainless steels) to be used as interconnect materials.<sup>3,4</sup> Another approach

towards addressing the above challenges is to design an SOFC with only one gas chamber. This type of SOFC is called a "single chamber SOFC" (SC-SOFC), wherein both anode and cathode are exposed to the same fuel-oxidant gas mixture. As a result, the gas-sealing problem can be inherently avoided since no separation between fuel and air is required, while carbon deposition is less of a problem due to the presence of a large amount of oxygen in the mixture. Materials used as the components in two-chamber SOFCs (LSM strontium-doped lanthanum manganite as a cathode, yttrium stabilized zirconia-YSZ as an electrolyte and Ni-YSZ cermet as an anode) are not appropriate for the use in an SC-SOFC due to their insufficient selectivity toward electrode reactions under operating conditions. However, there are only a few materials selective enough that can operate at the temperatures below 700 °C. Currently the most widely adopted SC-SOFC materials are gadolinium stabilized ceria (GDC) as electrolyte, Ni-GDC as anode and strontium-doped samarium cobaltite (SSC) as cathode. GDC is a better oxygen ionic conductor than

YSZ, as it has a higher ionic conductivity than YSZ in the temperature range from 300 °C to 700 °C.

Anode materials are usually prepared by mechanically mixing the separately synthesized powders of NiO and GDC that were formed, sintered and reduced to obtain Ni-GDC cermets.<sup>5–7</sup> In this way, an accurate chemical composition can be attained, but it is rather difficult to achieve a uniform distribution of separate phases in the anode composite that will result in a non-homogeneous structure and a poor anode performance. However, homogeneous composite powders of NiO-GDC were synthesized using a hydroxide co-precipitation.<sup>8,9</sup> The co-precipitation method is still a solution-based technique with several consecutive steps and, as such, it is rather time consuming. Consequently, the preparation of complex metal oxides by using combustion synthesis has recently become an interesting area of research based on the promising results of this technique surpassing the conventional method.<sup>10,11</sup> The main advantage of the combustion synthesis is the ability to produce complex oxide powders directly from the precursor solution. Therefore, the combustion synthesis could be, in principle, a good method for preparing the composite powder of Ni-GDC with a uniform distribution of fine Ni particles within the GDC framework.

The aim of this work was a synthesis and a subsequent thermal treatment of nano-scaled highly sinterable NiO-GDC dispersions prepared with the citrate-nitrate combustion synthesis technique. High sinterability of the prepared powders is of the prime importance for the preparation of dense bodies at the relatively low temperatures (close to 1200 °C). With an examination of the densification process of such ceramic powders, we also demonstrated a microstructure evolution from the synthesized NiO-GDC nano-powder to the Ni-GDC anode cermet.

## 2 EXPERIMENTAL PROCEDURES

The NiO-GDC powders were prepared with a modified citrate-nitrate combustion synthesis. The combustion system was based on the citrate-nitrate redox reaction. In this combustion method, the starting substances were  $\text{Ni}(\text{NO}_3)_2 \cdot 6\text{H}_2\text{O}$ ,  $\text{Ce}(\text{NO}_3)_3 \cdot 6\text{H}_2\text{O}$  and  $\text{Gd}(\text{NO}_3)_3 \cdot 6\text{H}_2\text{O}$ , nitric acid (65 %) and citric acid (analytical reagent grade). All solid compounds were dissolved with minimum additions of water in the amounts that allowed the Ni volume content in the final composite to be 50 %. The  $\text{Ce}(\text{NO}_3)_3 \cdot 6\text{H}_2\text{O}$  and  $\text{Gd}(\text{NO}_3)_3 \cdot 6\text{H}_2\text{O}$  additions were found to allow the GDC composition to be  $\text{Ce}_{0.8}\text{Gd}_{0.2}\text{O}_{1.9}$ . The reactive mixture was prepared by mixing the five reactant solutions and then kept over a water bath at 60 °C under vacuum ( $p = 5\text{--}7$  mbar) until it transformed into a light green gel (at least 5 hours). The initial citrate/nitrate molar ratios in the starting solution were 0.15 and 0.18. The corresponding citrate-nitrate gel was then gently milled in an agate

mortar and uni-axially pressed into pellets ( $\Phi = 12$  mm,  $h = 30$  mm,  $p = 17$  MPa). These samples were placed on a corundum plate and ignited at the top of the pellet with a hot tip to start an auto-ignition reaction. The samples were characterized by the X-ray powder diffraction technique using a PANalytical X'Pert PRO MPD apparatus. Data were collected in the  $2\theta$  range from 20° to 70° in steps of 0.033° for 1 s/°. After the synthesis, powders were milled in an agate mortar, uni-axially pressed into pellets (100 MPa) and subsequently also iso-statically pressed (750 MPa). Formed pellets were sintered at different temperatures (1200 °C, 1250 °C, 1300 °C, 1350 °C and 1400 °C) for 2 hours. Material shrinkage during the sintering was measured separately using a BÄHR DIL 802 dilatometer. For the microstructure determination, the sintered tablets were polished (3  $\mu\text{m}$  and 0.25  $\mu\text{m}$  diamond pastes), thermally etched, reduced at 900 °C (2 h) in an  $\text{H}_2/\text{Ar}$  atmosphere and subsequently analyzed with SEM FE Zeiss ULTRA plus. The quantitative analyses of the microstructures were performed on digital images (images were digitized into pixels with 255 different grey values) using the Zeiss KS300 3.0 image-analysis software.

## 3 RESULTS AND DISCUSSION

The main benefit of the combustion synthesis is the exothermic effect during the fuel (citrate) and nitrate redox reaction that is accompanied by a considerable gas release preventing the formation of hard agglomerates. The combustion reaction takes just a few seconds to turn a reaction mixture into the final product, while a much longer time is required for the same process to be conducted during the calcination process. In the case of an NiO-GDC citrate-nitrate self-sustaining reaction, the maximum temperature gradient (i.e., the heating rate)

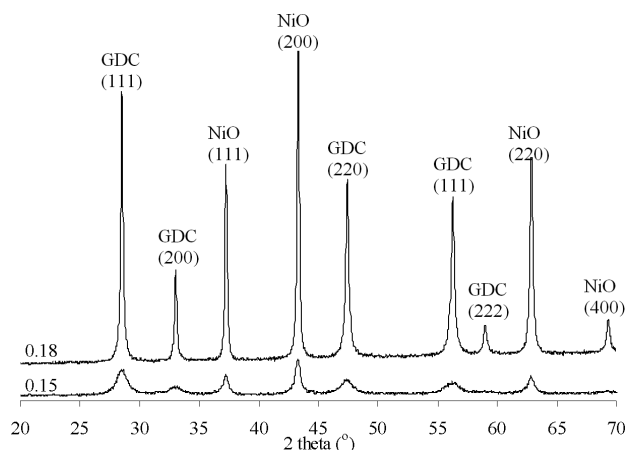


**Figure 1:** XRD diffraction spectra of the as-prepared powder mixtures of NiO-GDC (obtained from the reactive gels with  $c/n = 0.15$  or  $c/n = 0.18$ )

**Slika 1:** Rentgenska praškovna posnetka vzorcev NiO-GDC, pripravljenih iz raztopin s citratno-nitratnim razmerjem  $c/n = 0,15$  in  $c/n = 0,18$

inside the reaction zone (calculated on the basis of the temperature-profile measurements) was  $1164 \text{ K s}^{-1}$ . Such a high temperature gradient and short reaction times resulted in a unique powder mixture composed of nano-sized particles. The one-phase particle size and the degree of crystallization were found to be the functions of the citrate-nitrate initial ratio. In both samples ( $c/n = 0.18$  or  $0.15$ ) the two main phases corresponded to GDC and NiO (**Figure 1**). According to the Scherrer X-ray broadening of the peaks, the average crystallite sizes were calculated to be 4.3 nm and 40 nm for GDC and 7.6 nm and 48 nm for NiO for the samples with the  $c/n$  ratios of 0.15 and 0.18, respectively.

The ideal microstructure of the final Ni-GDC cermet is composed of very small grains of both phases (preferably sub-micrometre or nano-sized), where GDC mainly acts as a matrix to support the Ni electro-catalyst and hinder its fusion under the cell operating conditions. At the same time, GDC is also used to extend the Ni-GDC-gas triple-phase boundary (TPB) into the anode. The length of the TPB is related to the reaction rate for the electrochemical oxidation of hydrogen<sup>12,13</sup> in an operating fuel cell. For this reason, Ni-GDC also has to exhibit continuity of both phases throughout the cermet, since it must serve both as an electronically and ionically conductive material. In principle, high conductivity is achieved when a good contact between particles is ensured; this is normally accomplished through sintering. However, sintering also means grain growth, which is in contradiction to the desire to preserve the NiO-GDC nano-distribution. However, if the sintering temperatures required for the NiO-GDC densification can be lowered, then fine oxide mixtures can also be preserved in the sintered structures.

The determined sintering temperature of the prepared NiO-GDC mixture was influenced by a slight variation of the citrate-nitrate ratio (0.15 or 0.18) in the starting solutions. Being sintered at a significantly lower

temperature ( $T_{\text{sinter}} = 1120 \text{ }^{\circ}\text{C}$  for the sample with the  $c/n$  ratio of 0.15 and  $T_{\text{sinter}} = 1280 \text{ }^{\circ}\text{C}$  for the sample with the  $c/n$  ratio of 0.18), the sample 0.15 sinters through two consecutive stages as a result of the inter- and/or intra-agglomerate sintering, while the shrinkage in sample 0.18 can be described with only one broad densification process (**Figure 2**).

The relatively low sintering temperature determined for the sample with the  $c/n$  ratio of 0.15 may be very important from the applicability point of view, since a single cell is normally prepared in several sintering processes. First, the anode and electrolyte layers are co-sintered at higher temperatures (up to  $1400 \text{ }^{\circ}\text{C}$ ) and then the cathode layer is applied and co-sintered at the temperatures of up to  $1200 \text{ }^{\circ}\text{C}$ . Successful sintering of the NiO-GDC anode material at the temperatures below  $1200 \text{ }^{\circ}\text{C}$  may result in diverse SOFC-preparation procedures, in which all the layers are co-sintered in a single step.

In order to obtain more detailed information about the microstructure development, the NiO-GDC green bodies prepared from the as-synthesized powders were sintered under various sintering conditions. Sintering temperatures were defined according to the obtained shrinkage curves. The presented microstructures (**Figure 3**) revealed that the nano-sized cermet mixture was no longer present in the sintered and, subsequently, reduced cermets. Instead, the one-phase dominance grew, but remained well within the sub-micrometre range if the cermets had been sintered at the relatively low temperatures. Additionally, it is evident that a fine distribution of phases (metal, ceramic and porosity) can be obtained when using the sintering temperatures no higher than  $1200\text{--}1250 \text{ }^{\circ}\text{C}$  for the samples with a  $c/n$  ratio of 0.15, in which GDC serves as a continuous framework, within which the sub-micrometre Ni grains and pores are dispersed. However, in the case of the samples with a  $c/n$  ratio of 0.18 (sintered at  $1200 \text{ }^{\circ}\text{C}$  and  $1250 \text{ }^{\circ}\text{C}$ ) an excessive grain growth of the newly formed metallic Ni particles (during the reduction) may be found. This phenomenon is a consequence of a fairly different surface energy of Ni and GDC, causing the hetero-grains at the interface to lose their chemical affinity.

Consequently, the coarsening of the Ni phase proceeds appreciably due to a poor adhesion of the metal to the ceramic material at the elevated temperatures. From a practical point of view, an excessive growth of the Ni grains results in the TPB length reduction. In the samples with a  $c/n$  ratio of 0.18, the grain growth of Ni was noticeable, while in the samples with a  $c/n$  ratio of 0.15, the grain growth of both phases (in the reduced state) was controlled predominantly with the sintering temperature and no excessive enlargement of Ni-grains, after the reduction, was observed.

Dense structures after sintering ensure good contact between the particles and a continuity of both phases

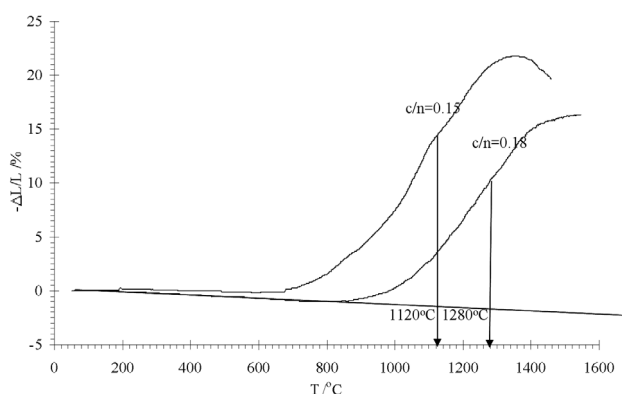


**Figure 2:** Relative shrinkage versus temperature of the NiO-GDC tablets (iso-statically pressed) prepared from the reaction mixtures with the  $c/n$  ratios of 0.18 or 0.15

**Slika 2:** Relativni skrčak NiO-GDC izostatsko stisnjenih vzorcev, pripravljenih iz reakcijskih zmesi s citratno-nitratnim razmerjem  $c/n$  0,18 in 0,15



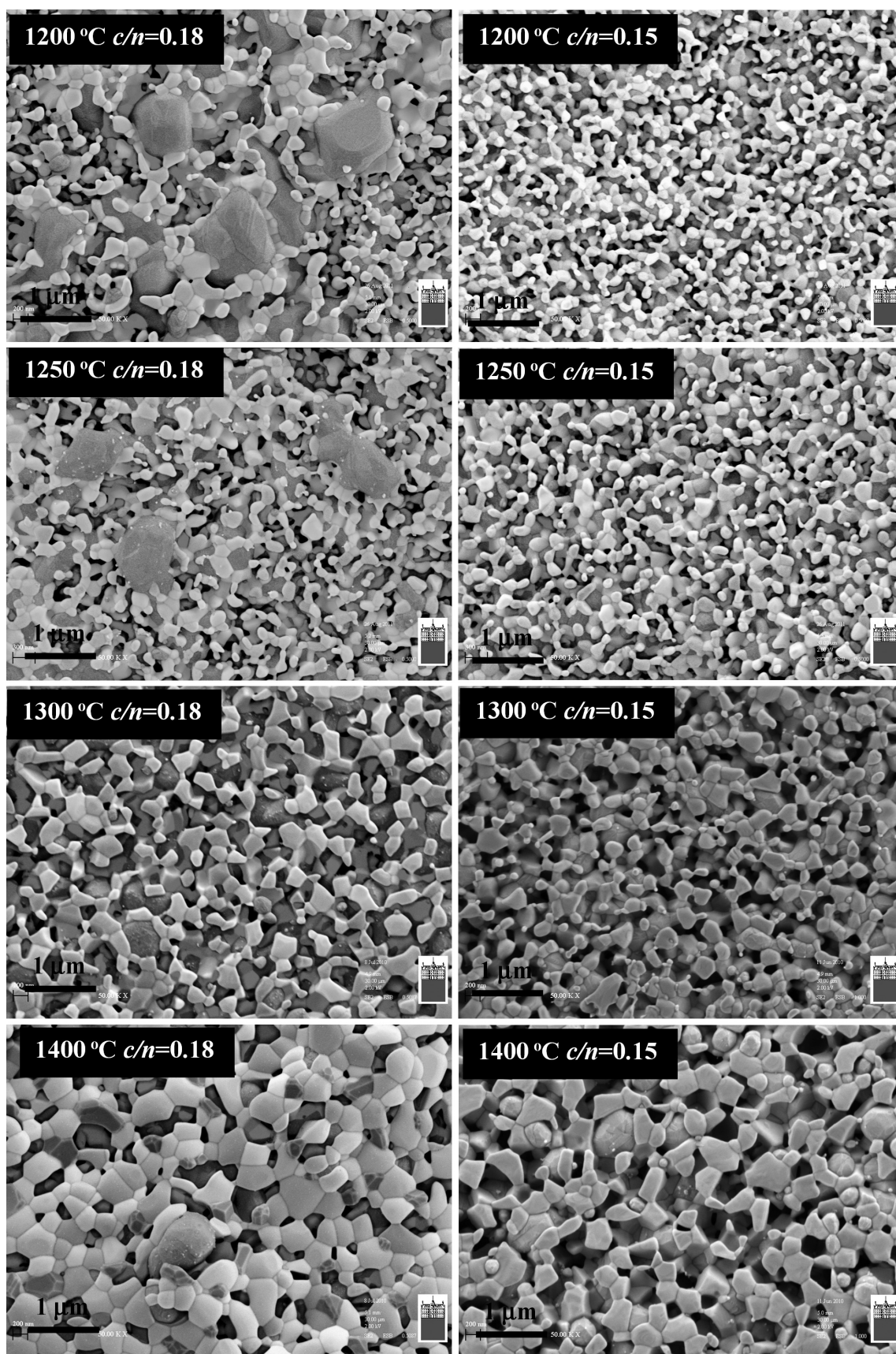


**Figure 3:** Microstructures of the sintered Ni-GDC samples after the reduction  
**Slika 3:** Mikrostrukture sintranih vzorcev Ni-GDC po redukciji



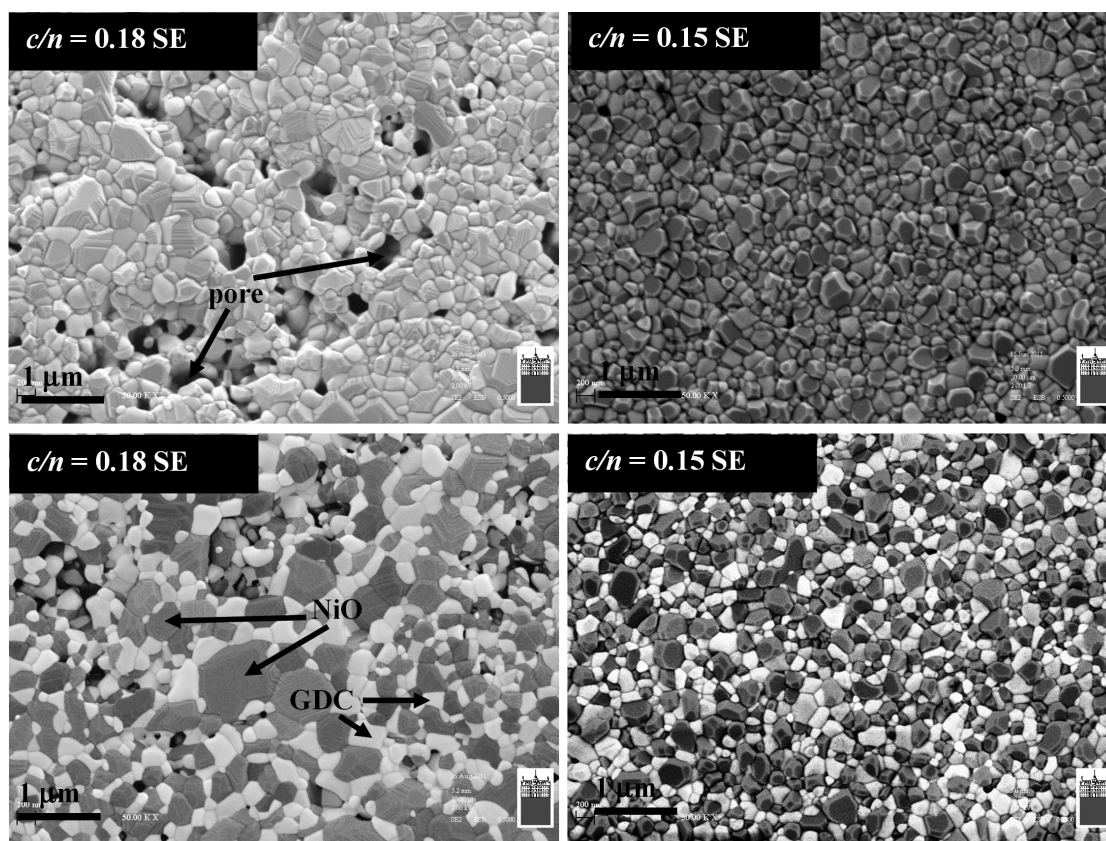


**Figure 4:** Microstructures of the samples with the  $c/n$  ratios of 0.18 and 0.15 sintered at 1250 °C

**Slika 4:** Mikrostruktura vzorcev (razmerje  $c/n$ : 0,18 in 0,15) sintranih pri 1250 °C

(NiO and GDC). The continuity of the phases is essential not only with regard to conductivity, but also for the microstructure stability. The reason for the inhomogeneous microstructure in the reduced samples may be due to the inhomogeneous and partly porous microstructure after sintering. One good example of an insufficiently stable NiO-GDC microstructure is shown in the case of a sample with a  $c/n$  ratio of 0.18 (sintered at 1250 °C), in which more porous regions, accompanied with the grains of both phases that are significantly larger than in an average sample, can be found (**Figure 4**).

One possible reason for the differences in the microstructure development in the samples with a  $c/n$  ratio of 0.18 or 0.15 is in the nature of the combustion reaction itself. A slight increase in the citrate-nitrate molar ratio from 0.15 to 0.18 may lead to a carbon residue after the synthesis (0.18 sample), followed by a porosity enlargement due to carbon burning during the sintering process. Additionally, the peak combustion temperature in the reaction mixture with a  $c/n$  ratio of 0.18 is close to 1180 °C, while the peak temperature in the reaction mixture with a  $c/n$  ratio of 0.15 does not exceed 600 °C. Higher combustion temperatures and higher temperature gradients within the combusting reaction mixture may cause the formation of hard agglomerates.

The microstructure parameters important for an exact cermet analysis and obtained with a detailed quantitative microstructure analysis of the sintered and reduced samples are summarized in **Tables 1** and **2**. For statistically reliable data, several different regions were analyzed in each case. Parameters  $\bar{d}$ ,  $d_x$  and  $d_y$ ,  $d_{\text{por}}$  and  $\psi$  are represented as the diameter of the area-analogue circle – DCIRCLE, the intercept lengths in the  $x$  and  $y$  directions – FERETX, Y, and the maximal intercept length – FERETMAX and FCIRCLE, respectively. Porosity  $\varepsilon$  was determined as the microstructural porosity (on the basis of a microstructure analysis).

According to the results of the quantitative microstructure analysis, the porosity of the sintered samples decreased with the sintering temperature as expected. The higher sintering temperature also resulted in a pronounced grain growth. The average particle size of NiO exceeds the GDC average particle size in all the samples; however, the difference between average particle sizes is less pronounced at higher sintering temperatures. From this fact we can deduce that NiO in a NiO-GDC composite sinters first and more intensely. The average particle sizes of NiO and GDC in the samples with a  $c/n$  ratio of 0.15 range from 92 nm to 230 nm and from 84 nm to 193 nm, respectively, while in the samples with a  $c/n$  ratio of 0.18 they range from 127 nm to 249 nm and from 96 nm to 247 nm, respectively.

**Table 1:** Quantitative microstructure analysis of the sintered NiO-GDC samples**Tabela 1:** Rezultati kvantitativne analize mikrostruktur sintranih vzorcev NiO-GDC

$T/^{\circ}\text{C}$	$c/n$	$\varepsilon/\%$ Mikr.	(nm)		$\psi$		$d_x/\text{nm}$		$d_y/\text{nm}$		$d_{\text{por}}/\text{nm}$
			NiO	GDC	NiO	GDC	NiO	GDC	NiO	GDC	
1200	0.15	12	92	84	0.70	0.70	107	98	106	97	187
1250	0.15	11	121	95	0.77	0.78	138	108	137	108	158
1300	0.15	8	143	128	0.75	0.74	161	147	162	146	167
1350	0.15	6	189	163	0.80	0.76	210	186	209	186	177
1400	0.15	3	230	193	0.78	0.71	257	223	255	227	236
1200	0.18	13	127	96	0.71	0.72	142	107	143	108	358
1250	0.18	10	155	122	0.72	0.73	174	137	176	138	274
1300	0.18	7	182	152	0.72	0.73	203	173	204	172	335
1350	0.18	6	214	197	0.74	0.73	235	218	235	216	382
1400	0.18	4	249	247	0.77	0.72	269	267	268	267	370

**Table 2:** Quantitative microstructure analysis of the reduced Ni-GDC samples**Tabela 2:** Rezultati kvantitativne analize mikrostruktur reduciranih vzorcev Ni-GDC

$T/^{\circ}\text{C}$	$c/n$	$\varepsilon/\%$ Mikr.	(nm)		$\psi$		$d_x/\text{nm}$		$d_y/\text{nm}$		$d_{\text{por}}/\text{nm}$
			Ni	GDC	Ni	GDC	Ni	GDC	Ni	GDC	
1200	0.15	34	73	86	0.75	0.70	84	102	80	100	352
1250	0.15	29	71	97	0.75	0.78	82	108	77	108	304
1300	0.15	26	85	125	0.71	0.79	100	140	100	137	351
1350	0.15	25	109	154	0.72	0.79	133	176	125	165	407
1400	0.15	23	146	192	0.72	0.78	173	217	168	214	646
1200	0.18	40	169	95	0.70	0.71	191	106	203	107	378
1250	0.18	36	143	121	0.71	0.76	160	135	165	135	438
1300	0.18	34	168	150	0.74	0.78	194	168	183	167	385
1350	0.18	35	193	195	0.75	0.77	224	217	193	216	413
1400	0.18	21	254	244	0.76	0.78	301	264	275	260	361

Additionally, with higher sintering temperatures, the grains of both phases became rounder ( $\psi$  parameter).

Comparing the sintered and reduced samples, the size of the Ni-grains is reduced relative to the NiO particle size and, consequently, the porosity is increased. When analysing the microstructure of the metal-ceramic anode layer, we find that its appropriate volume porosity is between 30 % and 40 %<sup>14–17</sup>. Considering that about 41.1 % of the initial NiO volume is transformed into pores during the reduction of NiO to Ni, we find that the porosity of the sintered materials should be close to 10 %.

For a high TPB value, an average particle size of both phases should remain as small as possible; for suitable electrical properties, the contact between the particles should be good. For these reasons, the sintering temperature for a sample with a  $c/n$  ratio of 0.15 is in the range from 1200 °C to 1250 °C, while for a sample with a  $c/n$  ratio of 0.18 the sintering temperature below 1300 °C may be considered to be too low due to the clear microstructural instability of the final Ni-GDC composite, which was characterized for its exaggerated Ni growth. The final average particle sizes of Ni and GDC in a sample with a  $c/n$  ratio of 0.15 were 73 nm and 86 nm after the sintering at 1200 °C, and 71 nm and 97 nm after the sintering at 1250 °C, respectively. Nevertheless, the nano-sized initial oxide mixture and careful powder

treatment enabled the preparation of well-sintered materials with the relative densities above 90 %, as well as subsequently reduced composites, in which the average particle sizes of both phases are still well within the sub-micrometer range.

#### 4 CONCLUSIONS

The nano-sized NiO-GDC composites were prepared using a citrate-nitrate self-sustaining reaction from the initial reactive gel. After the synthesis, the average crystallite sizes were calculated to be 4.3 nm and 40 nm for GDC and 7.6 and 48 nm for NiO for the samples with the  $c/n$  ratios of 0.15 and 0.18, respectively. Such crystallites, partially agglomerated, were the starting material for a pellet preparation and the subsequent microstructure-development investigations. Relatively dense bodies (not more than  $\approx 10$  % of the residual porosity) were prepared at the sintering temperatures as low as 1200 °C for the samples with a  $c/n$  ratio of 0.15. Higher sintering temperatures did not significantly decrease the porosity. For the samples with a  $c/n$  ratio of 0.18, the sintering temperatures lower than 1300 °C were recognised as insufficient due to a clear microstructure instability, where more porous regions accompanied with the grains of both phases, larger than in an average sample, can be found. The average grain size of the GDC



phase increased with the increasing sintering temperature. The NiO grains also grew with the increasing sintering temperature; however, the dimensions of the final Ni grains formed during the reduction were very much influenced by the microstructure stability of the GDC framework formed during the sintering. The smallest Ni grains, still well in the sub-micrometer range, with the average particle sizes of 73 nm and 71 nm were obtained in the sample with a  $c/n$  ratio of 0.15 sintered at 1200 °C and 1250 °C, respectively.

## Acknowledgements

This investigation was supported by the Centre of Excellence for Low-Carbon Technologies and the Slovenian Research Agency.

## 5 REFERENCES

- <sup>1</sup> J. F. Fergus, Oxide anode materials for solid oxide fuel cells, *Solid State Ionics*, 177 (2006), 1529–1541
- <sup>2</sup> M. Yano, A. Tomita, M. Sano, T. Hibino, Recent advances in single-chamber solid oxide fuel cells: A review, *Solid State Ionics*, 177 (2007), 3351–3359
- <sup>3</sup> S. Ping Jiang, A review of wet impregnation – An alternative method for the fabrication of high performance and nano-structured electrodes of solid oxide fuel cells, *Materials Science and Engineering A*, 418 (2006), 199–210
- <sup>4</sup> Y. J. Leng, S. H. Chan, S. P. Jiang, K. A. Khor, Low-temperature SOFC with thin film GDC electrolyte prepared in situ by solid-state reaction, *Solid State Ionics*, 170 (2004), 9–15
- <sup>5</sup> T. Ishihara, T. Shibayama, H. Nishiguchi, Y. Takita, Nickel-Gd-doped CeO<sub>2</sub> cermet anode for intermediate temperature operating solid oxide fuel cells using LaGaO<sub>3</sub>-based perovskite electrolyte, *Solid State Ionics*, 132 (2000), 209–216
- <sup>6</sup> C. Xia, M. Lui, Microstructures, conductivities, and electrochemical properties of Ce<sub>0.9</sub>Gd<sub>0.1</sub>O<sub>2</sub> and GDC-Ni anodes for low-temperature SOFCs, *Solid State Ionics*, 152–153 (2002), 423–430
- <sup>7</sup> S. Zha, W. Rauch, M. Liu, Ni-Ce<sub>0.9</sub>Gd<sub>0.1</sub>O<sub>1.95</sub> anode for GDC electrolyte-based low-temperature SOFCs, *Solid State Ionics*, 166 (2004), 241–250
- <sup>8</sup> C. Ding, H. Lin, K. Sato, T. Hashida, Synthesis of NiO-Ce<sub>0.9</sub>Gd<sub>0.1</sub>O<sub>1.95</sub> nanocomposite powders for low-temperature solid oxide fuel cell anodes by co-precipitation, *Scripta Materialia*, 60 (2009), 254–256
- <sup>9</sup> C. Ding, H. Lin, K. Sato, T. Kawada, J. Mizusaki, T. Hashida, Improvement of electrochemical performance of anode-supported SOFCs by NiO-Ce<sub>0.9</sub>Gd<sub>0.1</sub>O<sub>1.95</sub> nanocomposite powders, *Solid State Ionics*, 181 (2010), 1238–1243
- <sup>10</sup> A. Ringuete, J. A. Labrincha, J. R. Frade, A combustion synthesis method to obtain alternative cermet materials for SOFC anodes, *Solid State Ionics*, 141–142 (2001), 549–557
- <sup>11</sup> P. Duran, J. Tartaj, F. Capel, C. Moure, Processing and characterization of a fine nickel oxide/zirconia/composite prepared by polymeric complex solution synthesis, *J. Eur. Ceram. Soc.*, 23 (2003), 2125–2133
- <sup>12</sup> S. P. Jiang, Y. Y. Duan, J. G. Love, Fabrication of high-performance Ni/Y<sub>2</sub>O<sub>3</sub>-ZrO<sub>2</sub> cermet anodes of solid oxide fuel cells by ion impregnation, *J. Electrochem. Soc.*, 149 (2002), A1175
- <sup>13</sup> B. de Boer, M. Gonzales, H. J. M. Bouwmeester, H. Verweij, The effect of the presence of fine YSZ particles on the performance of porous nickel electrodes, *Solid State Ionics*, 127 (2000), 269–276
- <sup>14</sup> W. Hu, H. Guan, X. Sun, S. Li, M. Fukumoto, I. Okane, Electrical and Thermal Conductivities of Nickel-Zirconia Cermets, *J. Am. Ceram. Soc.*, 81 (1998) 8, 2209–2212
- <sup>15</sup> D. W. Dees, T. D. Claar, T. E. Eascher, D. C. Fee, F. C. Mrazek, Conductivity of Porous Ni/ZrO<sub>2</sub>-Y<sub>2</sub>O<sub>3</sub> Cermets, *J. Electrochem. Soc.*, 134 (1987) 9, 2141–2146
- <sup>16</sup> T. Kawashima, M. Hishinuma, Analysis of Electrical Conduction Paths in Ni/YSZ Participate Composites Using Percolation Theory, *Mater. Trans.*, 37 (1996) 7, 1397–1403
- <sup>17</sup> U. Anselmi-Tamburini, G. Chiodelli, M. Arimondi, F. Maglia, G. Spinolo, Z. A. Munir, Electrical Properties of Ni/YSZ Cermets Obtained by Combustion Synthesis, *Solid State Ionics*, 110 (1998), 35–43



# MODELING OF PM10 EMISSION WITH GENETIC PROGRAMMING

## MODELIRANJE EMISIJE PM10 Z GENETSKIM PROGRAMIRANJEM

Miha Kovačič<sup>1</sup>, Sandra Senčič<sup>2</sup>

<sup>1</sup>ŠTORE STEEL, d. o. o., Železarska cesta 3, 3220 Štore, Slovenia

<sup>2</sup>KOVA, d. o. o., Teharska cesta 4, 3000 Celje, Slovenia  
miha.kovacic@store-steel.si

*Prejem rokopisa – received: 2012-01-18; sprejem za objavo – accepted for publication: 2012-04-05*

To implement sound air-quality policies, regulatory agencies require tools to evaluate the outcomes and costs associated with various emission-reduction strategies. However, the applicability of such tools can also remain uncertain. It is furthermore known that source-receptor models cannot be implemented through deterministic modeling. The article presents an attempt of PM10 emission modeling carried close to a steel production area with the genetic programming method. The daily PM10 concentrations, daily rolling mill and steel plant production, meteorological data (wind speed and direction – hourly average, air temperature – hourly average and rainfall – daily average), weekday and month number were used for modeling during a monitoring campaign of almost half a year (23. 6. 2010 to 12. 12. 2010). The genetic programming modeling results show good agreement with measured daily PM10 concentrations. In future we will carry out genetic programming based dispersion modeling according to the calculated wind field, air temperature, humidity and rainfall in a 3D Cartesian coordinate system. The prospects for arriving at a robust and faster alternative to the well-known Lagrangian and Gaussian dispersion models are optimistic.

Keywords: steel plant, PM10 concentrations, modeling, genetic programming

V okviru uveljavljanja uredb o kakovosti zraka, s ciljem zmanjševanja emisij, nadzorne agencije zahtevajo ovrednotenje emisij in stroškov, povezanih z njimi. Uporabnost takih orodij je v splošnem negotova. Prav tako je znano, da pri modelih tipa vir-sprejemnik težko uporabimo deterministično modeliranje. V članku je predstavljen poskus modeliranja emisije delcev PM10 na področju železarnice z metodo genetskega programiranja. Osnova za modeliranje so bili podatki, zbrani v obdobju več kot pol leta (od 23. 6. 2010 do 12. 12. 2010): dnevne koncentracije PM10, produktivnost jeklarne, valjarne, meteorološki podatki (hitrost in smer vetra, temperatura zraka – urno povprečje ter padavine – dnevno povprečje) ter dan v tednu in zaporedna številka meseca. Rezultati modeliranja dnevnih koncentracij PM10 z genetskim programiranjem kažejo na dobro ujemanje z eksperimentalnimi podatki. V prihodnosti bomo izvedli modeliranje z genetskim programiranjem v kartezijskem 3D koordinatnem sistemu z upoštevanjem izračunanega vetrovnega polja, temperature zraka, vlažnosti in padavin. Možnosti za uporabo robustnih in hitrejših alternativ Lagrangovih in Gaussovih disperzijskih modelov so optimistične.

Ključne besede: železarna, koncentracije PM10, modeliranje, genetsko programiranje

### 1 INTRODUCTION

Particulate matter (PM) pollution is, especially in residential areas near industrial areas, a problem of great concern. This is not only because of the adverse health effects but also because of reduced visibility; on a global scale, effects on the radiative balance are also of great importance<sup>1-3</sup>.

To reduce PM levels in the air a deep knowledge of the contributing sources, background emissions, the influence of the meteorological conditions, as well as of PM10 formation and transport processes is needed.

However, current state-of-the-art PM10 modeling does not allow us to quantitatively model the whole range of emissions behavior, which is why the dispersion modeling is thus increasingly connected with intelligent algorithms such as artificial neural networks<sup>4-9</sup> and evolutionary computation<sup>9</sup>.

The objective of this work was to model PM10 emissions close to a steel plant area in Slovenia by means of a genetic programming method. Genetic programming has been proven to be an effective optimi-

zation tool for multicriterial and multiparametrical problems<sup>10-13</sup>. The genetic programming system for PM10 emission modeling imitates the natural evolution of living organisms, where in the struggle for natural resources the successful entities gradually become more and more dominant in adapting to the environment in which they live; the less successful ones, meanwhile, are only rarely present in subsequent generations. In the proposed concept the mathematical models for PM10 concentration prediction undergo adaptation. During the simulated evolution more and more successful organisms (PM10 emission models) emerge on the basis of given data (wind speed and direction – hourly average, air temperature – hourly average, rainfall – daily average, weekday and month number).

In order to allow for a self-contained paper the basic terms and experimental setup are stated in the beginning. Afterwards the idea of the proposed concept is presented. In the conclusion the main contributions of the performed research are summarized, while guidelines for further research are provided.

## 2 EXPERIMENTAL SETUP

### 2.1 Sampling sites

**Figure 1** shows the locations of the sampling sites, rolling mill, steel plant and residential areas. Due to rolling mill and steel plant PM10 contribution also several source categories influence the PM10 concentrations. These include combustion and non-combustion traffic sources, urban background concentrations, along with both contributions that are transported by regionally and long-range.

### 2.2 Sampling

Samples for this study were collected between 23. 6. 2010 and 12. 12. 2010. Sampling was performed 1.5 m above the ground. PM10 samples were collected for 24 h on Mondays using low-volume samplers equipped with EPA-equivalent size-selective inlets. Particles with diameter 10  $\mu\text{m}$  (PM10) were collected on cellulose esters membranes with high collection efficiencies (99 %). In total 172 PM10 samples for each sampling site were available.

Before and after the samplings were made the filters were exposed for 24–48 h on open but dust-protected sieve-trays in an air-conditioned weighing room. The gravimetric determination of the mass was carried out using an analytical microbalance (precision 1  $\mu\text{g}$ ) located in the weighing room. In order to remove static electricity from filters the balance is equipped with a special kit in a Faraday shield.

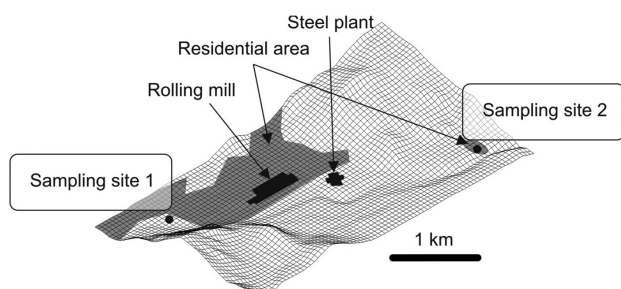


**Figure 1:** Topographic view of the study area

**Slika 1:** Topografski prikaz področja študije

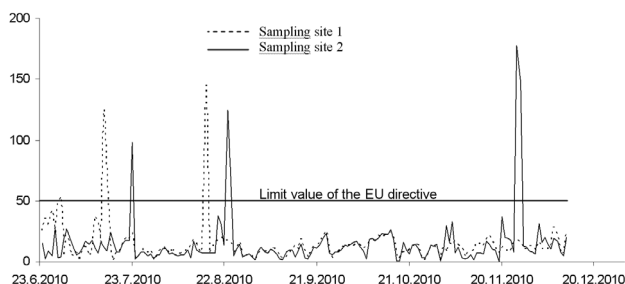


**Figure 2:** The measured PM10 concentrations during the study period for the sampling sites

**Slika 2:** Izmerjene koncentracije PM10 v obdobju študije za lokaciji vzorčenja

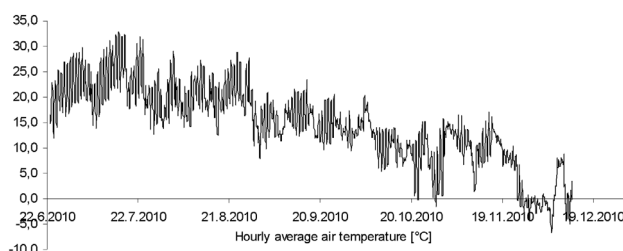


**Figure 3:** The hourly average temperatures during the study period

**Slika 3:** Urno povprečje temperature zraka v obdobju študije

The limit value of the EU directive – i.e. a daily mean PM10 concentration – is 50  $\mu\text{g}/\text{m}^3$ . At the sampling site 1 and 2 the measured PM10 concentration exceeded limit value four times and five times, respectively.

**Figure 2** shows the measured PM10 concentrations during the study period for the sampling sites.

### 2.3 Meteorological data

Hourly average air temperature, wind speed and direction and daily rainfall data were made available to the authors by the Slovenian Environment Agency.

**Figure 3** shows the hourly average temperatures during the study period.

**Figure 4** shows the frequency distribution of wind direction and wind speed obtained based on wind direction and speed data measured every hour during the study period.

**Figure 5** shows the daily rainfall during the period of the study.

The hourly data based on electric arc and rolling mill production was collected during the study period. During

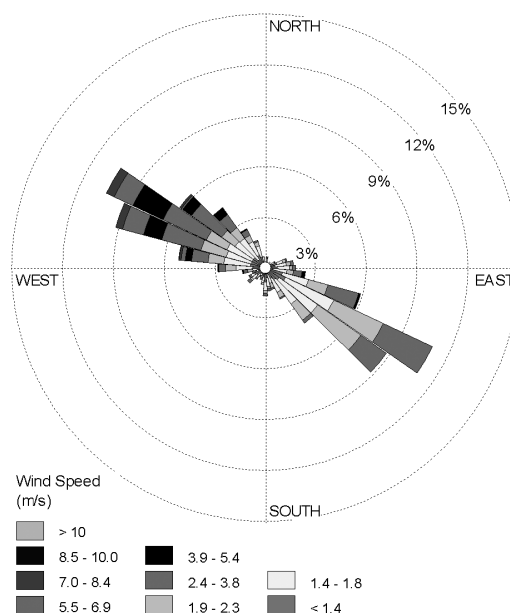


**Figure 4:** Frequency distribution of wind direction and wind speed

**Slika 4:** Frekvenčna porazdelitev smeri in hitrosti vetra

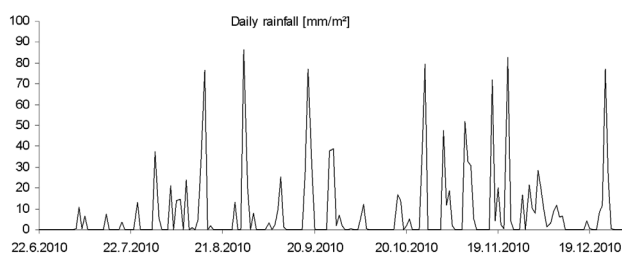


Figure 5: Daily rainfall during the study period

Slika 5: Dnevne padavine v obdobju študije

the study period, the electric arc furnace was stopped for 28 465 min and the rolling mill was stopped for 8 213 min. Figure 6 shows the minutes of stopping per day for the electric arc furnace and rolling mill during the study period.

### 3 GENETIC PROGRAMMING MODELING

Genetic programming is probably the most general evolutionary optimization method. The organisms that undergo adaptation are in fact mathematical expressions (models) for the PM10 concentrations prediction in the present work. The concentration prediction is based on the available function genes (i.e., basic arithmetical functions) and terminal genes (i.e., independent input parameters, and random floating-point constants). In the present case the models consist of the following function genes: addition (+), subtraction (−), multiplication (\*) and division (/), and the following terminal genes: weekday (WEEKDAY) and month number (MONTH), wind speed [m/s] (SPEED), wind direction [°] (DIRECTION), air temperature [°C] (TEMP), rainfall [mL] (RAIN), electro arc furnace efficiency [min/h] (EAF), rolling mill efficiency [min/h] (ROLLING). In order to ascertain the influence of seasons and traffic during workday hours the weekday and month number were also added as terminal genes. One of the randomly generated mathematical models – # – is schematically represented in Figure 7 as a program tree with included function genes (\*, +, /) and terminal genes (TEMP, RAIN, EAF and a real number constants 2 and 5.1).

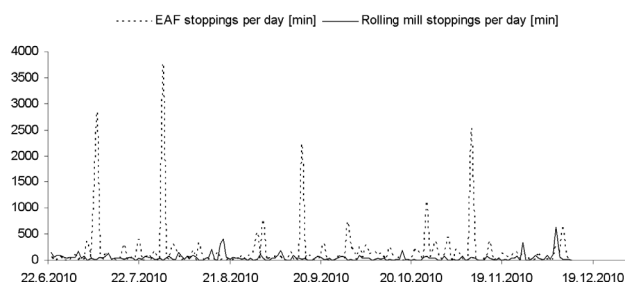


Figure 6: Minutes of stopping per day for the electric arc furnace and rolling mill during the study period

Slika 6: Dnevni zastoji elektrobočne peči in valjarne v minutah v obdobju študije

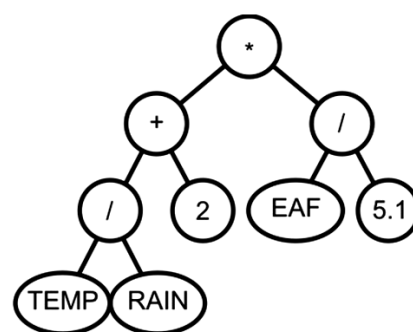


Figure 7: Randomly generated mathematical model for the PM10 concentrations prediction, represented in program tree form.

Slika 7: Naključno ustvarjen matematični model napovedovanja koncentracije PM10, predstavljen kot programsko drevo

Random computer programs of various forms and lengths are generated by means of the selected genes at the beginning of the simulated evolution. The varying of the computer programs is performed by means of the genetic operations during several iterations, known as generations. After the completion of the variation of the computer programs a new generation is obtained. Each generation is compared with the experimental data. The process of changing and evaluating organisms is repeated until the termination criterion of the process is fulfilled. The maximum number of generations is chosen as a termination criterion in the present algorithm.

The following evolutionary parameters were selected for the process of simulated evolutions: 500 for the size of the population of organisms, 100 for the maximum number of generations, 0.4 for the reproduction probability, 0.6 for the crossover probability, 6 for the maximum permissible depth in the creation of the population, 10 for the maximum permissible depth after the operation of crossover of two organisms, and 2 for the smallest permissible depth of organisms in generating new organisms. Genetic operations of reproduction and crossover were used. For selection of organisms the tournament method with tournament size 7 was used<sup>9–13</sup>. 100 independent civilizations of mathematical models for prediction of the PM10 concentration were developed. The best evolution sequence of 100 generations was computed in 8 h and 41 min on 2.39 GHz processor and 2 GB of RAM by an AutoLISP based in-house coded computer program.

The model fitness  $f$  has been defined as:

$$f = \sum_{i=1}^n (P_i - M_i) + N \cdot 10000 \quad (1)$$

where  $n$  is the size of sample data and,  $P_i$  is predicted PM10 concentration,  $M_i$  is measured PM10 concentration and  $N$  is the number of all cases when:

$$P_i < 50 \wedge M_i > 50 \vee M_i < 50 \wedge P_i > 50 \quad (2)$$

The limit value of the EU directive, i.e. a daily mean PM10 concentration, is 50  $\mu\text{g}/\text{m}^3$ . The number  $N$  tells us when the prediction is above that limit value, when in



order to assure PM10 concentration exceedance prediction by developed predictive model it should in fact be below the limit, and also when prediction by developed predictive model should be above the limit.

The simulated evolution in one run of the genetic programming system (out of 100) produced the following best model for prediction of PM10 concentration for sampling site 1:

$$\left( \text{DIRECTION} + \left( \text{DIRECTION} + \text{MONTH} + \text{WEEKDAY} + \frac{\text{SPEED}(-1.99563 + 3 \text{ WEEKDAY} + 4 \text{ MONTH WEEKDAY})}{\text{MONTH} - \text{WEEKDAY}} \right) + \frac{\text{WEEKDAY}(-1.99563 + \text{MONTH WEEKDAY})}{\text{MONTH} - \frac{1}{2} \text{ MONTH WEEKDAY}} \right) \left( \frac{-1.99563 + \text{MONTH WEEKDAY}}{\text{MONTH} + \text{WEEKDAY} - \frac{-1.99563 + \text{MONTH WEEKDAY}}{\text{MONTH WEEKDAY SPEED}}} + \left( (-1.99563 + \text{MONTH WEEKDAY}) \left( -\text{MONTH} + (\text{DIRECTION} - \text{WEEKDAY}) \right) \left( \text{DIRECTION} + \frac{\text{WEEKDAY} + \text{MONTH WEEKDAY} - \text{MONTH SPEED}(-1.99563 + \text{MONTH WEEKDAY})}{-\text{DIRECTION} + \text{MONTH} + \text{WEEKDAY}} - \frac{\text{MONTH}^2(-1.99563 + \text{MONTH WEEKDAY})}{\text{MONTH} - \frac{\text{WEEKDAY}}{\text{DIRECTION}}} \right) \right) \left( \text{MONTH} - \frac{2 \text{ WEEKDAY} + \text{MONTH WEEKDAY}}{\text{DIRECTION WEEKDAY}} \right) \left( \text{DIRECTION} - \text{RAIN} + \left( \text{MONTH} - \frac{\text{MONTH} - \text{WEEKDAY}}{\text{WEEKDAY}} \right) + \text{MONTH WEEKDAY} - \left( -\text{MONTH} + \left( \text{MONTH} - \frac{\text{MONTH} - \text{WEEKDAY}}{\text{SPEED}} \right) \right) (-1.99563 + \text{MONTH WEEKDAY}) \right) \right) \quad (3)$$

with fitness of 1019.95, number  $N = 0$  and average deviation of  $5.96 \mu\text{g}/\text{m}^3$ .

The best evolutionary developed model (out of 100) for prediction of PM10 concentration for sampling site 1 is:

$$\left( -5.76596 + \text{MONTH} + \frac{\text{TEMP}}{\text{DIRECTION}} \right) \left( \frac{\text{SPEED} - \frac{1 - \text{TEMP}}{\text{TEMP}}}{\text{MONTH}} + \frac{\left( \text{EAF} + \frac{\text{MONTH} - \text{TEMP WEEKDAY}}{\text{SPEED} - \frac{1 - \text{TEMP}}{\text{TEMP}}} \right) \text{WEEKDAY}}{\text{TEMP} + \frac{\text{TEMP} - \text{TEMP WEEKDAY}}{\text{DIRECTION}} + \frac{\text{EAF RAIN SPEED}}{\text{TEMP} - \frac{1 - \text{TEMP}}{\text{TEMP WEEKDAY}}}} \right) + \frac{\text{MONTH} - \frac{\text{WEEKDAY}^2}{\text{TEMP}} + \frac{\text{SPEED TEMP}^2}{\text{WEEKDAY}(\text{DIRECTION} + \frac{\text{TEMP} - \text{TEMP WEEKDAY}}{\text{DIRECTION}})} + 0.30872}{\text{DIRECTION} + \frac{\text{MONTH WEEKDAY} + \frac{\text{EAF WEEKDAY} - \text{TEMP WEEKDAY}}{\text{SPEED TEMP} - \frac{\text{TEMP WEEKDAY}}{\text{DIRECTION}}}}{\text{EAF RAIN} - \frac{\text{TEMP WEEKDAY} - \text{TEMP WEEKDAY}}{\text{DIRECTION}} + \frac{\text{EAF} + \text{TEMP WEEKDAY}^2}{\text{DIRECTION}}} \quad (4)$$

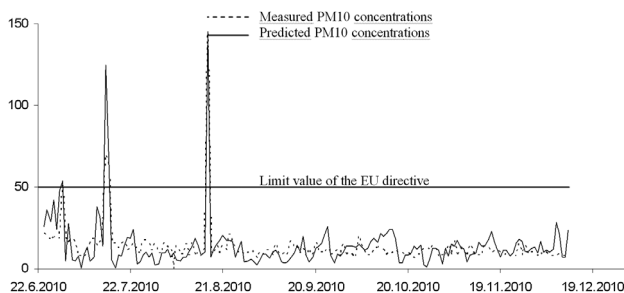


**Figure 8:** Measured and predicted PM10 concentrations [ $\mu\text{g}/\text{m}^3$ ] for sampling site 1

**Slika 8:** Izmerjene in napovedane koncentracije PM10 [ $\mu\text{g}/\text{m}^3$ ] za lokacijo vzorčenja 1

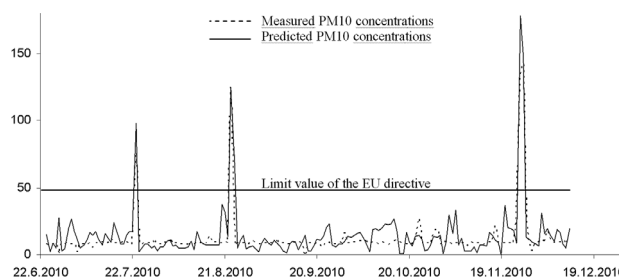


**Figure 9:** Measured and predicted PM10 concentrations [ $\mu\text{g}/\text{m}^3$ ] for sampling site 2

**Slika 9:** Izmerjene in napovedane koncentracije PM10 [ $\mu\text{g}/\text{m}^3$ ] za lokacijo vzorčenja 2

with fitness of 11 124.67, number  $N = 1$  (on the 30. 6. 2010 the measured PM10 concentrations were  $53.6 \mu\text{g}/\text{m}^3$  and predicted  $21.41 \mu\text{g}/\text{m}^3$ ), and average deviation of  $6.54 \mu\text{g}/\text{m}^3$ .

**Figures 8 and 9** show measured and predicted PM10 concentrations for sampling sites 1 and 2, respectively.

## 4 CONCLUSIONS

This paper presented the possibility of the PM10 concentration prediction close to a steel plant area with genetic programming. The daily PM10 concentrations, daily rolling mill and steel plant production, meteorological data (wind speed and direction – hourly average, air temperature – hourly average and rainfall – daily average), weekday and month number were used for modeling during a monitoring campaign of almost half a year (23. 6. 2010 to 12. 12. 2010). The special fitness function for genetic programming system was designed in order to assure also PM10 limit value exceedance prediction. For each sampling site the best models for PM10 prediction were obtained from 100 runs of the genetic programming system. The model for sampling sites 1 and 2 predicts concentrations within an average error range of  $5.96 \mu\text{g}/\text{m}^3$  and  $6.54 \mu\text{g}/\text{m}^3$ , respectively. All exceedances of the EU directive limit value ( $50 \mu\text{g}/\text{m}^3$ ) were administered at sampling site 1, but only 4 out of 5 of these occurred at sampling site 2. In the future we will carry out genetic programming based dispersion modeling according to the calculated wind field, air temperature, humidity and rainfall in a 3D Cartesian coordinate system. The prospects for arriving at a robust and faster alternative to the well-known Lagrangian and Gaussian dispersion models are optimistic.

## 5 REFERENCES

- <sup>1</sup> G. M. Marazzan, M. Ceriani, G. Valli, R. Vecchi, Source apportionment of PM10 and PM2.5 in Milan (Italy) using receptor modeling, *The Science of the Total Environment*, 317 (2003) 1–3, 137–147
- <sup>2</sup> J. G. Watson, Visibility: science and regulation, *Journal of the Air and Waste Management Association*, 52 (2002) 6, 628–713
- <sup>3</sup> E. Vrins, N. Schofield, Fugitive dust emission by an ironmaking site, *Journal of Aerosol Science*, 31 (2000), 524–525



- <sup>4</sup> J. Kukkonena, L. Partanen, A. Karppinen, J. Ruuskanen, H. Junninen, M. Kolehmainen, H. Niska, S. Dorling, T. Chatterton, R. Foxall, G. Cawley, Extensive evaluation of neural network models for the prediction of NO<sub>2</sub> and PM10 concentrations, compared with a deterministic modelling system and measurements in central Helsinki, *Atmospheric Environment*, 37 (2003), 4539–4550
- <sup>5</sup> H. Zhou, K. Cen, J. Fan, Modeling and optimization of the NO<sub>x</sub> emission, characteristics of a tangentially fired boiler with artificial neural networks, *Energy*, 29 (2004), 167–183
- <sup>6</sup> J. Hooyberghs, C. Mensink, G. Dumont, F. Fierens, O. Brasseur, A neural network forecast for daily average PM10 concentrations in Belgium, *Atmospheric Environment*, 39 (2005), 3279–3289
- <sup>7</sup> P. Perez, J. Reyes, An integrated neural network model for PM10 forecasting, *Atmospheric Environment*, 40 (2006), 2845–2851
- <sup>8</sup> G. Grivas, A. Chaloulakou, Artificial neural network models for prediction of PM10 hourly concentrations, in the Greater Area of Athens, Greece, *Atmospheric Environment*, 40 (2006), 1216–1229
- <sup>9</sup> M. Kovačič, P. Uratnik, M. Brezočnik, R. Turk, Prediction of the bending capability of rolled metal sheet by genetic programming, *Materials and Manufacturing Processes*, 22 (2007), 634–640
- <sup>10</sup> M. Kovačič, B. Šarler, Application of the genetic programming for increasing the soft annealing productivity in steel industry, *Materials and Manufacturing Processes*, 24 (2009) 3, 369–374
- <sup>11</sup> M. Kovačič, Genetic programming and Jominy test modeling, *Materials and Manufacturing Processes*, 24 (2009) 7, 806–808
- <sup>12</sup> M. Kovačič, S. Senčič, Critical inclusion size in spring steel and genetic programming, *RMZ – Materials and Geoenvironment*, 57 (2010) 1, 17–23
- <sup>13</sup> J. R. Koza, *Genetic Programming III.*, Morgan Kaufmann, San Francisco, 1999, 3–16



## EFFECT OF TEMPERING ON THE ROOM-TEMPERATURE MECHANICAL PROPERTIES OF X20CrMoV121 AND P91 STEELS

### VPLIV POPUŠČANJA NA MEHANSKE LASTNOSTI JEKEL X20CrMoV121 IN P91 PRI SOBNI TEMPERATURI

**Fevzi Kafexhiu, Franc Vodopivec, Jelena Vojvodič Tuma**

Institute of metals and technology, Lepi pot 11, 1000 Ljubljana, Slovenia  
fevzi.kafexhiu@imt.si

*Prejem rokopisa – received: 2012-01-23; sprejem za objavo – accepted for publication: 2012-04-19*

The effect of tempering time and temperature on the room-temperature tensile properties and hardness of two martensitic creep-resistant steels, X20CrMoV121 and P91, was investigated. Samples cut from industrial tubes were tempered for 17520 h at 650 °C and for 8760 h at 750 °C. On the tempered samples the yield stress, tensile strength, and hardness at room temperature were determined and an SEM examination was carried out.

It was found that the effect of tempering at 750 °C on the microstructural changes, room-temperature tensile properties and hardness was greater for both steels than the effect of tempering at 650 °C. The changes in the yield stress, tensile strength and hardness of both steels at a given tempering temperature were found to be very similar. Therefore, a general mathematical expression with specific coefficients for each property was deduced. These results are part of a larger investigation aimed at establishing a correlation between the particle spacing, yield stress, creep rate and hardness, which could be useful in an evaluation of the lifetime issues relating to the thermal-power-plant components.

**Keywords:** tempering, microstructure, mechanical properties, X20CrMoV121 and P91 steels

Vpliv časa in temperature popuščanja na razrzné lastnosti in trdoto pri sobni temperaturi je bil raziskan pri martenzitnih jeklih X20CrMoV121 in P91, ki sta odporni proti lezenju. Preizkušanci so bili izrezani iz industrijskih cevi in popuščeni do 17520 h pri 650 °C in 8760 h pri 750 °C. Na popuščenih vzorcih so bile določene meja plastičnosti, razrzná trdnost in trdota pri sobni temperaturi, mikrostruktura pa preiskana v SEM.

Ugotovljeno je bilo, da je vpliv popuščanja pri 750 °C na spremembo mikrostrukture, razrzné lastnosti pri sobni temperaturi in trdoto večji pri obeh jeklih, kot vpliv popuščanja pri 650 °C. Spremembe meje plastičnosti, trdnosti in trdote so bile podobne pri obeh jeklih pri dani temperaturi popuščanja. Razvita je bila zato matematična odvisnost s specifičnimi koeficienti za vsako lastnost. Rezultati so del širše raziskave, katere cilj je opredeliti korelacije med razdaljo med izločki, mejo plastičnosti, hitrostjo lezenja in trdoto, ki bi bile koristne pri oceni preostale trajnostne dobe komponent termoelektrarn.

**Ključne besede:** popuščanje, mikrostruktura, mehanske lastnosti, jekli X20CrMoV121 in P91

## 1 INTRODUCTION

In recent years there has been an increased demand to improve the efficiency of steam power plants for economical and environmental reasons.<sup>1-4</sup> A straightforward way to achieve this is to raise the inlet temperature and pressure of the steam that passes through the turbines. This directly saves the fuel and reduces the CO<sub>2</sub> emissions.<sup>5</sup>

The problems with higher steam temperature and pressure are largely material related. The microstructures of the materials operating under such conditions change with time and, consequently, several degradation mechanisms such as creep, fatigue, thermal fatigue, creep-fatigue, progressive embrittlement, corrosion/oxidation, etc., are accelerated. Among these damage mechanisms, the most important are the damages caused by an increase in the creep deformation. The main candidate materials for building the plants with more advanced steam parameters are 9–12 % chromium steels.<sup>6, 7</sup>

The risk of a failure due to creep deformation and other damage mechanisms is always present. Therefore,

periodical checking of their properties and residual lifetime after a determined period of operation of the power plants is always necessary. The checking of the creep rate and the creep strength is expensive and time consuming. For this reason, simpler methods using faster and less expensive tests that make it possible to identify the changes in the properties of the steels already employed in the vital parts of a power plant, have been developed. One of these methods is checking the room-temperature mechanical properties and the microstructure after a certain tempering time, simulating the changes in the microstructure and the properties that occur after longer operation periods (in real conditions). It has been shown recently that the time when the creep failure occurs is related to the yield stress and the tensile strength at creep temperature<sup>8,9</sup> and that hardness is related to creep life.<sup>10</sup> It was also shown<sup>11</sup> that within a certain range of the room-temperature yield stress (350 MPa to 650 MPa) the accelerated creep rate at 580 °C decreases continuously from  $8 \cdot 10^{-7} \text{ s}^{-1}$  to  $5 \cdot 10^{-9} \text{ s}^{-1}$ .

## 2 EXPERIMENTAL WORK

In the present work, the X20CrMoV121 and P91 steels were chosen for an investigation. The samples were cut from the pipelines with  $\phi = 38 \text{ mm} \times 8 \text{ mm}$  and  $\phi = 82 \text{ mm} \times 14.5 \text{ mm}$ . The quantometer chemical compositions for both steels are given in **Table 1**.

Before extracting the specimens for the room-temperature tests and examinations, the samples of both steels were tempered for discrete times up to 17520 h at 650 °C and for a shorter time up to 8760 h at 750 °C to simulate the changes in the microstructure that take place under real operating conditions in the power plants, and their effect on the room-temperature tensile properties and hardness.

Static-tensile tests at room (ambient) temperature were performed on the specimens extracted from the previously tempered samples. The tests were initially performed on the specimens prepared from the as-delivered tubes and then on the specimens tempered for 2 h, 4320 h and 8760 h at 650 °C and 750 °C, and up to 17520 h at 650 °C. All the tensile tests were performed on a 500-kN static-dynamic testing machine in the Laboratory for Mechanical Testing at the Institute of Metals and Technology. A part of these results was published in the proceedings of IPSSC.<sup>12</sup>

With the aim to assess the changes in the microstructure as a function of tempering time and temperature, the SEM specimens were prepared with the standard metallographic techniques.

A Jeol – JSM6500F Field Emission Scanning Electron Microscope (FE-SEM) was used to acquire images at three different magnifications, namely, 2000-, 5000- and 10000-times, with the working parameters of the 15-kV acceleration voltage, 7-nA probe current and 10-mm working distance. Images were acquired from the specimens in the initial (as-delivered) state and from those tempered for 2 h, 4320 h and 8720 h (1 year) at both 650 °C and 750 °C. In this way, the microstructural evolution of both steels as a function of tempering time and temperature could be observed.

The specimens prepared for the SEM imaging were usable also for the Vickers hardness measurements. The HV5 measurements were carried out with an Instron 2100B Vickers hardness tester. The measurements were performed before the isothermal tempering, i.e., in the as-delivered state and within the used tempering times. Three measurements were performed over the whole specimen area at a suitable distance from the specimen edge to avoid any edge inaccuracy.

## 3 RESULTS AND DISCUSSION

A comparison between a decrease in the yield stress ( $\sigma_y$ ) and the tensile strength ( $\sigma_m$ ) at both tempering temperatures indicates a similarity in the changing of these two properties for both steels.

From **Figures 1** and **2** it can be seen that the effect of tempering at 650 °C on the reduction of  $\sigma_m$  and  $\sigma_y$  is higher for the X20CrMoV121 steel, where  $\sigma_y$  drops by 34 N/mm<sup>2</sup> and  $\sigma_m$  by 55 N/mm<sup>2</sup>, than for the P91 steel, where  $\sigma_y$  drops by 19 N/mm<sup>2</sup> and  $\sigma_m$  by 24 N/mm<sup>2</sup>. It is

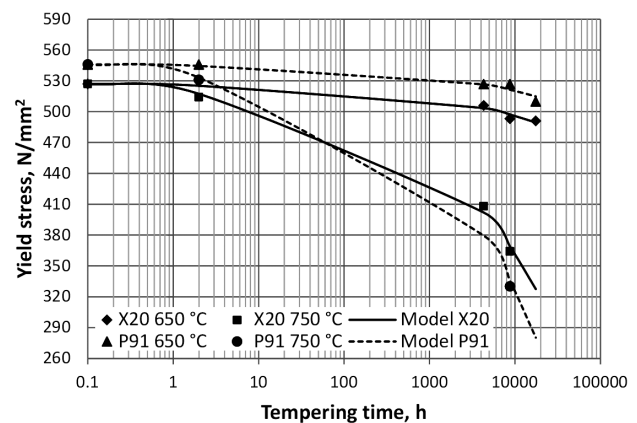


**Figure 1:** Actual and calculated dependences of the yield stress of the X20CrMoV121 and P91 steels on the tempering time at 650 °C and 750 °C

**Slika 1:** Dejanska in izračunana odvisnost meje plastičnosti jekel X20CrMoV121 in P91 od časa popuščanja pri 650 °C in 750 °C

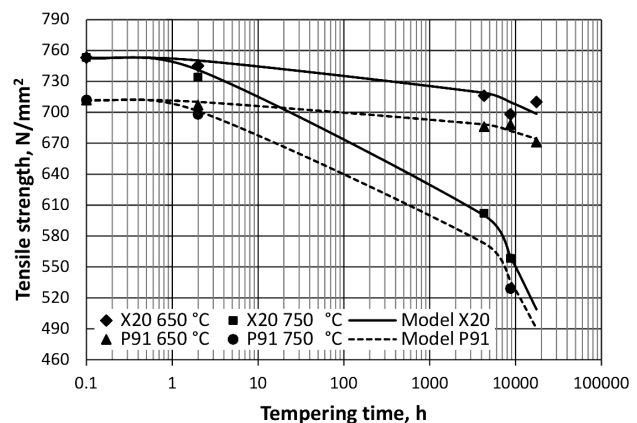


**Figure 2:** Actual and calculated dependences of the tensile strength of the X20CrMoV121 and P91 steels on the tempering time at 650 °C and 750 °C

**Slika 2:** Dejanska in izračunana odvisnost raztržne trdnosti jekel X20CrMoV121 in P91 od časa popuščanja pri 650 °C in 750 °C

**Table 1:** Chemical compositions of the X20CrMoV121 and P91 steels in mass fractions

**Tabela 1:** Kemična sestava jekel X20CrMoV121 in P91 v masnih deležih

Chemical composition, w/%													
Elements	C	Si	Mn	P	S	Cr	Ni	Mo	V	Cu	Nb	Al	N
X20CrMoV121	0.2	0.29	0.52	0.019	0.011	11	0.64	0.94	0.31	0.059	0.024	0.032	0.017
P91	0.1	0.38	0.48	0.012	0.002	7.9	0.26	0.98	0.23	0.14	0.11	0.016	0.064



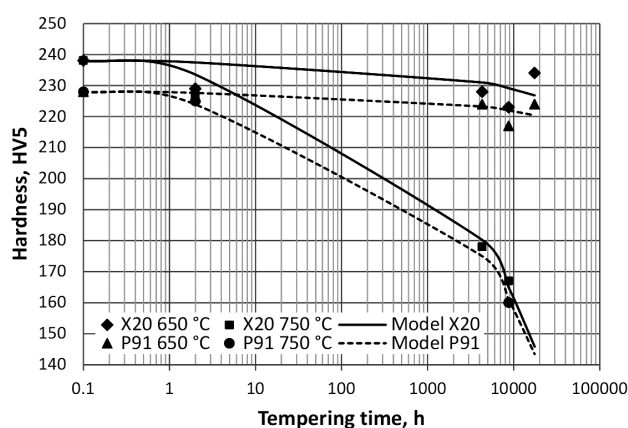


**Figure 3:** Actual and calculated dependences of the hardness of the X20CrMoV121 and P91 steels on the tempering time at 650 °C and 750 °C

**Slika 3:** Dejanska in izračunana odvisnost trdote jekel X20CrMoV121 in P91 od časa popuščanja pri 650 °C in 750 °C

also obvious that for both steels the reduction of  $\sigma_m$  is higher than the reduction of  $\sigma_y$ . It should be also pointed out that after a longer tempering time, i.e., 17520 h at the above temperature, the reduction of  $\sigma_y$  is, surprisingly, identical for both steels, i.e., 36 N/mm<sup>2</sup>, and similar behaviour was observed in the reduction of  $\sigma_m$ , i.e., 43 N/mm<sup>2</sup> for X20CrMoV121 and 41 N/mm<sup>2</sup> for P91.

On the other hand, the effect of tempering at 750 °C on the reduction of  $\sigma_m$  and  $\sigma_y$  is higher and their mutual correlation is different than in the case of tempering at 650 °C. For X20CrMoV121  $\sigma_y$  drops by 163 N/mm<sup>2</sup> and  $\sigma_m$  by 195 N/mm<sup>2</sup>, whereas for P91  $\sigma_y$  drops by 216 N/mm<sup>2</sup> and  $\sigma_m$  by 183 N/mm<sup>2</sup>.

The effect of the duration and the temperature of tempering on the hardness of both steels, shown in **Figure 3**, is similar to the effect on the yield stress and the tensile strength. In X20CrMoV121, after 8760 h of tempering at 650 °C, the hardness is reduced by 15 HV, whereas in P91, under the same tempering conditions, the hardness is reduced by 11 HV. At a higher temperature and the same tempering time, i.e., at 750 °C for 8760 h, the hardness reduction in X20CrMoV121 is 71 HV, whereas in P91 this reduction is 68 HV. The reduction of hardness indicates that the size, the amount and the distribution of precipitates have a lower effect on the hardness than on the yield stress of the steels investigated. This could be explained with the fact that the yield stress is more related to deformation hardening than hardness.

There is a clear similarity between the dependences of hardness HV, tensile strength  $\sigma_m$  and yield stress  $\sigma_y$  on the tempering time and the temperature and, for all three properties the general mathematical expression was deduced:

$$y(t) = k_1 - k_2 t^x$$

where  $y(t)$  stands for either  $\sigma_m$ ,  $\sigma_y$  or HV as a function of tempering time  $t$ ,  $k_1$  and  $k_2$  are constants and  $x$

represents the exponent, which can take the values of 1/2, 1/3, etc., depending on the way the curve obtained from the equation (1) best fits the experimental data of each property.

Experimental vs. theoretical curve fittings are given in **Figures 1, 2** and **3**. They are obtained by using the values for  $x$ ,  $k_1$  and  $k_2$  given in **Table 2** and applying them in equation (1) for all three properties, both steels and both tempering temperatures. The value of exponent  $x$  was appropriated to 1/3,  $k_1$  holds the values for each of the measured properties at the as-delivered state, whereas the  $k_2$  was calculated with the least-square method using the R-project for statistical computing.<sup>13</sup> It should be pointed out that the fitting for the yield stress and the tensile strength is quite good, whereas for the hardness this equation does not give a good fit for a longer tempering time at 650 °C.

**Table 2:** Parameters for calculating the yield stress, tensile strength and hardness change of the X20CrMoV121 and P91 steels for both tempering temperatures with equation (1)

**Tabela 2:** Parametri za izračun meje plastičnosti, razrzne trdnosti in trdote za jekli X20CrMoV121 in P91 pri obeh temperaturah popuščanja z enačbo (1)

Properties	Parameters	X20CrMoV121		P91	
		650 °C	750 °C	650 °C	750 °C
$\sigma_y$	$k_1$	527	527	546	546
	$k_2$	1.444	7.682	1.197	10.231
	$x$	1/3	1/3	1/3	1/3
$\sigma_m$	$k_1$	753	753	712	712
	$k_2$	2.096	9.4	1.456	8.539
	$x$	1/3	1/3	1/3	1/3
HV	$k_1$	238	238	228	228
	$k_2$	0.43	3.548	0.292	3.256
	$x$	1/3	1/3	1/3	1/3

The influence of tempering on the microstructures of both steels is greater after tempering at 750 °C than at

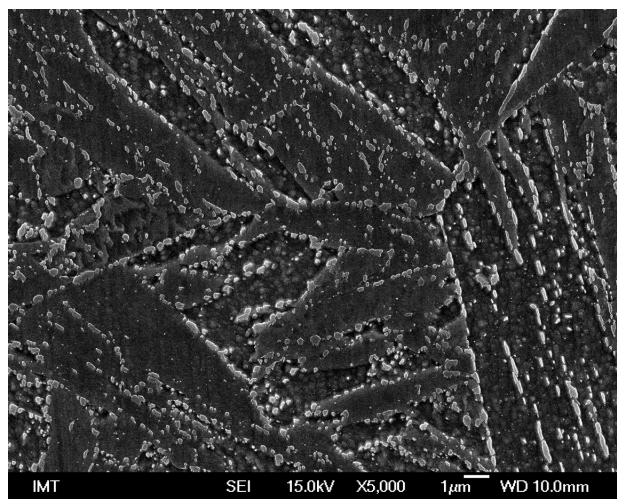


**Figure 4:** Microstructure of the X20CrMoV121 steel at the initial (as-received) state

**Slika 4:** Mikrostruktura jekla X20CrMoV121 v začetnem (dobavljenem) stanju

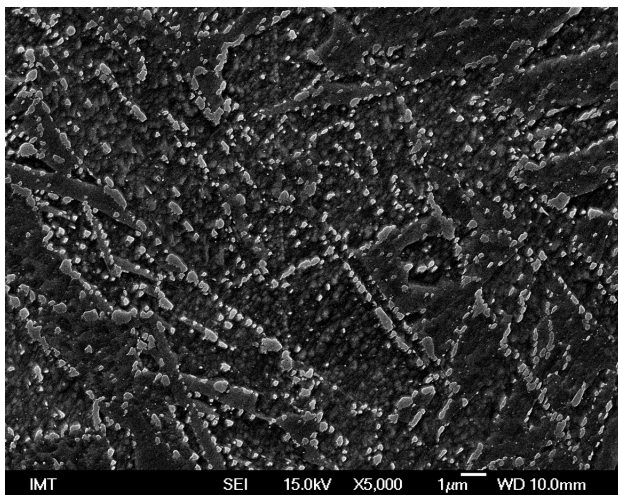


**Figure 5:** Microstructure of the X20CrMoV121 steel after 8760 h of tempering at 650 °C

**Slika 5:** Mikrostruktura jekla X20CrMoV121 po 8760 h popušćanja pri 650 °C

650 °C (**Figures 4 to 9**), because the diffusivity of the carbide-forming elements (Cr, Mo, Fe, V, and Nb), found in the solid solution in the ferrite matrix is temperature dependent, and is higher at higher temperatures.<sup>14–17</sup>

Due to tempering, both the size and the inter-particle spacing of carbide particles increase. In addition, the carbide-particles distribution changes from stringers along the grain and sub-grain boundaries to a uniform structure. Images in **Figures 4 and 7** show the as-delivered-state microstructures of the X20CrMoV121 and P91 steels, respectively. In both cases, the majority of particles are cementite  $\text{Fe}_3\text{C}$ , containing also chromium, or they are chromium carbides  $\text{Cr}_{23}\text{C}_6$ , containing also iron and molybdenum.<sup>18,19</sup> The carbide particles are found in the stringers distributed along the grain and

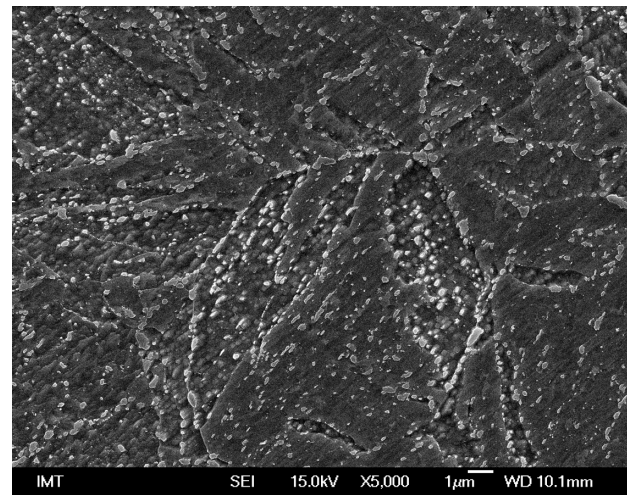


**Figure 7:** Microstructure of the P91 steel at the initial (as-received) state

**Slika 7:** Mikrostruktura jekla P91 v začetnem (dobavljenem) stanju

sub-grain boundaries of martensite, and there is no difference between the size of the  $\text{Fe}_3\text{C}$ ,  $\text{M}_{23}\text{C}_6$  and VC particles. After 8760 h of tempering at 650 °C the precipitates are almost evenly distributed and there is a difference between the size of VC (small white particles) and  $\text{M}_{23}\text{C}_6$ , which grow larger in both steels (**Figures 5 and 8**). In addition, the grain and subgrain boundaries of martensite are much less pronounced and some of them have already disappeared.

From **Figures 6 and 9** it is obvious that the tempering at 750 °C for 8760 h causes much greater changes in the microstructures of both steels, where the size of the  $\text{M}_{23}\text{C}_6$  particles and the spacing between them is drastically increased. On the other hand, the number density of these particles has clearly dropped, so the Ostwald ripening effect, where larger particles coarsen at the expense of smaller ones is quite obvious in this case.

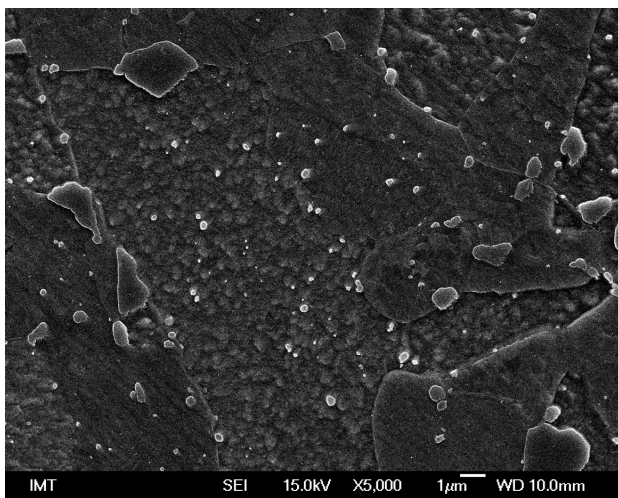


**Figure 6:** Microstructure of the X20CrMoV121 steel after 8760 h of tempering at 750 °C

**Slika 6:** Mikrostruktura jekla X20CrMoV121 po 8760 h popušćanja pri 750 °C

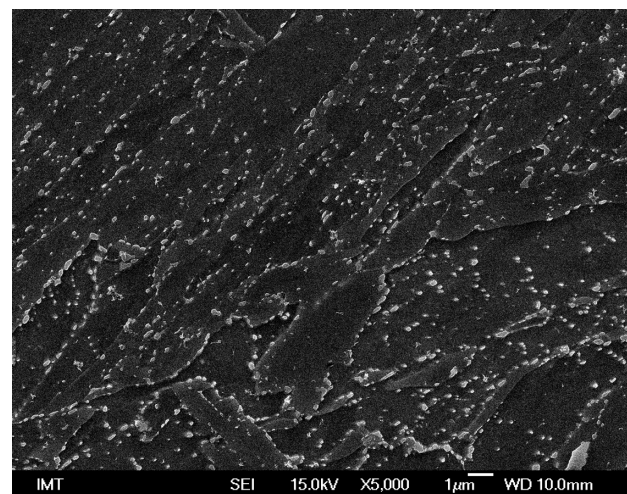


**Figure 8:** Microstructure of the P91 steel after 8760 h of tempering at 650 °C

**Slika 8:** Mikrostruktura jekla P91 po 8760 h popušćanja pri 650 °C



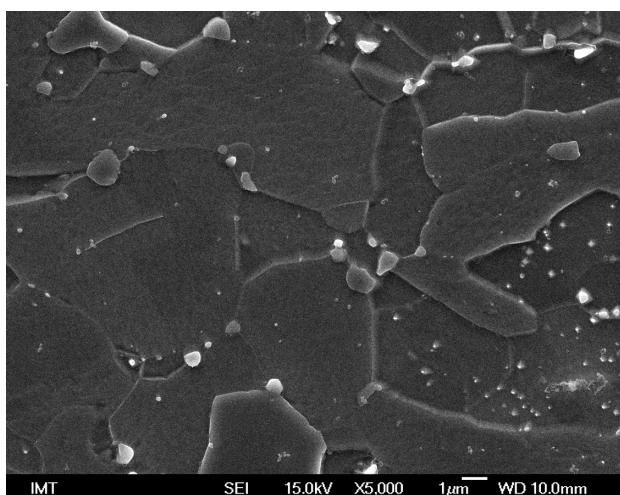


**Figure 9:** Microstructure of the P91 steel after 8760 h of tempering at 750 °C

**Slika 9:** Mikrostruktura jekla P91 po 8760 h popušćanja pri 750 °C

Since carbide precipitates represent the most important strengthening mechanism in 9–12% Cr steels, and having in mind the fact that mechanical properties deteriorate as both the size and the inter-particle spacing increase, it is obvious that they are in some kind of mutual correlation, investigated and confirmed by many authors.<sup>14–18</sup>

## 4 CONCLUSIONS

The effect of the tempering time and the temperature of the creep-resistant martensitic steels, X20CrMoV121 and P91, which differ in chemical composition, on the room-temperature tensile properties and hardness was determined.

According to the results obtained, the following is concluded:

- The effect of tempering at both temperatures separately is the same for both steels investigated.
- When tempering at the temperature of 650 °C, the changes in yield stress  $\sigma_y$  and tensile strength  $\sigma_m$  are relatively small, whereas when tempering at a higher temperature, i.e., 750 °C, the changes are greater for both properties, and for steel X20CrMoV121  $\sigma_y$  is decreased by 163 N/mm<sup>2</sup> and  $\sigma_m$  by 195 N/mm<sup>2</sup>, whereas for steel P91  $\sigma_y$  is decreased by 216 N/mm<sup>2</sup> and  $\sigma_m$  by 183 N/mm<sup>2</sup> after 8760 h of tempering at 750 °C.
- The dependence of  $\sigma_y$  and  $\sigma_m$  on the tempering time and the temperature is for both steels virtually the same and can be mathematically expressed with the relation:  $y(t) = k_1 - k_2 t^x$ . All three parameters,  $k_1$ ,  $k_2$  and  $x$  have different values depending on the tempering conditions, the steel chemical composition, etc.
- Hardness evolution is similar to that of  $\sigma_y$  and  $\sigma_m$  and it could therefore be expressed with the same mathe-

matical relation, however, with different values for all three parameters.

- The effect of microstructural changes, particle size and spacing as well as particle distribution is caused by coarsening the particles. The coarsening rate depends on diffusion, which is greater at higher temperatures.

## Acknowledgement

The authors are indebted to the company TEŠ Šoštanj for supporting the investigation and to Mr. D. Kmetič for the mechanical tests.

## 5 REFERENCES

- <sup>1</sup> J. Hald, Microstructure and long-term creep properties of 9–12 % Cr steels, *International Journal of Pressure Vessels and Piping*, 85 (2008), 30–37
- <sup>2</sup> M. Yoshizawa, M. Igarashi, Long term creep deformation characteristics of advanced ferritic steels for USC power plants, *International Journal for Pressure Vessels and Piping*, 84 (2007), 37–43
- <sup>3</sup> R. L. Klueh, Elevated temperature ferritic and martensitic steels and their application to future nuclear reactors, *International Materials Reviews*, 50 (2005), 287–310
- <sup>4</sup> C. Scheu, F. Kauffmann, G. Zies, K. Maile, S. Straub, K. H. Mayer, Requirements for microstructural investigations of steels used in modern power plants, *Zeitschrift für Metallkunde*, 96 (2005), 653–659
- <sup>5</sup> D. V. Thornton, K. H. Mayer, European high temperature materials development for advanced steam turbines, in: *Advanced heat resistant steels for power generation*, ed. R. Viswanathan and J. Nutting, 708 (1999), 349–364
- <sup>6</sup> A. Shibli, F. Starr, Some aspects of plant and research experience in the use of new high strength martensitic steel P91, *International Journal of Pressure Vessels and Piping*, 84 (2007), 114–122
- <sup>7</sup> F. Abe, T. U. Kern, R. Viswanathan, *Creep-resistant steels*, Woodhead Publishing, CRC Press, Cambridge, England, 2008
- <sup>8</sup> F. Abe, Heat to heat variation in long term creep strength of some ferritic steels, in: *Creep and Fracture in: Creep & Fracture in High Temperature Components*, ed. I. A. Shibli, S. R. Holdsworth, DEStech Publ. Inc, 2009, 5–18
- <sup>9</sup> F. Masuyama, T. Tokumaga, N. Shimahata, T. Yamamoto, M. Hirano, Comprehensive approach to creep life assessment of martensitic heat resistant steels, in: *Creep & Fracture in High Temperature Components*, ed. I. A. Shibli, S. R. Holdsworth, DEStech Publ. Inc, 2009, 19–30
- <sup>10</sup> D. J. Allen, A hardness normalized model of creep rupture for P91 steel, in: *Creep & Fracture in High Temperature Components*, ed. I. A. Shibli, S. R. Holdsworth, DEStech Publ. Inc, 2009, 659–688
- <sup>11</sup> F. Vodopivec, J. Vojvodić - Tuma, M. Jenko, R. Celin, B. Šuštaršič, Dependence of accelerated creep rate at 580 °C and room temperature yield stress for two creep resistant steels, *Steel research*, 81 (2010) 7, 576–580
- <sup>12</sup> F. Kafexhiu, F. Vodopivec, J. V. Tuma, Tempering effects on the microstructure, mechanical properties and creep rate of X20CrMoV121 and P91 steels, *Proceedings of 4th Jožef Stefan International Postgraduate School Students Conference*, Ljubljana, 2012, 241–246
- <sup>13</sup> R-project, <http://www.r-project.org/>
- <sup>14</sup> F. Vodopivec, M. Jenko, R. Celin, B. Žužek, D. A. Skobir Balantič, Creep resistance of microstructure of welds of creep resistant steels, *Mater. Tehnol.*, 45 (2011) 2, 139–143

- <sup>15</sup> D. A. Skobir Balantič, M. Jenko, F. Vodopivec, R. Celin, Effect of change of carbide particles spacing and distribution on creep rate of martensite creep resistant steels, *Mater. Tehnol.*, 45 (2011) 6, 555–559
- <sup>16</sup> F. Vodopivec, D. Kmetič, J. Vojvodič-Tuma, D. A. Skobir Balantič, Effect of operating temperature on microstructure and creep resistance of 20CrMoV121 steel, *Mater. Tehnol.*, 38 (2004) 5, 233–239
- <sup>17</sup> F. Vodopivec, M. Jenko, J. Vojvodič-Tuma, Stability of MC carbide particles size in creep resisting steels, *Metalurgija* 45 (2006) 3, 147–153
- <sup>18</sup> D. A. Skobir Balantič, F. Vodopivec, M. Jenko, S. Spaić, B. Markoli, *Zeitschrift für Metallkunde*, 95 (2004) 11, 1020–1024
- <sup>19</sup> D. A. Skobir Balantič, F. Vodopivec, M. Jenko, S. Spaić, B. Markoli, The influence of tempering on the phase composition of the carbide precipitates in X20CrMoV121 steel, *Mater. Tehnol.*, 37 (2003) 6, 353–358



## STRUCTURE AND PROPERTIES OF AlMgSi ALLOYS AFTER ECAP AND POST-ECAP AGEING

### STRUKTURA IN LASTNOSTI ZLITIN AlMgSi, STARANIH PRED ECAP IN PO NJEM

Martin Fujda<sup>1</sup>, Miloš Matvija<sup>1</sup>, Tibor Kvačkaj<sup>2</sup>, Ondrej Milkovič<sup>1</sup>, Pavol Zubko<sup>1</sup>,  
Katarína Nagyová<sup>1</sup>

<sup>1</sup>Department of Materials Science, Faculty of Metallurgy, Technical University of Košice, Slovakia

<sup>2</sup>Department of Metals Forming, Faculty of Metallurgy, Technical University of Košice, Slovakia  
martin.fujda@tuke.sk

*Prejem rokopisa – received: 2012-02-10; sprejem za objavo – accepted for publication: 2012-03-22*

The mechanical properties and the microstructures of the EN AW 6082 and EN AW 6063 aluminium alloys subjected to pre-ECAP solutionizing heat treatment, equal channel angular pressing (ECAP), and post-ECAP artificial ageing are compared. The quenched alloy states were severely deformed at room temperature by the ECAP technique following route B<sub>C</sub>. Repetitive ECAP caused formation of the ultra-fine subgrain microstructure with a high dislocation density and high strain hardening of the alloys, thus exhibiting an improvement in strength, but also a degradation of the analysed alloys' ductility. The application of the optimal artificial-ageing regimes after a severe plastic deformation improved only the tensile ductility of the alloys, while their strength was slightly decreased because the softening effect caused by the solid-solution recovery and the relaxation of the internal stress dominated over the hardening effect caused by the expected metastable  $\beta''$ - and  $\beta'$ -Mg<sub>2</sub>Si phase precipitation during the artificial ageing treatment.

Keywords: aluminium alloys, ECAP, ageing, microstructure, mechanical properties

Primerjali smo lastnosti EN AW 6082 in EN AW 6063 aluminijevih zlitin, raztopno žarjenih pred stiskanjem skozi pravokotni kanal (ECAP), po stiskanju ECAP in umetno staranih po ECAP-postopku. Zlitine v gašenem stanju so bile močno deformirane pri sobni temperaturi s tehniko ECAP po poti B<sub>C</sub>. Ponovljena ECAP je povzročila nastanek ultra drobnostne podmikrostrukture z veliko gostoto dislokacij, velikim utrjevanjem zlitin in s tem povečanje trdnosti ter poslabšanje duktilnosti preiskovanih zlitin. Optimalni režim umetnega staranja po veliki plastični deformaciji je povzročil samo izboljšanje natezne duktilnosti materiala, njihova trdnost pa je bila zmanjšana zaradi učinka mehčanja pri popravi trdne raztopine in sproščanju notranjih napetosti, ki prevladujejo nad učinkom utrjevanja z izločanjem izločkov metastabilne  $\beta''$ - in  $\beta'$ -Mg<sub>2</sub>Si faze med postopkom umetnega staranja.

Ključne besede: aluminijeve zlitine, ECAP, staranje, mikrostruktura, mehanske lastnosti

## 1 INTRODUCTION

At present, the equal-channel angular pressing (ECAP) technique is a very effective method of severe plastic deformation, and has been widely used for producing ultra-fine grain microstructures of Al-based alloys with significantly improved mechanical properties, including enhanced superplasticity, high strength, etc.<sup>1–10</sup> The severe plastic deformation (SPD) made by the ECAP process also markedly increases the density of lattice defects in the solid solution, and can thus accelerate the precipitation process of the strengthening particles during the post-ECAP ageing treatment applied to the age-hardenable aluminium alloys.<sup>11–13</sup> However, the ultra-fine-grained age-hardenable alloys often exhibit low tensile ductility at room temperature. Therefore, it is important to obtain ductility comparable to that of the conventional coarse-grained age-hardenable Al-based alloys.

EN AW 6063 and 6082 are the most used AlMgSi alloys that are suitable for different miscellaneous structural applications in the building, automotive and aircraft industries due to their strength-modification

options, low density, good corrosion properties, and good weldability.<sup>14,15</sup> The optimal combination of heat treatment and the SPD by repetitive ECAP led to a significantly increased strength and a relatively good ductility of these alloys caused by the ultra-fine grained structure formation and the strengthening precipitation of the  $\beta'$ -Mg<sub>2</sub>Si phase particles during the post-ECAP ageing treatment.<sup>4,16–21</sup>

The aim of the present work is to investigate the effect of the SPD by repetitive ECAP and the subsequent artificial ageing on the microstructure and the mechanical properties of the EN AW 6082 and EN AW 6063 aluminium alloys.

## 2 EXPERIMENTAL WORK

The experiments were carried out on the EN AW 6082 and EN AW 6063 aluminium alloys, the chemical composition of which is presented in **Table 1**. The analyzed alloys in the form of extruded rods, subjected to artificial ageing (T5 temper), were used as the initial states. Prior to the deformation in an ECAP die, the specimens of the initial states were solution annealed for

1.5 h at 550 °C (6082 alloy) or at 510 °C (6063 alloy) and subsequently cooled to room temperature by water quenching. The purpose of these heat-treatment regimes was to obtain a supersaturated solid solution.

**Table 1:** Chemical composition of the EN AW 6082 and EN AW 6063 aluminium alloys (w/%)

**Tabela 1:** Kemijska sestava aluminijevih zlitin EN AW 6082 in EN AW 6063 v masnih deležih (w/%)

alloy	Mg	Si	Mn	Fe	Zn	Cu	Al
EN AW 6082	0.60	1.0	0.49	0.21	0.02	0.06	bal.
EN AW 6063	0.44	0.52	0.03	0.21	0.02	0.03	bal.

The quenched specimens were subjected to a deformation in an ECAP die with a channel intersection angle  $\Phi = 90^\circ$ , and an arc of curvature  $\Psi = 37^\circ$  up to 4 (6082 alloy) or 6 passes (6063 alloy), respectively. The repetitive ECAP of the specimens of size  $\phi = 10 \text{ mm} \times 100 \text{ mm}$  was realized at room temperature following route B<sub>C</sub> (the sample was rotated in the same sense by  $90^\circ$ ). After ECAP, the specimens were subjected to artificial ageing in the temperature range of 60–180 °C as a function of time to determine the post-ECAP artificial-ageing condition for the highest peak hardness.

The microstructures of the investigated alloys obtained after quenching, deformation in the ECAP die, and after the post-ECAP peak-ageing treatment were analyzed in the central zones of the specimens' cross-sections using a transmission electron microscopy (TEM). The samples for TEM were prepared from the 1-mm-thick slices that were ground and polished to a thickness of about 0.15 mm. These slices were finally electrolytically thinned in a solution of 25 % HNO<sub>3</sub> and 75 % CH<sub>3</sub>OH at a temperature of  $-30^\circ\text{C}$ . The average grain size of the solid solution for all the analysed alloy states was determined according to ASTM E112.

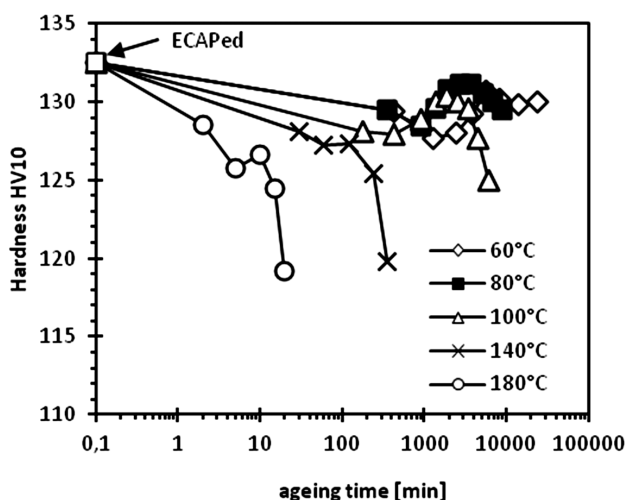


**Figure 1:** Vickers hardness of the ECAPed EN AW 6082 alloy state as a function of artificial ageing time at various ageing temperatures

**Slika 1:** Vickersova trdota zlitine EN AW 6082 po ECAP kot funkcija časa umetnega staranja pri različnih temperaturah staranja

The influence of the severe plastic deformation by the ECAP process and post-ECAP artificial ageing on the mechanical properties of the analyzed alloys was evaluated with the Vickers hardness measurement (HV 10) and a tensile test. The tensile test (the initial strain rate of  $2.5 \times 10^{-4} \text{ s}^{-1}$ ) was carried out on short specimens ( $d_0 = 5 \text{ mm}$ ,  $l_0 = 10 \text{ mm}$ ) made from quenched, ECAP-processed and post-ECAP peak-aged alloy billets. Subsequently, the characteristics of the strength ( $R_{p0.2}$  – yield strength and  $R_m$  – tensile strength), the uniform tensile elongation ( $A_g$ ), the tensile elongation ( $A$ ), and the reduction in the area ( $Z$ ) were determined.

### 3 RESULTS AND DISCUSSION

#### 3.1 Hardness

The Vickers hardness of the analyzed alloy states is summarized in **Table 2**. **Figures 1 and 2** show the variation of the Vickers hardness of the ECAPed analyzed alloys as a function of artificial ageing time at a temperature range of 60–180 °C. A significant increase in the alloys' hardness value (by about 120 % for the 6082 alloy and about 202 % for the 6063 alloy) was achieved by the ECAP processing of the quenched alloy states. A post-ECAP artificial-ageing treatment was applied to increase the hardness of the ECAPed alloys. The ECAPed alloy state reached peak hardness after about 60 h of the artificial ageing at 80 °C, but the

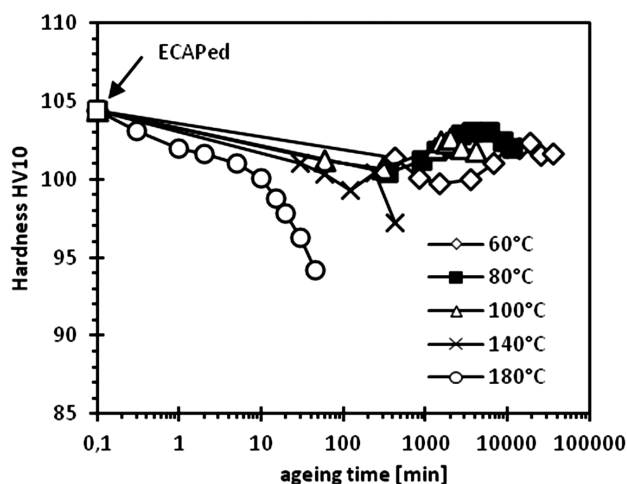


**Figure 2:** Vickers hardness of the ECAPed EN AW 6063 alloy state as a function of artificial ageing time at various ageing temperatures

**Slika 2:** Vickersova trdota zlitine EN AW 6063 po ECAP kot funkcija časa umetnega staranja pri različnih temperaturah staranja

**Table 2:** Vickers hardness of the analyzed alloy states

**Tabela 2:** Vickersova trdota analiziranih stanj zlitin

alloy/state	Q	E	post-ECAP peak-aged				
			60 °C	80 °C	100 °C	140 °C	180 °C
EN AW 6082	60.2	132.5	130.7	131.1	130.5	127.3	126.6
EN AW 6063	34.6	104.4	102.3	103.0	102.6	100.4	–

Q-quenched, E-ECAPed

maximum values were only slightly lower (by about 1.4 HV) than those of the ECAPed alloy states. The increase of the ageing temperature from 60 °C to 100 °C resulted in the peak-ageing-time shortening. However, the maximum alloys' hardness was the highest after being aged at 80 °C. During the post-ECAP ageing at higher temperatures (140 °C and 180 °C), the hardness of the ECAPed alloy states was decreased in a very short time.

### 3.2 Microstructure

**Figure 3** shows the recrystallized microstructure of the 6082-alloy quenched state that consists of fine solid-solution grains (average size: 14.6  $\mu\text{m}$ ). However, very coarse grains (average size: 115.6  $\mu\text{m}$ ) of the recrystallized solid solution were observed after the quenching of the 6063 alloy (**Figure 4**).

In the case of the 6082 alloy (containing the mass fraction 0.49 % of Mn), no considerable solid-solution

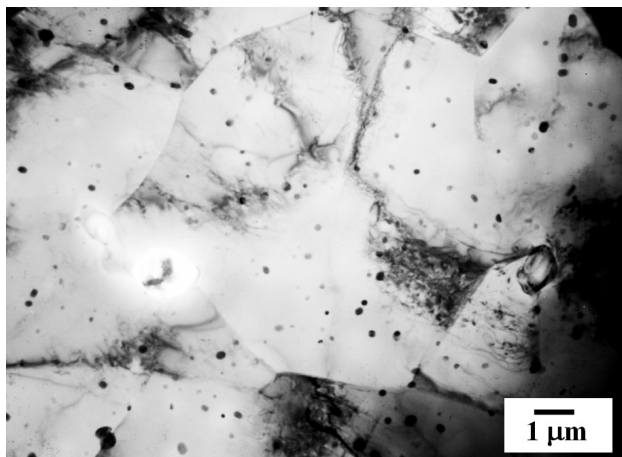


**Figure 3:** Microstructure of the quenched EN AW 6082 alloy state (550 °C + water quenching), TEM

**Slika 3:** Mikrostruktura gašene zlitine EN AW 6082 (550 °C + gašenje v vodi), TEM

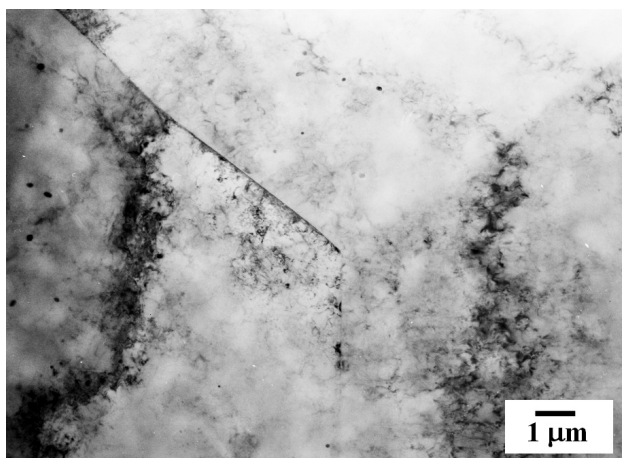


**Figure 4:** Microstructure of the quenched EN AW 6063 alloy state (510 °C + water quenching), TEM

**Slika 4:** Mikrostruktura gašene zlitine EN AW 6063 (510 °C + gašenje v vodi), TEM

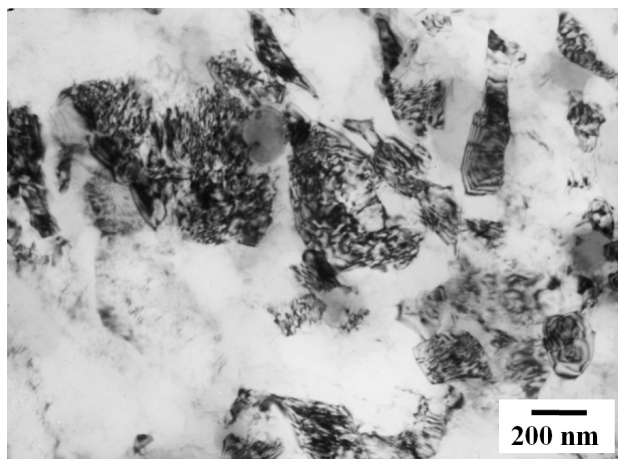


**Figure 5:** Microstructure of the ECAPed EN AW 6082 alloy state, TEM

**Slika 5:** Mikrostruktura zlitine EN AW 6082 po ECAP, TEM

grain growth during the applied solution annealing at 550 °C was prevented by the grain-boundary pinning effect of the fine, dispersive, Mn-rich phase particles (**Figure 3**; particle size: 30–300 nm). The role of these dispersive particles is to inhibit the recrystallization process and the matrix grain growth.<sup>22–25</sup> Comparing **Figures 3** and **4**, it is obvious that the volume fraction of the fine dispersive particles in the coarse-grained matrix of the 6063 alloy (Fe-rich phase particles with the average size of 150 nm) was lower than in the 6082-alloy matrix. Both types of dispersive particles were mostly distributed homogeneously throughout the equiaxed solid-solution grains, which exhibited a relatively low dislocation density in both quenched alloy states.

During the repetitive ECAP applied to the quenched alloy state, the solid-solution grains were heterogeneously refined. A cell-dislocation substructure, equiaxed ultra-fine subgrains, and high dislocation

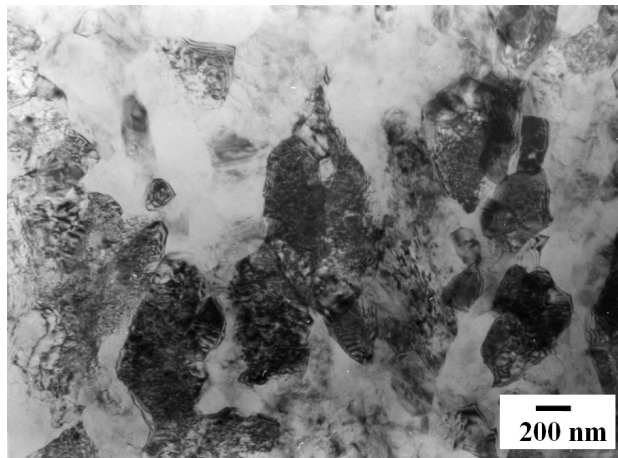


**Figure 6:** Microstructure of the post-ECAP aged EN AW 6063 alloy treated for 60 h at 80 °C, TEM

**Slika 6:** Mikrostruktura zlitine EN AW 6063 po ECAP, starane 60 h pri 80 °C, TEM



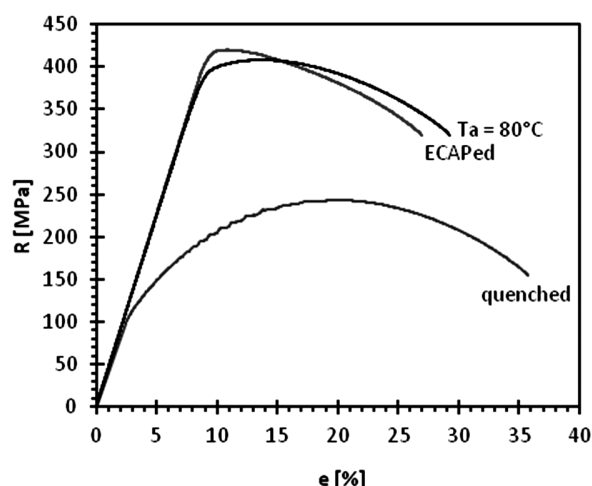


**Figure 7:** Stress-strain curves of the EN AW 6082 alloy states  
**Slika 7:** Krivulja napetost – raztezek za različna stanja zlitine EN AW 6082

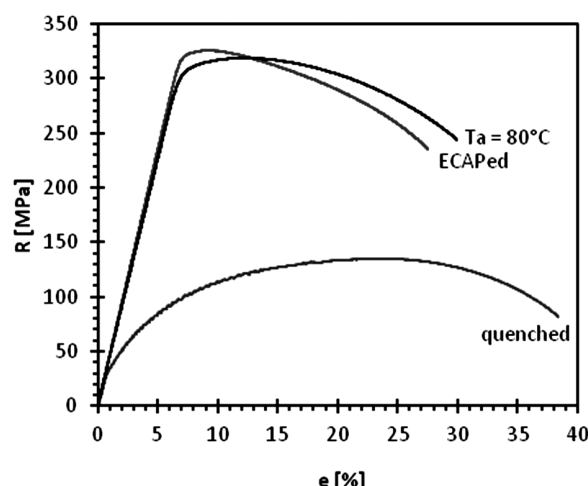


**Figure 8:** Stress-strain curves of the EN AW 6063 alloy states  
**Slika 8:** Krivulja napetost – raztezek za različna stanja zlitine EN AW 6063

density within the subgrains were observed in the microstructure of the ECAPed alloys (**Figure 5**). The average subgrain size (180 nm) measured for the ECAPed 6082 alloy was a little bit smaller than the size of the subgrains (220 nm) of the quenched 6063-alloy state formed during ECAP. This was a result of the supersaturation of the severely deformed solid solution, obtained for the quenched 6082 alloy prior to the use of repetitive ECAP that was higher than that obtained for the 6063 alloy with lower Mg and Si contents. With an increase in the content of the alloying elements in the solid solution of the Al-based alloys, the microstructure formed after ECAP becomes finer and the dislocation density inside the ultrafine grains is higher.<sup>26</sup> After the peak ageing of the ECAPed alloy states (**Figure 6**), a slight dislocation recovery was observed in the subgrains, still having a very high dislocation density, and in the dislocation cells. In addition, the ultra-fine subgrains grew to a size of about 250 nm and 280 nm during the peak ageing of the 6082 and 6063 alloys, respectively.

### 3.3 Tensile test

The values of the tensile strength ( $R_m$ ), the yield strength ( $R_{p0.2}$ ) and the tensile ductility ( $A_g$ ,  $A$ ,  $Z$ ), which are presented in **Table 3**, and the stress-strain curves shown in **Figures 7** and **8**, provide a comparison of the mechanical properties determined for the quenched, ECAPed and post-ECAP peak-aged (for 60 h at 80 °C) states of the analyzed alloys. An elimination of the strengthening effect of the nanoparticles of the  $\beta''$ - and  $\beta'$ -Mg<sub>2</sub>Si phases through their dissolution into the solid solution of the quenched alloy states is indicated by their low yield strength, ultimate tensile strength and high ductility. The ultimate tensile strength and, especially, the yield stress of the quenched alloy states increased significantly ( $R_{p0.2}$  by about 293 MPa and 283 MPa for the 6082 and 6063 alloys, respectively) due to the

repetitive ECAP, while the tensile ductility ( $A$ ,  $Z$ ) deteriorated. The tensile-deformation behaviour of these deformed alloy states (**Figures 7** and **8**) is typical for the severely strain-hardened (ECAPed) AlMgSi alloys<sup>19,21</sup> for which the low values of the uniform tensile elongation ( $A_g$ ) and a high  $R_{p0.2}/R_m$  ratio have been found.

Despite the fact that the hardness values of the post-ECAP peak-aged alloy states are only a little bit lower than those of the ECAPed ones, the yield strength and the ultimate tensile strength of the ECAPed alloys decreased by about 5.5 % and 2.5 %, respectively, during the applied peak-ageing treatment. It is obvious that the applied ageing of the ECAPed alloys resulted in an improved tensile ductility (mainly the uniform tensile elongation  $A_g$ ). This softening of the alloys occurred because the softening effect caused by the microstructure low recovery and the relaxation of the internal stresses dominates the hardening effect caused by the expected sequence precipitation of the metastable Mg<sub>2</sub>Si-phase (GP-zones,  $\beta''$ - and  $\beta'$ -phase) particles.<sup>27,28</sup>

**Table 3:** Mechanical properties of the analyzed alloy states

**Tabela 3:** Mehanske lastnosti analiziranih stanj zlitin

Alloy	State	$R_{p0.2}$ / MPa	$R_m$ / MPa	$A_g$ / %	$A$ / %	$Z$ / %
EN AW 6082	Q	115	243	14.1	31.9	72.5
	E	408	420	1.6	19.8	39.8
	pEa	384	408	4.7	22.1	42.7
EN AW 6063	Q	34	135	20.2	36.4	86.5
	E	317	326	2.3	22.5	43.1
	pEa	300	319	5.2	24.5	42.9

Q-quenched, E-ECAPed, pEa-post-ECAP aged

## 4 CONCLUSIONS

The severe plastic deformation of the quenched EN AW 6082 and EN AW 6063 aluminium alloys realized



with the ECAP process caused a refinement and an intensive strain hardening of the alloy solid solution. The result was the increased hardness and strength of the alloys and, on the other hand, a decrease in the alloys' tensile ductility. The increased supersaturation of the severely deformed solid solution obtained for the quenched 6082 alloy was a reaction to its higher strengthening caused by the ECAP processing and was higher than that obtained for the 6063 alloy with the lower Mg and Si contents. The artificial post-ECAP peak-ageing of the alloys was effective only in slightly improving the tensile ductility of the ECAPed alloys, which was a consequence of the low recovery of the ECAPed alloy and the relaxation of internal stresses.

### Acknowledgements

This work was supported by the Scientific Grant Agency of the Slovak Republic within the grant project VEGA No. 1/0866/09.

### 5 REFERENCES

- <sup>1</sup> V. M. Segal, V. I. Reznikov, A. E. Drobyshvskiy, V. I. Kopylov, *Russian Metallurgy*, 1 (1981), 99–105
- <sup>2</sup> M. Furukawa, Z. Horita, M. Nemoto, T. G. Langdon, *Journal of Materials Science*, 36 (2001), 2835–2843
- <sup>3</sup> J. Bidulská, R. Kočíško, R. Bidulský, M. Actis Grande, T. Donič, M. Martikán, *Acta Metallurgica Slovaca*, 16 (2010), 4–11
- <sup>4</sup> Z. Horita, T. Fujinami, M. Nemoto, T. G. Langdon, *Journal of Materials Processing Technology*, 117 (2001), 288–292
- <sup>5</sup> R. K. Islamgaliev, N. F. Yunusova, R. Z. Valiev, N. K. Tsenev, V. N. Perevezentsev, T. G. Langdon, *Scripta Materialia*, 49 (2003), 467–472
- <sup>6</sup> S. Lee, M. Furukawa, Z. Horita, T. G. Langdon, *Materials Science and Engineering, A* 342 (2003), 294–301
- <sup>7</sup> R. Z. Valiev, N. A. Enikeev, T. G. Langdon, *Metallic Materials*, 49 (2011), 1–9
- <sup>8</sup> Z. Horita, S. Lee, S. Ota, K. Neishi, T. G. Langdon, *Materials Science Forum*, 357–359 (2001), 471–476
- <sup>9</sup> K. Turba, P. Malek, M. Cieslar, *Metallic Materials*, 45 (2007), 165–170
- <sup>10</sup> M. J. Starink, N. Gao, M. Furukawa, Z. Horita, C. Xu, T. G. Langdon, *Reviews on Advanced Materials Science*, 7 (2004), 1–12
- <sup>11</sup> W. J. Kim, C. S. Chung, D. S. Ma, S. I. Hong, H. K. Kim, *Scripta Materialia*, 49 (2003), 333–338
- <sup>12</sup> M. Y. Murashkin, M. V. Markushev, Y. V. Ivanisenko, R. Z. Valiev, *Solid State Phenomena*, 114 (2001), 91–96
- <sup>13</sup> J. K. Kim, W. J. Kim, *Solid State Phenomena*, 124–126 (2007), 1437–1440
- <sup>14</sup> T. Kvačák, R. Bidulský (Eds.), *Aluminium Alloys, Theory and Applications*, InTech, Rijeka 2011
- <sup>15</sup> J. R. Davis (Ed.), *Aluminium and Aluminium Alloys*, ASM Specialty Handbook, ASM International, Ohio 1993
- <sup>16</sup> J. Zrník, Z. Nový, T. Kvačák, V. Bernášek, D. Kešner, M. Slámová, *Acta Metallurgica Slovaca*, 10 (2004), 277–284
- <sup>17</sup> B. Cherukuri, T. S. Nedkova, R. Srinivasan, *Materials Science and Engineering, A* 410–411 (2005), 394–397
- <sup>18</sup> J. C. Werenskiold, H. J. Roven, *Materials Science and Engineering, A* 410–411 (2005), 174–177
- <sup>19</sup> H. J. Roven, H. Nesboe, J. C. Werenskiold, T. Seibert, *Materials Science and Engineering, A* 410–411 (2005), 426–429
- <sup>20</sup> P. Leo, E. Cerri, P. P. De Marco, H. J. Roven, *Journal of Materials Processing Technology*, 182 (2007), 207–214
- <sup>21</sup> W. J. Kim, J. Y. Wang, *Materials Science and Engineering, A* 464 (2007), 23–27
- <sup>22</sup> N. Parson, J. Hankin, K. Hicklin, C. Jowett, Comparison of the extrusion performance and product characteristics of three structural extrusion alloys: AA6061, AA6082 and AA6005A, In.: *Proceedings of the 7th International Aluminium Extrusion Technology Seminar*, Vol. 1, Aluminium Association, Washington DC, 2000, 1–12
- <sup>23</sup> G. F. Vander Voort (Ed), *Metallography and Microstructures*, ASM Handbook, Vol. 9, ASM International, Ohio 2004
- <sup>24</sup> A. L. Dons, *Journal of Light Metals*, 1 (2001), 133–149
- <sup>25</sup> L. Lodgaard, N. Ryum, *Materials Science and Engineering, A* 283 (2000), 144–152
- <sup>26</sup> J. May, M. Dinkel, D. Amberger, H. W. Höppel, M. Göken, *Metallurgical and Materials Transactions, A* 38 (2007), 1941–1945
- <sup>27</sup> M. Hockauf, L. W. Meyer, D. Nickel, G. Alisch, T. Lampke, B. Wielage, L. Krüger, *Journal of Materials Science*, 43 (2008), 7409–7417
- <sup>28</sup> K. Hockauf, L. W. Meyer, M. Hockauf, T. Halle, *Journal of Materials Science*, 45 (2010), 4754–4760



# APPLICATION OF A TAGUCHI-BASED NEURAL NETWORK FOR FORECASTING AND OPTIMIZATION OF THE SURFACE ROUGHNESS IN A WIRE-ELECTRICAL-DISCHARGE MACHINING PROCESS

## UPORABA TAGUCHIJEVE NEVRONSKE MREŽE ZA NAPOVEDOVANJE IN OPTIMIRANJE POVRŠINSKE HRAPAVOSTI PRI POSTOPKU ŽIČNE EROZIJE

Yigit Kazancoglu<sup>1</sup>, Ugur Esme<sup>2</sup>, Mustafa Kemal Kulekci<sup>2</sup>, Funda Kahraman<sup>2</sup>,  
Ramazan Samur<sup>3</sup>, Adnan Akkurt<sup>4</sup>, Melih Turan Ipekci<sup>5</sup>

<sup>1</sup>Izmir University of Economics, Department of Business Administration, 35330, Balcova-Izmir, Turkey

<sup>2</sup>Mersin University Tarsus Technical Education Faculty, Department of Mechanical Education, 33140 Tarsus-Mersin, Turkey

<sup>3</sup>Marmara University Technical Education Faculty, Department of Metal Education, 34722 Goztepe-Istanbul, Turkey

<sup>4</sup>Gazi University Industrial Arts Education Faculty, Department of Technological Education, 06830 Golbasi-Ankara, Turkey

<sup>5</sup>Gazi University, Department of Mechanical Engineering, 06570 Maltepe-Ankara, Turkey  
uguresme@gmail.com

*Prejem rokopisa – received: 2012-02-16; sprejem za objavo – accepted for publication: 2012-06-01*

Wire-electrical-discharge machining (WEDM) is a modification of electro-discharge machining (EDM) and has been widely used for a long time for cutting punches and dies, shaped pockets and other machine parts on conductive materials. WEDM erodes workpiece materials by a series of discrete electrical sparks between the workpiece and an electrode flushed or immersed in a dielectric fluid. The WEDM process is particularly suitable for machining hard materials as well as complex shapes. In this paper, a neural network and the Taguchi design method have been implemented for minimizing the surface roughness in a WEDM process. A back-propagation neural network (BPNN) was developed to predict the surface roughness. In the development of a predictive model, machining parameters of open-circuit voltage, pulse duration, wire speed and dielectric flushing pressure were considered as the input model variables of the AISI 4340 steel. An analysis of variance (ANOVA) was used to determine the significant parameter affecting the surface roughness ( $R_a$ ). Finally, the Taguchi approach was applied to determine the optimum levels of machining parameters.

**Keywords:** WEDM, Taguchi-design method, neural network, surface roughness

Žična erozija (WEDM) je modifikacija potopne erozije (EDM) in se uporablja že dolgo časa za izdelavo rezilnih in drugih orodij ter strojnih delov. WEDM erodira obdelovanec z iskrenjem med obdelovancem in elektrodo, ki se spira, oziroma je potopljena v dielektrično tekočino. WEDM-postopek je še posebej primeren za obdelavo trdih materialov, kot tudi za kompleksne oblike. V tem članku sta bili uporabljeni nevronska mreža in Taguchijeva metoda načrtovanja za zmanjšanje hrupavosti površine. Pri razvoju modela za napovedovanje hrupavosti so bili upoštevani parametri obdelave: električna napetost, trajanje pulza, hitrost žice in tlak dielektrične tekočine za spiranje kot vhodne spremenljivke pri obdelavi jekla AISI 4340. Analiza variance (ANOVA) je bila uporabljena za določanje vplivnih parametrov, ki vplivajo na površinsko hrupavost ( $R_a$ ). Na koncu je bil uporabljen Taguchijev približek za določitev optimalnih parametrov procesa.

**Ključne besede:** WEDM, Taguchi oblikovanje, nevronska mreža, površinska hrupavost

## 1 INTRODUCTION

The technologies of the wire-electrical-discharge machining (WEDM) have been emphasized significantly and have improved rapidly in recent years due to the requirements in various manufacturing fields. WEDM is used to produce complex two- and three-dimensional shapes through electrically conductive workpieces by using a wire electrode<sup>1-3</sup>. As shown in **Figure 1**, the sparks are generated between the conductive workpiece and a wire electrode flushed with, or immersed in, a dielectric fluid<sup>2</sup>. The degree of accuracy of the workpiece dimensions obtainable and the fine surface finishes make WEDM particularly valuable for the applications involving the manufacture of stamping dies, extrusion dies and prototype parts.<sup>2</sup>

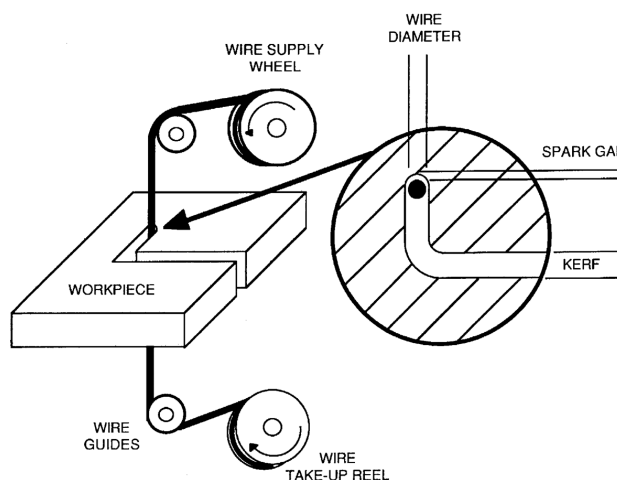


**Figure 1:** Working principle of a WEDM process<sup>4</sup>  
**Slika 1:** Shematičen prikaz WEDM-postopka<sup>4</sup>

The most important performance measures in WEDM are cutting speed, workpiece surface roughness and cutting width.<sup>2</sup> Discharge current, discharge capacitance, pulse duration, pulse frequency, wire speed, wire tension, average working voltage and dielectric flushing conditions are the machining parameters that affect the performance measures.<sup>1-4</sup>

An optimization of the process parameters is the key step of the Taguchi method in achieving high quality without an increased cost. This is because an optimization of the process parameters can improve the quality, and the optimum process parameters obtained with the Taguchi method are insensitive to the variation of environmental conditions and other noise factors. Basically, the classical process-parameter design is complex and not easy to use.<sup>5,6</sup> An advantage of the Taguchi method is that it emphasizes the mean-performance characteristic value close to the target value rather than a value within certain specification limits, thus improving the product quality. Additionally, the Taguchi method for experimental design is straightforward and easy to apply to many engineering situations, making it a powerful yet simple tool. It can be used to quickly narrow the scope of a research project or to identify problems in a manufacturing process from the data already in existence.<sup>5-8</sup>

A large number of experiments have to be carried out when the number of the process parameters increases. To solve this task, the Taguchi method uses a special design of orthogonal arrays to study the entire process-parameter space with only a small number of experiments. Using an orthogonal array to design the experiment can help the designers to study the influence of multiple controllable factors on the average quality characteristics and variations in a fast and economic way, while using a signal-to-noise ratio ( $S/N$ ) to analyze the experimental data can help the designers of a product, or a manufacturer, to easily find out optimum parametric combinations.<sup>5-8</sup>

Investigations into the influences of the machining input parameters on the performance of WEDM have been widely reported. Huang et al.<sup>1</sup> determined the effect of the WEDM process parameters (pulse-on time, pulse-off time, table feed rate, flushing pressure and workpiece surface, and machining history) on the gap width, the surface roughness and the white layer depth of a machined workpiece surface using the Taguchi method. Tosun et al.<sup>2</sup> investigated the effect and optimization of the machining parameters on the cutting width and the material-removal rate (MRR) in WEDM based on the Taguchi method. The experimental studies were conducted with a varying pulse duration, open-circuit voltage, wire speed and dielectric flushing pressure. Mohammadi et al.<sup>3</sup> applied the statistical analysis of WEDM turning on MRR using the Taguchi techniques. They considered the effects of the input parameters (power, time-off, voltage, servo, wire speed, wire tension

and rotational speed) on the responses (MRR, surface roughness). Lin et al.<sup>9</sup> investigated the effects of the machining parameters in electrical discharge machining on the machining characteristics of the SKH 57 high-speed steel. Moreover, they determined the optimum combination levels of the machining parameters based on the Taguchi method. Tosun and Cogun<sup>10</sup> experimentally investigated the effects of the cutting parameters on the wire-electrode wear in WEDM. On the basis of ANOVA and F-Test, they found that the most effective parameters of the wire-wear ratio are the open-circuit voltage and pulse durations.

Tarng et al.<sup>11</sup> developed a neural-network system to determine the settings of pulse duration, pulse interval, peak current, open-circuit voltage, servo-reference voltage, electric capacitance and wire speed for an estimation of the cutting speed and the surface finish. Scott et al.<sup>12</sup> used a factorial-design method to determine the optimum combination of control parameters in WEDM, the measures of the machining performance being the MRR and the surface finish. It was found that discharge current, pulse duration and pulse frequency are significant control factors. Spedding and Wang<sup>13</sup> developed mathematical models using the response-surface methodology (RSM) and an artificial neural network in the WEDM process. They considered the effects of the input parameters (pulse width, time between two pulses, wire mechanical tension and wire-feed speed) on the responses (cutting speed and surface roughness). Yuan et al.<sup>14</sup> carried out a multi-objective optimization based on the Gaussian process regression to optimize the high-speed WEDM process, considering mean current, on-time and off-time as the input parameters and MRR and surface roughness as the output responses. Kung and Chiang<sup>15</sup> developed mathematical models using RSM to investigate the influences of the machining parameters on the performance characteristics of MRR and surface roughness in a WEDM process. Esme et al.<sup>16</sup> constructed both a mathematical model and a neural-network model to predict, reproduce and compare the types of surface roughness under different machining conditions. On the basis of a literature review some insight has been gained

**Table 1:** Comparison between neural networks and the Taguchi design method<sup>17</sup>

**Tabela 1:** Primerjava med nevronskimi mrežami in Taguchi metodo oblikovanja<sup>17</sup>

Comparison	Neural networks	Taguchi design
Computational time	Long	Medium
Model development	Yes*	No
Optimization	Through a model	Straight
Understanding	Moderate	Normal
Software availability	Available	Available
Optimization sensitivity	High	Normal
Application rate (usage frequency)	Frequent	Rare

\* No factor-interaction effects



into the use of neural networks and Taguchi design methods for modeling and optimizing different WEDM processes. The main advantage of the neural-network method is that it provides modeling and predictions. The main advantage of the Taguchi design method is that it provides an optimization and analyzes the effect of each process parameter on the responses. **Table 1** shows a comparison between neural networks and the Taguchi modeling and optimization method<sup>17</sup>.

In the present work, two of the techniques, namely, the neural network with a back-propagation network (BPN) and the Taguchi design method have been employed. Qwiknet 2.23 software and Taguchi Soft program were used for the NN modeling and the Taguchi optimization technique, respectively. Open voltage, pulse duration, wire speed and dielectric flushing pressure were selected as the input factors, whereas surface roughness ( $R_a$ ) was selected as the response. A BPN model was developed for the prediction of the surface roughness. An analysis-of-variance (ANOVA) table was used to determine the significant WEDM parameter affecting the surface roughness. An approach to determine the optimum machining-parameter setting was proposed on the basis of the Taguchi design method.

## 2 EXPERIMENTAL SET-UP AND THE TEST PROCEDURE

In this experimental study, all experiments were conducted on an Acutex WEDM machine. The WEDM machining set-up is shown in **Figure 2**.

The work material, electrode and other machining conditions are given in **Table 2**.

**Table 2:** Constant machining condition set-up

**Tabela 2:** Podatki o nastavitvi naprave

Workpiece	AISI 4340
Wire material	CuZn37
Workpiece dimensions (mm)	150 × 150 × 10
Table feed rate (mm/min)	8.2
Pulse-interval time (μs)	18
Wire diameter (mm)	0.25
Wire tensile strength (N/mm <sup>2</sup> )	900
Machining cut-off length (mm)	0.8
Traversing length (mm)	5

Open-circuit voltage (150–250 V), pulse duration (600, 800, 1000) ns, wire speed (6, 8, 10) mm/min and dielectric flushing pressure (10, 12, 14) kg/cm<sup>2</sup> were selected as the input parameters and surface roughness was selected as the output parameter. Surface-roughness ( $R_a$ ) measurements were made by using a Phynix TR-100 portable surface-roughness tester with  $\lambda = 0.03$  mm for the cut-off length. Three measurements were taken and their average was calculated as  $R_a$  value. According to the Taguchi orthogonal-design concept an  $L_{18}$  mixed orthogonal-array table was chosen for the experiments.

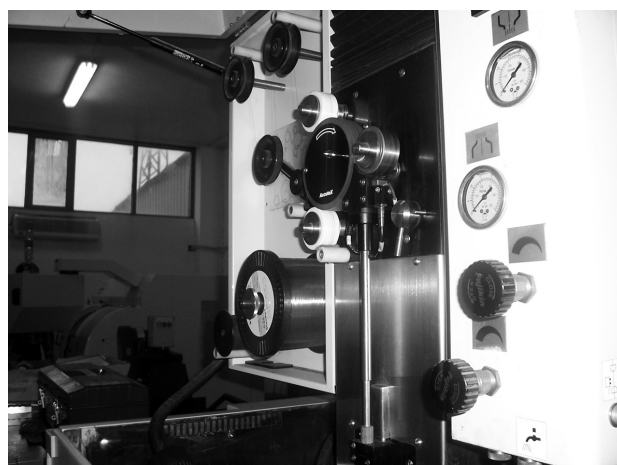


**Figure 2:** WEDM machining set-up

**Slika 2:** WEDM-naprava

The orthogonal-array table used in the Taguchi design method was applied to BPN as testing data. BPN was developed to predict the surface roughness. The optimum machining-parameter combination was obtained by using an analysis of the signal-to-noise ( $S/N$ ) ratio. The signal-to-noise ( $S/N$ ) ratio is a measure of the magnitude of the data set relative to the standard deviation. If the  $S/N$  is large, the magnitude of the signal is large relative to the noise, as measured with the standard deviation.<sup>8,18,19</sup> There are several  $S/N$  ratios available depending on the types of characteristics. The nominal ratio is the best, higher is better and lower is better. We would select the  $S/N$  if the system is optimized when the response is as small as possible.<sup>1–5</sup> The  $S/N$  ratio for the *LB* (lower is better) characteristic is calculated by using Equations (1) and (2)<sup>5</sup>:

$$L_j = \frac{1}{n} \sum_{k=1}^n y_i^2 \quad (1)$$

$$\eta_j = -10 \lg L_j \quad (2)$$

where  $y_i$  is the response value,  $L_j$  is the loss function,  $\eta_j$  is the  $S/N$  ratio.

## 3 EXPERIMENTAL RESULTS AND DATA ANALYSIS

A neural network based on back propagation is a multilayered architecture made up of one or more hidden layers placed between the input and output layers. The components of the input pattern consisted of the control variables of the machining operation (open-circuit voltage, pulse duration, wire speed and dielectric flushing pressure), whereas the output-pattern components represented the measured factor (surface roughness). **Table 3** shows a Taguchi  $L_{18}$  orthogonal-array plan of the experiment and a training set for the neural-network application.

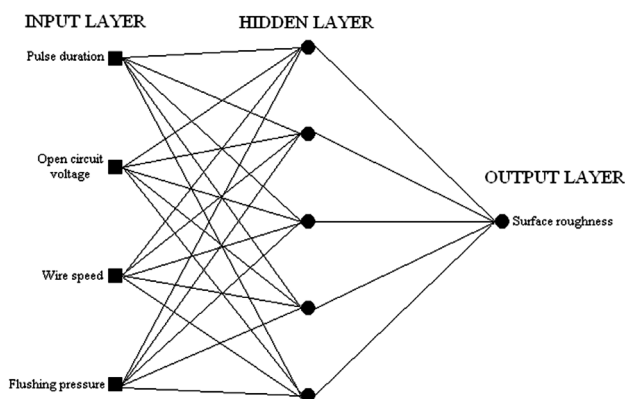
**Table 3:**  $L_{18}$  orthogonal array and a neural-network training set**Tabela 3:**  $L_{18}$  ortogonalna matrika za usposabljanje nevronske mreže

Exp. no.	Open voltage (V)	Pulse duration (ns)	Wire speed (m/min)	Flushing pressure (kg/cm <sup>2</sup> )	Surface roughness (μm)
1	150	600	6	10	2.08
2	150	600	8	12	2.20
3	150	600	10	14	2.21
4	150	800	6	10	2.48
5	150	800	8	12	2.51
6	150	800	10	14	2.52
7	150	1000	6	12	2.79
8	150	1000	8	14	2.82
9	150	1000	10	10	2.86
10	250	600	6	14	2.62
11	250	600	8	10	2.69
12	250	600	10	12	2.72
13	250	800	6	12	3.10
14	250	800	8	14	3.06
15	250	800	10	10	3.09
16	250	1000	6	14	3.36
17	250	1000	8	10	3.40
18	250	1000	10	12	3.45

The orthogonal-array table used in the Taguchi design method was applied to BPN as testing data. The network structure was selected to be of the 4 : 5 : 1 type. The used BPN model is shown in **Figure 3**.

The testing validity of the regression analysis and the neural-network results was achieved by using the input parameters according to the design matrix given in **Table 4**.

The performance of each BPN was calculated with the absolute error (%) of the tested subset. The average absolute error was calculated as 1.08 %. The surface roughness for various machining conditions can be predicted in a quick and accurate manner; the BPN results showed that the predicted values were very close to the experimental values. The value of the multiple coefficient  $R^2$  is 0.99, which means that the explanatory

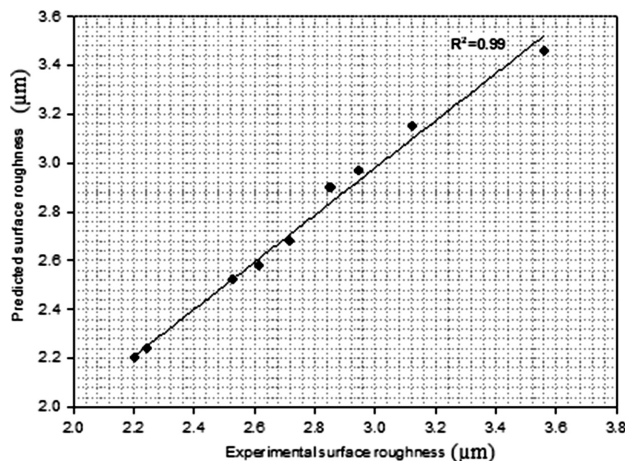
**Figure 3:** 4 : 5 : 1 (4 inputs, 1 hidden layer with 5 neurons and 1 output) type of the BPN algorithm used for modeling**Slika 3:** 4 : 5 : 1 (4 vhodni podatki, 1 skriti nivo s 5 nevroni in 1 izhodni podatek) vrsta BPN algoritma, uporabljenega pri modeliranju**Table 4:** Test set for the validity of the constructed neural network**Tabela 4:** Zbirka podatkov za preizkušanje postavljene nevronske mreže

Exp. no.	Open voltage (V)	Pulse duration (ns)	Wire speed (m/min)	Flushing pressure (kg/cm <sup>2</sup> )	Surface roughness (μm)	
					Experimental	Predicted
1	150	600	8	10	2.20	2.20
2	250	600	6	12	2.62	2.58
3	150	800	8	10	2.53	2.52
4	250	800	6	14	2.95	2.97
5	150	1000	8	10	2.85	2.90
6	150	1000	6	14	2.72	2.68
7	250	1000	10	10	3.56	3.46
8	250	800	10	12	3.13	3.15

Average maximum error: 1.08 %

variables explain 99 % of the variability in the response variable. The predicted values of the surface roughness were compared with the experimental values as shown in **Figure 4**.

The effect and optimization of machining settings for the minimum surface roughness was investigated experimentally. The optimum machining-parameter combination was obtained by analyzing the  $S/N$  ratio. ANOVA was used to consider the effects of the input factors on the response and was performed on experimental data.

**Figure 4:** Comparison of experimental and predicted values**Slika 4:** Primerjava eksperimentalnih in napovedanih vrednosti**Table 5:** Results of ANOVA for the surface roughness**Tabela 5:** Rezultati analize variance (ANOVA) za hrapavost površine

Parameter code	Factors	DF	SS	F	MS	Contribution percentage (%)
A	Open-circuit voltage	1	1.404	1378.58	1.401	49.36
B	Pulse duration	2	1.440	711.42	0.720	50.03
C	Wire speed	2	0.015	7.32	0.007	0.52
D	Flushing pressure	2	0.003	1.68	0.001	0.10
Error		10	0.020	—	0.003	—
Total		17	2.844	—		100

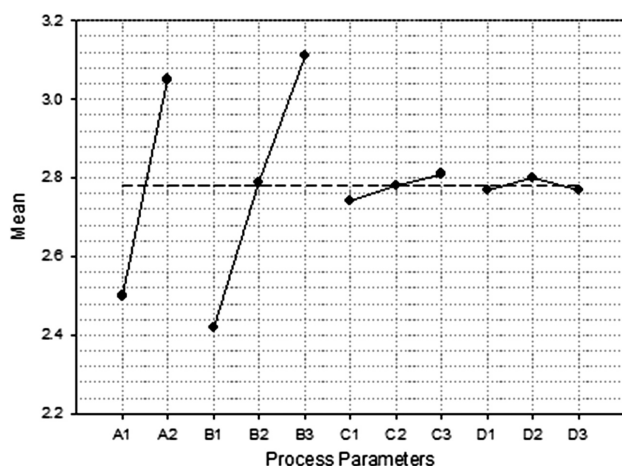


**Figure 5:** The effect of machining parameters on the surface roughness

**Slika 5:** Učinek parametrov obdelave na hrapavost površine

The confidence level was selected as 95 %. The results of ANOVA for the surface roughness are shown in **Table 5**.

After analyzing **Table 4**, it is observed that the open-circuit voltage and the pulse duration have a great influence on the obtained surface roughness. The wire speed and dielectric flushing pressure do not affect significantly the obtained surface roughness. The plot of the mean-factor effects is shown in **Figure 5**.

The  $S/N$  graph for the surface roughness is shown in **Figure 6**. It is evident that open-circuit voltage (49.36 %) and pulse duration (50.03 %) have the most significant effect on the surface roughness, which means that by increasing these two parameters we also increase the surface roughness. Wire speed (0.52 %) has little effect on the surface roughness. The effect of dielectric flushing pressure (0.10 %) is negligible.

Optimum factor levels and  $S/N$  ratios obtained at the end of the Taguchi design technique are summarized in **Table 6**.

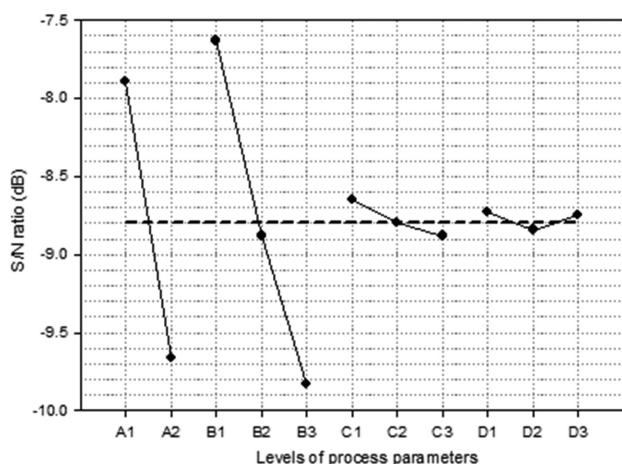


**Figure 6:**  $S/N$  graph for the surface roughness

**Slika 6:**  $S/N$ -diagram za hrapavost površine

**Table 6:** Optimum factor levels and their  $S/N$  ratios

**Tabela 6:** Nivoji optimalnih faktorjev in njihova  $S/N$ -razmerja

Code	Factors	$S/N$ ratio (dB)				
		Level 1	Level 2	Level 3	Max-min	Rank
A	Open-circuit voltage	-7.89	-9.66	–	1.77	2
B	Pulse duration	-7.63	-8.88	-9.83	2.20	1
C	Wire speed	-8.65	-8.80	-8.88	0.23	3
D	Flushing pressure	-8.73	-8.84	-8.75	0.11	4

Average  $S/N$  = -8.80

Based on the  $S/N$  ratio plot in **Figure 6**, the optimum machining parameters for the surface roughness are open-circuit voltage at level 1, pulse duration at level 1, wire speed at level 1 and dielectric flushing pressure at level 1 ( $A_1B_1C_1D_1$ ).

#### 4 CONFIRMATION TESTS

A confirmation experiment is the final step in the first iteration of designing an experiment process.<sup>5,8</sup> The purpose of the confirmation experiment is to validate the conclusions drawn during the analysis phase. The confirmation experiment is performed by conducting a test with a specific combination of the factors and levels previously evaluated.<sup>8,20</sup> In this study, after determining the optimum conditions and predicting the response under these conditions, a new experiment was designed and conducted with the optimum levels of the welding parameters. The final step is to predict and verify the improvement of the performance characteristic. The predicted  $S/N$  ratio  $\hat{\eta}$  using the optimum levels of the welding parameters can be calculated as:<sup>5,8,20</sup>

$$\hat{\eta} = \eta_m + \sum_{i=1}^n (\bar{\eta}_i - \eta_m) \quad (3)$$

where  $\eta_m$  is the total mean of the  $S/N$  ratio,  $\bar{\eta}_i$  is the mean of the  $S/N$  ratio at the optimum level, and  $n$  is the number of the main welding parameters that significantly affect the performance.<sup>8,18–20</sup> The result of the experimental confirmation using the optimum surface roughness is shown in **Table 7**.

**Table 7:** Results of the confirmation experiments for the surface roughness

**Tabela 7:** Rezultati potrditvenih eksperimentov za hrapavost površine

	Initial parameters	Optimum parameters
Parameter level	$A_1B_3C_3D_1$	$A_1B_1C_1D_1$
Surface roughness ( $\mu\text{m}$ )	2.86	2.10
$S/N$ ratio (dB)	-9.13	-6.57

The improvement in the  $S/N$  ratio from the initial machining parameters to the optimum machining parameters is 2.56 dB. Based on the result of the

confirmation test, the surface roughness is decreased 1.36 times.

## 5 CONCLUSIONS

This study presents a prediction, optimization and modeling of the surface roughness of the AISI 4340 steel in a wire-electrical-discharge machining (WEDM) process based on the Taguchi-based neural network with the back-propagation algorithm method. The following conclusions can be drawn from this study:

- The main WEDM parameters that affect the surface roughness of the machined parts were determined as pulse duration and open-circuit voltage among four controllable factors influencing the surface roughness using ANOVA,
- A neural network based on the back-propagation network (BPN) algorithm was constructed for predicting the surface roughness. The predicted values were found to be very close to the experimental values,
- The optimum parameter combination for the minimum surface roughness was obtained by using the Taguchi design method with an analysis of the S/N ratio,
- The confirmation test supports the finding that the surface roughness is greatly decreased by using the optimum design parameters,
- The obtained results indicate that the BPN model agreed well with the Taguchi analysis.

## 6 REFERENCES

- <sup>1</sup> J. T. Huang, Y. S. Lmiao, W. J. Hsue, *Journal of Materials Processing Technology*, 87 (1999), 69–81
- <sup>2</sup> N. Tosun, C. Cogun, G. Tosun, *Journal of Materials Processing Technology*, 152 (2004), 316–322
- <sup>3</sup> A. Mohammadi, A. F. Tehrani, E. Emanian, D. Karimi, *Journal of Materials Processing Technology*, 205 (2008), 283–289
- <sup>4</sup> D. Scott, S. Boyina, K. P. Rajurkar, *Int. J. Prod. Res.*, 29 (1991), 2189–2207
- <sup>5</sup> D. C. Montgomery, *Design and Analysis of Experiments*, Wiley, Singapore 1991
- <sup>6</sup> S. Fraley, M. Oom, B. Terrien, J. Z. Date, *The Michigan Chemical Process Dynamic and Controls Open Text Book*, USA, 2006
- <sup>7</sup> U. Esme, *The Arabian Journal for Science and Engineering*, 34 (2009), 519–528
- <sup>8</sup> S. C. Juang, Y. S. Tarn, *Journal of Materials Processing Technology*, 122 (2002), 33–37
- <sup>9</sup> Y. C. Lin, C. H. Cheng, B. L. Su, L. R. Hwang, *Materials and Manufacturing Process*, 21 (2006), 922–929
- <sup>10</sup> N. Tosun, C. Cogun, *Journal of Materials Processing Technology*, 134 (2003), 273–278
- <sup>11</sup> Y. S. Tarn, S. C. Ma, L. K. Chung, *International Journal of Machine Tools & Manufacture*, 35 (1995), 1693–1701
- <sup>12</sup> D. Scott, S. Boyina, K. P. Rajurkar, *International Journal Production Research*, 11 (1991), 2189–2207
- <sup>13</sup> T. A. Spedding, Z. Q. Wang, *Precision Engineering*, 20 (1997), 5–15
- <sup>14</sup> J. Yuan, K. Wang, T. Yu, M. Fang, *International Journal of Machine Tools & Manufacture*, 48 (2008), 47–60
- <sup>15</sup> K. Y. Kung, K. T. Chiang, *Materials and Manufacturing Process*, 23 (2008), 241–250
- <sup>16</sup> U. Esme, A. Sagbas, F. Kahraman, *Iranian Journal of Science & Technology, Transaction B, Engineering*, 33 (2009), 231–240
- <sup>17</sup> K. Y. Benyounis, A. G. Olabi, *Advances in Engineering Software*, 39 (2008), 483–496
- <sup>18</sup> D. S. Holmes, A. E. Mergen, *Signal to noise ratio—What is the right size*, [www.qualitymag.com/.../Manuscript%20Holmes%20&%20Mergen.pdf](http://www.qualitymag.com/.../Manuscript%20Holmes%20&%20Mergen.pdf), USA, 1996, 1–6
- <sup>19</sup> Y. Kazancoglu, U. Esme, M. Bayramoglu, O. Guven, S. Ozgun, *Mater. Tehnol.*, 45 (2011) 2, 105–110
- <sup>20</sup> P. J. Ross, *Taguchi Techniques for Quality Engineering*, 2nd ed., McGraw-Hill, New York 1996



# PREDICTION OF THE THERMODYNAMIC PROPERTIES FOR LIQUID Al-Mg-Zn ALLOYS

## NAPOVEDOVANJE TERMODINAMIČNIH LASTNOSTI TEKOČE ZLITINE Al-Mg-Zn

**Dragana Živković<sup>1</sup>, Yong Du<sup>2</sup>, Ljubiša Balanović<sup>1</sup>, Dragan Manasijević<sup>1</sup>,  
Duško Minić<sup>3</sup>, Nadežda Talijan<sup>4</sup>**

<sup>1</sup>University of Belgrade, Technical Faculty, Bor, Serbia

<sup>2</sup>State Key Laboratory of Powder Metallurgy, Central South University, Changsha, Hunan, China

<sup>3</sup>University of Priština, Faculty of Technical Sciences, Kosovska Mitrovica, Serbia

<sup>4</sup>University of Belgrade, Institute of Chemistry, Technology and Metallurgy, Belgrade, Serbia  
dzivkovic@tf.bor.ac.rs

*Prejem rokopisa – received: 2012-02-22; sprejem za objavo – accepted for publication: 2012-03-29*

The results of a thermodynamic-property prediction for liquid Al-Mg-Zn alloys using the general solution model are presented in this paper. Calculations were done in nine sections of the system with different molar ratios of Mg:Zn, Zn:Al and Al:Mg in the temperature range of 900–1200 K. Partial and integral molar quantities – including the activities for all three components, the integral molar excess Gibbs energies and the integral molar enthalpies of mixing – were obtained. Some of the calculation results were compared with the experimental data available in the literature, showing a good agreement with it.

**Keywords:** thermodynamics of alloys, Al-Mg-Zn system, general solution model

V članku so predstavljeni rezultati raziskav termodinamičnih lastnosti tekočih zlitin Al-Mg-Zn, napovedanih z uporabo splošnega modela raztapljanja. Izračuni so bili izvršeni v devetih prerezih sistema z različnimi molarnimi deleži Mg:Zn, Zn:Al in Al:Mg v območju temperatur 900–1200 K. Dobljene so bile parcialne in celotne molarne količine, vključno z aktivnostmi za vse tri komponente, skupni molarni presežek Gibbsove energije in skupna molarna entalpija mešanja. Ugotovljeno je dobro ujemanje izračunanih rezultatov z razpoložljivimi eksperimentalnimi podatki iz literature.

**Ključne besede:** termodinamika zlitin, sistem Al-Mg-Zn, splošni model raztapljanja

## 1 INTRODUCTION

The so-called ZA alloys – zinc-aluminum-based alloys – have a wide application in different fields of industry<sup>1,2</sup>. The ternary Al-Mg-Zn system belongs to this group of materials, which are of interest as the lead-free solders for die attach<sup>1–4</sup>. Therefore, different properties of this system were investigated in order to define it more completely<sup>5–9</sup>.

The thermodynamics and the phase equilibria of the Al-Mg-Zn system have been examined widely<sup>10–20</sup>. Most of the literature data is related to the phase-diagram determination<sup>10–17</sup>. A complete reference compilation concerning the experimental data obtained for the above-mentioned ternary alloys up to 1998 can be found in the work of Liang et al.<sup>19</sup>, while the last review is given in an article by Raghavan<sup>15</sup> from 2010.

The liquidus projection of the Al-Mg-Zn system is shown in **Figure 1**, according to Refs.<sup>14</sup> and <sup>17</sup>.

Among the numerous researches, there are only a few thermodynamic studies<sup>17–19</sup>. Experimental thermodynamic investigations of the Al-Mg-Zn system in the liquid state were done for the chosen sections at the temperatures of 883 K and 933 K using vapor-pressure measurements<sup>17</sup>, EMF<sup>18</sup> and mixing calorimetry<sup>19</sup>, while the thermodynamic assessments can be found in<sup>20,21</sup>.

Considering the available literature and the lack of a complete thermodynamic data with respect to the wider temperature and concentration ranges, the results of the thermodynamic-property prediction for the liquid Al-Mg-Zn alloys in the temperature interval of 900–1200 K, using the general solution model, are given in this paper as a contribution to a full thermodynamic description of this ternary system.

## 2 THEORETICAL FUNDAMENTALS

The general solution model for the calculation of the thermodynamic properties of ternary systems based on the known binary thermodynamic data has been provided by Chou<sup>22,23</sup>. It breaks down the boundary between symmetrical and asymmetrical models, and has already been proved in some practical examples<sup>24,25</sup> as the correct and accurate model. This model was developed for multicomponent systems and its basic equations are as follows<sup>22</sup>:

$$\Delta G^E = \sum_{\substack{i,j=1 \\ i \neq j}}^m x_i x_j \left[ A_{ij}^0 + A_{ij}^1 \cdot \left( (x_i - x_j) + \sum_{\substack{k=1 \\ k \neq i,j}}^m A_{ij}^1 x_k (2S_{i(j)}^{(k)} - 1) \right) \right] \quad (1)$$

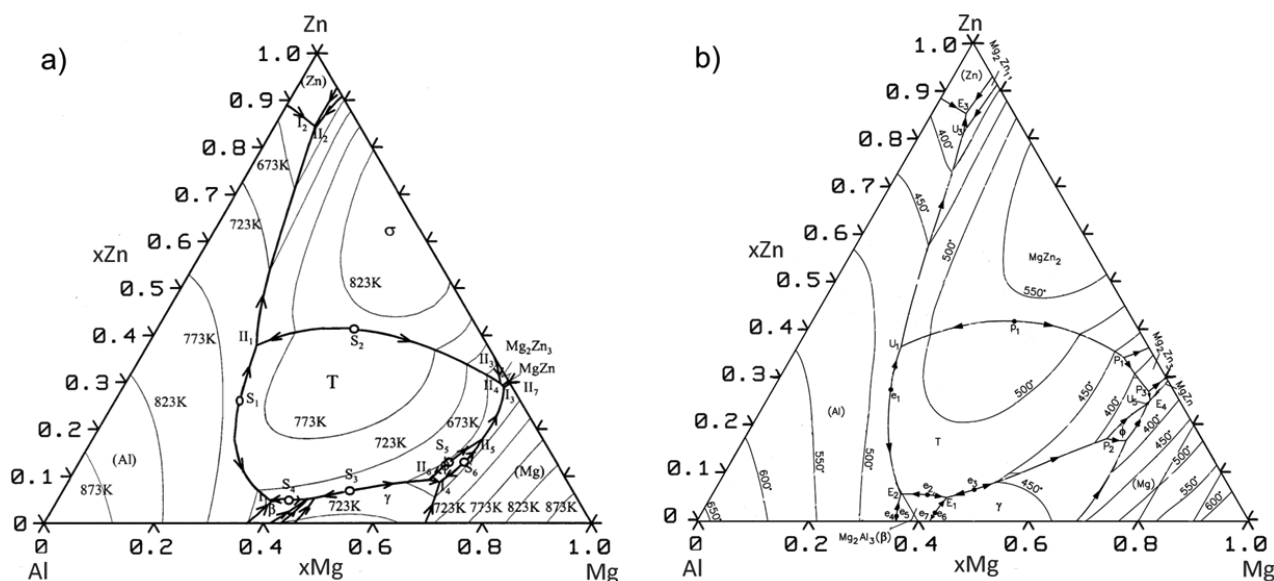


Figure 1: Al-Mg-Zn liquidus projection: a) <sup>17</sup> and b) <sup>14</sup>  
 Slika 1: Projekcija likvidusa Al-Mg-Zn: a) <sup>17</sup> in b) <sup>14</sup>

where  $A_{ij}^0$ ,  $A_{ij}^1$ ,  $A_{ij}^2$  are the regular-solution parameters for the binary system  $ij$  independent of the composition, relying only on the temperature:

$$\Delta G_{ij}^E = X_i X_j (A_{ij}^0 + A_{ij}^1 (X_i - X_j) + A_{ij}^2 (X_i - X_j)^2 + \dots + A_{ij}^n (X_i - X_j)^n) \quad (2)$$

where  $X_i$  and  $X_j$  indicate the mole fractions of components  $i$  and  $j$  in the  $ij$  binary system, which is expressed as:

$$X_{i(ij)} = x_{i+} \sum_{k=1}^m x_k \xi_{i(ij)}^{(k)} \quad (3)$$

and where the coefficient entered as  $\xi_{i(ij)}^{(k)}$  in Eq.(3) presents the similarity coefficient of component  $k$  to component  $i$  in the  $ij$  system, and is defined as:

$$\xi_{i(ij)}^{(k)} = \frac{\eta(ij, ik)}{\eta(ij, ik) + \eta(ji, jk)} \quad (4)$$

where  $\eta(ij, ik)$  is the function related to the excess Gibbs free energy of the  $ij$  and  $ik$  binaries:

$$\eta(ij, ik) = \int_{x_i=0}^{x_i=1} (\Delta G_{ij}^E - \Delta G_{ik}^E)^2 dx_i \quad (5)$$

In all the equations given,  $\Delta G^E$  and  $\Delta G_{ij}^E$  refer to the integral molar excess free energies for the multicomponent and binary systems, respectively, while  $x_1$ ,  $x_2$ ,  $x_3$  refer to the mole fraction of the components in the investigated multicomponent system.

### 3 RESULTS AND DISCUSSION

Thermodynamic calculations in the Al-Mg-Zn ternary system were carried out in nine sections along the lines of the following constant molar ratios: Mg : Zn

= 1 : 3, 1 : 1, 3 : 1 – the sections from the Al corner; Zn-Al = 1 : 3, 1 : 1, 3 : 1 – the sections from the Mg corner; and Al : Mg = 1 : 3, 1 : 1, 3 : 1 – the sections from the Zn corner. The basic data necessary for the calculation was taken from the literature<sup>20,26,27</sup>. The Redlich-Kister polynomials for the constitutional binaries in the investigated ternary Al-Mg-Zn system are presented in Table 1.

Table 1: Redlich-Kister parameters for the liquid phase in the constitutional binaries of the Al-Mg-Zn system

Tabela 1: Redlich-Kisterjevi parametri za staljeno fazu v sestavnih binarnih sistemih iz sistema Al-Mg-Zn

System $ij$	Al-Mg (20)	Mg-Zn (20)	Al-Zn (26)
$A_{ij}^0(T)$	$-12000 + 8.566 * T$	$-77729.24 + 680.52266 * T - 95 * T * \ln(T) + 40E - 3 * T^2$	$10465.55 - 3.39259 * T$
$A_{ij}^1(T)$	$1894 - 3 * T$	$3674.72 + 0.57139 * T$	/
$A_{ij}^2(T)$	2000	-1588.15	/

The prediction was done according to the fundamentals of the latest version of the general-solution model<sup>22,23</sup>. Based on the starting data in Table 1, similarity coefficients were determined and further calculations were carried out for 81 alloys in all the selected cross sections of the investigated ternary Al-Mg-Zn system in the temperature interval of 900–1200 K, as shown with Eqs.(1–5). The integral molar enthalpies of mixing were additionally calculated according to following expression:

$$\frac{d(\Delta G^E / T)}{dT} = - \frac{\Delta H^M}{T^2} \quad (6)$$

The results of the thermodynamic predictions, including the values of the ternary integral molar excess Gibbs

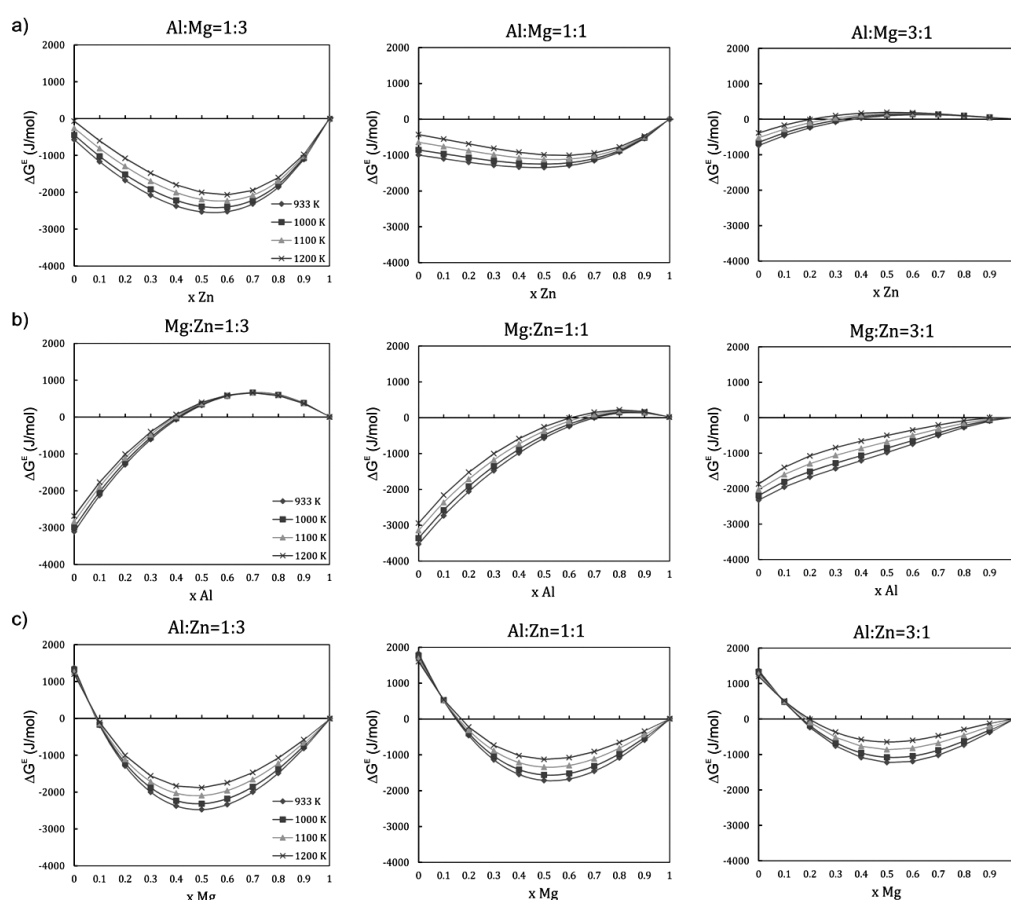


**Figure 2:** Dependence of the integral molar excess energy on the composition and temperature in the Al-Mg-Zn system: a) sections from the zinc corner; b) sections from the aluminum corner; c) sections from the magnesium corner

**Slika 2:** Odvisnost skupne molarne presežne energije od sestave in temperature v sistemu Al-Mg-Zn: a) prerez iz cinkovega kota; b) prerez iz aluminijevega kota; c) prerez iz magnezijevega kota

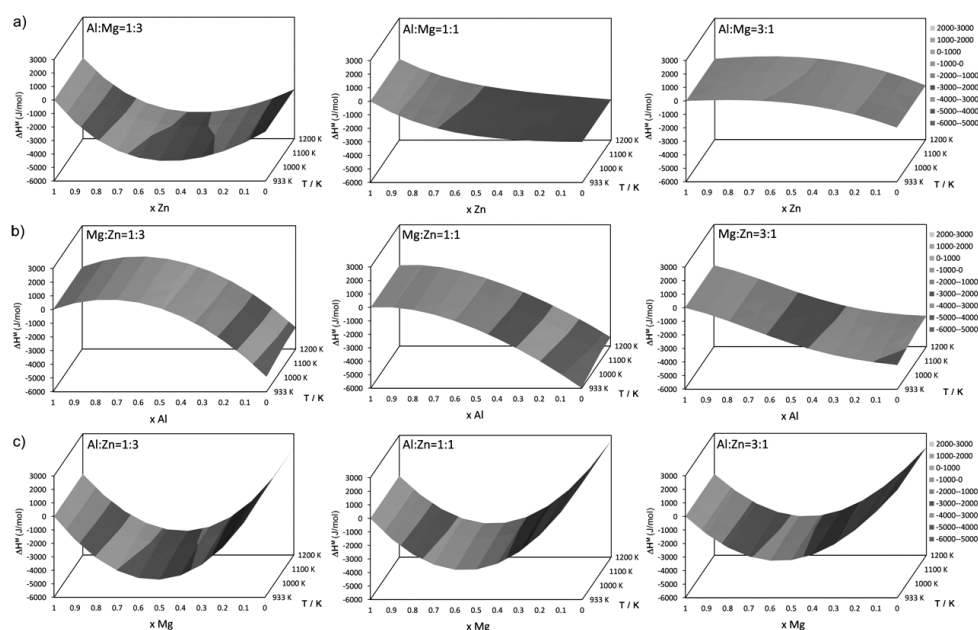


**Figure 3:** Dependence of the integral molar enthalpies of mixing on the composition and temperature in the Al-Mg-Zn system: a) sections from the zinc corner; b) sections from the aluminum corner; c) sections from the magnesium corner

**Slika 3:** Odvisnost skupne molarne entalpije mešanja od sestave in temperature v sistemu Al-Mg-Zn: a) prerez iz cinkovega kota; b) prerez iz aluminijevega kota; c) prerez iz magnezijevega kota

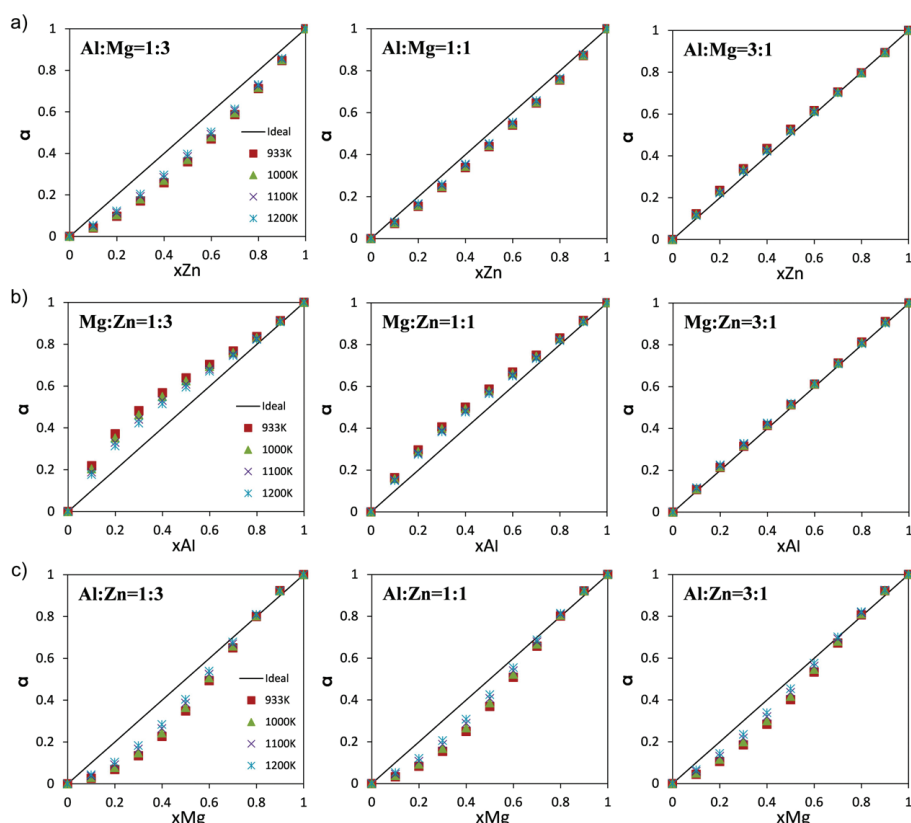


**Figure 4:** Activity dependence on the composition and temperature in the investigated Al-Mg-Zn system: a) sections from the zinc corner; b) sections from the aluminum corner; c) sections from the magnesium corner

**Slika 4:** Odvisnost aktivnosti od sestave in temperature v preiskovanem sistemu Al-Mg-Zn: a) prerez iz cinkovega kota; b) prerez iz aluminijevega kota; c) prerez iz magnezijevega kota

energy, the ternary molar enthalpy of mixing and the activities of all three components in the liquid phase, were calculated for all the investigated sections at the investigated temperatures, and presented in **Table 2** and

**Figures 2 to 4**, respectively. The calculated activity values for all three components were used for the construction of the iso-activity diagrams at 1000K and shown in **Figure 5**.

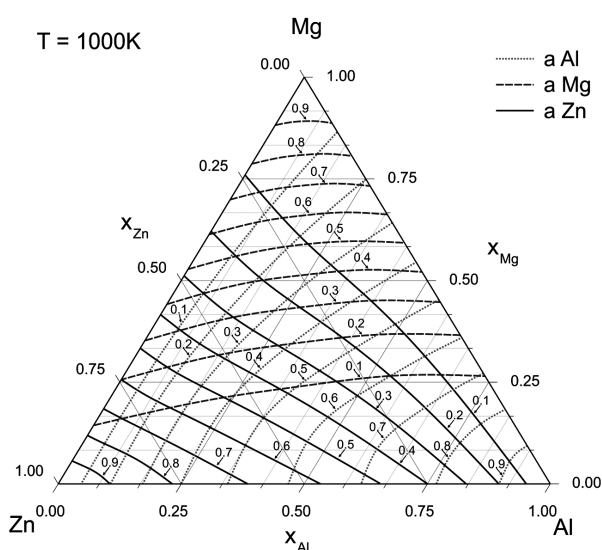


**Figure 5:** Iso-activity diagrams for the constitutive elements in the ternary Al-Mg-Zn system at 1000 K

**Slika 5:** Diagram izoaktivnosti za sestavne elemente v ternarnem sistemu Al-Mg-Zn pri 1000 K

Negative values of the integral molar excess Gibbs energies were obtained for most of the concentration range at all the investigated temperatures (**Figure 2**). The most negative value of about  $-3.5$  kJ/mol was present in the section from the aluminum corner with a molar ratio of  $\text{Mg} : \text{Zn} = 1 : 1$  for the low aluminum concentrations, while the highest positive values of about  $0.2$  kJ/mol were noticed for the higher contents of zinc and aluminum in sections  $\text{Mg} : \text{Zn} = 1 : 1$  and  $\text{Al} : \text{Mg} = 3 : 1$ . In the case of the integral molar enthalpies of mixing, the minimum value of  $-5$  kJ/mol was noticed for the low aluminum contents in the section  $\text{Mg} : \text{Zn} = 1 : 1$ , while the maximum value of about  $+3$  kJ/mol was obtained for the low magnesium contents in section  $\text{Al} : \text{Zn} = 1 : 1$ .

Different deviations from Raoult law were detected considering three constituent metals in the Al-Mg-Zn system. Aluminum shows a positive deviation in the whole composition range of the investigated ternary system, moving towards almost an ideal behavior in the case of the section with a molar ratio of  $\text{Mg} : \text{Zn} = 3 : 1$ . On the other hand, magnesium shows a uniform negative deviation for all the examined sections of the system,



**Table 2:** Characteristic dependencies of the integral molar excess energies and the integral molar enthalpies of mixing on the composition of the ternary Al-Mg-Zn alloys expressed as  $\Delta G^E$  (J/mol) =  $Ax^2 + Bx + C$  and  $\Delta H^M$  (J/mol) =  $Dx^2 + Ex + F$  at the investigated temperatures

**Tabela 2:** Značilna odvisnost skupne presežne molarne energije in skupne molarne entalpije mešanja od sestave ternarne Al-Mg-Zn zlitine, izražena kot  $\Delta G^E$  (J/mol) =  $Ax^2 + Bx + C$  in  $\Delta H^M$  (J/mol) =  $Dx^2 + Ex + F$  pri preiskovanih temperaturah

933K

Section	A	B	C	D	E	F
Mg:Zn=1:3	-7444.08	10598.36	-3114.3	-10228	15172	-4917
Mg:Zn=1:1	-4584.48	8210.277	-3522.5	-5510.5	11645	-6040.4
Mg:Zn=3:1	-564.357	2931.14	-2279.32	2085.3	2368.8	-4300.3
Al:Zn=1:3	13523.87	-14194.9	1171.436	22679	-24340	1791.2
Al:Zn=1:1	11246.21	-12525.6	1697.977	20338	-22847	2566.1
Al:Zn=3:1	8269.261	-9230.4	1314.962	16806	-22847	2028.8
Al:Mg=1:3	8058.779	-8123.02	-463.269	13330	-11380	-2168.7
Al:Mg=1:1	2852.942	-2223.04	-930.149	4233.1	-1474.4	-2892.2
Al:Mg=3:1	-2062.89	2678.725	-717.506	-3290	5185.5	-1942.2

1000K

Section	A	B	C	D	E	F
Mg:Zn=1:3	-7301.1	10323.32	-2990.65	-10006	14727	-4694.9
Mg:Zn=1:1	-4608.32	8045.501	-3351	-5214.3	11053	-5744.2
Mg:Zn=3:1	-844.82	3049.588	-2143.19	2307.4	1924.6	-4078.2
Al:Zn=1:3	12810.45	-13429.3	1126.216	21791	-23452	1791.2
Al:Zn=1:1	10540.78	-11745.5	1636.327	19746	-22255	2566.1
Al:Zn=3:1	7633.816	-8521.86	1264.693	16510	-18548	2028.8
Al:Mg=1:3	7728.575	-7927.42	-334.914	12441	-10492	-2168.7
Al:Mg=1:1	2754.998	-2275.25	-785.379	3640.8	-882.13	-2892.2
Al:Mg=3:1	-1990.84	2513.915	-628.224	-3586.1	5481.6	-1942.2

1100K

Section	A	B	C	D	E	F
Mg:Zn=1:3	-7124.355	9967.950	-2827.029	-9799.6	14315	-4488.7
Mg:Zn=1:1	-4692.6	7872.956	-3122.95	-4939.3	10503	-5469.2
Mg:Zn=3:1	-1299.82	3281.329	-1960.96	2513.6	1512.1	-3872
Al:Zn=1:3	11814.41	-12358.4	1059.365	20966	-22627	1791.2
Al:Zn=1:1	9524.121	-10620.6	1544.861	19196	-21705	2566.1
Al:Zn=3:1	6700.34	-7480.99	1189.845	16235	-18273	2028.8
Al:Mg=1:3	7304.49	-7707.24	-142.743	11616	-9666.6	-2168.7
Al:Mg=1:1	2644.862	-2392.36	-568.803	3090.8	-332.13	-2892.2
Al:Mg=3:1	-1868.6	2251.542	-494.81	-3861.1	5756.6	-1942.2

1200K

Section	A	B	C	D	E	F
Mg:Zn=1:3	-6979.237	9651.942	-2674.257	-9743.3	14202	-4432.4
Mg:Zn=1:1	-4817.76	7751.966	-2909.49	-4864.3	10353	-5394.2
Mg:Zn=3:1	-1784.52	3551.037	-1789.76	2569.9	1399.6	-3815.7
Al:Zn=1:3	10843.84	-11317.1	993.472	20741	-22402	1791.2
Al:Zn=1:1	8512.729	-9505.34	1454.325	19046	-21555	2566.1
Al:Zn=3:1	5765.485	-6441.27	1115.435	16160	-18198	2028.8
Al:Mg=1:3	6905.864	-7515.85	50.01534	11391	-9441.6	-2168.7
Al:Mg=1:1	2538.665	-2517.19	-351.668	2940.8	-182.13	-2892.2
Al:Mg=3:1	-1749.7	1990.177	-361.146	-3936.1	5831.6	-1942.2

while zinc behaves differently – showing a slightly positive deviation for section Al : Mg = 3 : 1 and negative deviations in the other two sections.

The temperature influence on the calculated thermodynamic properties was not significant in the investigated interval 933–1200 K.

The described tendencies indicate a prevalent existence of the mutual mixing tendencies between the constitutive components in the Al-Mg-Zn system at the investigated temperatures, where magnesium and zinc exhibit a more significant mixing tendency than aluminum.

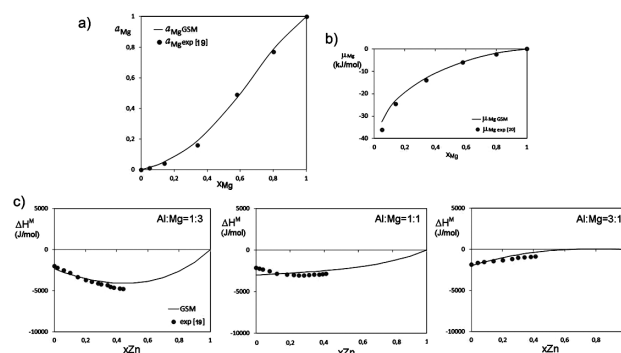


**Figure 6:** Comparison of calculated and reference-literature experimental values<sup>19,20</sup>

**Slika 6:** Primerjava izračunanih podatkov z literaturnimi eksperimentalnimi vrednostmi<sup>19,20</sup>

The calculated thermodynamic quantities were compared with the available literature data at the temperature of 933 K<sup>19,20</sup> in order to test the accuracy of the applied prediction model. These comparisons are shown in **Figure 6** for different examples – the magnesium activity (**Figure 6a**), the magnesium chemical potential (b) and the integral molar enthalpies of mixing for the three sections from the zinc corner (c). As can be seen, a good agreement was noticed between the results of this work and the reference experimental data<sup>19,20</sup>.

## 4 CONCLUSION

The calculation of the thermodynamic properties in the ternary Al-Mg-Zn system was done by applying the general solution model. On the basis of the thermodynamic parameters from the constituent binary subsystems, the integral molar excess Gibbs energies and the integral molar enthalpies of mixing were calculated for the whole system, in nine sections from different corners, in the temperature range of 900–1200 K. The obtained data showed a mostly negative deviation from Raoult law, indicating predominantly mutual mixing tendencies in the investigation system.

We found that: (i) experimental investigation and thermodynamic-property determination at the selected temperatures are rather difficult to perform due to the evaporation of zinc and oxidation of magnesium in the case of the investigated Al-Mg-Zn alloys; (ii) there is a good agreement between the available experimental data and the data calculated in this paper; and (iii) due to the incomplete thermodynamic data relating to the investigated system recorded in the reference literature, the predicted results from this paper can be taken as relevant thermodynamic data relating to the examined multicomponent ZA-based system. This can be done because the accuracy of the model, used in different cases, had already been proven as cited in literature<sup>24,25</sup> and it is important to continuously examine the Al-Mg-Zn alloys<sup>28</sup> and other Al-based ternary alloys<sup>29,30</sup>.

## Acknowledgment

The results of this paper were obtained in the frame of Project OI 172037 financed by the Ministry of Science and Technological Development, the Republic of Serbia, and a bilateral scientific and technological cooperation project between the Republic of Serbia and the People's Republic of China (2011–2012).

## 5 REFERENCES

- <sup>1</sup> T. Shimizu, H. Ishikawa, I. Ohnuma, K. Ishida, *Journal of Electronic Materials*, 28 (1999), 1172
- <sup>2</sup> M. Rettenmayr, P. Lambracht, B. Kempf, C. Tschudin, *Journal of Electronic Materials*, 31 (2002) 4, 278
- <sup>3</sup> Lj. Balanović, D. Živković, A. Mitovski, D. Manasijević, Ž. Živković, *Journal of Thermal Analysis and Calorimetry*, 103 (2011) 3, 1055
- <sup>4</sup> P. Brož, D. Živković, J. Medved, N. Talić, D. Manasijević, G. Klančnik, Experimental and theoretical study of thermodynamic properties and phase equilibria in ternary Al-Zn-X alloys, in COST MP0602 Book (Volume 3 Chapter 6), in print
- <sup>5</sup> G. Bergman, J. L. T. Waugh, L. Pauling, *Acta Crystallographica*, 10 (1957), 254
- <sup>6</sup> T. Takeuchi, S. Murasaki, A. Matsumoro, U. Mizutani, *Journal of Non Crystalline Solids*, 156–158 (1993), 914
- <sup>7</sup> A. Niikura, A. P. Tsai, N. Nishiyama, A. Inoue, T. Matsumoto, *Materials Science Engineering*, 181/182 A (1994), 1387
- <sup>8</sup> N. K. Mukhopaghyay, J. Bhatt, A. K. Pramanick, B. S. Murty, P. Paufler, *Journal of Materials Science*, 39 (2004), 5155
- <sup>9</sup> M. Zhu, G. Yang, D. Wan, Z. Wang, Y. Zhou, *Rare Metals*, 28 (2009) 4, 401
- <sup>10</sup> P. Donnadiou, A. Quivy, T. Tarfa, P. Ochin, A. Dezellus, M. G. Harmelin, P. Liang, H. L. Lukas, H. J. Seifert, F. Aldinger, G. Effenberg, *Zeitschrift für Metallkunde*, 88 (1997) 12, 911
- <sup>11</sup> D. Petrov, A. Watson, J. Grobner, P. Rogl, J. C. Tedenac, M. Bulanova, Turkevich, *Aluminium-magnesium-zinc, Ternary Alloys Systems*, Vol.11A3, G. Effenberg, S. Ilyenko, Ed., Springer, Germany, 2006
- <sup>12</sup> Y. P. Ren, G. W. Qin, W. L. Pei, Y. Gio, H. D. Zhao, H. X. Li, M. Jiang, S. M. Hao, *Journal of Alloys and Compounds*, 481 (2009), 176
- <sup>13</sup> M. Ohno, D. Mirković, R. Schmid-Fetzer, *Materials Science Engineering*, 421A (2006), 328
- <sup>14</sup> V. Raghavan, *Journal of Phase Equilibria and Diffusion*, 28 (2007), 203
- <sup>15</sup> V. Raghavan, *Journal of Phase Equilibria and Diffusion*, 31 (2010), 29
- <sup>16</sup> A. L. Voskov, G. F. Voronin, *Russian Journal of Physical Chemistry A*, 84 (2010), 525
- <sup>17</sup> Z. Kozuka, J. Moriyama, I. Kushima, *Journal of the Electrochemical Society of Japan*, 28 (1960), 298
- <sup>18</sup> A. M. Pogodaev, E. E. Lukashenko, *Russian Metallurgy*, 6 (1974), 74
- <sup>19</sup> Y. B. Kim, F. Sommer, B. Predel, *Journal of Alloys and Compounds*, 247 (1997), 43
- <sup>20</sup> P. Liang, T. Tarfa, J. A. Robinson, S. Wagner, P. Ochin, M. G. Harmelin, H. J. Seifert, H. L. Lukas, F. Aldinger, *Thermochimica Acta*, 314 (1998), 87
- <sup>21</sup> H. Liang, S. L. Chen, Y. A. Chang, *Metallurgical and Materials Transactions*, 28A (1997), 1725
- <sup>22</sup> K. C. Chou, K. Wei S., *Metallurgical and Materials Transactions*, 28B (1997), 439
- <sup>23</sup> K. C. Chou, *CALPHAD*, 19 (1995), 315
- <sup>24</sup> D. Živković, Ž. Živković, Y. H. Liu., *Journal of Alloys and Compounds*, 265 (1998), 176
- <sup>25</sup> D. Živković, I. Katayama, L. Gomidželović, D. Manasijević, R. Novaković, *International Journal of Materials Research*, 98 (2007) 10, 1025
- <sup>26</sup> S. Sabine an Mey, *Zeitschrift für Metallkunde*, 84 (1993) 7, 451
- <sup>27</sup> A. T. Dinsdale, A. Kroupa, J. Vizdal, J. Vreštal, A. Watson, A. Zemanova, *COST 531 Database for Lead-free Solders*, Ver. 3.0, 2008
- <sup>28</sup> H. R. Zaid, A. M. Hatab, A. M. A. Ibrahim, *Journal of Mining and Metallurgy, Section B-Metallurgy*, 47 (2011) 1, 31
- <sup>29</sup> G. Klančnik, J. Medved, J. Min. Metall. Sect. B-Metall., 47 (2) B (2011), 179
- <sup>30</sup> X. Fang, M. Song, K. Li, Y. Du, J. Min. Metall. Sect. B-Metall., 46 (2) B (2010), 171

## FRICION-STIR WELDING OF ALUMINIUM ALLOY 5083

### VARJENJE S TRENJEM IN MEŠANJEM ALUMINIJEVE ZLITINE 5083

**Damjan Klobčar<sup>1</sup>, Ladislav Kosec<sup>2</sup>, Adam Pietras<sup>3</sup>, Anton Smolej<sup>2</sup>**

<sup>1</sup>Faculty of Mechanical Engineering, University of Ljubljana, Aškerčeva 6, 1000 Ljubljana, Slovenia

<sup>2</sup>Faculty of Natural Sciences and Engineering, University of Ljubljana, Aškerčeva 12, 1000 Ljubljana, Slovenia

<sup>3</sup>Instytut Spawalnictwa, Ul. Bł. Czesława 16/18 Gliwice, Poland  
damjan.klobcar@fs.uni-lj.si

*Prejem rokopisa – received: 2012-02-22; sprejem za objavo – accepted for publication: 2012-03-16*

A study was made of the weldability of 4-mm-thick aluminium-alloy 5083 plates using friction-stir welding. A plan of experiments was prepared based on the abilities of a universal milling machine, where the tool-rotation speed varied from 200 r/min to 1250 r/min, the welding speed from 71 mm/min to 450 mm/min and the tool tilt angle was held constant at 2°. The factors feed per revolution (FPR) and revolution per feed (RPF) were introduced to get a better insight into the friction-stirring process. Samples for microstructure analyses, Vickers micro-hardness measurements and special miniature tensile-testing samples were prepared. The microstructure was prepared for observation on a light microscope under a polarised light source. A set of optimal welding parameters was determined at a FPR of 0.35 mm/r, at which quality welds can be made with a minimal increase in the weld hardness and an up to 15 % drop in the tensile strength.

**Keywords:** friction-stir welding, EN-AW 5083, welding parameters, mechanical properties, welding defects

Izdelana je študija varivosti 4 mm debele pločevine iz aluminijeve zlitine 5083 pri varjenju s trenjem in mešanjem. Načrt eksperimentov je bil pripravljen na podlagi sposobnosti univerzalnega frezalnega stroja. Spreminjali smo hitrost vrtenja orodja od 200–1250 r/min, hitrost varjenja 71–450 mm/min, kot nagiba orodja pa je bil konstanten pri 2°. Vpeljana sta bila faktorja podajanje na vrtljaj (FPR) in obratov na podajanje (RPF), s katerima bolj nazorno prikažemo vpliv parametrov procesa. Iz izdelanih varov smo pripravili vzorec za analizo mikrostrukture, vzorec za meritev trdote po Vickersu ter posebne miniaturne epruvete za natezni preizkus. Mikrostruktura je bila pripravljena za opazovanje na svetlobnem mikroskopu v polarizirani svetlobi. Optimalni parametri varjenja so bili ugotovljeni pri FPR 0,35 mm/r, pri čemer dobimo kakovostne zware, z minimalnim povečanjem trdote vara in do 15-odstotnim padcem natezne trdnosti.

**Ključne besede:** varjenje s trenjem in mešanjem, EN-AW 5083, varilni parametri, mehanske lastnosti, napake v varu

## 1 INTRODUCTION

The 5083 aluminium alloy exhibits good corrosion resistance to seawater and the marine atmosphere, moderate mechanical properties and a high fatigue-fracture resistance. It has good formability, machinability and weldability using arc processes (metal inert gas – MIG or tungsten inert gas – TIG) or resistance welding.<sup>1,2</sup> This alloy is used for the production of welded components for shipbuilding and railway vehicles, different panels and platforms for boats and trains, storage tanks, cryogenics, pressure vessels, piping, tubing, welded tank trailers and welded dump bodies for the automotive industry, collapsible bridges, armour plates and the bodies of military vehicles. It can be subject to inter-crystalline and stress-corrosion cracking after undergoing an unsuitable thermal treatment (welding). It should not to be used above 65 °C for an extended time if later exposed to a corrosive environment.<sup>3</sup> If the aluminium alloys are friction-stir processed (FSP) then superplastic properties are obtained, as a consequence of the grain refinement.<sup>4–7</sup> The surface of the aluminium alloys can be modified using shot pining and laser shot pinning, with a consequent influence on the microhard-

ness, residual stresses, fatigue strength and corrosion resistance.<sup>8–10</sup>

Friction-stir welding (FSW) is a solid-state joining method that is energy and environmentally friendly and versatile. FSW joints have a high fatigue strength, require less preparation, and little post-weld dressing. These welds have fewer defects than fusion welds and the process enables the welding of dissimilar metals.<sup>11</sup> FSW has attracted significant research interest from industries like aerospace and transportation. Many studies were made on the weldability of 5083 aluminium alloy.<sup>12–14</sup> Some researchers studied the influence of FSW parameters on fatigue life.<sup>12,14</sup> They discovered that the rotational speed governs defect occurrence and a strong correlation between the frictional power input, the tensile strength and the low-cycle fatigue life is obtained. Han et al.<sup>15</sup> investigated the optimal conditions for FSW in correlation with welds' mechanical properties. These mechanical properties were similar to the base alloy at tool rotations between 500 r/min and 800 r/min at a weld-tool travel speed of 124 mm/min. Hirata et al.<sup>16</sup> investigated the influence of the FSW parameters on the grain size and the formability. They discovered that a decrease of the frictional heat flow during FSW

**Table 1:** Physical and mechanical properties of aluminium alloy 5083<sup>3</sup>

Property	$\rho/\text{kg m}^{-3}$	$R_m/\text{MPa}$	$R_{p0.2}/\text{MPa}$	$E/\text{GPa}$	$T_{\text{sol}}/^\circ\text{C}$	$T_{\text{liq}}/^\circ\text{C}$
AA5083-O	2.660	275–300	125–149	71	580	640

decreases the grain size, increases the ductility and improves the formability. Sato et al.<sup>17</sup> studied the influence of an oxide array on the formability of tailored blanks.<sup>18</sup> They discovered that a band of collective oxide particles could act as an initiation site for cracking during the forming processes. The research of Zucchi et al.<sup>19</sup> investigated the pitting and stress-corrosion cracking (PSCC) resistance of the 5083 aluminium alloy during FSW and MIG welding. The FSW welds showed better resistance to PSCC than the base alloy and much better resistance than MIG welds.

In this study the weldability of the 5083 aluminium alloy using friction-stir welding (FSW) was investigated. Welding parameters, i.e., the tool-rotation speed, the welding speed and the tilt angle have an influence on the formation of welding defects, the weld apices appearance, the microstructure and the weld strength. The aim of this research was to discover the welding parameters providing a weld microstructure without defects. The FSW employed a tool-rotation speed from 200 r/min to 1250 r/min, a welding speed from 71 mm/min to 450 mm/min and the tool-tilt angle was held constant at 2°. The factors feed per revolution (FPR) and revolutions per feed (RPF) were introduced to get a better insight into the friction-stirring process. The RPF gives information about the heat input per weld length. Miniature samples for tensile testing were prepared from the welds. The welds were examined under the light of an optical microscope and the Vickers hardness was measured.

## 2 EXPERIMENTAL

### 2.1 Dimensions and composition of the workpieces

The standard EN-AW 5083 aluminium alloy with chemical composition in mass fractions: 4.35 % Mg, 0.42 % Mn, 0.12 % Si, 0.087 % Cr, 0.29 % Fe, 0.019 %

Zn, 0.013 % Ti and the rest Al, and temper O, was used for testing. The workpiece dimensions were 180 mm × 60 mm × 4 mm. The physical and mechanical properties of the alloy for temper O were not determined but taken according to the standard (Table 1).<sup>3</sup>

### 2.2 FSW tool

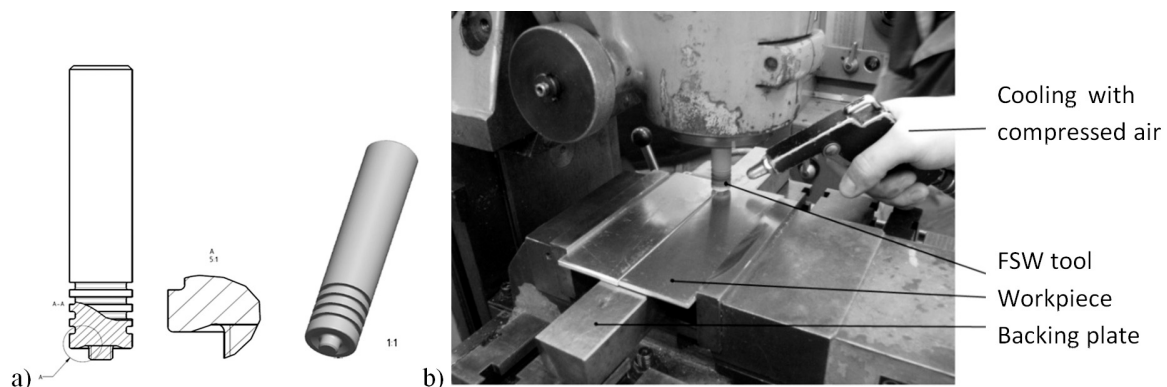
The FSW tool was made from standard EN 42CrMo4 steel<sup>20</sup>. A basic FSW tool geometry was used with a threaded pin that was 3.9 mm long (M6 × 1.5) and the concave shoulder ( $\phi = 16$  mm) for producing pressure under the tool shoulder (Figure 1).

### 2.3 Friction-stir welding

A plan of experiments was prepared regarding the capabilities of the universal milling machine used (Prvomajska ALG 100E). Different combinations of tool rotations and welding speeds were tested at a constant tilt angle of 2°. The FSW tool rotated from 200 r/min to 1250 r/min, and the welding speeds changed from 71 mm/min to 450 mm/min. The factors of feed per revolution (FPR) in  $\mu\text{m/r}$  and revolution per feed (RPF) in r/mm were introduced to better distinguish between the different welding parameters. The FPR varied from 56  $\mu\text{m/r}$  to 2250  $\mu\text{m/r}$ . RPF, which represents the "frictional heat input" per weld length, was between 17.6 r/min and 0.44 r/mm. A backing plate underneath the workpiece enabled the creation of pressure under the tool shoulder by preventing the aluminium alloy from flowing away from the seam. The two workpieces were clamped in a vice.

### 2.4 Preparation of samples and testing

From the FSW welds the miniature tensile test samples (Figure 2) were sectioned perpendicular to the

**Figure 1:** a) FSW tool geometry and b) experimental FSW

**Slika 1:** a) Geometrija orodja za FSW in b) potek eksperimenta FSW



welding direction, and weld cross-sections for analyses of the microstructure and the macrostructure were prepared. Before sectioning the samples with a water jet, the workpiece surfaces were milled to remove the weld underfill and the toe flash.

The uniaxial tensile tests were made using a computer-controlled Zwick/Roell Z050 tensile testing machine. The measurements were made using Testexpert software. The strain was measured with extensometer fixed directly on the sample.

The samples for analysis of the microstructure and macrostructure were sectioned, grinded and polished. The samples for the macrostructure analysis were etched using Keller reagent (1125 mL HCl, 558 mL HNO<sub>3</sub>, 200 mL HF and 1 500 mL H<sub>2</sub>O) and the microstructure was analysed using an optical microscope. The samples for the microstructure analysis were anodized with Baker's reagent. The microstructure was examined using an optical microscope under polarised light and with a digital camera for acquiring the pictures. The Vickers micro-hardness HV1 (load equal to 9.807 N) was measured across the welds.

### 3 RESULTS AND DISCUSSION

#### 3.1 Visual assessment of the FSW welds

**Figure 3** shows a top view of the FSW welds. The end of the weld is indicated with a hole, which is a negative of the FSW tool pin. A visual assessment of the weld apices reveals smooth weld apices for FPR between 50  $\mu\text{m/r}$  and 1000  $\mu\text{m/r}$ , i.e., for a RPF between 20 r/min and 1 r/mm (**Figure 3**). For sample 7 (**Figure 3a**) the frictional heat input was the highest (RPF = 17.6 r/mm). For this sample the tool moved a little too much into the workpiece, due to the higher frictional heat input, which then softened the material. For samples 5 and 6 (**Figures 3b, c**) the RPF was 2.86 r/mm and 1.77 r/mm and the weld apices were smooth. When the tool speed was increased to a 0.71 r/mm and 0.44 r/mm (**Figures 3d, e**) the heat input become too small and the weld apices become rough with traces of material tearing.

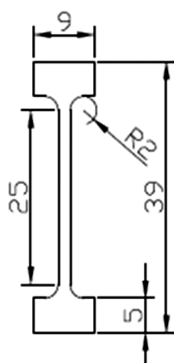


**Figure 2:** Drawing of miniature tensile test sample  
**Slika 2:** Risba miniaturnega vzorca za natezni test

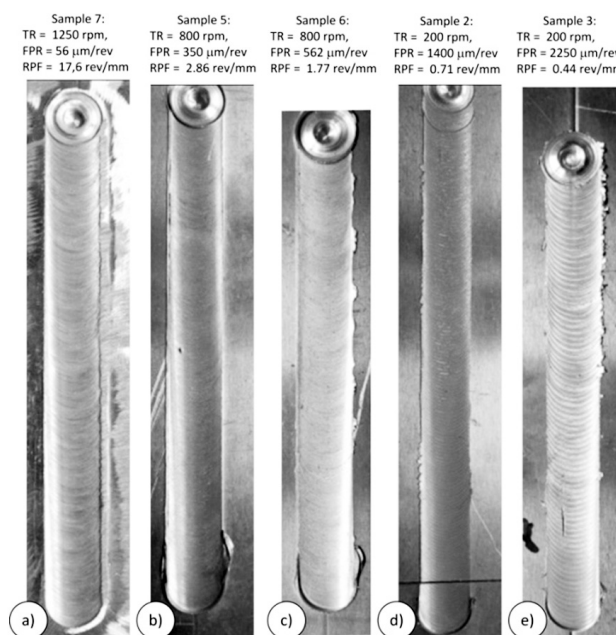


**Figure 3:** A top view of the FSW welds  
**Slika 3:** Pogled na temena FSW varov

The research of the influence of the width of the joint gap on the weldability showed that gaps wider than 0.5 mm could not be successfully welded, due to an inability to move the tool into the material to overcome the lack of material.

#### 3.2 Weld microstructure

Macrographs of the selected FSW welds are shown in **Figure 4**. **Figure 4a** presents a macrograph of sample 7, which was welded with the highest frictional heat input

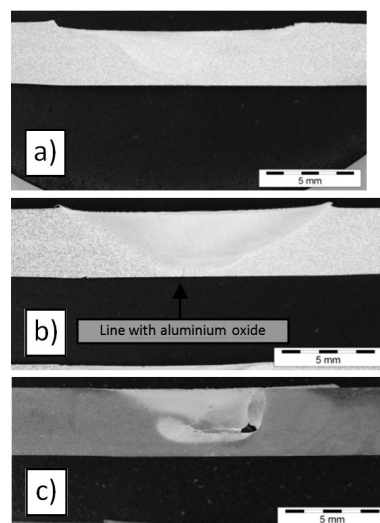


**Figure 4:** Macrostructure of FSW welds obtained at 200 r/min: a) sample 7 (FPR = 56  $\mu\text{m/r}$ ), b) sample 1 (FPR = 350  $\mu\text{m/r}$ ), c) sample 2 (FPR = 1400  $\mu\text{m/r}$ ) and c) sample 3 (FPR = 2250  $\mu\text{m/r}$ )

**Slika 4:** Makrostruktura FSW varov, izdelanih pri 200 r/min: a) vzorec 7 (FPR = 56  $\mu\text{m/r}$ ), b) vzorec 1 (FPR = 350  $\mu\text{m/r}$ ), c) vzorec 2 (FPR = 1400  $\mu\text{m/r}$ ) in c) vzorec 3 (FPR = 2250  $\mu\text{m/r}$ )

(RPF = 17.6 r/mm). The weld is without defects, except for possible under-fill, due to the higher heat input. A trace of the oxide line is present across the weld that was welded at 200 r/min and a 71 mm/min welding speed (FPR = 0.355 mm/r and RPF = 2.81 r/mm) (**Figure 4b**). The presence of  $\text{Al}_2\text{O}_3$  on the surface of the touching planes in the weld joint before the welding is the reason for such a defect. This is why the oxide layer should be removed from the weld joint prior to welding. **Figure 4c** shows the FSW weld with a "worm hole" defect or "tunnelling" defect. This weld was produced at 200 rpm and a 280 mm/min welding speed (FPR = 1.4 mm/r and RPF = 0.71 r/mm). The "worm hole" defect appears if the welding is carried out with insufficient heat input or if the welding force in the axial direction is not large enough.

The weld microstructures on the top of the weld, inside the weld and at weld root are shown in **Figure 5**. The grain size is very small at the top of the weld (**Figure 5b**), which was in the vicinity of the tool shoulder. Small-sized grains are obtained across the whole weld (**Figure 5c**). At the weld root the material is not stirred to the bottom of the workpiece (**Figure 5d**). The oxide surface of contacting the workpieces is clearly seen as a line of oxides. Such an oxide line/layer could represent the initiation site for cracking during loading during forming or exploitation.

The analysis of the grain size showed that with a lower RPF, i.e., frictional heat input, the grain size decreases (**Figure 6**). For a higher frictional heat input the weld is heated well above the temperatures of recrystallization up to the temperatures where the grain growth takes place. When the RPF was 17.6 r/mm, the grain size of the weld and the base alloy were almost identical (**Figures 5 and 6a**). When the RPF was

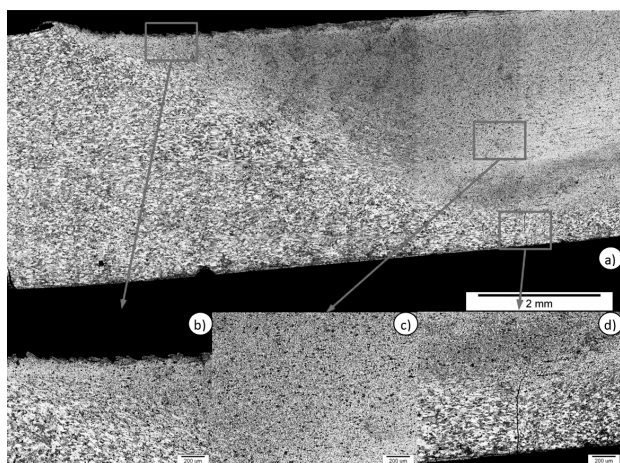


**Figure 5:** Microstructure (polarised light microscopy images) of FSW weld produced at 200 r/min FPR = 350  $\mu\text{m}/\text{r}$  (sample 1): a) weld with HAZ and base alloy, b) weld apices and HAZ, c) weld and d) weld root

**Slika 5:** Mikrostruktura (polarizirana svetlobna mikroskopija) FSW vara, izdelanega pri 200 r/min in FPR = 350  $\mu\text{m}/\text{r}$  (vzorec 1): a) var z TVP in osnovno zlitino, b) teme vara in TVP, c) var in d) koren vara

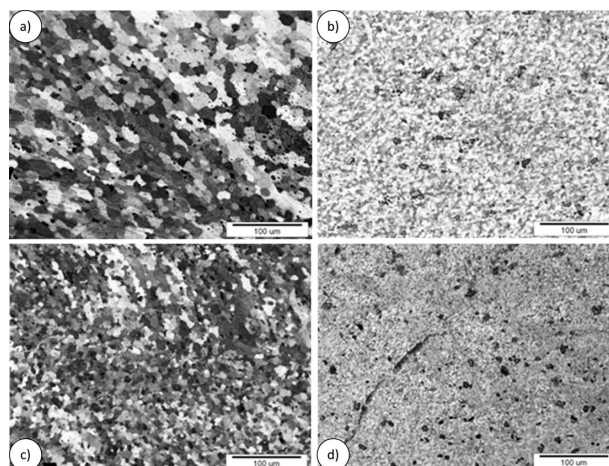


**Figure 6:** Microstructure (polarised light microscopy images) of FSW weld produced at: a) 1250 r/min and RPF = 17.6 r/mm (sample 7), b) 200 r/min and RPF = 2.82 r/mm (sample 1), c) 1250 r/min and RPF = 2.78 r/mm (sample 0) and d) 200 r/min and RPF = 0.44 r/mm (sample 3)

**Slika 6:** Mikrostruktura (polarizirana svetlobna mikroskopija) FSW varov, izdelanih pri: a) 1250 r/min in RPF = 17,6 r/mm (vzorec 7), b) 200 r/min in RPF = 2,82 r/mm (vzorec 1), c) 1250 r/min in RPF = 2,78 r/mm (vzorec 0) in d) 200 r/min in RPF = 0,44 r/mm (vzorec 3)

approximately 2.8 r/mm, the grain size becomes approximately half the size of the base alloy (**Figures 6b, c**). The reason for this could be smaller heat input and the lower temperature of the workpiece. When welding with a RPF of 0.44 r/mm, the heat input was so low so that the stirring, i.e., cold deformations had a major role in grain refinement. In this case the grains were very small (**Figure 6c**) and the weld became harder.

### 3.3 Hardness

The Vickers hardness HV1 was measured across the weld (2 mm below the surface) over a total distance of 26 mm. The hardness is shown for the samples 7, 1, 0 and 3 (**Figure 7**). The centre of the weld is shown with the "dash-dot" line and the

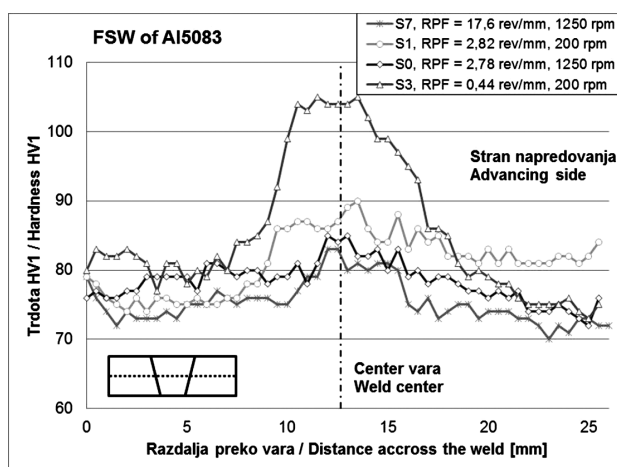


**Figure 7:** Hardness HV1 across the weld, HAZ and base alloy  
**Slika 7:** Trdota HV1 preko vara, TVP in osnovnega materiala



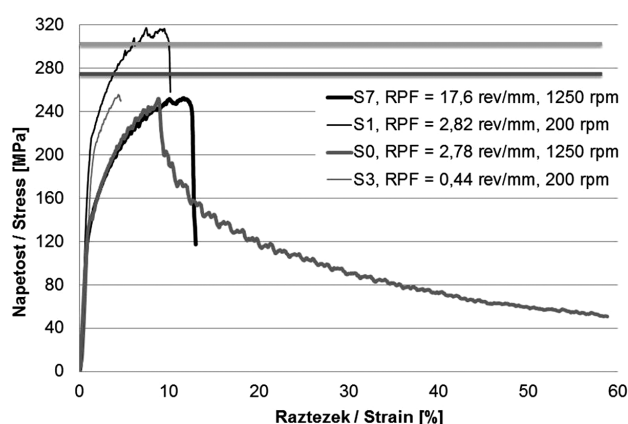


Figure 8: Results of tensile tests

Slika 8: Rezultati nateznega testa

advancing side of the weld is on the right-hand side of the plot of **Figure 7**. When welding with a higher frictional heat input of 17.6 r/mm, the whole workpiece was heated above the temperature of recrystallization, where the grain growth occurs. The hardness was the lowest among all the compared samples ( $\approx 74$  HV1 in the base metal and HAZ, and 82 HV1 in the weld). When welding with optimal welding parameters (sample 0 and 1), the hardness across the weld was slightly higher ( $\approx 84$  HV1), similar to the base alloy where it was  $\approx 80$  HV1. A higher frictional heat input for the advancing side of the weld resulted in a lower hardness in the HAZ ( $\approx 75$  HV1). When the frictional heat input was very low ( $\approx 0.44$  r/mm) the weld hardness increased up to 105 HV1. Here, a deformational hardening was the dominating process due to a lower heat input. As a result of the higher frictional heat input on the advancing side of the weld, the hardness on the advancing side is generally lower than on the retreating side.

### 3.4 Tensile properties

The tensile strength of the base alloy used for the experimental workpiece was not measured for the experimental workpiece, but taken from the literature data (**Table 1**). The yield strength of the aluminium alloy 5083 is between 125 MPa and 149 MPa and the ultimate tensile strength between 275 MPa and 300 MPa (**Table 1**). Since non-standard test specimens were used, the results could not easily be compared with the results from the literature. The ultimate tensile strength of the tensile test specimens was generally in the range of the base aluminium alloy (**Figure 8**). When welding with 2.82 r/mm (sample 1), the tensile strength was even higher, i.e., 320 MPa. When welding with almost the same frictional heat input (sample 0), a strain at a tensile test of 60 % was measured, indicating the good potential for formability of the weld. When the heat input was low, i.e., the RPF was 0.44 r/mm, a strain of  $\approx 5\%$  was achieved as a consequence of the deformation-hardened microstructure.

## 4 CONCLUSIONS

Based on the analysed results the following can be concluded:

Smooth weld apices could be obtained when welding with an FPR between 50  $\mu\text{m/r}$  and 1000  $\mu\text{m/r}$ , i.e., for a RPF between 20 r/min and 1 r/mm.

When welding with the high frictional heat input ( $\approx 20$  r/mm): a) a risk of over-plunging and excessive flash generation is present, b) the stirred material heats well above the recrystallization temperature and the grain growth occurs, c) the hardness of the weld, the HAZ and the closer base alloy drops below the initial base-alloy hardness and d) an approximately 15 % lower tensile strength compared to the base alloy is obtained.

When welding with a medium heat input in the optimal range of welding parameters ( $\approx 3$  r/mm): a) the weld hardness increases slightly compared to the base alloy, b) the grains refine to half the size of the base alloy, due to the deformational hardening combined with the recrystallization, c) the weld has a higher tensile strength, and d) for higher tool rotations, a strain of around 60 % was measured, indicating the good forming potential of the weld.

When welding with a low heat input (RPF = 1 r/mm): a) the weld apices become rough and a tearing takes place, due to a too low frictional heat input, b) a "tunneling" or "elongated cavity" defect is usually present, c) the weld hardness increases since the deformation hardening becomes the dominating process, and d) an approximately 15 % lower tensile strength compared to base alloy is obtained.

A lower hardness was observed for the advancing side of the weld due to the slightly higher heat input compared to the retreating side.

## Acknowledgement

The authors would like to thank M. Hrzenjak and N. Breskvar for the preparation of the samples and the microscopy, and A. Skumavc for reviewing the paper and editing. The research was sponsored by the Slovenian Research Agency (ARRS) under the project L2-4183 entitled "Friction stir welding and processing of aluminium alloys".

## 5 REFERENCES

- 1 J. Tušek, IEEE Trans. Plasma Sci., 28 (2000) 5, 1688
- 2 P. Podržaj, I. Polajnar, J. Diaci, Z. Kariž, Science and Technology of Welding and Joining, 13 (2008) 3, 215
- 3 <http://aluminium.matter.org.uk/aluselect/>
- 4 A. Smolej, B. Skaza, B. Markoli, D. Klobčar, V. Dragojević, E. Slaček, Materials Science Forum, 706–709 (2012) 706, 395
- 5 R. Mishra, Z. Ma, Materials Science and Engineering: R: Reports, 50 (2005) 1–2, 1
- 6 Z. Ma, R. Mishra, Scripta Materialia, 53 (2005) 1, 75
- 7 Z. Ma, S. Sharma, R. Mishra, Scripta Materialia, 54 (2006) 9, 1623

- <sup>8</sup> U. Trdan, J. Grum, M. R. Hill, Materials Science Forum, 681 (2011) 480
- <sup>9</sup> U. Trdan, J. L. Ocaña, J. Grum, Strojniški vestnik – Journal of Mechanical Engineering, 57 (2011) 05, 385
- <sup>10</sup> S. Žagar, J. Grum, Strojniški vestnik – Journal of Mechanical Engineering, 57 (2011) 04, 334
- <sup>11</sup> T. Debroy, H. K. D. H. Bhadeshia, Science and Technology of Welding & Joining, 15 (2010) 4, 266
- <sup>12</sup> D. G. H. M. James, G. R. Bradley, International Journal of Fatigue, 25 (2003) 12
- <sup>13</sup> D. Hattingh, C. Blignault, T. Vanniekerk, M. James, Journal of Materials Processing Technology, 203 (2008) 1–3, 45
- <sup>14</sup> H. Lombard, D. Hattingh, A. Steuwer, M. James, Engineering Fracture Mechanics, 75 (2008) 3–4, 341
- <sup>15</sup> S. J. L. Min-Su Han, J. C. Park, S. C. Ko, Y. B. Woo, S. J. Kim, Trans. Nonferrous Met. Soc. China, 19 (2009), 17
- <sup>16</sup> T. Hirata, T. Oguri, H. Hagino, T. Tanaka, S. Chung, Y. Takigawa, K. Higashi, Materials Science and Engineering: A, 456 (2007) 1–2, 344
- <sup>17</sup> Y. S. Sato, F. Yamashita, Y. Sugiura, S. H. C. Park, H. Kokawa, Scripta Materialia, 50 (2004) 3, 365
- <sup>18</sup> J. Tušek, Z. Kampuš, M. Suban, J. Mater. Process. Technol., 119 (2001) 1/3, 180
- <sup>19</sup> F. Zucchi, G. TrabANELLI, V. Grassi, Materials and Corrosion, 52 (2001), 853
- <sup>20</sup> Steel Selector Metal Ravne. 2012; Available from: <http://www.metalravne.com/selector/steels/vcmo140.html>



## INFLUENCE OF SEGREGATIONS ON THE FRACTURE TOUGHNESS $K_{Ic}$ OF HIGH-STRENGTH SPRING STEEL

### VPLIV IZCEJ NA LOMNO ŽILAVOST $K_{Ic}$ VISOKOTRDNOSTNEGA VZMETNEGA JEKLA

Bojan Senčič<sup>1,2</sup>, Vojteh Leskovšek<sup>2,3</sup>

<sup>1</sup>ŠTORE STEEL, d. o. o., Železarska cesta 3, 3220 Štore, Slovenia

<sup>2</sup>Jožef Stefan International Postgraduate School, Jamova 39, 1000 Ljubljana, Slovenia

<sup>3</sup>Institute of Metals and Technology, Lepi pot 11, 1000 Ljubljana, Slovenia  
bojan.sencic@store-steel.si

*Prejem rokopisa – received: 2012-03-19; sprejem za objavo – accepted for publication: 2012-05-07*

The results of this investigation showed that using the proposed method it was possible to draw, for the normally used range of working hardnesses, a tempering diagram (Rockwell-C hardness – fracture toughness  $K_{Ic}$  – tempering temperature) for the vacuum-heat-treated high-strength spring-steel grade 51CrV4. Based on measurements of the mechanical properties we have also created a classic tempering diagram, i.e., Tensile strength  $R_m$  – Yield stress  $R_{p0.2}$  – Elongation  $A_5/\%$  – Necking  $Z/\%$  – Tempering temperature, and a tempering diagram, i.e., Hardness HRC – Impact toughness Charpy-V – Tempering temperature. According to these tempering diagrams we can conclude that the investigated spring steel 51CrV4 is suitable for the production of high-strength springs when using the proper heat treatment. Fractographic and metallographic analyses of the  $K_{Ic}$  test specimens showed the presence of segregations in the steel. Therefore, we focused on examining the impact of segregations on the fracture toughness  $K_{Ic}$ . We found that the widths of the positive segregation bands and the matrix bands between the samples vary considerably. We have also discovered that the number and the width of the segregation bands influence significantly the fracture toughness  $K_{Ic}$  due to the presence of bainite in the matrix bands.

**Keywords:** fracture toughness, segregations, high-strength spring steel, vacuum heat treatment, tempering diagrams, microstructure

Pri opravljenih preiskavah smo želeli ugotoviti, ali lahko standardizirano preizkušanje lomne žilavosti (ASTM E399-90) nadomestimo z nestandardnim postopkom preizkušanja lomne žilavosti s cilindričnim nateznim preizkušancem z zarezo po obodu in utrujenostno razpoko v dnu zareze. Inovativen način preiskav je pokazal, da lahko s predlagano metodo konstruiramo diagram popuščanja (trdota Rockwell-C – lomna žilavost  $K_{Ic}$  – temperatura popuščanja) za vakuumsko toplotno obdelano visokotrdnostno vzmetno jeklo. Na osnovi meritev mehanskih lastnosti smo izdelali poleg klasičnega diagrama popuščanja: natezna trdnost  $R_m$  – meja plastičnosti  $R_{p0.2}$  – raztezek  $A_5/\%$  – kontrakcija  $Z/\%$  – temperatura popuščanja, še diagram popuščanja trdota HRC – udarna žilavost Charpy-V – temperatura popuščanja. Iz izdelanih diagramov popuščanja lahko ugotovimo, da je preiskovano vzmetno jeklo 51CrV4 primerno za izdelavo visokotrdnostnih vzmeti ob ustrezno izvedeni toplotni obdelavi. Med fraktografsko in metalografsko analizo  $K_{Ic}$  preizkušancev smo odkrili prisotnost izcej v jeklu. Zato smo se posvetili ugotavljanju vpliva izcejanja na lomno žilavost  $K_{Ic}$ . Ugotovili smo, da se širina trakov pozitivnih izcej in trakov matriksa pri različnih vzorcih precej razlikuje. Prav tako smo odkrili, da število in širina izcej zaradi prisotnosti bainita v matriksu pomembno vplivata na lomno žilavost  $K_{Ic}$ .

**Ključne besede:** lomna žilavost, izcejanje, visokotrdnostno vzmetno jeklo, vakuumsko toplotna obdelava, diagrami popuščanja, mikrostruktura

## 1 INTRODUCTION

A producer of spring steel must provide a technical description of the steel, which includes the chemical composition and the basic mechanical, physical and technological properties of the steel. Among the technological properties, information concerning the heat treatment is very important for the manufacturer of the springs.

Charpy-V notch (CVN) impact-test values are used in toughness specifications for spring steels, even though the fracturing energy is not directly related to the spring design. It is surprising that there is no demand for the fracture toughness  $K_{Ic}$  value (the plain-strain stress-intensity factor at the onset of unstable crack growth) in the delivery conditions for spring-steel producers. To the spring designer the  $K_{Ic}$  values are more useful than the CVN values, because the design calculations for the

springs from high-strength steels should also take into account the strength and the toughness of the materials in order to prevent rapid and brittle fracture.

A spring's durability is limited by the plastic deformation, the fatigue and the fracturing. Therefore, the use of spring steel with the following properties is recommended: high ductility and toughness at operating temperatures from  $-40\text{ }^{\circ}\text{C}$  to  $+50\text{ }^{\circ}\text{C}$  and good hardenability, which provides the required mechanical properties. As a consequence of the manufacturing route, steels with a similar chemical composition may behave differently due to the variety of mechanical properties. Assuming that the chemical composition and initial microstructure of the steel correspond to those prescribed for the steel grade 51CrV4 (DIN 17221 and DIN 17222), the mechanical properties for a specific application depend mainly on the appropriately selected heat-treatment parameters.

An investigation was conducted to determine whether standardized fracture-toughness testing (ASTM E399-90), which is difficult to perform reliably for hard and low-ductility materials, could be replaced with a non-standard testing method using circumferentially notched and fatigue-precracked tensile specimens. The aim of this innovative investigation approach was to enable us to draw, for the normally used range of working hardness, combined tempering diagrams (Rockwell-C hardness – fracture toughness  $K_{Ic}$  – tempering temperature) for the vacuum-heat-treated high-strength spring-steel grade 51CrV4.

In addition, we also wanted to create, for the spring steel 51CrV4, at a selected austenitizing temperature, a classic tempering diagram, i.e., tensile strength  $R_m$  – yield stress  $R_{p0.2}$  – elongation  $A_5$  – necking  $Z$  – tempering temperature, and a tempering diagram, i.e., hardness HRC – impact toughness Charpy-V – tempering temperature. Using these tempering diagrams we wanted to confirm the suitability of the investigated steel for the production of high-strength springs with the required tensile strength between 1500 MPa and 1800 MPa.

In accordance with the plan of experiments the heat treatment was carried out on the basis of trial preliminary research and modelling results by measurements of the mechanical properties, analysis of the fractured surfaces and the examination of the microstructure of the  $K_{Ic}$  samples. Then, based on the mechanical properties the tempering diagrams for the spring steel 51CrV4, at a selected austenitizing temperature, were created.

Fractographic and metallographic analyses of the  $K_{Ic}$  test specimens showed the presence of segregations in the steel. Therefore, we also focused on examining the impact of segregations on the fracture toughness  $K_{Ic}$ . Using optical and electron (SEM + EDS) microscopy we determined the number and the width of the positive segregations bands and of the matrix bands just under the fractured surface of the  $K_{Ic}$  test specimens. We studied the influence of the number and the width of the segregation bands on the fracture toughness  $K_{Ic}$ .

## 2 EXPERIMENTAL

### 2.1 Hardness and fracture-toughness tests

Circumferentially notched and fatigue-precracked tensile-test specimens<sup>1</sup> with the dimensions indicated in **Figure 1** were used for the investigation. The Rockwell-C hardness (HRC) was measured on individual groups of  $K_{Ic}$  test specimens using a Wilson 4JR hardness machine.

The advantage of the  $K_{Ic}$  test specimens used here over standardized CT specimens (ASTM E399-90) is in the radial symmetry, which makes them particularly suitable for studying the influence of the microstructure of metallic materials on the fracture toughness. The

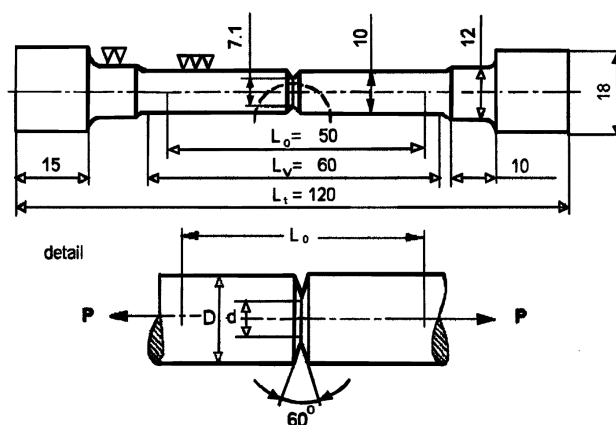


**Figure 1:** Circumferentially notched and fatigue-precracked  $K_{Ic}$  test specimen. Dimensions in mm.

**Slika 1:** Cilindrični natezni preizkušalec za merjenje lomne žilavosti z zarezo po obodu in utrujenostno razpoko v dnu zareze. Dimenzije so v milimetrih.

advantage of these specimens is related to the heat transfer, which ensures a uniform microstructure.

Due to the high notch sensitivity of hard and brittle metallic materials, such as continuous-cast spring-steel grade 51CrV4, it is very difficult – sometimes even almost impossible – to create a fatigue crack in the test specimen. However, with the  $K_{Ic}$  test specimens the fatigue crack can be created with rotating-bending loading before the final heat treatment<sup>2</sup>. The second advantage of such test specimens is that plain-strain conditions can be achieved using specimens with smaller dimensions than those of conventional CT test specimens<sup>3</sup>.

For the linear elastic behaviour up to fracture of such specimens<sup>4</sup> the following equation is applied:

$$K_{Ic} = \frac{P}{D^{3/2}} \left( -1.27 + 1.72 \frac{D}{d} \right) \quad (1)$$

where  $P$  is the load at failure,  $D$  is the outside diameter, and  $d$  is the notched-section diameter of the test specimen. Equation (1) is valid as long as the condition  $0.5 < d/D < 0.8$  is fulfilled.

The measurements of the fracture toughness were performed at room temperature using an Instron 1255 tensile-test machine. A cross-head speed of 1.0 mm/min was used for the standard tensile tests on specimens with a nominal test length of 100 mm. In the tests two specially prepared cardan fixed jaws, ensuring the axially of the tensile load, were used. During the tests the tensile-load/displacement relationship until failure was recorded. In all cases this relationship was linear, and the validity of equation (1) for the tests was confirmed.

### 2.2 Impact test

In order to obtain the tempering diagram, i.e., hardness HRC – Charpy-V – tempering temperature, we

measured the impact toughness using the Charpy impact test, known also as the Charpy V-notch test (ISO 148). The measurement with an instrumented Charpy hammer allows us to estimate the total impact work, the work needed for crack initiation and the work necessary for crack propagation.

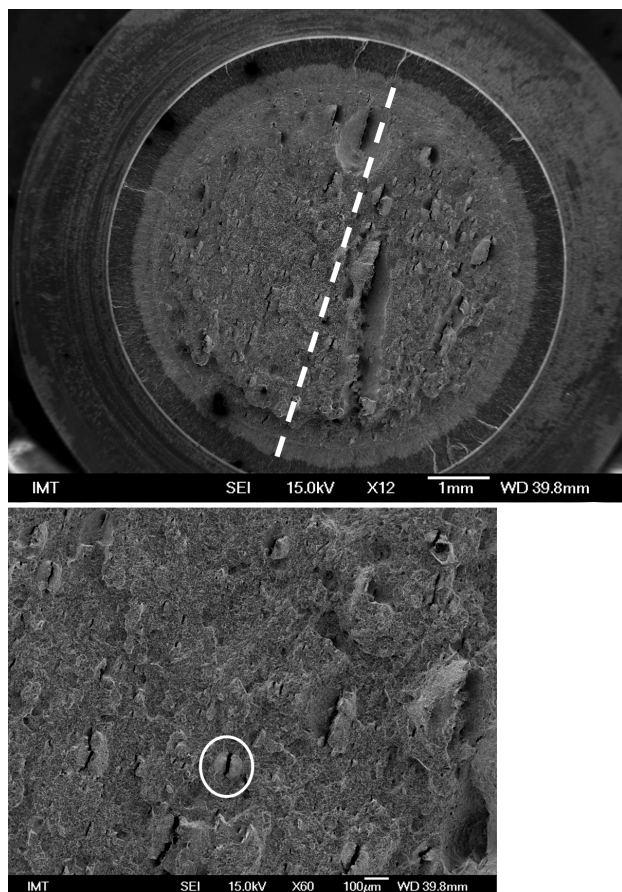


**Figure 2:** SEM image of fractured surface of  $K_{Ic}$  specimen

**Slika 2:** SEM posnetek prelomne površine preizkušanca za merjenje lomne žilavosti

The hardness  $HRC$  was measured on an Instron B 2000 device according to the standard SIST EN ISO 6508-1.

### 2.3 Tensile test

The standard tensile test (SIST EN ISO 6892-1) was applied to measure the tensile strength  $R_m$ , the yield stress  $R_{p0.2}$ , the elongation  $A_5$  and the necking  $Z$ .

### 2.4 Material, sampling and vacuum heat treatment

Samples from continuous-cast, high-strength, spring-steel, grade 51CrV4, delivered as hot-rolled and soft-annealed bars of dimensions 100 mm × 25 mm × 6000 mm were used.

The circumferentially notched and fatigue-precracked  $K_{Ic}$  test specimens were cut from the middle of the bar in the rolling direction with a fatigue crack at the notch root in the transverse direction. They were heat treated in a horizontal vacuum furnace with uniform, high-pressure gas-quenching using nitrogen ( $N_2$ ) at a pressure of 5 bar. After the first preheat (650 °C) the specimens were heated at a rate of 10 °C/min to the austenitizing temperature of 870 °C, soaked for 10 min, gas quenched to 80 °C, and then single tempered for one hour at different temperatures between 200 °C and 575 °C. At each tempering temperature 16 test specimens for the tensile test ( $R_m$  specimen), for the determination of the fracture toughness ( $K_{Ic}$  specimen) and of the Charpy-V toughness (CVN specimen), as well as two metallographic samples  $\phi$  19 mm × 9 mm were heat treated.

### 2.5 Measurement of the number and the width of the segregations

A fractured surface of a  $K_{Ic}$  specimen was observed on the SEM, **Figure 2**. The dotted line shows the orientation of the MnS sulphides. An example of the MnS inclusion inside the crack is shown in the circle.

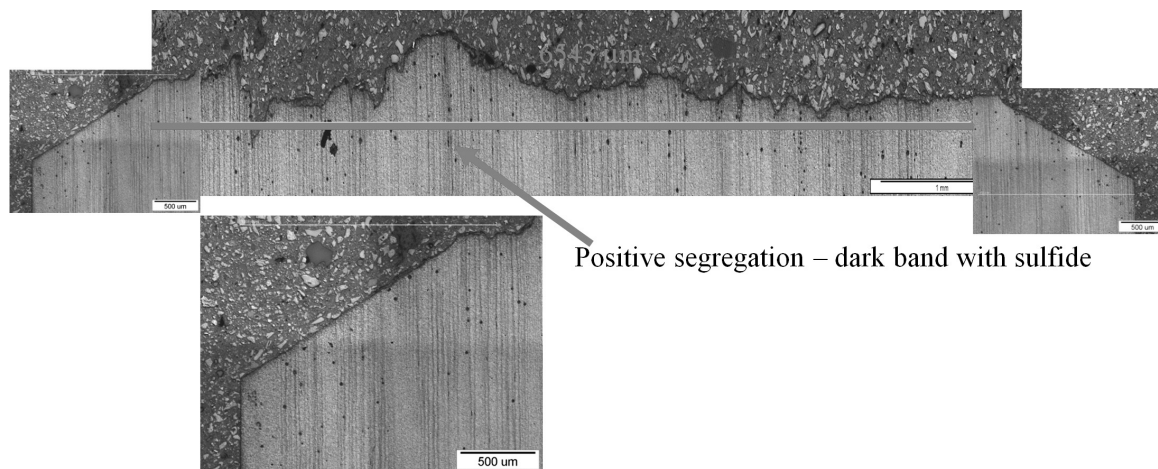


**Figure 3:** Combined image of segregations just under the fractured surface

**Slika 3:** Sestavljena slika izcej tik pod prelomno površino





**Figure 4:** Microstructure of test specimen D99: positive segregations – tempered martensite (dark bands), 4% picral

**Slika 4:** Mikrostruktura preizkušanca D99: pozitivne izceje – popuščeni martenzit (temni pasovi), 4 % pikral

The presence of MnS in the crack was confirmed by EDS. Inclusions of MnS are present in positive segregations that are oriented in the rolling direction. To determine the number of segregations the  $K_{Ic}$  specimens were cut perpendicularly to the orientation of the MnS sulphides.

The number of segregations just under the fractured surface was counted using an optical microscope, as shown in **Figure 3**, on a sample etched in 4 % picral to make the segregations visible. The dark bands as positive segregations were confirmed by the presence of sulphides and by measuring the microhardness.

The assessment of the number and the width of the segregations is shown in **Figure 4**.

### 3 RESULTS AND DISCUSSION

In a classic tempering diagram for an austenitizing temperature of 870 °C the average measured values of the mechanical properties (tensile strength  $R_m$ /MPa, yield strength  $R_{p0.2}$ /MPa, elongation  $A_5$ /% and necking  $Z$ /%) are shown as a function of the tempering temperature in the range between 300 °C and 700 °C in **Figure 5**.

Given that we had for each selected tempering temperature a statistically relevant number of  $R_m$  specimens, for each group we performed a statistical analysis. As can be seen from the diagram, the minimum dispersion of results is within  $\pm 2\sigma$  across the whole range of selected tempering temperatures in tensile strength and elongation, while it is higher only for the necking.

The tempering diagram indicates that the requirement from the standard DIN EN 10089:2003-4 for the elongation (minimum 8 %) and necking (minimum 30 %) can be achieved after the tempering of the investigated steel in the temperature range between 300 °C and 700 °C, while the required tensile strength (1350–1650 MPa) and

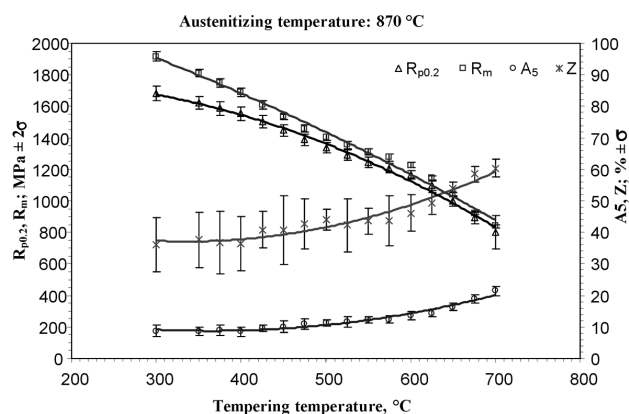


**Figure 5:** Classic tempering diagram for continuous-cast, hot-rolled, flat, spring steel 51CrV4, for an austenitizing temperature of 870 °C  
**Slika 5:** Klasični diagram popuščanja za kontinuirno lito, vroče valjano vzmetno jeklo 51CrV4, temperatura avstenitizacije 870 °C

yield-strength (minimum 1200 MPa) can be achieved with a tempering temperature below 530 °C.

The required tensile strength for high-strength spring steel (1500–1800 MPa) can be achieved if the tempering temperature is below 475 °C.

The tempering diagram, hardness HRC – Charpy-V – tempering temperature, for the selected austenitizing temperature of 870 °C and the selected tempering temperature in the range of 200 °C to 625 °C for the high-strength steel 51CrV4 is shown in **Figure 6**. The diagram shows that the curves for the hardness and impact toughness Charpy-V over the entire range of tempering temperatures are similar to the curves of the hardness and the fracture toughness  $K_{Ic}$  in the tempering diagram shown in **Figure 7**. Similar to the fracture toughness, the impact toughness Charpy-V also increases to a temperature of 525 °C, then it decreases to 550 °C, and then the toughness increases again. This trend can be attributed to the kinetics of precipitation

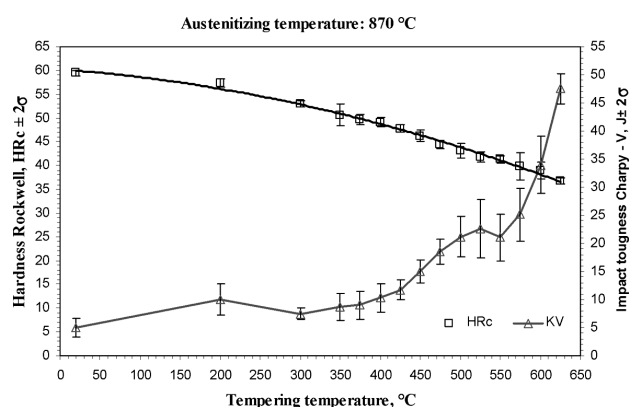


**Figure 6:** Effect of tempering temperature on the hardness HRC and the impact toughness Charpy-V of a continuous-cast, hot-rolled, flat, spring steel 51CrV4

**Slika 6:** Vpliv temperature popuščanja na trdoto HRC in udarno žilavost Charpy-V za kontinuirno lito, vroče valjano vzmetno jeklo 51CrV4



during the tempering. In the diagram, the dispersion of results within  $\pm 2\sigma$  in the quenched and tempered condition using a temperature of 475 °C is of the same magnitude. The dispersion of results is increased above the tempering temperature of 500 °C. The results of the measurements of the Charpy-V toughness in the range of tempering temperature 525–575 °C show that the toughness is even reduced, which confirms the observations made when measuring the fracture toughness, so we assume that this is an area of irreversible temper embrittlement<sup>5,6</sup>.

In the case of the CVN-specimens, which were quenched and tempered at the same temperature, the reason for the scattering of the results is the heterogeneity of the investigated steel and also, but less of a factor, the geometry and surface roughness of the notch.

The requirement from the standard DIN EN 10089: 2003-04 for the impact energy (minimum 8 %) can be achieved if the tempering temperature is above 200 °C.

High-strength spring steels are very notch sensitive, for this occasion, it is also important to measure fracture toughness  $K_{Ic}$ , which can be described as the ability of a material to resist, under tensile loading, the progress of existing cracks. We determined the fracture toughness  $K_{Ic}$  by the use of circumferentially notched and fatigue-precracked  $K_{Ic}$  test specimens which were linear elastic loaded to fracture. The tempering diagram, hardness HRC – fracture toughness  $K_{Ic}$  – tempering temperature, for the selected austenitizing temperature of 870 °C and the selected tempering temperature in the range of 200 °C to 625 °C for the steel 51CrV4 is shown in **Figure 7**.

Given that we had for each selected tempering temperature a statistically relevant number of  $K_{Ic}$  specimens, for each group we performed a statistical analysis. As can be seen from the diagram, the minimum dispersion of results within  $\pm 2\sigma$  is in the quenched state and in  $K_{Ic}$  specimens that were quenched and tempered at 200 °C. At higher tempering temperatures between 300 °C and 525 °C, the scattering of the results slightly

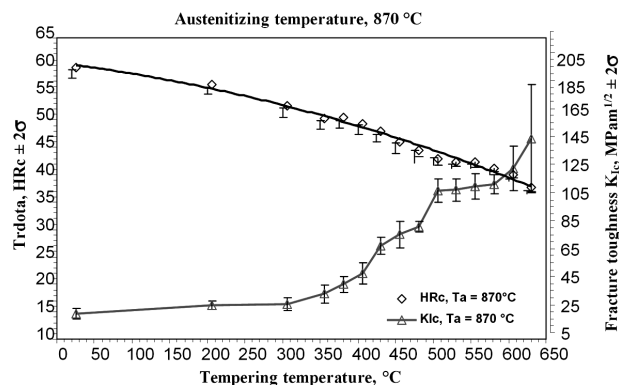


**Figure 7:** Effect of tempering temperature on the hardness HRC and the fracture toughness  $K_{Ic}$  of the continuous-cast, hot-rolled, flat, spring steel 51CrV4

**Slika 7:** Vpliv temperature popuščanja na trdoto HRC in lomno žilavost  $K_{Ic}$  za kontinuirno lito, vroče valjano vzmetno jeklo 51CrV4

increased. This trend can be attributed to the kinetics of extracting precipitates during tempering. The reason for the dispersion of the results within each group of  $K_{Ic}$  specimens that were quenched and tempered at the same temperature is the heterogeneity of the investigated steel.

The highest hardness of 58 HRC is achieved in the as-quenched condition after vacuum quenching from the austenitizing temperature of 870 °C. In examining the evolution of the properties by an increase of the tempering temperatures, it is observed that the minimum scatter of results within  $\pm 2\sigma = 3.2 \text{ MPa m}^{1/2}$  is found in the as-quenched state and after single tempering at 200 °C. At higher tempering temperatures between 300 °C and 575 °C, the scatter of the  $K_{Ic}$  results slightly increased up to  $\pm 2\sigma = 9.4 \text{ MPa m}^{1/2}$ , while the scatter of the Rockwell-C hardness is up to  $\pm 2\sigma = 1.2 \text{ HRC}$  across the whole range of used tempering temperatures. Within each group of  $K_{Ic}$  specimens that were quenched and tempered at the same temperature, this can be attributed to the kinetics of the carbides' precipitation during tempering at selected temperatures as well as to the

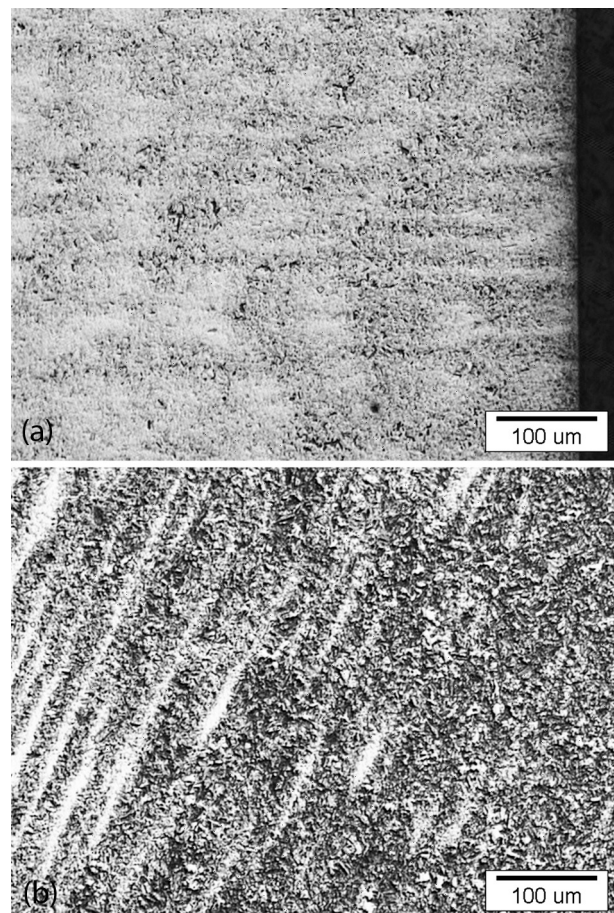


**Figure 8:** The microstructure of the  $K_{Ic}$  test specimen in the as-quenched condition (transverse direction); a) specimen with the lowest fracture toughness ( $K_{Ic} = 16.2 \text{ MPa m}^{1/2}$ , 58.1 HRC), b) specimen with the highest fracture toughness ( $K_{Ic} = 22.3 \text{ MPa m}^{1/2}$ , 58.1 HRC)

**Slika 8:** Mikrostruktura  $K_{Ic}$  preizkušanca v kaljenem stanju (prečna smer); a) z najmanjšo lomno žilavostjo ( $K_{Ic} = 16,2 \text{ MPa m}^{1/2}$ , 58,1 HRC), b) z največjo lomno žilavostjo ( $K_{Ic} = 22,3 \text{ MPa m}^{1/2}$ , 58,1 HRC)



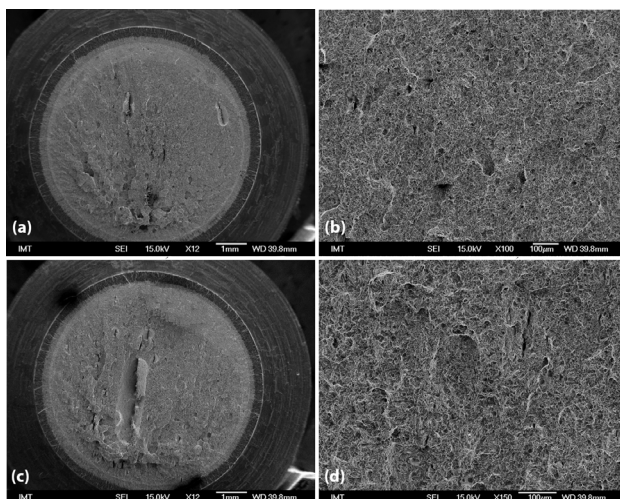


**Figure 9:** Fractured surfaces of  $K_{Ic}$  test specimen, tempered at 475 °C with an equal hardness; a, b) specimen with the lowest fracture toughness ( $K_{Ic} = 67.0 \text{ MPa m}^{1/2}$ , 44.8 HRC), c, d) specimen with the highest fracture toughness ( $K_{Ic} = 76.1 \text{ MPa m}^{1/2}$  in 44.8 HRC)

**Slika 9:** Prelomne površine  $K_{Ic}$  preizkušancev popuščenih pri 475 °C z enako trdoto; a, b) z najmanjšo lomno žilavostjo ( $K_{Ic} = 67,0 \text{ MPa m}^{1/2}$ , 44,8 HRC), c, d) z največjo lomno žilavostjo ( $K_{Ic} = 76,1 \text{ MPa m}^{1/2}$  in 44,8 HRC)

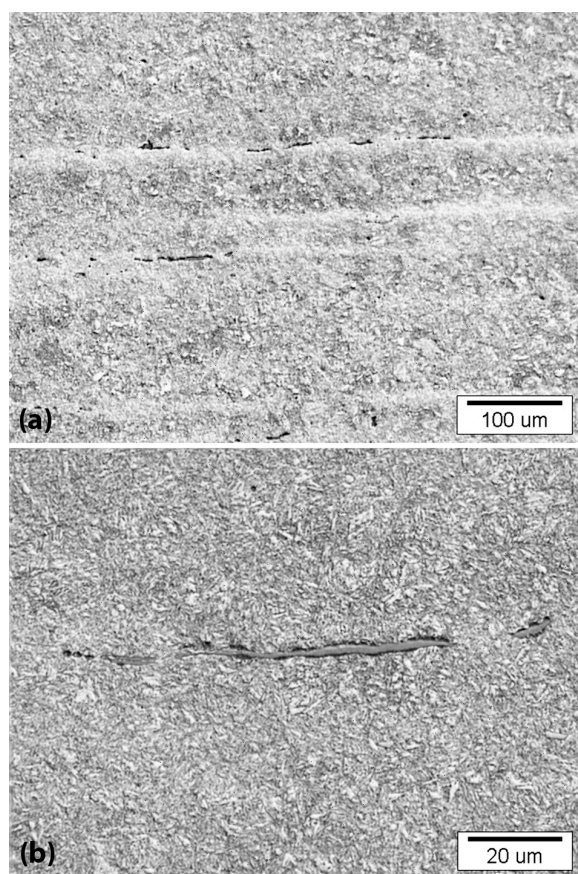


**Figure 10:** Typical microstructure of  $K_{Ic}$  test specimens ( $K_{Ic} = 75.7 \text{ MPa m}^{1/2}$ , 43.8 HRC) in the longitudinal direction. Sulphide inclusions are located in the positive segregations.

**Slika 10:** Značilna mikrostruktura  $K_{Ic}$  preizkušanca ( $K_{Ic} = 75,7 \text{ MPa m}^{1/2}$ , 43,8 HRC) v vzdolžni smeri. Sulfidi se nahajajo v pozitivnih izcejih.

heterogeneity of the investigated steel. Since the austenitizing temperature is the same, it is clear that the fracture toughness,  $K_{Ic}$ , is a very selective mechanical property with regard to the tempering temperature. It should be noted that the  $K_{Ic}$  test specimens were taken from the middle of the bar, and therefore the microstructures of the  $K_{Ic}$  test specimens with lowest and highest fracture toughnesses are comparable.

In the as-quenched condition, the microstructure consists of untempered martensite and lower bainite, **Figure 8**. Strong positive (bright) and negative (dark) segregations are visible due to the lower etching intensity of the untempered martensite.

The fractured surface of the  $K_{Ic}$  test specimens was examined in SEM at magnification of 12-times, **Figure 9**. The presence of inclusions (sulphides in cracks) in positive segregations is evident. The density of positive segregations is higher on the fractured surface of the  $K_{Ic}$  test specimen with the highest fracture toughness in comparison to the fractured surface of the  $K_{Ic}$  test specimen with the lowest fracture toughness with the

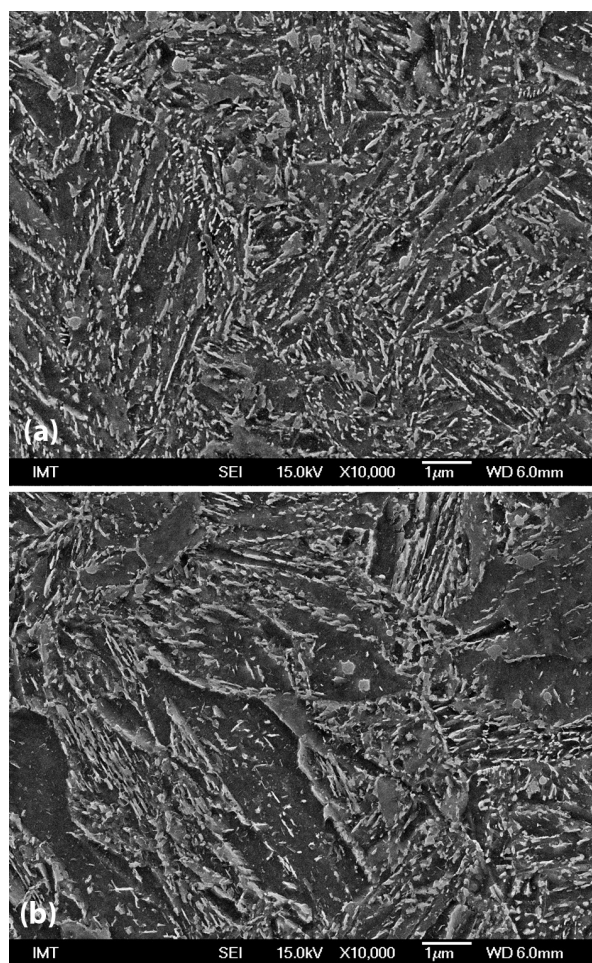


**Figure 11:** SEM microstructure of the  $K_{Ic}$  test specimens with the highest fracture toughness: a) positive segregations and b) negative segregations (matrix), longitudinal direction

**Slika 11:** SEM-mikrostruktura  $K_{Ic}$  preizkušanca z največjo lomno žilavostjo: a) pozitivna izceja, b) negativna izceja, vzdolžna smer



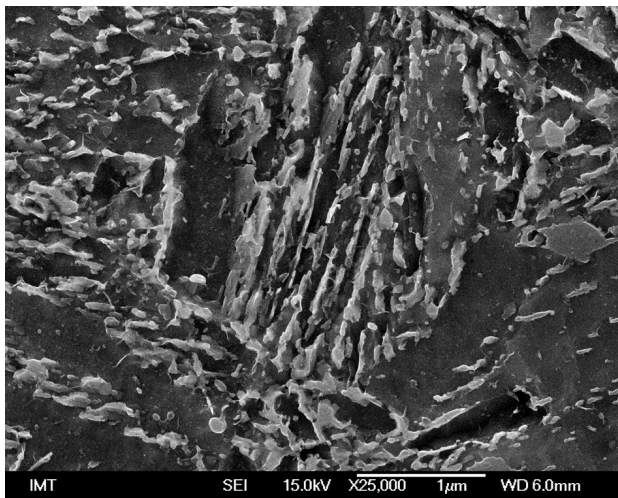


Figure 12: Bainite grain from Figure 11  
Slika 12: Kristalno zrno bainita s slike 11

same hardness. Also, the distribution is more even and the size of the segregations is smaller.

The microstructure of the same  $K_{Ic}$  specimens just below the fractured surface was examined in an optical microscope, Figure 10. The fractured  $K_{Ic}$  specimen was cut perpendicularly to the direction of segregations determined by the position of the sulphide inclusions. Then the number of segregations in the transverse direction was counted and for the specimen with the lowest fracture toughness ( $K_{Ic} = 67.0 \text{ MPa m}^{1/2}$ , 44.8 HRC) 98 segregations and specimen with the highest fracture toughness ( $K_{Ic} = 76.1 \text{ MPa m}^{1/2}$ , 44.8 HRC) 147 segregations were found. We also measured the widths of the segregation bands. The specimen with the lowest fracture toughness has an average width of the segregation bands equal to  $29 \mu\text{m}$  and that with the highest fracture toughness has an average width of the segregation bands equal to  $33 \mu\text{m}$ .

The microstructure in the quenched and tempered condition consists of tempered martensite and bainite ( $\approx 20 \%$ , volume fraction). In the microstructure, non-metallic inclusions of the sulphide type located in positive segregations and oriented in the rolling direction are observed.

The microstructure of the  $K_{Ic}$  test specimen was examined in the SEM and it was found that the microstructure in the positive segregations consisted of tempered martensite and in the negative (matrix) of tempered martensite with islands of bainite, Figures 11 and 12.

From a comparison of the microstructures of the  $K_{Ic}$  test specimens with the lowest and highest fracture toughnesses from the same heat and with the same hardness, it can be concluded that the density, the size and the distribution of segregations have a significant influence on the fracture toughness. The increase of

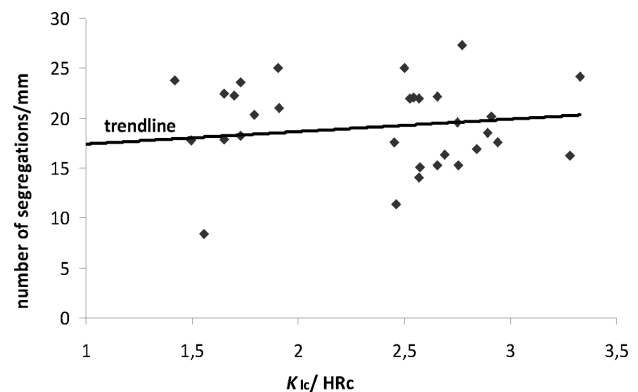


Figure 13: Influence of the number of segregations on the fracture toughness  $K_{Ic}$

Slika 13: Vpliv števila izcej na lomno žilavost  $K_{Ic}$

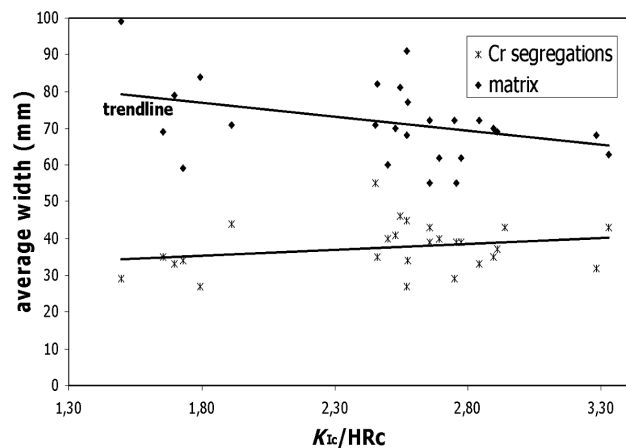


Figure 14: Influence of the average width of the matrix bands and the segregation bands on the fracture toughness  $K_{Ic}$

Slika 14: Vpliv povprečne širine pasov negativnih in pozitivnih izcej na lomno žilavost  $K_{Ic}$

fracture toughness can probably be ascribed to the presence of bainite in the matrix of negative segregations.

To find out the influence of segregation on the fracture toughness the number of segregations and their width just under the fractured surface were assessed, Figures 13 and 14.

It can be seen that there is a trend for the fracture toughness  $K_{Ic}$  to increase with a larger number of segregations. It is also evident that the average width of the segregations affects the fracture toughness  $K_{Ic}$ . The broad bands of the positive segregations increase the fracture toughness  $K_{Ic}$ , while it is lowered by narrow bands of the matrix. This can also be associated with the number of segregations. If there are more segregations, the average width of the matrix bands decreases.

#### 4 CONCLUSIONS

The investigated high-strength, spring-steel grade 51CrV4 was successfully quenched in a horizontal vacuum furnace with uniform high-pressure gas-quench-

ing using nitrogen ( $N_2$ ) at a pressure of 5 bar. The Rockwell-C hardness was  $(58.4 \pm 0.8)$  HRC in the quenched state, which is high enough to obtain the required hardnesses from 35 HRC to 50 HRC after a single tempering.

The obtained microstructure consisting of tempered martensite and bainite ( $\approx 20$  % volume fraction) meets the requirements of TB1402 (Scania Standard STD512090 and STD4153), thus we can conclude that the investigated high-strength spring steel 51CrV4 with a thickness up to 20 mm is suitable for heat treatment in a vacuum furnace with uniform, high-pressure gas-quenching using nitrogen ( $N_2$ ) at a pressure of 5 bar or higher.

Our investigation showed that standardized fracture-toughness testing (ASTM E399-90) could be replaced with a non-standard testing method using circumferentially notched and fatigue-precracked tensile specimens ( $K_{Ic}$  test specimen). The results of this innovative approach to the investigation have shown that using the proposed method it was possible to draw, for the normally used range of working hardness, combined tempering diagrams (Rockwell-C hardness – Fracture toughness  $K_{Ic}$  – Tempering temperature) for vacuum-heat-treated, high-strength, spring-steel grade 51CrV4.

According to the tempering diagrams the tensile strength  $R_m$  – Yield stress  $R_{p0.2}$  – Elongation  $A_5$  – Necking  $Z$  – Tempering temperature and the tempering diagram, Hardness HRC – Impact toughness Charpy-V – Tempering temperature, we can conclude that the investigated spring steel 51CrV4 is suitable for the production of high-strength springs when the proper heat treatment is performed.

The presence of segregations was confirmed by fractographic and metallographic analyses of the  $K_{Ic}$  test specimens. We found that the width of the positive segregation bands and matrix bands between the samples varied considerably. We have also discovered that the number and the width of the segregation bands influenced significantly the fracture toughness  $K_{Ic}$  due to the presence of bainite in the matrix bands. Our investigation shows that there is a trend of fracture toughness  $K_{Ic}$  increase with a larger number of segregations.

These findings will be checked in future investigations.

### Acknowledgement

Štore Steel, d. o. o., Železarska 3, SI-3220 Štore, Slovenia, is thanked for the supply of test material as well for the financial support. Thanks also to Prof. dr. Franc Vodopivec for helpful discussions.

### 5 REFERENCES

- <sup>1</sup> B. Senčič, V. Leskovšek, Mater. Tehnol., 45 (2011) 1, 67–73
- <sup>2</sup> A. Sandberg, M. Nzotta, High performance matrix tool steels produced via a clean steel concept, 7<sup>th</sup> Tooling Conference, Torino, 2006
- <sup>3</sup> V. Leskovšek, Optimization of the vacuum heat treatment of high-speed steels, University of Zagreb, 1999 (Ph. D. thesis)
- <sup>4</sup> H. F. Bueckner, ASTM STP 381, 1965, 82
- <sup>5</sup> A. Shekhter, S. Kim, D. G. Carr, A. B. L. Croker, S. P. Ringer, International Journal of Pressure Vessels and Piping, 79 (2002), 611–615
- <sup>6</sup> B. Ule, F. Vodopivec, M. Pristavec, F. Grešovnik, Železarski zbornik, 24 (1990), 35–40



## MECHANICAL AND TRIBOLOGICAL CHARACTERISTICS OF STIR-CAST Al-Si10Mg AND SELF-LUBRICATING Al-Si10Mg/MoS<sub>2</sub> COMPOSITES

### MEHANSKE IN TRIBOLOŠKE LASTNOSTI Z MEŠANJEM ULITIH KOMPOZITOV Al-Si10Mg IN SAMOMAZALNIH KOMPOZITOV Al-Si10Mg/MoS<sub>2</sub>

**Kannappan Somasundara Vinoth<sup>1</sup>, Ramanathan Subramanian<sup>2</sup>,  
Somasundaram Dharmalingam<sup>3</sup>, Balu Anandavel<sup>2</sup>**

<sup>1</sup>Department of Production Engineering, PSG College of Technology, 641 004 Coimbatore, India

<sup>2</sup>Department of Metallurgical Engineering, PSG College of Technology, 641 004 Coimbatore, India

<sup>3</sup>Department of Mechanical Engineering, PSG Polytechnic College, 641 004 Coimbatore, India  
vinothks@yahoo.com

*Prejem rokopisa – received: 2012-03-20; sprejem za objavo – accepted for publication: 2012-05-24*

The mechanical and tribological characteristics of aluminium-molybdenum-disulphide self-lubricating composites have been investigated and compared to the Al-Si10Mg alloy. Al-Si10Mg/4MoS<sub>2</sub> display the finest microstructures due to a higher fraction of MoS<sub>2</sub> added. The densities of Al-Si10Mg/2MoS<sub>2</sub> and Al-Si10Mg/4MoS<sub>2</sub> were marginally higher than in the case of the aluminium alloy by 1 % and 2 % mass fractions, respectively. The ultimate tensile strength decreases considerably due to the additions of 2 % and 4 % MoS<sub>2</sub> by 15 % and 22 %, respectively, compared to the Al-Si10Mg alloy. It was seen that while the Al-Si10Mg alloy shows a predominantly ductile fracture (fibrous regions), the composite specimens (with an MoS<sub>2</sub> addition) show an increase in the mixed mode (ductile and brittle regions). Al-Si10Mg/2MoS<sub>2</sub> and Al-Si10Mg/4MoS<sub>2</sub> show an enormous decrease in the wear rate by 55 % and 65 %, respectively, compared with the Al-Si10Mg alloy. The decrease in the wear occurs due to the presence of an MoS<sub>2</sub> layer, which forms a film on the wear surface.

Keywords: aluminium-molybdenum-disulphide self-lubricating composites

Preiskovane so bile mehanske in tribološke značilnosti aluminij-molibden disulfidnih samomazalnih kompozitov in primerjane z zlitino Al-Si10Mg. Al-Si10Mg/4MoS<sub>2</sub> ima najdrobnejšo mikrostrukturo zaradi večjega deleža dodanega MoS<sub>2</sub>. Gostota Al-Si10Mg/2MoS<sub>2</sub> in Al-Si10Mg/4MoS<sub>2</sub> je bila navidezno večja za masni delež 1 % oziroma 2 %. Končna natezna trdnost se je v primerjavi z zlitino Al-Si10Mg občutno zmanjšala za 15 % oziroma 22 % pri dodatku 2 % oziroma 4 % masnega deleža MoS<sub>2</sub>. Izkazalo se je, da pri zlitini Al-Si10Mg prevladuje žilav prelom (vlaknata področja), pri kompozitnih vzorcih (z dodatkom MoS<sub>2</sub>) pa mešan prelom (duktilna in krhka področja). Al-Si10Mg/2MoS<sub>2</sub> in Al-Si10Mg/4MoS<sub>2</sub> izkazujeta občutno povečanje odpornosti proti obrabi, in sicer 55 % oziroma 65 % v primerjavi z zlitino Al-Si10Mg. Zmanjšanje obrabe je zaradi sloja MoS<sub>2</sub>, ki tvori tanko plast na obrabni površini.

Ključne besede: aluminij-molibden disulfidni samomazalni kompoziti

## 1 INTRODUCTION

Aluminium-silicon alloys and composites are being used in automotive applications like pistons, brake rotors and engine-block cylinder liners<sup>1,2</sup>. Tribological behaviour is an important aspect in the use of aluminium metal-matrix composites in automotive applications. The wear behaviour of Al-Si alloys can be further enhanced by adding ceramic particles. Abrasive particles like silicon carbide, alumina, and diamond are added to improve the tribological behaviour by increasing the hardness of a composite<sup>3-5</sup>. Nevertheless, lubricating particles like graphite and MoS<sub>2</sub> have also been added to improve the tribological behaviour of different materials by providing a solid lubricating layer<sup>6,7</sup>. The additions of these particles considerably affect the mechanical behaviour of the composites.

There are various methods of producing composites like blending and consolidation, vapour deposition and consolidation, stir casting, infiltration process, spray

deposition and consolidation, as well as in-situ reacting process<sup>8</sup>. Of all these processes, stir casting is the simplest and the most economical method. Stir-cast self-lubricating composites have been successfully developed by adding graphite particles<sup>9</sup>. It has also been suggested that these composite materials have the capacity to achieve low friction and wear of the contact surfaces without any external supply of lubrication during the sliding. However, graphite films fail in lower loads and shorter lifetimes compared with MoS<sub>2</sub><sup>10</sup>. Self-lubricating Al-MoS<sub>2</sub> composites have been prepared by using the powder-metallurgy route<sup>11</sup>. However, neither the preparation of MoS<sub>2</sub>- based composites by stir casting nor the characterisation of Al-Si10Mg/MoS<sub>2</sub> composites have been reported in literature.

In this investigation, two self-lubricating composites of molybdenum disulphide, namely, Al-Si10Mg/2MoS<sub>2</sub> and Al-Si10Mg/4MoS<sub>2</sub> have been produced with the stir-casting route. The changes in the mechanical and

tribological properties caused by the addition of MoS<sub>2</sub> are studied and compared with the Al-Si10Mg alloy.

## 2 MATERIALS AND METHODS

### 2.1 Preparation of the composite

The Al-Si10Mg aluminium alloy (**Table 1**) with a density of 2640 kg/m<sup>3</sup> was used in this investigation as the matrix material. The Al-Si10Mg alloy has excellent

resistance to corrosion in both normal atmospheric and marine environments collectively exhibiting high strength and hardness.

**Table 1:** Chemical composition of the aluminium alloy used (mass fractions, w/%)

**Tabela 1:** Kemijska sestava uporabljene aluminijeve zlitine (mas. deleži, w/%)

Mg	Si	Fe	Mn	Others*	Al
0.2 to 0.6	10.0 to 13.0	0.6 max	0.3 to 0.7	1.5 max	balance

\* (Cu, Ni, Zn, Pb, Sn and Ti)

The Al-Si10Mg alloy was charged into an electrical resistance-heated furnace modified for this investigation. The melting of the Al-Si10Mg alloy was carried out under argon atmosphere at 1073 K. Molybdenum-disulphide (MoS<sub>2</sub>) solid lubricant with an average particle size of 1.5 µm and a density of 4600 kg/mm<sup>3</sup> (**Figure 1**) was used as the reinforcement in this investigation. The MoS<sub>2</sub> particulates were incorporated into the molten metal and stirred continuously for ten minutes. The molten mixture was solidified in a cast-iron die in the form of a cylindrical pin with a diameter of 14 mm and a length of 70 mm.

### 2.2 Testing of the materials

The density of composites was determined using a top-loading electronic balance (Mettler Toledo make) according to the Archimedean principle. The microstructure of the composite specimens was identified using a Carl Zeiss Goettingen optical microscope. The specimens were metallographically polished to obtain an average roughness value of 0.8 µm. The tensile testing was carried out using a Hounsefield tensometer. The ultimate tensile strength of the specimens was calculated from the load at which a fracture occurred. The morphology of worn surfaces of the composite specimens was examined by using a JEOL T100 Scanning Electron Microscope (SEM). The hardness was measured by using a Zwick hardness tester at a load of 100 g. The dry-sliding wear behaviour of the composites was studied using a pin-on-disc apparatus. The disc material was made of the EN-32 steel with a hardness of 65 HRC. The difference in weights before and after the test was taken as weight loss. The wear rate was calculated on the basis of the difference in the weights of a specimen using the following formula:

$$\text{Wear rate } [WR] = \frac{W}{9.81\rho D} \quad \text{mm}^3/\text{km} \quad (1)$$

where  $W/\text{kg}$  = mass loss,  $\rho/(\text{kg}/\text{mm}^3)$  = density of the material,  $D$  = sliding distance

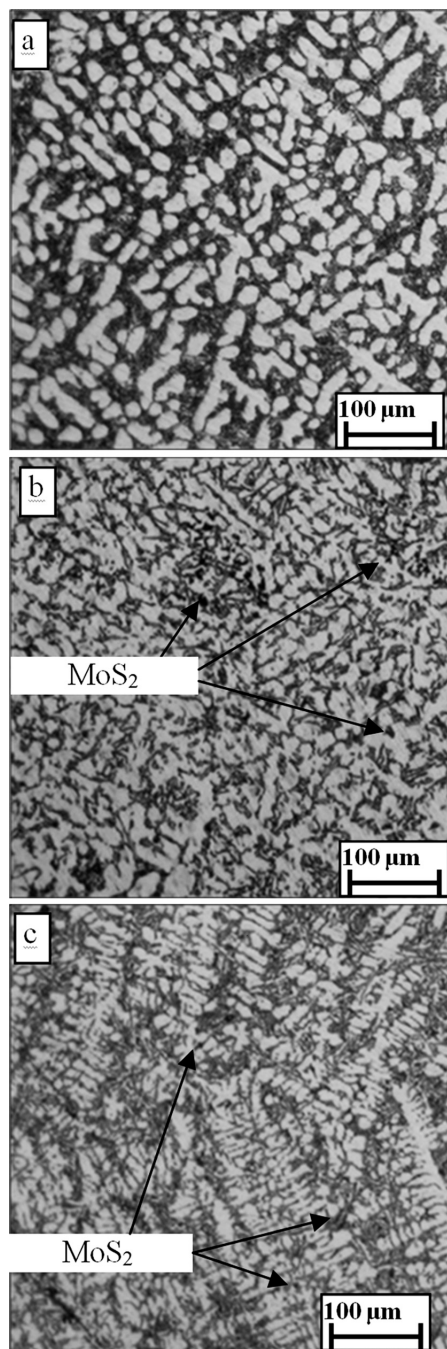


**Figure 1:** Microstructures of the materials: a) Al-Si10Mg, b) Al-Si10Mg/2MoS<sub>2</sub>, c) Al-Si10Mg/4MoS<sub>2</sub>

**Slika 1:** Mikrostruktura materiala: a) Al-Si10Mg, b) Al-Si10Mg/2MoS<sub>2</sub>, c) Al-Si10Mg/4MoS<sub>2</sub>

**Table 2:** Mechanical properties of the Al-Si10Mg alloy and the composites**Tabela 2:** Mehanske lastnosti Al-Si10Mg zlitine in kompozitov

Material	Density kg/m <sup>3</sup>	UTS MPa	Hardness HV	Elongation %	Decrease in UTS, %	Increase in hardness, %
Al-Si10Mg	2640	218.45	102	1.66	-	-
Al-Si10Mg/2MoS <sub>2</sub>	2670	185.31	145	1.22	15	42
Al-Si10Mg/4MoS <sub>2</sub>	2697	170.28	148	1.10	22	45

### 3 RESULTS AND DISCUSSION

#### 3.1 Microstructures

Optical micrographs of the Al-Si10Mg alloy and of the composites (**Figures 1a to c**) show as-cast (dendritic) structures consisting of silicon particles in a eutectic

matrix. The microstructures of the composites (Al-Si10Mg/2MoS<sub>2</sub> and Al-Si10Mg/4MoS<sub>2</sub>) are significantly finer, affected probably by the heterogeneous nucleation caused by MoS<sub>2</sub> particles. Al-Si10Mg/4MoS<sub>2</sub> exhibits the finest microstructure due to the higher fraction of MoS<sub>2</sub> added. Figures 1b and 1c show that MoS<sub>2</sub> particles were uniformly distributed in the matrix.

#### 3.2 Mechanical properties

The mechanical properties of the composites (density, hardness, and tensile strength), given in **Table 2**, show the average properties of various test specimens at different positions.

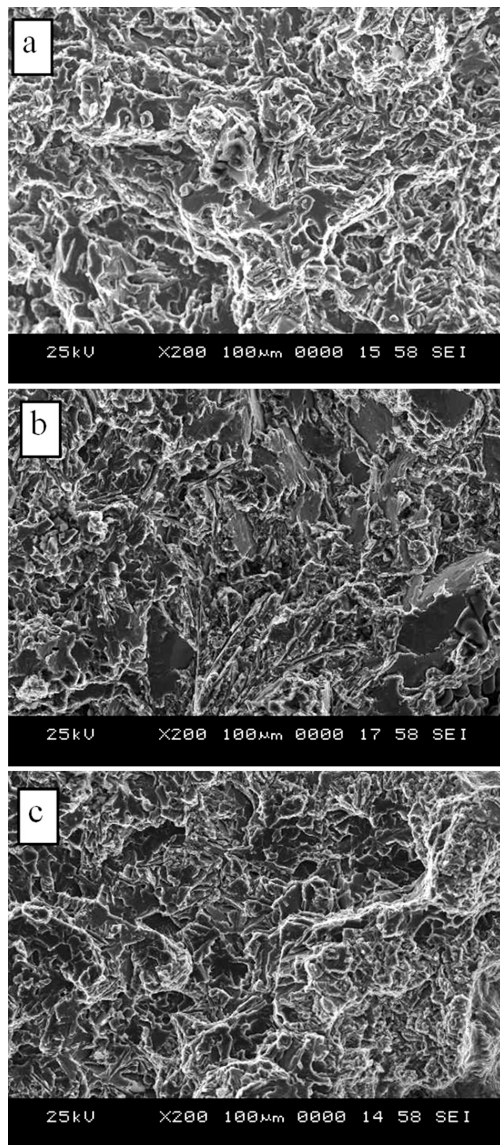
The density of MoS<sub>2</sub> is higher than that of the aluminium alloy and hence an increase in the MoS<sub>2</sub> content will raise the density of the composite. The densities of Al-Si10Mg/2MoS<sub>2</sub> and Al-Si10Mg/4MoS<sub>2</sub> were marginally higher than the density of the aluminium alloy by 1 % and 2 %, respectively. A similar increase in the density of the composites was achieved by adding SiC<sup>12</sup> and Al<sub>2</sub>O<sub>3</sub><sup>13</sup> by various authors.

The ultimate tensile strength [UTS] of Al-Si10Mg was approximately 218 MPa. It was reported in previous researches that an addition of alumina to AA6061 and AA7005 causes an increase in the tensile strength<sup>14</sup>. Similar results were reported for SiCp/aluminium-alloy composites<sup>15</sup> and aluminium-alumina, aluminium-illite and aluminium-silicon carbide particle composites<sup>5</sup>. In contrast to this, the studies on an addition of alumina to the 2024 Al alloy have shown a decrease in UTS<sup>16</sup>. Similar results were obtained for an addition of graphite to aluminium<sup>17</sup>. The tensile strength decreases considerably due to the additions of 2 % and 4 % by mass MoS<sub>2</sub> by 15 % and 22 %, respectively. The observed decrease in UTS may be due to various mechanisms like the particle pull-out and crack propagation, which are initiated by the presence of MoS<sub>2</sub>.

The elongation of the composites decreases slightly less than in the case of the Al-Si10Mg alloy indicating that an addition of MoS<sub>2</sub> lowers the ductility of a composite. A similar result was observed in the SiC reinforcement of the 2124, 7075 alloys and monolithic aluminium<sup>18,19</sup>.

#### 3.3 Fracture surface

**Figures 2a to c** show the SEM fractographs of Al-Si10Mg, Al-Si10Mg/2MoS<sub>2</sub> and Al-Si10Mg/4MoS<sub>2</sub>,

**Figure 2:** Fracture analysis of the materials: a) Al-Si10Mg, b) Al-Si10Mg/2MoS<sub>2</sub>, c) Al-Si10Mg/4MoS<sub>2</sub>**Slika 2:** Analiza prelomov materiala: a) Al-Si10Mg, b) Al-Si10Mg/2MoS<sub>2</sub>, c) Al-Si10Mg/4MoS<sub>2</sub>



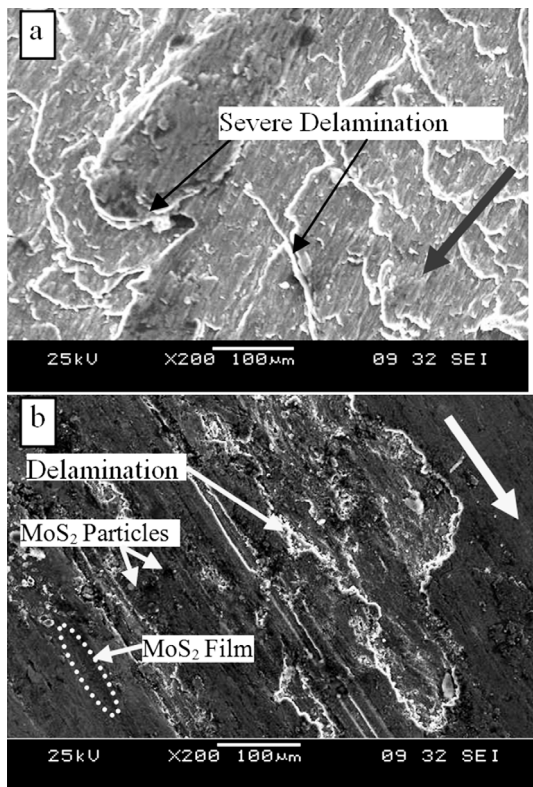


**Figure 3:** Wear behaviour of the Al-Si10Mg alloy and the composites  
**Slika 3:** Obraba Al-Si10Mg-zlitine in kompozitov

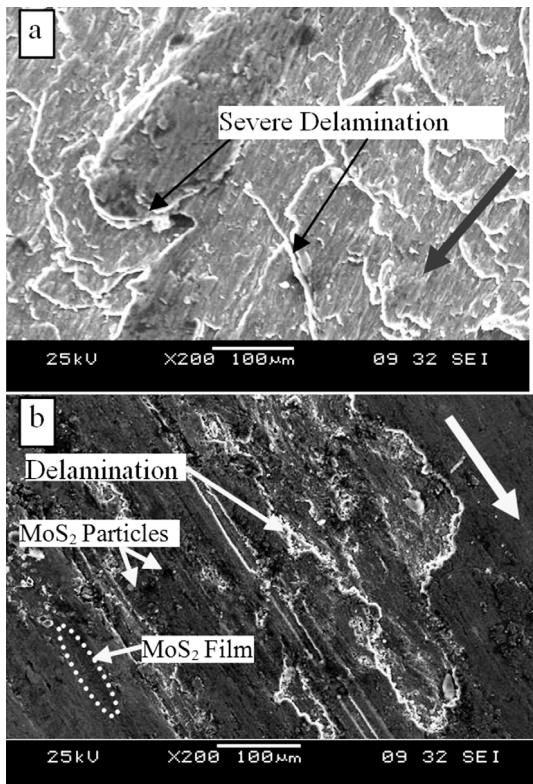


**Figure 4:** Wear-surface SEM micrographs at a load of 50 N and a speed of 5 m/s of: a) Al-Si10Mg, b) Al-Si10Mg/2MoS<sub>2</sub>  
**Slika 4:** SEM-posnetek obrabljene površine pri obremenitvi 50 N in hitrosti 5 m/s za: a) zlitine Al-Si10Mg, b) Al-Si10Mg/2MoS<sub>2</sub>

respectively. From the fractographs of the tensile-test specimens (**Figure 2**) it can be seen that, in the aluminium-matrix alloy, the fracture was primarily transgranular with a microscopic void formation; later the progressive growth and the final coalescence around the reinforcement particles can be observed. It can also be seen that while the Al-Si10Mg alloy shows a predominantly ductile fracture (fibrous regions), the composite specimens show an increase in the mixed mode [ductile and brittle regions]. In addition, the composite samples also show the features like particle pullout, crack growth, and propagation typical of a brittle fracture.

### 3.4 Wear behaviour

Dry-sliding wear tests were conducted according to ASTM G-99 using a pin on a disc apparatus under an applied load of 50 N for a sliding speed of 5 m/s. The wear rate plotted against the sliding distance is shown in **Figure 3**.

The Al-Si10Mg alloy experiences the maximum wear rate. The wear mechanism was studied using a SEM micrograph of the worn surface of the Al-Si10Mg alloy (**Figure 4a**), revealing severe delamination that is an indication of an adhesive wear. Al-Si10Mg/2MoS<sub>2</sub> and Al-Si10Mg/4MoS<sub>2</sub> show an enormous decrease in the wear rate by 55 % and 65 %, respectively, compared with the Al-Si10Mg alloy. The decrease in the wear is due to the presence of the MoS<sub>2</sub> layer, which forms a film on the wear surface. This is evident in the SEM micrograph of Al-Si10Mg/2MoS<sub>2</sub> (**Figure 4b**) where the MoS<sub>2</sub> particles form a film in certain regions, partially reducing the ploughing and delamination.

## 4 CONCLUSION

In this research work, Al-Si10Mg/MoS<sub>2</sub> composites were fabricated using the stir-casting technique and the mechanical and tribological characteristics were studied. The following important observations can be noted:

1. UTS, elongation percentage and hardness decrease with an addition of MoS<sub>2</sub> particles to Al-Si10Mg. However, the densities of the composites are higher than the density of the Al-Si10Mg alloy.
2. A uniform distribution of MoS<sub>2</sub> is observed on the optical micrographs.
3. The improved wear resistance of Al-Si10Mg/MoS<sub>2</sub> composites is better than the wear resistance of the Al-Si10Mg alloy.

## 5 REFERENCES

- <sup>1</sup> P. Rohatgi, Cast Metal Matrix Composites: Past, Present and Future, Transactions of the American Foundry Society, 109 (2001), 1–25
- <sup>2</sup> M. M. Haque, A. Sharif, Study on wear properties of aluminium-silicon piston alloy, Journal of Materials Processing Technology, 118 (2001), 69

- <sup>3</sup> A. T. Alpas, J. Zhang, Effect of SiC particulate reinforcement on the dry sliding wear of aluminium-silicon alloys (A356), *Wear*, 155 (1992), 83
- <sup>4</sup> P. W. Ruch, O. Beffort, S. Kleiner, L. Weber, P. J. Uggowitzer, Selective interfacial bonding in Al(Si)-diamond composites and its effect on thermal conductivity, *Composites Science and Technology*, 66 (2006), 2677–2685
- <sup>5</sup> M. K. Surappa, P. K. Rohatgi, Preparation and properties of cast aluminium-ceramic particle composites, *Journal of Materials Science*, 16 (1981), 983–993
- <sup>6</sup> B. N. P. Bai, E. S. Dwarakadasa, S. K. Biswas, Scanning electron microscopy studies of wear in LM13 and LM13-graphite particulate composite, *Wear*, 76 (1982), 211
- <sup>7</sup> B. Šuštaršič, L. Kosec, M. Kosec, B. Podgornik, S. Dolinšek, The influence of MoS<sub>2</sub> additions on the densification of water-atomized HSS powders, *Journal of Materials Processing Technology*, 173 (2006) 3, 291–300
- <sup>8</sup> M. K. Surappa, Aluminium matrix composites: Challenges and opportunities, *Sadhana*, 28 (2003), 319–334
- <sup>9</sup> P. L. Menezes, P. K. Rohatgi, M. R. Lovell, Self-Lubricating Behavior of Graphite Reinforced Metal Matrix Composites, in: M. Nosonovsky, B. Bhushan (Eds.), *Green Tribology*, Springer, Berlin Heidelberg 2012, 445–480
- <sup>10</sup> A. J. Haltner, C. S. Oliver, Frictional Properties of Some Solid Lubricant Films under High Load, *J. Chem. Eng. Data*, 6 (1961), 128–130
- <sup>11</sup> H. Kato, M. Takama, Y. Iwai, K. Washida, Y. Sasaki, Wear and mechanical properties of sintered copper-tin composites containing graphite or molybdenum disulfide, *Wear*, 255 (2003), 573–578
- <sup>12</sup> Y. Sahin, Preparation and some properties of SiC particle reinforced aluminium alloy composites, *Materials & Design*, 24 (2003), 671
- <sup>13</sup> M. Kok, Production and mechanical properties of Al<sub>2</sub>O<sub>3</sub> particle-reinforced 2024 aluminium alloy composites, *Journal of Materials Processing Technology*, 161 (2005), 381–387
- <sup>14</sup> L. Ceschini, G. Minak, A. Morri, Tensile and fatigue properties of the AA6061/20 vol. % Al<sub>2</sub>O<sub>3</sub>p and AA7005/10 vol. % Al<sub>2</sub>O<sub>3</sub>p composites, *Composites Science and Technology*, 66 (2006), 333–342
- <sup>15</sup> Ü. Cöcen, K. Önel, Ductility and strength of extruded SiCp/aluminium-alloy composites, *Composites Science and Technology*, 62 (2002), 275–282
- <sup>16</sup> A. N. Abdel-Azim, Y. Shash, S. F. Mostafa, A. Younan, Casting of 2024-Al alloy reinforced with Al<sub>2</sub>O<sub>3</sub> particles, *Journal of Materials Processing Technology*, 55 (1995), 199–205
- <sup>17</sup> C. B. Lin, R. J. Chang, W. P. Weng, A study on process and tribological behavior of Al alloy/Gr (p) composite, *Wear*, 217 (1998), 167–174
- <sup>18</sup> T. J. A. Doel, P. Bowen, Tensile properties of particulate-reinforced metal matrix composites, *Composites Part A: Applied Science and Manufacturing*, 27 (1996), 655–665
- <sup>19</sup> J. N. Hall, J. Wayne Jones, A. K. Sachdev, Particle size, volume fraction and matrix strength effects on fatigue behavior and particle fracture in 2124 aluminum-SiCp composites, *Materials Science and Engineering A*, 183 (1994), 69–80





## COMPUTER-AIDED MODELING OF THE RUBBER-PAD FORMING PROCESS

### RAČUNALNIŠKO MODELIRANJE PREOBLIKOVALNEGA PROCESA Z VMESNIKOM IZ GUME

**Muamar Benisa, Bojan Babic, Aleksandar Grbovic, Zoran Stefanovic**

University of Belgrade, Faculty of Mechanical Engineering, Kraljice Marije 16, 11120 Belgrade, Serbia  
bbabic@mas.bg.ac.rs

*Prejem rokopisa – received: 2012-03-22; sprejem za objavo – accepted for publication: 2012-06-01*

The conventional way to develop press-formed metallic components requires a burdensome trial-and-error process for setting-up the technology, whose success depends largely on the operator's skill and experience. The finite element (FE) simulations of a sheet-metal-forming process help a manufacturing engineer to design a forming process by shifting the costly press-shop try-outs to the computer-aided design environment. Numerical simulations of a manufacturing process, such as rubber-pad forming, have been introduced in order to avoid the trial-and-error procedure and shorten the development phases when tight times-to-market are demanded. The main aim of the investigation presented in this paper was to develop a numerical model that would be able to successfully simulate a rubber-pad forming process. The finite-element method was used for blank- and rubber-behavior predictions during the process. The study was concerned with a simulation and investigation of significant parameters (such as forming force and stress, and strain distribution in a blank) associated with the rubber-pad forming process and the capabilities of this process regarding the manufacturing of aircraft wing ribs. The simulation and investigation carried out identified the stress and strain distribution in a blank as well as the forming force. Experimental analyses of a rib with a lightening hole showed a good correlation between FE simulations and experimental results.

**Keywords:** rubber-pad forming, sheet-metal bending, finite-element simulation, aircraft manufacturing

Običajna pot pri razvoju stiskanih kovinskih komponent zahteva za postavitev tehnologije zamuden postopek z analiziranjem napak pri preizkusih, pri čemer je uspešnost odvisna od izvajalčeve spretnosti in izkušenj. Simulacija postopka preoblikovanja pločevine s stiskanjem po metodi končnih elementov (FEM) pomaga inženirjem pri postavljanju preoblikovalnega postopka z nadomeščanjem dragih preizkusov v računalniškem okolju. Da bi se izognili postopkom preizkušanja z analizo napak in ko je odločujoč kratek rok za trženje, so bile vpeljane numerične simulacije preoblikovalnega procesa, kot je preoblikovanje z vmesnikom iz gume. Glavni namen predstavljene preiskave je bil razvoj numeričnega modela, ki bi bil sposoben uspešne simulacije preoblikovalnega procesa z vmesnikom iz gume. Za napovedovanje dogajanj v stiskancu in v vmesniku iz gume je bila uporabljena metoda končnih elementov. Študija je obsegala simulacije in preiskave pomembnih parametrov (kot so preoblikovalna sila, napetosti ter razporeditev deformacije v preoblikovancu), povezanih s preoblikovanjem z vmesnikom iz gume in z zmogljivostmi tega procesa pri izdelavi reber letalskega krila. Izvršena simulacija in preiskava je odkrila napetosti in razporeditev deformacije v preoblikovancu, kot tudi sile pri preoblikovanju. Analiza reber z luknjo za zmanjšanje mase je pokazala dobro ujemanje med FE-simulacijo in eksperimentalnimi rezultati.

**Ključne besede:** preoblikovanje z vmesnikom iz gume, krivljenje pločevine, simulacija končnih elementov, izdelovanje letal

## 1 INTRODUCTION

Stamping is a metal-forming process, with which the sheet metal is punched using a press tool that is mounted on a machine or a stamping press forming the sheet into the desired shape. The conventional stamping process is performed through a punch, which, together with a blank holder, forces the sheet metal to slide into a die and comply with the shape of the die itself. Computers allow us to obtain and process data to improve and accelerate an analysis of the information required to optimize the processes of metal forming and to minimize the production costs.<sup>1</sup>

Rubber-pad forming is a metalworking process where sheet metal is pressed between a die and a rubber block. In general, an elastic upper die, usually made of rubber, is connected to a hydraulic press. A rigid lower die, often called a form block, provides the mold for the sheet metal to be formed. Because the upper (male) die can be used with different lower (female) dies, the process is relatively cheap and flexible. However, rubber pads exert

less pressure in the same circumstances than the non-elastic parts, which may lead to a lower accuracy of the forming process. The form-block height is usually less than 100 mm.<sup>2</sup>

In the rubber-pad forming process an aluminum blank is placed between a die and a rubber pad (flexible punch), which is held in a container to enclose the flexible punch (**Figure 1a**). At this stage, the flexible punch (rubber-pad) is fixed on the arm of a pressing machine and the punch is on a machine table. As the rubber-pad moves down the rubber deforms elastically and offers a counter pressure. Due to this pressure the rubber-pad and the blank flow into the cavity of the die. This process can be divided into three steps: the first, self-forming of the rubber, the second, when the blank moves to the bottom of the die and produces the outer bending, and the third when the rubber pad pushes the blank into the cavity of the die.

In the aircraft industry most of the sheet parts, such as ribs, frames, doors and windows, are fabricated using

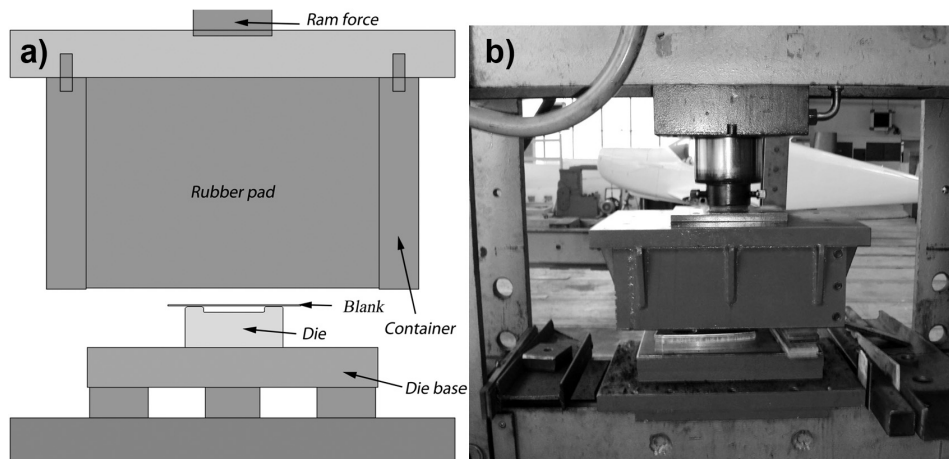


**Figure 1:** a) Schematic representation of a rubber-pad forming process, b) Experimental tool set-up

**Slika 1:** a) Shematski prikaz preoblikovalnega procesa z vmesnikom iz gume, b) eksperimentalno orodje

the rubber-pad forming processes (flexible tools). The advantages of using the rubber-pad forming process instead of the conventional metallic tools are: (i) the same flexible pad can be used to form several different work-piece shapes, because a rubber pad has the ability to return to its original shape; (ii) the tool costs are lower than the costs for the conventional forming processes; (iii) the thinning of the work metal, which occurs during the conventional deep drawing, is reduced considerably; (iv) the set-up time can be reduced considerably in this process, because no die clearance or alignment checks need to be made; (v) lubrication is not necessary and good surface finish can be achieved, because no tool marks are created. However, the rubber-pad forming processes have several disadvantages, such as: (i) the lifetime of a flexible pad is limited (this depends on the severity of forming combined with the pressure level); (ii) a lack of a sufficient forming pressure results in the parts with a lower sharpness or with wrinkles, which requires the reworking of the parts to their correct shape and dimensions; (iii) a low production rate, so that they are suitable mostly for small series (typical of the aircraft industry).<sup>2-5</sup>

Several studies have been carried out to analyze the rubber-pad forming. Browne and Battikha<sup>6</sup> presented an experimental study of the rubber-pad forming process to investigate the capability of the process and optimize the process parameters. Sala<sup>3</sup> optimized the rubber-pad forming of an aluminum-alloy fuselage frame belonging to an AerMacchi MB-339 trainer aircraft using his own finite-element code. Several effects have been investigated depending on stamping velocity, geometry, heat treatment of the sheet metal and rubber-pad parameters. Dirikolu and Akdemir<sup>7</sup> investigated the influence of rubber hardness and blank-material type on stress distribution using a 3D finite-element-simulation study of a flexible forming process. The investigation showed that the variation of pad thickness does not cause a big change in the forming stress in a blank. Madoliat and

Narimani<sup>8</sup> presented sheet forming by using a rubber pad and also investigated, experimentally and numerically, the design for the tooling set. Thiruvardhelvan,<sup>9</sup> presented in this overview, highlighted the role of urethanes that are considered to be the best materials for flexible tools because of their good oil and solvent resistance, good wear resistance, high thermal stability and load-bearing capacity. Ramezani and Ahmed<sup>5</sup> carried out a numerical simulation of a rubber-pad forming process, along with an experimental validation, using a die of a flexible punch. They studied some forming parameters such as rubber type, stamping velocity, etc., and found that silicone rubber has a shorter lifetime than polyurethane and natural rubber. As a result, it cannot be used to form blanks with sharp edges. No significant change in the blank thinning was discovered for 5 different stamping velocities. Lee et al.<sup>10</sup> have investigated the deformation characteristic using the rubber-pad bending of a structural aluminum tube. A 3D finite-element analysis was used to examine the effect of process parameters on deformation characteristics of an extruded aluminum tube, and the influence of the formable radius of a tube curvature on bending resistance. The relation between the bent profile of a material and the roller stroke was defined. Fabrizio and Loredana<sup>11</sup> studied flexible forming of thin sheets from aluminum alloys using different geometries and materials for the flexible die. They have investigated the forming force during a forming process for different dies.

These investigations showed that a numerical model can help us better understand the forming procedure, and the correlations with experimental results were good. M.W. Fu and H. Li<sup>12</sup> have presented 3D-FE simulations and investigated the deformation behavior of the flexible-die-forming process. The comparison between the conventional deep drawing and a viscoplastic carrying medium based on flexible-die forming was conducted in terms of wall-thickness reduction, hydro-

static pressure, principle-stress distribution and damage factor. The concave and convex rubber-pad forming processes were investigated by Liu, et al.,<sup>13</sup> using FE simulations and experimental methods. The investigations of the forming load, thickness variation of the formed plate and variations in the channel-width-to-rib-width ratio were also performed. A fabrication of a metallic bipolar plate for a proton membrane in fuel cells is presented in<sup>14</sup>. The FE analyses were used to describe the rubber-pad forming process and to investigate the main parameters (such as rubber hardness and dimensions of the rigid die). It was found that the smaller the internal radius, the harder it is to fill the cavity of a rigid die. The authors examined whether the blank filled the cavity of the rigid die by using a 3D-laser-scanning measurement system.

In this paper, numerical simulations of rubber-pad forming processes are used to analyze the blank and the rubber behaviors during a production of supporting ribs, as well as to analyze different punch geometries. A non-linear FE analysis was conducted to predict stress and strain distributions, and forming forces during the rubber-pad forming process. The main goal was to develop a computer model that would be able to simulate the process and, therefore, to develop the right design for a tooling set.

## 2 FINITE-ELEMENT MODELING AND EXPERIMENTAL VERIFICATION

Numerical simulations of the rubber-pad forming processes are complicated mainly because of a large deformation of a rubber pad. As a consequence, a mesh distortion may occur in a simulation, which can lead to inaccurate and incomplete results. This is why FE analyses must be carried out carefully and with an understanding of the physical phenomena of the rubber-pad forming process.

The commercial finite-element software Ansys® was used to make an FE simulation in this study. In order to reduce the processing time and improve the precision of the calculations, 2D FE models were created for three different sheet-metal elements (straight rib, stringer and rib with a lightening hole) and analyses were carried out for each model. **Figure 2** illustrates these three geometrical models. The models in FE analyses included three elements only: a rigid die, a blank and a rubber pad (flexible punch). In order to simplify the numerical model, the container of the rubber pad was not modeled. To eliminate the influence of the container, the frictionless support constraints were applied on the opposite sides of the rubber, while a displacement constraint was applied on the upper edge of the 2D rubber model (**Figure 3**).

The die was modeled as a rigid body because the stress and strain of the die were not analyzed and the die material (steel) is much less deformable than the material

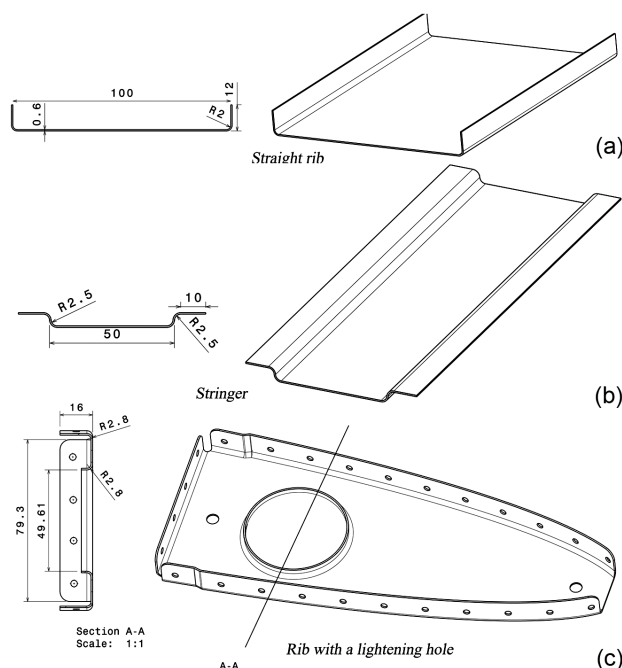


**Figure 2:** Geometrical models used in the investigation: a) straight rib, b) stringer and c) rib with a lightening hole

**Slika 2:** Geometrijski modeli, uporabljeni pri preizkušanju: a) ravno rebro, b) rebrasto rebro in c) rebro z luknjo za zmanjšanje mase

of the blank (aluminum). So, the material properties attached to the die were not important, and the mesh was not generated either. This eliminated unnecessary calculations causing a decrease in both the run time and the errors in the numerical solution.

Because the blank undergoes a large plastic-strain deformation during the forming process, the stress-strain test data up to a failure was required to define the blank material in the simulation (**Figure 4**). The blank was considered as a multilinear isotropic hardening material. In the FE simulations of the blank behavior, the von Mises yield criterion coupled with an isotropic work-hardening assumption<sup>15</sup> was used.

The rubber pad undergoes a nonlinear hyper-elastic deformation. The behavior of the nonlinear hyper-elastic and incompressible rubber-like material is usually described with the Mooney-Rivlin model that uses a strain-energy function  $W$ . The derivative of  $W$ , with

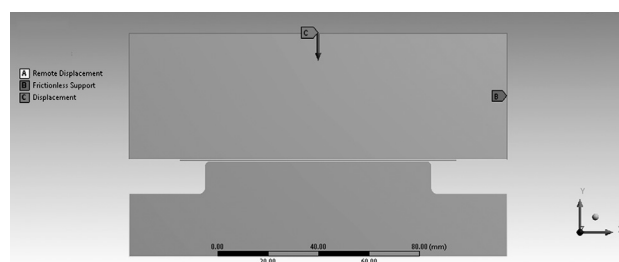


**Figure 3:** Constraints used in the FE simulation

**Slika 3:** Omejitve, uporabljene pri FE-simulaciji



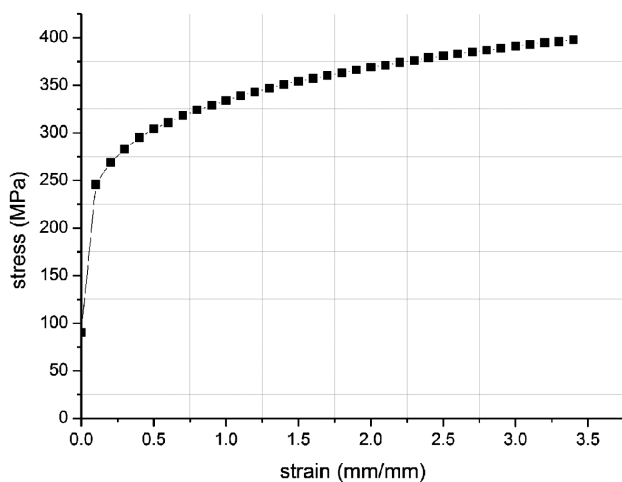


**Figure 4:** Experimental tensile-stress-strain curve for the aluminum blank sheet

**Slika 4:** Eksperimentalna krivulja napetost – raztezek za aluminijevo pločevino

respect to the strain component, determines the corresponding stress component:

$$\sigma_{ij} = \frac{\partial W}{\partial \epsilon_{ij}} \quad (1)$$

$$W = \sum_{k+m+1}^n C_{km} (I_1 - 3)^k + (I_2 - 3)^m + \frac{1}{2} k (I_3 - 1)^2 \quad (2)$$

where  $I_1$ ,  $I_2$  and  $I_3$  ( $I_3 = 1$ ) are the strain invariants,  $k$  is the bulk modulus and  $C_{km}$  is the constant of the Mooney-Rivlin material model for the incompressible material. Usually, two Mooney-Rivlin parameters,  $C_{10}$  and  $C_{01}$ , are used to describe the hyper-elastic rubber deformation.<sup>7</sup> In the FE models, the polyurethane rubber with the Shore A hardness of 70 (HD70) was used for the rubber pad. The values of  $C_{10}$  and  $C_{01}$  were 0.736 MPa and 0.184 MPa, respectively.<sup>5,7,13,14</sup>

An aluminum plate with a thickness of 0.6 mm was used as the blank. The aluminum properties were determined via the stress-strain curve obtained from the tensile tests,<sup>7,16</sup> as shown in **Figure 5**. For this alloy, the elastic module ( $E$ ) is 71 GPa and the Poisson's ratio ( $\nu$ ) is 0.334.

During the rubber-pad forming process, the materials exhibit large deformations and rotations. There is a friction contact at the blank interfaces, too. At the same time, geometric nonlinearities arise from a nonlinear strain-displacement relationship, as well as the nonlinearities associated with the material properties. According to that, the geometric nonlinearity option was activated in the nonlinear solution procedure.

The friction behavior between the two different pairs of contact (rubber pad–blank and blank–die) was assumed to follow the Coulomb's model.<sup>5,7</sup> The friction coefficients for the former and latter contact pairs were considered to be 0.2 and 0.1, respectively.<sup>5,7,13</sup> **Table 1** shows the specifications of the contact region.

The interface contacts of the blank–rubber pad, blank–die and die–rubber were modeled as deformable and the software used solves these tasks on the basis of the contact-target-surface approach with an adjustable impenetrability constraint that assures contact compatibility. The CONTA 175 (a node-to-surface contact) finite element was used on the blank's surfaces at the interface between the blank and the die and on the rubber surface at the interface between the rubber and the die. The CONTA171 (a surface-to-surface contact) was used on the surface of the rubber pad at the interface between the blank and the rubber pad. The other surfaces at each interface were modeled with the TARGE169 element. It can be summarized that, in all the interface contacts, the upper surfaces of the die and the blank were considered as a target, while the lower surface of the blank and the upper surface of the rubber pad were considered as a contact.<sup>17</sup>

As mentioned above, the container was not modeled, so – in order to fix the rubber pad correctly – frictionless supports had to be applied on the side edges of the rubber. A remote displacement was applied on the lower edge of the die. A displacement was applied on the top edge of the rubber in order to simulate a forming load on the blank (**Figure 3**). All deformable materials were modeled with a Plane-183 finite element (a 2-D element with 8 or 6 nodes). Plane 183 has quadratic displacement, plasticity, hyper-elasticity, creep, stress stiffening, large deflection and large strain-simulation capabilities. The number of nodes and elements used for the blank and the rubber pad are presented in **Table 2**.

**Table 1:** Interface contacts

**Tabela 1:** Vmesni stiki

Parts in the contact	Contact type
Die & Blank	Frictional contact (0.1) node to surface
Blank & Rubber	Frictional contact (0.2) surface to surface
Die & Rubber	Frictional contact (0.1) node to surface

**Table 2:** Numbers of the nodes and elements for three models

**Tabela 2:** Število vozlov in elementov za tri modele

Modes	Blank		Rubber pad		Rigid die	
	Nodes	Element	Nodes	Element	Nodes	Element
Straight rib	2161	1680	4253	3958	205	204
Stringer	768	157	7254	2299	304	152
Rib with a lightening hole	863	615	5490	5181	208	207

In order to validate the FE simulations results, the rubber-pad forming experiments were carried out for the stamping of an aluminum blank. An experimental set-up (shown in **Figure 1b**) was used, together with the assembly of a die set shown in **Figure 1a**. The die and the rubber-pad container were made of steel, while polyurethane rubber with a Shore A hardness of 70 (HD70) was used as a rubber pad. A hydraulic press machine (produced by REXROTH), with the maximum



**Figure 5:** Rib with a lightening hole fabricated by the rubber-pad forming process and the die

**Slika 5:** Rebro z luknjo za zmanjšanje mase, izdelano z vmesnikom iz gume in orodje

capacity of 160 t was used in the rubber-pad forming process. The process begins with the die placed on the base of the hydraulic press machine. The aluminum blank is then introduced between the die and the flexible punch. After this the flexible punch moves down to stamp the blank. One of the formed parts fabricated during the rubber-pad forming process and the die used during the fabrication are shown in **Figure 5**.

### 3 RESULTS AND DISCUSSION

In this study, as mentioned above, the forming force was presented as a displacement applied on the upper

edge of the rubber pad. **Figure 6** illustrates the step-by-step forming process using the rubber pad. It is clear that the process can be divided into three stages (or steps). The first stage is a self-deformation of the flexible die (the rubber pad); the second stage includes a blank deformation (under the pressure of the rubber pad when it reaches the bottom of the rigid die); and, finally, during the third stage the blank fills the die cavities until they are completely filled.

The convergences of the forming forces for each model, obtained through the FE simulations, are shown in **Figure 7**. This figure shows that the highest value of a forming force is present in the rib with a lightening hole (6735 N), while the lowest value is achieved in the straight rib (867 N). It can be seen that the magnitude of a forming force increases as the geometry of a rib becomes more complex, i.e., as more bending regions have to be obtained (**Table 3**).

The FE simulation of the forming process for the stringer and the rib with a lightening hole goes through three stages/steps (corresponding to the forming process), while the straight-rib forming can be performed in the first two steps (because there is no cavity to fill). During the first step – the self-forming of the rubber – the rubber deforms elastically and offers a counter pressure, so the forming load is very small (**Figure 6**). The time needed for this step is short (between 0.2 s and 0.35 s in the simulation – **Figure 7**). After 0.2 second (the straight rib) and 0.35 second (the other models), the second step starts and the forming load increases slightly to produce the outer bending (**Figure 5**). During the last step, after approximately 0.65 second, the blank starts to fill the cavity of the rigid die and the forming force increases sharply (**Figures 6 and 7**). According to the results of the FE simulations, it is obvious that the highest value of the forming force will be obtained in the

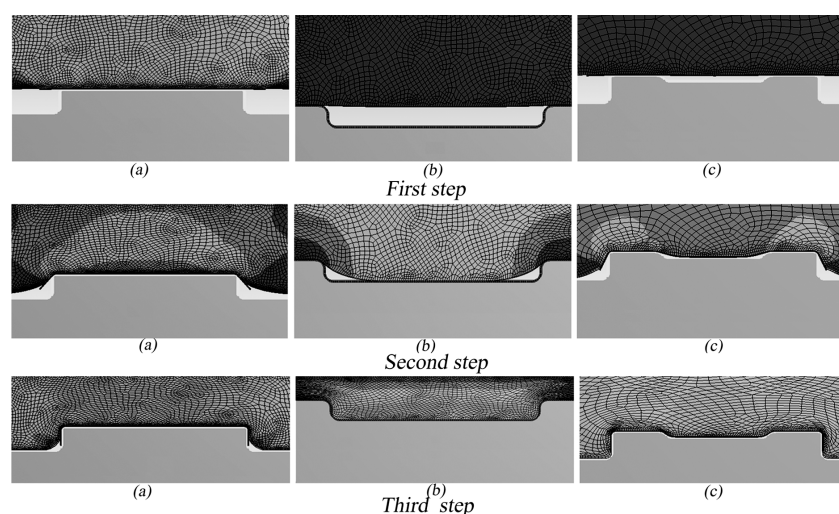


**Figure 6:** Forming steps during the rubber-pad forming including the first, the second and the third steps: a) straight rib, b) stringer and c) rib with a lightening hole

**Slika 6:** Stopnje med preoblikovanjem z gumijastim vmesnikom, vključno s prvo, drugo in tretjo stopnjo: a) ravno rebro, b) rebrasto rebro, c) rebro z luknjo za zmanjšanje mase

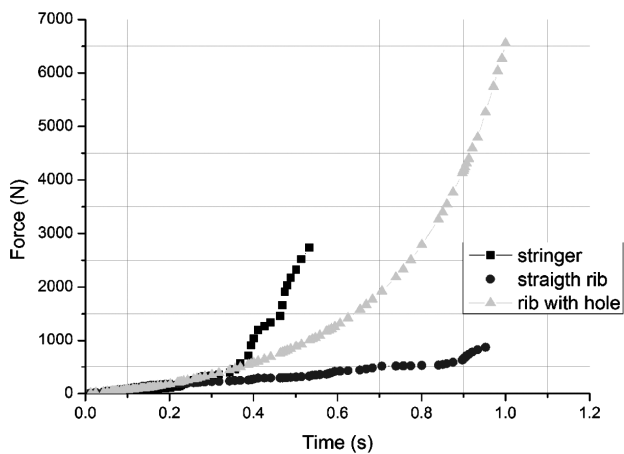


Figure 7: Forming force in three models

Slika 7: Preoblikovalna sila pri treh modelih

case of the most complex sheet-metal geometry (the rib with a lightening hole), where several bends with different radii must be produced. This is in correlation with the empirical data<sup>3,7,13,14</sup>, which means that the used FE models have been well defined.

Along with the calculation of the forming force, stress and strain analyses were performed. As was expected, the stress and strain concentrations in a blank accumulate in the last two stages. Figure 8 shows the equivalent stresses (in MPa, left column) and plastic strains (in mm/mm, right column) in the blanks at the end of the forming processes for all FE models. The summarization of the maximum and minimum stress and

strain values, presented in Figure 8, is given in Table 3. Table 3 shows that the maximum equivalent stress and plastic strain appear in the rib with a lightening hole (241.45 MPa and 0.206 mm/mm, respectively), while the minimum values of the equivalent stress and plastic strain are in the straight rib (224.74 MPa and 0.115 mm/mm, respectively). As can be seen in Table 3, the stress and plastic strain increase with an increased complexity of the rib geometry, as well as with an increased number of bend radii. The reason for that, according to Sala<sup>3</sup>, is that the blank is exposed not only to the tensile and tangential stresses, but also to the stress arising from the bending pressure imposed by the tool. Consequently, the thinning phenomenon occurs homogeneously and, finally, the necking appears. The necking can induce a crack, which is not unusual in this forming process<sup>5</sup>. The crack starts when the blank undergoes stretching forces and when the ultimate stress is reached during the second or third stage of the forming process.

According to Sala<sup>3</sup> and Takuda<sup>15</sup>, the maximum plastic strain that can be considered for the forming of this type of aluminum alloy is approximately 0.186 mm/mm. This value of plastic strain was used as a reference for the crack-appearance predictions in the FE simulations presented in this paper. The value of the plastic strain obtained in the forming simulation of the rib with a lightening hole (0.206 mm/mm) indicated the possibility of a crack appearance in the outer radius of the lightening hole, while the plastic-strain values for the other two models were less than 0.186 mm/mm.

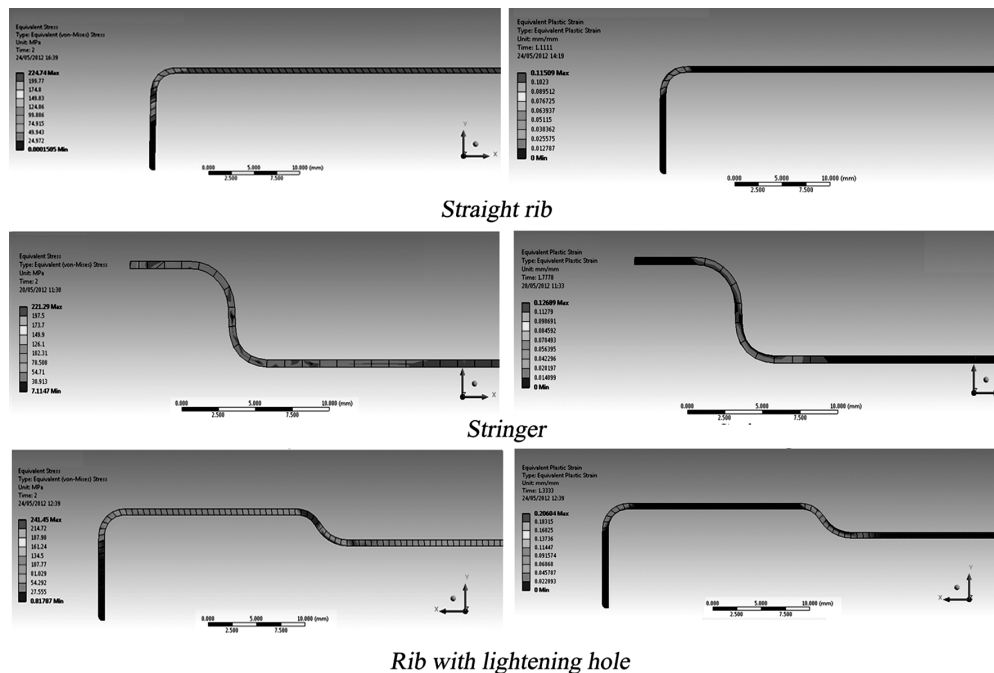


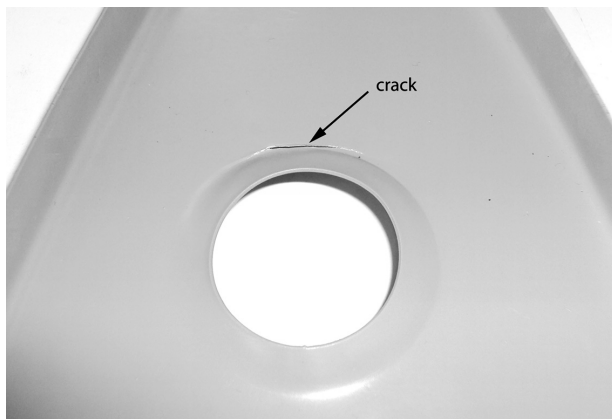
Figure 8: Equivalent stress (left column) and plastic strain (right column) in the straight rib, the stringer and the rib with a lightening hole (from the top)

Slika 8: Ekvivalentna napetost (leva kolona) in plastična deformacija (desna kolona) v ravnem rebri, rebrastem rebri in rebri z luknjo za zmanjšanje mase (od zgoraj navzdol)



**Table 3:** Summarization of the engineering requirements for the rubber-pad sheet-metal forming process**Tabela 3:** Povzetek inženirskih zahtev pri preoblikovalnem procesu z vmesnikom iz gume

MODEL	Model 1 (straight rib)	Equivalent stress (MPa)	Equivalent plastic strain (mm/mm)	Reaction force N
Model 1 Straight rib	Maximum	224.74 (occurs on the blank)	0.115 (occurs on the blank)	866.43
	Minimum	1.2e-4	0.0	
Model 2 Stringer	Maximum	221.29 (occurs on the blank)	0.1268 (occurs on the blank)	2 734.7
	Minimum	7.032	0.0	
Model 3 Rib with a lightening hole	Maximum	241.45 (occurs on the blank)	0.206 (occurs on the blank)	6 553.8
	Minimum	0.101	0.0	

**Figure 9:** Rib with a crack around the lightening hole**Slika 9:** Rebro z razpoko okrog luknje za zmanjšanje mase

The experiments with the rubber pad showed that the FE predictions were good. **Figure 9** shows the crack that appeared in the region around the rib hole during the third stage of the forming process, as predicted by the FE simulation. This was the proof of the quality of the developed finite-element model, as well as of the criterion proposed for this alloy (with the maximum plastic strain not exceeding 0.186 mm/mm). On the basis of these findings, more FE models of a rib with a lightening hole (with different values of the fillet radii) were developed and analyzed in order to find the connections between the values of a fillet radius and a plastic strain. These simulations showed that the values of stress and strain strongly depended on the rib geometry (i.e., the values of the fillet radii), but more investigations need to be performed in order to clearly define these dependencies.

#### 4 CONCLUSION

A finite-element simulation of the rubber-pad forming process could be a very useful tool for understanding and improving the forming operations because it provides important data for determining the forming parameters and the operation time. The developed FE models and the method proposed in this

paper have proved to be sufficiently effective in predicting the final shape of the component and the regions of a possible crack appearance.

The FE simulations showed that the maximum stresses and strains in all the cases were at the flanges and the corners. The minimum stress and plastic strain were achieved in the straight rib (the rib with the simplest geometry), while the maximum stress and plastic strain were found in the rib with a lightening hole (the most complex geometry). These results have been validated with the experiments, as well as with the fracture criterion used for the crack predictions. The FE simulations proved that simpler tools would reduce the lead times and enable a rapid production of small parts without a possibility of a crack appearance during the forming. On the other hand, the geometry of more complicated, but necessary, tools must be defined very carefully, with a determination of the fillet radii that will minimize the chance of a fracture. FEM can help us with this determination, too, while additional potential applications – such as 3D model simulations and tool optimization – are also possible.

However, it must be noticed that the optimization procedure of the press-forming processes – owing to the presence of the hardly reproducible phenomena like friction and lubrication – should never be limited to simple numerical simulations because the above phenomena can contribute a lot towards saving the costs and reducing the time-to-market, currently held up by empirical trial-and-error processes.

Sheet-metal-forming-simulation results, today, are reliable and accurate enough so that even the try-out tools and the time-consuming try-out processes may be eliminated, or at least reduced significantly.

#### 5 REFERENCES

- <sup>1</sup> A. Shramko, I. Mamuzic, V. Danchenko, The application of the program QFORM 2D in the stamping of wheels for railway vehicles, *Mater. Tehnol.*, 43 (2009) 4, 207–211
- <sup>2</sup> ASM Handbook Vol. 14B Metal Working: Sheet Forming, 2006
- <sup>3</sup> G. Sala, A numerical and experimental approach to optimize sheet stamping technologies: part II – aluminium alloys rubber-forming, *Material and Design*, 22 (2001) 4, 299–315

- <sup>4</sup> E. L. Deladi, Static friction rubber metal contact with application to rubber pad forming process, PhD Thesis, University of Twente, 2006
- <sup>5</sup> M. Ramezani, Z. M. Ripin, R. Ahmad, Sheet metal forming with the aid flexible punch, numerical approach and experimental validation, CIRP Journal of Manufacturing Science and Technology, 3 (2010) 3, 196–203
- <sup>6</sup> D. J. Browne, E. Battikha, Optimization of aluminium sheet forming using a flexible die, Journal of Materials Processing Technology, 55 (1995) 3/4, 218–223
- <sup>7</sup> M. H. Dirikolu, E. Akdemir, Computer aided modelling of flexible forming process, Journal of Materials Processing Technology, 148 (2004) 3, 376–381
- <sup>8</sup> R. Madoliat, R. Narimani, H. Rahrovan, Investigation of sheet metal forming using rubber pad forming, The SMEIR 2005 International Conference in Manufacturing Engineering, 2005, 1–9
- <sup>9</sup> S. Thiruvarduchelvan, The potential role of flexible tools in metal forming, Journal of Materials Processing Technology, 122 (2002) 2/3, 293–300
- <sup>10</sup> J. W. Lee, H. C. Kwon, M. H. Rhee, Y. T. Im, Determination of forming limit of a structural aluminum tube in rubber pad bending, Journal of Materials Processing Technology, 140 (2003) 1–3, 487–493
- <sup>11</sup> F. Quadrini, L. Santo, E. A. Squeo, Flexible forming of thin aluminum alloy sheets, International Journal of Modern Manufacturing Technologies, 2 (2010) 1, 79–84
- <sup>12</sup> M. W. Fu, H. Li, J. Lu, S. Q. Lu, Numerical study on the deformation behaviors of the flexible die forming by using viscoplastic pressure-carrying medium, Computational Materials Science, 46 (2009) 4, 1058–1068
- <sup>13</sup> Y. Liu, L. Hua, J. Lanm, X. Wei, Studies of the deformation styles of the rubber-pad forming process used for manufacturing metallic bipolar plates, Journal of Power Sources, 195 (2010) 24, 8177–8184
- <sup>14</sup> Y. Liu, L. Hua, Fabrication of metallic bipolar plate for proton exchange membrane fuel cells by rubber pad forming, Journal of Power Sources, 195 (2010) 11, 3529–3535
- <sup>15</sup> H. Takuda, N. Hatta, Numerical Analysis of formability of an Aluminum 2024 alloy sheet and Its Laminates with Steel Sheets, Metallurgical and Material Transactions A, 29 (1998) 11, 2829–2834
- <sup>16</sup> W. Eichlseder, Enhanced fatigue analysis – incorporating downstream manufacturing processes, Mater. Tehnol., 44 (2010) 4, 185–192
- <sup>17</sup> H. H. Lee, Finite Element Simulation with ANSYS Workbench12, Schroff Development Corporation, Taiwan, 2010

## EFFECT OF FLY-ASH AMOUNT AND CEMENT TYPE ON THE CORROSION PERFORMANCE OF THE STEEL EMBEDDED IN CONCRETE

### UČINEK KOLIČINE LETEČEGA PEPELA IN VRSTE CEMENTA NA KOROZIJO JEKLA V BETONU

Ahmet Raif Boğa<sup>1</sup>, İlker Bekir Topçu<sup>2</sup>, Murat Öztürk<sup>3</sup>

<sup>1</sup>Afyon Kocatepe University, Faculty of Engineering, Civil Engineering Department, Afyonkarahisar, Turkey

<sup>2</sup>Eskişehir Osmangazi University, Faculty of Engineering and Architecture, Civil Engineering Department, 26480 Eskişehir, Turkey

<sup>3</sup>Selçuk University, Faculty of Engineering and Architecture, Civil Engineering Department, Konya, Turkey  
muratozturk@selcuk.edu.tr

*Prejem rokopisa – received: 2011-10-10; sprejem za objavo – accepted for publication: 2012-03-01*

In this study the corrosion performance of the steel embedded in the concrete produced by using three different types of cement (CEM II/B-M (P-L) 32.5 R, CEM I 42.5 R and CEM I 52.5 R) was investigated. 300 kg/m<sup>3</sup> and 375 kg/m<sup>3</sup> dosages of the cement with (0, 10 and 20) % of fly-ash (FA) replacements of cement were used to produce the concretes. These concretes were cured for 28 d and 180 d. The mechanical properties of the concretes were determined and the corrosion performances of the reinforced-concrete specimens were determined using the impressed voltage test. After the impressed voltage test weight losses occurred because of the corrosion that was determined. The results of this study show that using composite cement and an FA replacement of the cement are useful in combating corrosion.

Keywords: concrete, corrosion, mechanical properties, fly ash

V tej študiji je bilo preiskovano korozijsko vedenje jekla, vgrajenega v beton, izdelan iz treh vrst cementa (CEM II/B-M (P-L) 32,5 R, CEM I 42,5 R in CEM I 52,5 R). Odmerki 300 kg/m<sup>3</sup> in 375 kg/m<sup>3</sup> cementa z (0, 10 in 20) % letečega pepela (FA) kot nadomestila za cement, so bili uporabljeni za izdelavo betona. Beton je bil preskušen po 28 d in po 180 d. Določene so bile mehanske lastnosti betona. Korozijske lastnosti armiranega betona so bile določene s pospešenim korozijskim napetostnim preizkusom. Pri pospešenem napetostnem korozijskem preizkusu se je zaradi korozije pojavilo zmanjšanje mase. Rezultati te študije kažejo, da je za zmanjšanje korozije ugodna uporaba kompozita cementa z letečim pepelom, ki nadomesti cement.

Gljučne besede: beton, korozija, mehanske lastnosti, leteči pepel

## 1 INTRODUCTION

Corrosion of the steel embedded in concrete plays a vital role in the determination of the life and durability of the concrete structures.<sup>1</sup> The durability of reinforced concrete is largely controlled by the capability of the concrete cover to protect the steel reinforcement from corrosion. Chemical protection is provided by the concrete's high alkalinity and physical protection is afforded by the concrete cover acting as a barrier to the access of aggressive species.<sup>2</sup> The corrosion of the steel in concrete is retarded by the passivating ferric-oxide film ( $\gamma$ -FeOOH) formed in the concrete medium (that is highly alkaline with a pH of around 13).<sup>1</sup> Corrosion of the reinforcing-steel bars is initiated to form an inactive thin layer that can be broken when immersed in carbonate, chloride or sulphate solutions.<sup>3</sup> Corrosion of steel produces rust products that have a volume three to eight times greater than that of the original metal. This generates stress and causes cracking and spalling of the concrete cover, which further accelerates corrosion.<sup>4</sup> Various methods have been applied to protect reinforced steel against corrosion; these methods include variation of the concrete formulation, cathodic protection, surface treatment of the rebar and addition of inhibitors and

mineral admixtures.<sup>5</sup> It is generally recognized that the incorporation of fly ash (FA) in blended cements helps to protect concrete against the chloride-induced corrosion of steel reinforcement by reducing its permeability, particularly for chloride-ion transportation, and increasing the resistivity of the concrete.<sup>6,7</sup>

In this study, the corrosion performance of the steel embedded in the concrete produced by using three different types of cement was investigated. Cements in 300 kg/m<sup>3</sup> and 375 kg/m<sup>3</sup> dosages and also (0, 10 and 20) % FA replacements of cement were used to produce the concretes. The mechanical properties of the concretes were determined. The impressed voltage test was performed on the reinforced concrete specimens. In conclusion, the best cement type, FA ratios and curing times for the corrosion performance of the steel embedded in concrete were determined.

## 2 GENERAL OBSERVATIONS ABOUT THE BUILDING STOCK IN TURKEY

According to the studies in various regions of Turkey, the average concrete compressive strength is approximately 10 MPa.<sup>8,9</sup> Several identified improper practices for fabricating an in-situ concrete caused this signifi-





**Figure 1:** Corrosion of the reinforcement in a damaged column observed after the Van earthquake of 23 October 2011 (Murat Öztürk's archive)

**Slika 1:** Korozija armature v poškodovanem stebru med potresom 23. 10. 2011 (arhiv Murat Öztürk)

cantly low concrete quality. Important factors include the ignorance of the aggregate gradation, the use of unwashed sea sand and/or river sand, and the use of the aggregate sizes that are too large. One of the most negative factors contributing to a low concrete quality is the use of the sea sand or river sand in a concrete

mixture. According to the obtained results, the significantly high chloride content in the sea-sand concrete is an indication of a high tendency for the corrosion of the reinforcement in the reinforced concrete structures. The observations of the building rubbles showed that most rebars had corroded due to the use of the river/sea sand, thereby reducing the efficiency of the longitudinal rebar area and the anchorage (**Figure 1**).

### 3 EXPERIMENTAL STUDIES

#### 3.1 Materials used

##### 3.1.1 Cement

The experimental studies used the CEM I 42.5 R Portland cement and the CEM II/ B-M (P-L) 32.5 R Portland composite cement, produced by the Eskisehir cement factory according to TS EN 197-1 : 2 000 standards. The CEM II/B-M (P-L) cement contains natural pozzolans and limestone in the ratio of 21–35 % by weight. In addition, the CEM I 52.5 R Portland cement was used. The results of the chemical and physical analyses of these cements, which were provided by the factories, are given in **Table 1**.

##### 3.1.2 FA

In the experiment, the Tunçbilek thermal power plant's FA was used. The chemical composition and the physical properties are given in **Table 1**. Because the  $\text{SiO}_2 + \text{Al}_2\text{O}_3 + \text{Fe}_2\text{O}_3$  content exceeds 70 % and the CaO value is under 10 %, the FA of Tunçbilek is of class F (low lime) according to the ASTM C 618 standard.

##### 3.1.3 Aggregates

The Osmaneli sand and the Söğüt Zemzemiye crushed-stone aggregates were used. The maximum particle size of the aggregates was 31.5 mm. According to the results of the experiment, the specific gravities of the sand and the crushed stones I and II are 2620, 2710 and 2710 and the unit weights are (1550, 1720 and 1770)  $\text{kg/m}^3$ , respectively. (35, 30 and 35) %, of the sand and the crushed stones I and II, respectively, were used in the grain mixture.

##### 3.1.4 Steel reinforcements and the NaCl solution

14-mm-diameter deformed steel reinforcement was used for the preparation of the reinforced concrete specimens to attempt the corrosion tests. According to TS 708 the minimum yield strength of this steel is 420 MPa and the minimum tensile strength is 500 MPa. In the experimental setup for the corrosion testing, an industrial type of the NaCl salt was used for obtaining the solution.

#### 3.2 Mix proportions of the concrete

Three different types of cement, CEM II/B-M(P-L) 32.5R (CII-3), CEM I 42.5R (CI-4) and CEM I 52.5R (CI-5), were used in the concrete mixtures. By using 300

**Table 1:** Chemical and physical properties of the cements and fly ash  
**Tabela 1:** Kemijske in fizikalne lastnosti cementov in letečega pepela

Chemical Composition, %	Cement Type			FA
	CEM I 52.5 R	CEM I 42.5 R	CEM II/B-M (P-L) 32.5 R	
SiO <sub>2</sub>	20.47	20.74	30.88	58.25
Al <sub>2</sub> O <sub>3</sub>	5.68	5.68	8.01	16.66
Fe <sub>2</sub> O <sub>3</sub>	3.08	4.12	3.57	12.91
CaO	62.66	63.70	47.78	1.95
MgO	1.1	1.22	1.30	5.08
Na <sub>2</sub> O	0.20	0.17	0.12	0.33
K <sub>2</sub> O	0.75	0.53	1.33	1.37
SO <sub>3</sub>	2.5	2.29	1.67	0.41
Cl	0.010	0.019	0.011	0.002
Loss of ignition	1.9	1.34	6.20	2.09
Insoluble residue	0.7	0.57	0.27	–
Free lime	1.0	1.29	1.31	0.16
Physical Properties				
Specific gravity	3.17	3.14	2.85	2.34
Specific surface, cm <sup>2</sup> /g	3700	3450	3580	
Compressive Strength, MPa				
2 days	27	26	13	–
7 days	41	38	27	–
28 days	59	59	43	–

**Table 2:** Mix proportions of the concrete for 1 m<sup>3</sup>**Tabela 2:** Delež sestavin v 1 m<sup>3</sup> betona

Cement Type	Dosage	FA %	Cement	Sand	Crushed Stone I	Crushed Stone II	Water	FA
CII-3	375	0	375	611	541	632	188	–
		10	337.5	608	539	629	188	37.5
		20	300	605	537	626	188	75
	300	0	300	669	593	692	150	–
		10	270	667	591	690	150	30
		20	240	665	590	688	150	60
CI-4	375	0	375	622	553	645	188	–
		10	337.5	618	550	642	188	37.5
		20	300	614	547	638	188	75
	300	0	300	678	603	704	150	–
		10	270	675	601	701	150	30
		20	240	672	598	698	150	60
CI-5	375	0	375	623	554	646	188	–
		10	337.5	619	551	643	188	37.5
		20	300	615	548	639	188	75
	300	0	300	679	604	705	150	–
		10	270	676	602	702	150	30
		20	240	673	599	699	150	60

\*Superplasticiser (SP) was used as 0.4 % by mass of binder (cement and FA)

kg/m<sup>3</sup> and 375 kg/m<sup>3</sup> dosages of each cement, the concrete specimens were also produced as reference specimens containing 10 % and 20 % of FA. These specimens were cured for two different periods: 28 d and 180 d. Thus, 36 series of the concrete mixture were produced. The mix proportions of the concrete are given in **Table 2**.

### 3.3 Specimen preparation and testing

#### 3.3.1 Compressive test

The compressive strength test was carried out on the specimens with the cube dimensions of 150 mm × 150 mm × 150 mm. The specimens were demoulded after 24

h and immersed in water at (20 ± 2) °C. The compressive strength tests were made after 28 d and 180 d of curing.

#### 3.3.2 Splitting tensile test

The splitting tensile test was carried out for the cylinder specimens with the dimensions of  $\phi 150$  mm × 300 mm. The specimens were demoulded after 24 hours and immersed in water at (20 ± 2) °C. The splitting tensile tests were carried out after 28 d of curing.

#### 3.3.3 Tests for the ultrasonic pulse velocity and the modulus of dynamic elasticity

The tests of measuring the ultrasonic pulse velocity and the modulus of dynamic elasticity were carried out for the specimens that were prepared for the splitting tensile tests.

#### 3.3.4 Impressed voltage test

The setup for this test included a DC power source, a test specimen and a plastic dish containing a 4 %-NaCl solution, two steel plates and a data logger. The impressed-voltage test setup is shown in **Figure 2**. The reinforced concrete specimens for the accelerated-corrosion tests were the cylinder specimens with the dimensions of  $\phi 150$  mm × 300 mm, in which a 14-mm-diameter steel reinforcement was centrally embedded. A 250-mm part of the steel reinforcement was embedded into each concrete cylinder. The specimens were demoulded after 24 h and immersed in water at (20 ± 2) °C. The impressed voltage tests were carried out after 28 d and 180 d of curing. The steel reinforcement (the working electrode) of the reinforced concrete specimen was connected to the positive terminal and the steel plates (the counter electrodes) were connected to the negative terminal of the DC power source applying 30 V of fixed stress to the system. A similar impressed-voltage test setup has been reported by other researchers.<sup>7,10</sup> Every five minutes the corrosion current of every reservoir was saved using a data logger and the corrosion current-time figures were drawn using the impressed voltage test system.



**Figure 2:** Setup for the impressed voltage test  
**Slika 2:** Skica pospešenega napetostnega preizkusa

### 3.3.5 Weight loss method

The method proposed in the ASTM G1-03 standard was used for the determination of the weight loss of a steel bar.<sup>11</sup> After the impressed voltage tests, steel bars were demounted from the reinforced concrete specimens and the weight losses were found by cleaning these steel bars with a Clarke solution, which contained 1000 mL HCL, 24 g  $\text{Sb}_2\text{O}_3$  and 71.3 g  $\text{SnCl}_2 \cdot 2\text{H}_2\text{O}$ .

## 4 RESULTS AND DISCUSSION

### 4.1 Compressive strength

Changes in the compressive strengths due to the amount of FA are shown in **Figures 3 and 4**. According to the figures for the 28 d and 180 d compressive strengths, the strength results of the concrete produced with the CI-5 cement are higher than those of the others. With the increase in the FA amount in the specimens, the compressive strengths of the specimens cured for 28 d decreased because the mineral admixtures like FA cannot

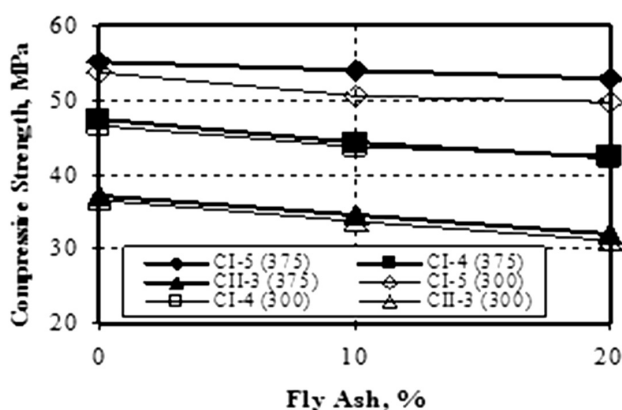


**Figure 3:** Relationship between the compressive strength and the FA amount in 28-day specimens

**Slika 3:** Odvisnost med tlačno trdnostjo in deležem letečega pepela (FA) v vzorcu po 28 dneh

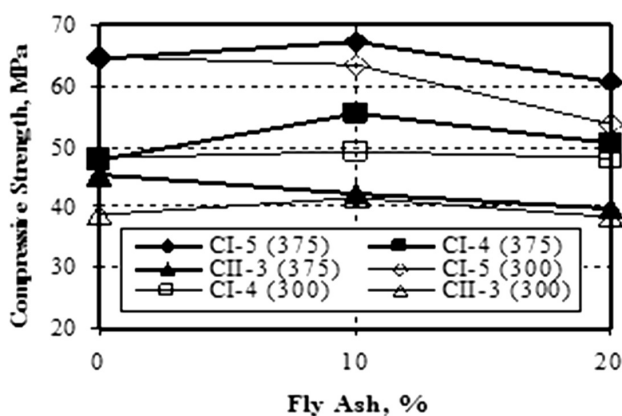


**Figure 4:** Relationship between the compressive strength and the FA amount in 180-day specimens

**Slika 4:** Odvisnost med tlačno trdnostjo in deležem letečega pepela (FA) v vzorcu po 180 dneh

fully complete the pozzolanic reactions.<sup>12</sup> If **Figure 4** is examined, it can be seen that the strength values increase as the dosage increases. Looking at **Figure 4**, by using 10 % of FA instead of the CI-5 and CI-4 cements in the 375 dosed specimens, the compressive strength of the specimens increases respectively by 4.5 % and 15.66 % according to the control specimens and it decreases at the ratio of 6.42 % in the specimens produced with CII-3. If 20 % of FA is used in the specimens, the compressive strength decreases at the ratio of 6.06 % and 12.17 % for the specimen series produced with the CI-5 and CII-3 cements, but increases at the ratio of 5.43 % for the specimen series produced with the CI-4 cement. If **Figures 3 and 4** are compared to each other, it is seen that the compressive strength increases as the curing time increases.

### 4.2 Splitting tensile strength

According to a general assessment from **Figure 5**, the splitting tensile strengths of the specimens produced with the CI-4 and CI-5 cements are very similar to each other. The minimum strengths are found with the specimens produced with the CII-3 cement. As the amount of FA increases in the specimens produced with CII-3, the splitting tensile strength decreases but it increases in the specimens produced with the other cements. According to **Figure 5**, the splitting tensile strength is seen to increase as the dosage of the cement is increased.

### 4.3 Tests for the ultrasonic pulse velocity and modulus of dynamic elasticity

The ultrasonic pulse velocity and modulus of dynamic elasticity test results are shown in **Table 3**. Considering the ultrasonic pulse velocity of the 375 kg/m<sup>3</sup> and 300 kg/m<sup>3</sup> dosage specimens, it can be seen that the ultrasonic pulse velocity of all the specimens produced with CII-3 are fine. The ultrasonic pulse velocity results of the specimens produced with CI-4 and CI-5 are seen to be better than those of CII-3. Depending on the

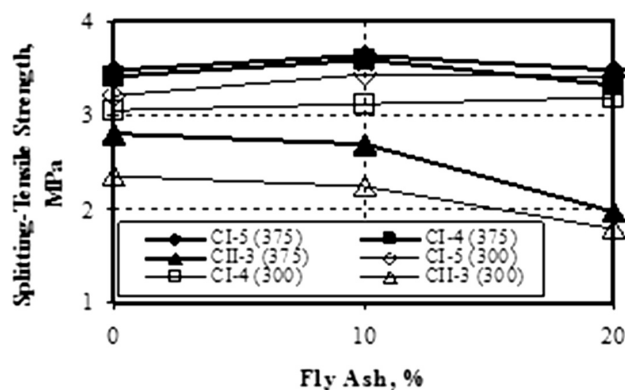


**Figure 5:** Relationship between the splitting tensile strength and the FA amount

**Slika 5:** Odvisnost med porušno natežno trdnostjo in deležem letečega pepela (FA)



ultrasonic pulse velocity values, the best results are seen to be in the specimens produced with the CII-5 cement and without any FA. According to the assessment in **Table 3**, it can be seen that the modulus of dynamic elasticity decreases as the amount of FA increases. The minimum  $E_{din}$  values are for the specimens produced using the CII-3 cement with the dosages of 300 kg/m<sup>3</sup> and 375 kg/m<sup>3</sup>. As seen in **Table 3**, for the other series, the  $E_{din}$  values are similar.

**Table 3:** Test results for ultrasonic pulse velocity and modulus of dynamic elasticity

**Tabela 3:** Rezultati preizkusov za hitrost ultrazvočnega impulza in modul dinamične elastičnosti

Cement Type	FA/%	Ultrasonic pulse velocity /(km/s)		$E_{din}$ /GPa	
		375 Dosage	300 Dosage	375 Dosage	300 Dosage
CII-3	0	4.35	4.52	45.7	49.4
	10	4.46	4.46	47.9	48.0
	20	4.29	4.40	43.6	46.3
CI-4	0	4.62	4.62	52.3	53.1
	10	4.63	4.50	52.3	49.9
	20	4.62	4.60	51.3	51.5
CI-5	0	4.66	4.63	53.5	52.8
	10	4.56	4.56	50.5	50.5
	20	4.65	4.55	52.1	50.5

#### 4.4 Impressed voltage test

After the impressed voltage tests, steel in the reinforced concrete corroded and the specimens were damaged. The damaged specimens are shown in **Figure 6**. Since the volume of the corrosion products (rust) are 2.5–6 times greater than the volume of the steel used in the concrete, these corrosion products lead to higher internal tensile stresses in the hardened concrete. Being exposed to these stresses, the hardened concrete cracks and splits off.<sup>12</sup>

The compressive strength results and damage occurrence times (DOTs) of the accelerated-corrosion specimens are shown in **Table 4**. As seen in **Table 4**, the DOT ranges between 251 h and 394 h. According to **Table 4**, as is the case with the 300 kg/m<sup>3</sup> dosage specimens, an increase in the FA amount leads to a



**Figure 6:** Damaged specimens after the impressed voltage test  
**Slika 6:** Poškodovani vzorci po pospešenem napetostnem preizkusu

longer DOT. With respect to DOTs, it is observed that the best results are obtained for the specimens produced with CII-3 and 20 % FA cured for 28 d, and the specimens produced with CI-5 and 20 % FA cured for 180 d.

A comparison between the 300 kg/m<sup>3</sup> and 375 kg/m<sup>3</sup> dosage specimen results shows that the DOT extends as the cement dosage increases. Generally, if the cement dosage increases, the compressive strength of the concrete increases as well. There is a general relationship between the compressive strength of the concrete and the permeability.<sup>12</sup> According to **Table 4**, the DOT is extended even if the compressive strengths of the concretes produced with the CII-3 cement are low. Actually, the concretes produced with the CII-3 cement that have low compressive strengths are damaged in a shorter time than the concretes produced with the CI-4 and CI-5 cements, because the concretes produced with CII-3 are more porous than the other concretes, as can be understood from the compressive strengths.

**Table 4:** Compressive strengths and damage occurrence times (DOTs) of the 300 – (375) dosage specimens

**Tabela 4:** Tlačne trdnosti in časi do pojava napak (DOT) vzorcev z odmerkom 300 – (375)

Cement Type	FA/%	Compressive Strength, MPa 300 (375)		Damage Occurrence Time Hour – 300 (375)	
		28 days	180 days	28 days	180 days
CII-3	0	36.7 (37.2)	38.9 (45.2)	291 (325)	368 (308)
	10	33.8 (34.7)	41.6 (42.3)	311 (323)	381 (324)
	20	31.2 (32.0)	38.3 (39.7)	325 (366)	394 (373)
CI-4	0	46.5 (47.5)	48.2 (47.9)	279 (287)	303 (306)
	10	43.7 (44.4)	49.2 (55.4)	310 (315)	324 (326)
	20	42.6 (42.2)	48.1 (50.5)	319 (326)	327 (329)
CI-5	0	53.6 (55.2)	64.7 (64.4)	251 (300)	304 (315)
	10	50.7 (54.0)	63.4 (67.3)	268 (316)	343 (368)
	20	49.8 (52.8)	53.6 (60.5)	287 (292)	376 (389)

However, it is known from the previous studies that fly ash, ground granulated blast furnace slag, silica fume and pozzolans bind chloride ions; thus, the chloride permeability decreases.<sup>13–16</sup> The concretes produced with the CII-3 cement are highly porous and permeable due to a high percentage of FA and natural pozzolans that do not pozzolanically react with water and lime. Therefore, these FA and pozzolan particles react with chloride ions and bind them. In this way, the chloride permeabilities of these concretes are lower than those of the control ones.

**Figure 7** shows that the corrosion-time curves of the 28 d cured concretes were produced with a 300 kg/m<sup>3</sup> dosage of the CII-3, CI-4 and CI-5 cements, and 10 % and 20 % FA replacements of the cement. According to the assessment in **Figure 7**, for the concretes produced with the CII-3, CI-4 and CI-5 cements, the curves 2, 3, 5, 6, 8 and 9 show that an increase in the FA amount in the concrete, used as a replacement for the cement, reduces the corrosion currents. According to these results the use



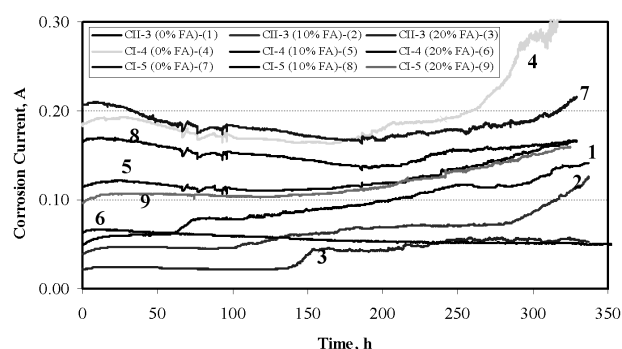


**Figure 7:** Variation of the corrosion current according to time (a 300-kg/m<sup>3</sup> dosage and 28-day specimens)

**Slika 7:** Spreminjanje korozivskega toka glede na čas (odmerek 300 kg/m<sup>3</sup> in vzorec po 28 dneh)

of FA is beneficial. It has been observed that FA binds chloride ions.<sup>15,16</sup> As a result, the corrosion currents decrease as seen in **Figure 7**.

**Figure 8** shows the current-time relations for the corrosion of the concretes that are cured for 28 d and produced by using FA as the 10 % and 20 % replacements of the cement weight with a 375 kg/m<sup>3</sup> dosage of the CII-3, CI-4 and CI-5 cements. The series produced by using the CII-3 cement gives better test results. However, the best test results are achieved with the concretes produced with a 20 % FA replacement of the CI-4 cement. It is seen that the corrosion current of the specimens is reduced by using the FA replacement for a 375 kg/m<sup>3</sup> dosage of the CI-5 cement with the given ratios. By using FA, the corrosion currents are reduced, but better results are achieved than with the other concrete specimens. According to **Figure 8**, the corrosion currents increase with time and it is seen that some series have sudden increases. The corrosion current-time relations are shown in **Figure 9** for the concretes that are cured for 180 d and produced by using FA as the 10 % and 20 % replacements of the cement weight for a 300 kg/m<sup>3</sup> dosage of the CII-3, CI-4 and CI-5 cements. Looking at **Figure 9**, with the concretes produced with the CI-4 and CI-5 cements, and without

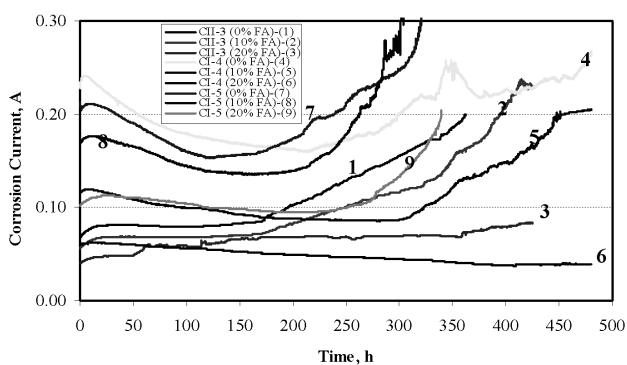


**Figure 8:** Variation of the corrosion current according to time (a 375-kg/m<sup>3</sup> dosage and 28-day specimens)

**Slika 8:** Spreminjanje korozivskega toka glede na čas (odmerek 375 kg/m<sup>3</sup> in vzorec po 28 dneh)

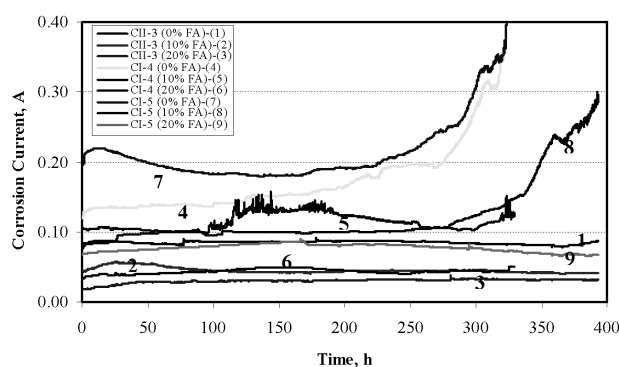


**Figure 9:** Variation of the corrosion current according to time (a 300-kg/m<sup>3</sup> dosage and 180-day specimens)

**Slika 9:** Spreminjanje korozivskega toka glede na čas (odmerek 300 kg/m<sup>3</sup> in vzorec po 180 dneh)

any FA, they are seen to have a corrosion current above 0.1 A. All the other specimens have a corrosion current under 0.1 A at the beginning. The concretes cured for 180 days and produced with a 300-kg/m<sup>3</sup> dosage of the CI-4 cement depending on their FA ratio (0 %, 10 % and 20 %) have (0.12, 0.08 and 0.04) A corrosion currents in turn. However, the same series that were cured for 28 d have corrosion currents of (0.18, 0.12 and 0.09) A in turn. According to these results an increase in the curing time reduces the corrosion currents. The corrosion current-time relations are shown in **Figure 10** for the concretes cured for 180 d and produced by using FA as the 10 % and 20 % replacements of the cement weight for the 375 kg/m<sup>3</sup> dosage of the CII-3, CI-4 and CI-5 cements. With respect to **Figure 10**, the best results are achieved for the concretes produced with a 20 % FA replacement of the weight of the CII-3 cement.

#### 4.5 Weight loss method

The steel reinforcements cleaned with a Clarke solution are shown in **Figure 11**. The weight losses of the steel reinforcements in various concrete mixtures that were exposed to corrosion are shown in **Figures 12** and **13**. According to a general assessment of these figures,

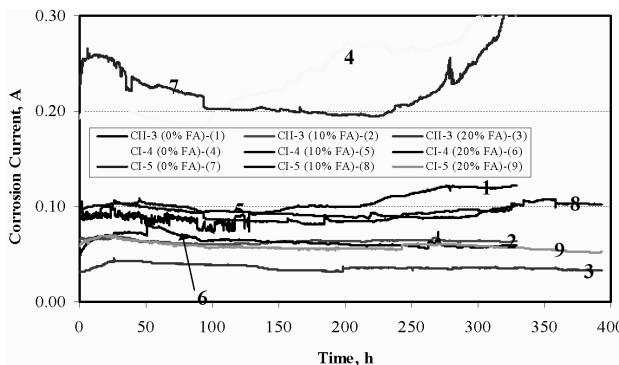


**Figure 10:** Variation of the corrosion current according to time (a 375-kg/m<sup>3</sup> dosage and 180-day specimens)

**Slika 10:** Spreminjanje korozivskega toka glede na čas (odmerek 375 kg/m<sup>3</sup> in vzorec po 180 dneh)



Figure 11: Steel reinforcements cleaned with a Clarke solution  
Slika 11: Z raztopino Clarke očiščena jeklena armatura

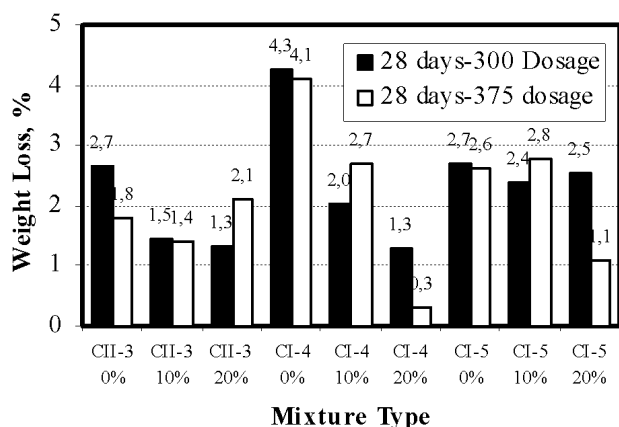


Figure 12: Variation of weight loss by mixture type for 28-day specimens

Slika 12: Razlike v izgubi mase glede na vrsto mešanice v vzorcih po 28 dneh

the weight loss is seen to decrease as the amount of FA, being the concrete replacement of the cement, is increased. Increasing the dosage reduces the weight loss in some series, but increases it in others. As it is seen in Figure 12, the maximum weight loss is observed with the concretes that did not have any FA and were produced with CI-4. According to Figure 13, the weight

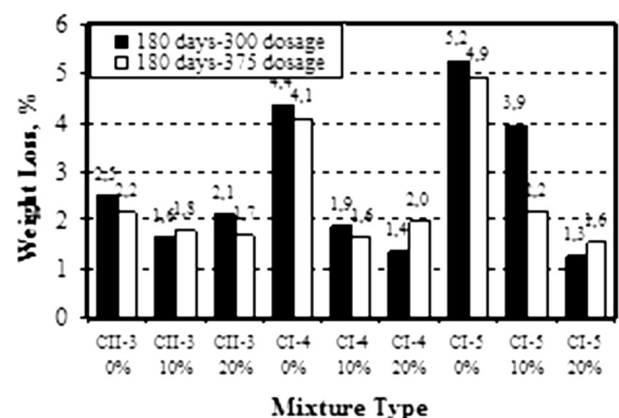


Figure 13: Variation of weight loss by mixture type for 180-day specimens

Slika 13: Razlike v izgubi mase glede na vrsto mešanice v vzorcih po 180 dneh

losses decrease as the amount of FA increases in the concretes. According to the increase in the curing time, by comparing Figures 12 and 13, in some series the weight loss of the reinforcements is seen to increase and in some series it decreases.

## 5 CONCLUSIONS

After the tests it was observed that the mechanical properties of the concretes and the corrosion performances of the steel embedded in the concrete changed with different cement types, dosages, FA amounts used as the replacements for the cement and the curing time.

- The compressive strength of the specimens increased after an increase in the curing time and the cement dosage. The maximum compressive strengths were observed with the concretes that were produced with the CI-5 cement.
- The splitting tensile test results of the specimens that were produced with the CI-4 and CI-5 cements were very similar. The minimum strengths were observed with the specimens that were produced with CII-3.
- According to a general assessment of the results, an increase in the dosage, the curing time and the FA amount used to replace the cement caused an increase in the DOT of the reinforced concrete specimens.
- With respect to the assessment of the DOTs, the most positive results were observed with the specimens that were produced with the CII-3 cement. Compatible results were observed with the specimens that were produced with the other cements and the 20 % FA amount.
- Consequently, the corrosion of the steel embedded in the concrete depends significantly on the cement type, the cement dosage and the curing time. To combat the corrosion of the steel reinforcement in the concrete, the permeability of concrete by water and hazardous ions has to be prevented. This is possible by producing an impermeable concrete. For this reason, impermeable and high-quality concretes have to be produced by using various mineral admixtures such as FA and SF.

## 6 REFERENCES

- <sup>1</sup> T. Parthiban, R. Ravi, G. T. Parthiban, S. Srinivasan, K. R. Ramakrishnan, M. Raghavan, Neural network analysis for corrosion of steel in concrete, *Corr. Sci.*, 47 (2005), 1625–1642
- <sup>2</sup> E. Güneyisi, T. Özturan, M. Gesoğlu, Effect of initial curing on chloride ingress and corrosion resistance characteristics of concretes made with plain and blended cements, *Build. and Environ.*, 42 (2007), 2676–2685
- <sup>3</sup> K. Sakr, Effect of cement type on the corrosion of reinforcing steel bars exposed to acidic media using electrochemical techniques, *Cem. Concr. Res.*, 35 (2005), 1820–1826
- <sup>4</sup> K. Y. Ann, H. S. Jung, H. S. Kim, S. S. Kim, H. Y. Moon, Effect of calcium nitrite-based corrosion inhibitor in preventing corrosion of embedded steel in concrete, *Cement and Concrete Research*, 36 (2006), 530–535

- <sup>5</sup> A. A. Gürten, K. Kayakırlmaz, M. Erbil, The effect of thiosemicarbazide on corrosion resistance of steel reinforcement in concrete, *Const. and Buil. Mater.*, 21 (2007), 669–676
- <sup>6</sup> P. Chindapasirt, C. Chotithanorn, H. T. Cao, V. Sirivivatnanon, Influence of fly ash fineness on the chloride penetration of concrete, *Const. Build. Mater.*, 21 (2007), 356–361
- <sup>7</sup> E. Güneyisi, T. Özturan, M. Gesoğlu, A study on reinforcement corrosion and related properties of plain and blended cement concretes under different curing conditions, *Cem. Concr. Compos.*, 27 (2005), 449–461
- <sup>8</sup> M. Y. Kaltakci, M. Kamanli, M. Ozturk, M. H. Arslan, H. H. Korkmaz, Sudden Complete Collapse of Zumur Apartment Building and It's Causes, *Journal of Performance of Constructed Facilities*, doi:http://dx.doi.org/10.1061/(ASCE)CF.1943-5509.0000337
- <sup>9</sup> M. H. Arslan, H. H. Korkmaz, What is to be Learned from Damage and Failure of Reinforced Concrete Structures During Recent Earthquakes in Turkey, *Engineering Failure Analysis*, 14 (2007), 1–22
- <sup>10</sup> E. Güneyisi, M. Gesoğlu, A study on durability properties of high-performance concretes incorporating high replacement levels of slag, *Materials and Structures*, 41 (2008), 479–493
- <sup>11</sup> ASTM G1–03, Standard Practice for Preparing, Cleaning, and Evaluating Corrosion Test Specimens, *ASTM Book of Standards Volume: 3. 2.* 2003
- <sup>12</sup> T. Y. Erdogan, *Concrete*, METU Press, Ankara, Turkey, 2003
- <sup>13</sup> K. Y. Yeau, E. K. Kim, An experimental study on corrosion resistance of concrete with ground granulate blast-furnace slag, *Cem. and Concr. Res.*, 35 (2005), 1391–1399
- <sup>14</sup> K. M. A. Hossain, M. Lachemi, Corrosion resistance and chloride diffusivity of volcanic ash blended cement mortar, *Cem. and Concrete Res.*, 34 (2004), 695–702
- <sup>15</sup> S. P. Shah, S. H. Ahmad, *High performance concretes and applications*, Hodder Headline Group, 1994
- <sup>16</sup> R. B. Polder, W. H. A. Peelen, Characterisation of chloride transport and reinforcement corrosion in concrete under cyclic wetting and drying by electrical resistivity, *Cem. Concr. Compos.*, 24 (2002), 427–435

## EFFECT OF THE DELTA-FERRITE CONTENT ON THE TENSILE PROPERTIES IN NITRONIC 60 STEEL AT ROOM TEMPERATURE AND 750 °C

### VPLIV VSEBNOSTI DELTA FERITA NA NATEZNE LASTNOSTI JEKLA NITRONIC 60 PRI SOBNI TEMPERATURI IN PRI 750 °C

Almaida Gigović-Gekić<sup>1</sup>, Mirsada Oruč<sup>2</sup>, Sulejman Muhamedagić<sup>1</sup>

<sup>1</sup>University of Zenica, Faculty of Metallurgy and Materials Science, Travnička cesta 1, Zenica, Bosnia and Herzegovina

<sup>2</sup>Metallurgical Institute "Kemal Kapetanović", Zenica, Bosnia and Herzegovina  
almaida.gigovic@fammm.unze.ba

*Prejem rokopisa – received: 2011-10-19; sprejem za objavo – accepted for publication: 2012-03-15*

This paper presents the results of the tensile testing of the austenitic stainless steel Nitronic 60 at room temperature and 750 °C in the solution-annealed condition. It also presents the results of the optical and SEM analyses of the tested samples. The microstructural analysis showed the presence of a delta-ferrite phase in the austenite matrix at room temperature. The content of the delta ferrite was calculated using a Feritscope MP30. The content of the delta ferrite depends on the chemical composition. An increase in the Si and Cr contents causes an increase in the delta-ferrite content. The results also show that an increase in the delta-ferrite content leads to an increase in the strength and a decrease in the ductility at room temperature. After testing the samples at 750 °C, the presence of a sigma phase was noticed. Precipitation of the sigma phase causes a slight increase in the strength and a decrease in the ductility of the tested material. An analysis of the fracture surface shows the presence of ductile fracture in the samples tested at room temperature and a combination of ductile and brittle fractures occurring at 750 °C.

**Keywords:** austenitic steel, Nitronic 60, tensile properties, SEM analysis, delta ferrite, sigma phase

Članek predstavlja rezultate nateznih preizkusov avstenitnega nerjavnega jekla Nitronic 60 v raztopno žarjenem stanju pri sobni temperaturi in pri 750 °C. Predstavljeni so tudi rezultati preiskav vzorcev s svetlobno in SEM analizo. Analiza mikrostrukture pri sobni temperaturi je pokazala prisotnost delta ferita v avstenitni osnovi. Vsebnost dela ferita je bila določena z uporabo naprave Feritscope MP30. Vsebnost delta ferita je odvisna od kemijske sestave. Povečanje vsebnosti Si in Cr poveča tudi vsebnost delta ferita. Iz rezultatov izhaja, da povečanje vsebnosti delta ferita poveča trdnost in zmanjša preoblikovalnost pri sobni temperaturi. Po preizkušanju pri 750 °C je bila opažena prisotnost sigma faze. Izločanje te faze rahlo poveča trdnost in poslabša preoblikovalnost preizkušene materiala. Analiza prelomov kaže žilav prelom pri vzorcih, preizkušanih pri sobni temperaturi in kombinacijo žilavega in krhkega preloma pri 750 °C.

**Ključne besede:** avstenitno jeklo, Nitronic 60, natezne lastnosti, SEM-analiza, delta ferit, sigma faza

## 1 INTRODUCTION

Microstructure stability is the most important requirement needed to obtain proper mechanical properties for an austenitic stainless steel (ASS).<sup>1</sup> To achieve a stable microstructure, the samples are usually solution heat treated at a temperature between 1000 °C and 1120 °C<sup>2</sup> and then water quenched. The microstructure of Nitronic 60 is primarily monophasic, i.e., austenitic. However, precipitation of the delta ferrite ( $\delta$ -ferrite) in an austenite matrix is possible, too. A higher volume fraction of the  $\delta$ -ferrite can be achieved in the microstructure of the samples by changing the chemical composition of steel in terms of increasing the content of the  $\delta$ -ferrite-stabilising elements<sup>1</sup> such as Cr, Si, Ti, Mo, etc. The presence of the  $\delta$ -ferrite, which has a BCC crystalline structure, slows the grain growth and increases the strength properties of the steel because the interphase boundaries act as strong barriers to the dislocation motion<sup>3</sup>. During the annealing at 600–900 °C the intermetallic phases and carbides precipitate from the austenite and/or the  $\delta$ -ferrite.<sup>2,4</sup> One of the most common phases in ASS is the sigma phase ( $\sigma$ -phase).<sup>2,5</sup> As a result

of the heat-treatment temperature, the  $\delta$ -ferrite can transform in the austenite and the  $\sigma$ -phase.<sup>4-10</sup> The  $\sigma$ -phase is an intermetallic compound with a complex, tetragonal, crystal structure. The chemical composition of this phase varies considerably and it is therefore difficult to define this phase in the form of unique formulas. At room temperature this phase is hard, brittle and nonmagnetic,<sup>10</sup> therefore having a negative effect on the mechanical properties especially on the toughness and ductility. The presence of the  $\delta$ -ferrite reduces the incubation period of the precipitation of the  $\sigma$ -phase. The rate of the  $\sigma$ -phase precipitation from the  $\delta$ -ferrite is about 100 times more rapid than the rate of the  $\sigma$ -phase precipitation directly from austenite<sup>4</sup>. The temperature interval, in which this phase occurs with most of the commercial steels, is between 590 °C and 870 °C, but the phase decomposes at temperatures above 1000 °C. To make the samples free of the  $\sigma$ -phase, the heat-treatment temperature has to be higher than 1000 °C, followed by rapid cooling.

The aim of the research is an investigation of the influence of  $\delta$ -ferrite on the tensile properties of the tested materials at room and elevated temperatures



because the Nitronic 60 parts are intended to operate at elevated temperatures.

For the research project we tested six melts with different contents of the alloying elements of Si, Cr, Mn and Ni in order to get the samples with different contents of the  $\delta$ -ferrite.

## 2 EXPERIMENTAL WORK

The melts were prepared by using a vacuum induction furnace with an argon protective atmosphere with the chemical composition corresponding to the standard ASTM A276,<sup>11</sup> as shown in **Table 1**. The requirements relating to the chemical composition and the tensile properties of the tested material correspond to the requirements for the steel UNS S21800.<sup>11</sup> The average  $\delta$ -ferrite content was determined with a Feritscope MP30 (Fisher, Germany) using broken specimens after the tensile testing at room temperature and 750 °C, as seen in **Table 1**. The content of the  $\delta$ -ferrite was determined with the method that takes advantage of the fact that the  $\delta$ -ferrite is magnetic, while austenite and the  $\sigma$ -phase are not. The average value was calculated on the basis of ten measurements.

A microstructural analysis was carried out with an Olympus optical microscope and a scanning electron microscope (Jeol JSM 5610 operating at 20kV, a take-off angle of 35°, and an elapsed livetime of 60 %) using broken specimens after the tensile testing. The samples for the microstructure analysis were prepared with the standard grinding and polishing techniques and etched with an aqua regia. In addition, a fractographic analysis was carried out on broken specimens after the tensile testing with the scanning electron microscope.

The tensile testing was performed on the samples obtained from a rod with a  $\phi$  of 15 mm. Before the testing, the samples were solution annealed at 1020 °C for 60 min followed by water quenching. The samples were tested at room temperature and 750 °C. The tensile test was carried out on a universal hydraulic machine for static testing (200 kN). The sampling and testing procedures were realized in accordance with the standards BAS EN 10002-1/02 and BAS EN 10002-5/01.

## 3 RESULTS AND DISCUSSION

### 3.1 Microstructure

The microstructure analysis of the samples tested at room temperature shows the presence of a two-phase microstructure. The microstructure consists of  $\delta$ -ferrite islands in an austenite matrix.<sup>12</sup> The  $\delta$ -ferrite islands are elongated in the rolling direction. The precipitation of the  $\delta$ -ferrite occurs mainly at the grain boundaries as shown in **Figure 1a**. **Figure 1b** shows the microstructure

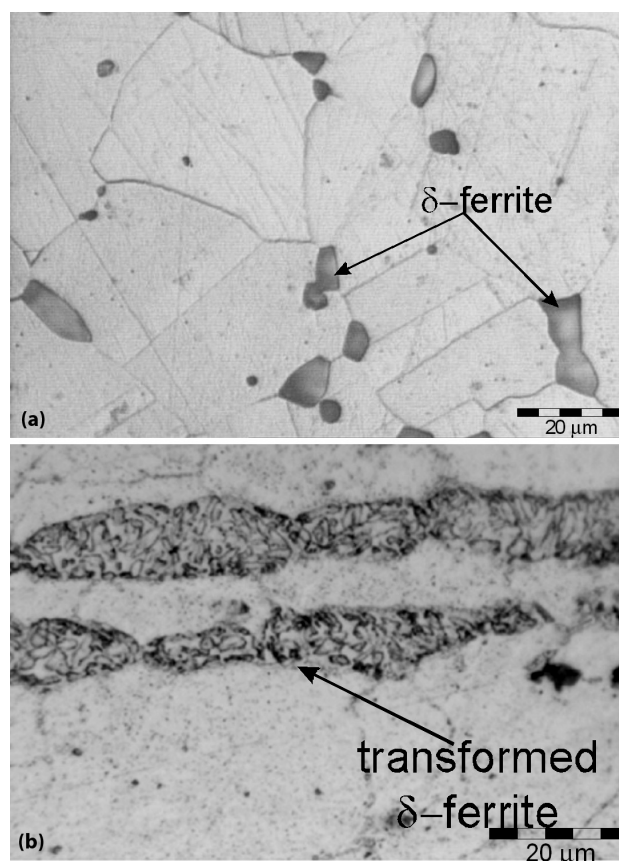


**Figure 1:** Microstructure of steel Nitronic 60 at: a) room temperature and b) 750 °C

**Slika 1:** Mikrostruktura jekla Nitronic 60 pri: a) sobni temperaturi in b) 750 °C

**Table 1:** Chemical composition and the average  $\delta$ -ferrite content of steel Nitronic 60

**Tabela 1:** Kemijska sestava in povprečna vsebnost  $\delta$ -ferita v jeklu Nitronic 60

Melt	Chemical composition, w/%								$\delta$ -ferrite /% (Room temp.)	$\delta$ -ferrite /% (750 °C)
	C	Si	Mn	Cr	Ni	P	S	N		
Prescribed ASTM A 276	max. 0.10	3.5–4.5	7.0–9.0	16.0–18.0	8.0–9.0	max. 0.06	max. 0.03	0.08–0.18		
1	0.04	4.41	7.4	18.0	8.1	0.007	0.005	0.18	10.43	0.52
2	0.04	3.74	8.6	18.0	8.0	0.007	0.005	0.16	6.30	0.31
3	0.04	4.25	8.4	16.0	8.8	0.006	0.010	0.14	3.37	0.77
4	0.05	3.5	7.9	16.9	8.6	0.005	0.005	0.12	1.30	0.58
5	0.04	3.5	7.2	16.6	8.0	0.006	0.012	0.15	1.14	0.59
6	0.05	3.8	8.9	17.0	9.0	0.007	0.005	0.16	0.82	0.46

of a sample tested at 750 °C exhibiting an austenite matrix and a transformed  $\delta$ -ferrite phase.

The SEM analysis of the sample tested at 750 °C with a higher magnification is shown in **Figure 2**, confirming the transformation of the  $\delta$ -ferrite. The nucleation of the sigma phases predominantly occurred at the austenite/ $\delta$ -ferrite grain boundaries, because these grain boundaries and the interfaces are the high-energy regions. The average compositions of the constituent phases were determined with an EDS analysis and presented in **Table 2**. The results show that the  $\sigma$ -phase has the highest content of Cr and that the content of Ni is quite high, too. The austenite is rich in Ni and Mn, but depleted in Cr and Si. In the case of the  $\delta$ -ferrite, it is depleted in Ni and rich in Cr.

**Table 2:** Chemical compositions of the constituent phases in mass fractions (w/%) obtained with an EDS analysis

**Tabela 2:** Kemijska sestava faz v masnih deležih (w/%), določena z EDS-analizo

Elements	Constituent phases		
	$\delta$ -ferrite	$\sigma$ -phase	Austenite
Si	3.50	4.96	3.12
Cr	19.15	36.30	17.50
Mn	6.28	5.94	8.52
Ni	5.06	8.02	7.22

The  $\delta$ -ferrite is decomposed into the  $\sigma$ -phase and the austenite with a eutectoid transformation.<sup>9</sup> The rate of the  $\sigma$ -phase precipitation from the  $\delta$ -ferrite is more rapid than its precipitation directly from the austenite<sup>4</sup>, and the  $\delta$ -ferrite is not in the state of equilibrium at this temperature. The high susceptibility of the  $\delta$ -ferrite phase to  $\sigma$ -phase formation is associated with the chemical composition of the  $\delta$ -ferrite phase. This phase is rich in Cr and Si, which stimulate the formation of the  $\sigma$ -phase.<sup>9,13</sup> In the case of the alloys with the contents of Cr below 25 %, an addition of Mn and Ni can also stimulate the formation of the  $\sigma$ -phase.<sup>4,14</sup>

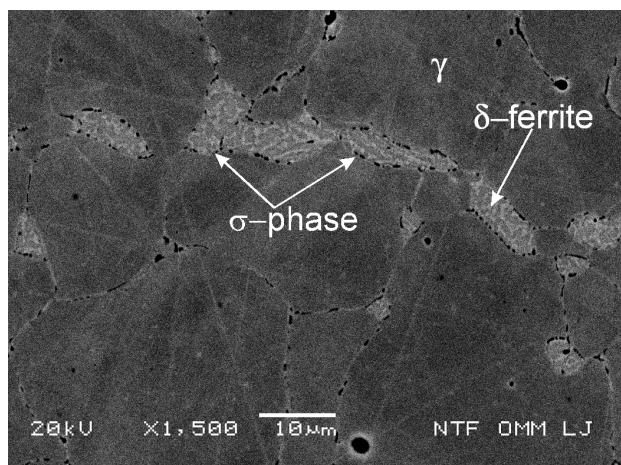


**Figure 2:** SEM microstructure samples tested at 750 °C  
**Slika 2:** SEM-posnetek vzorca, preizkušene pri 750 °C

### 3.2 Fracture surface

The analysis of the samples' fracture surfaces shows that the samples tested at room temperature have ductile fracture but the samples tested at 750 °C have intergranular brittle fracture as a consequence of the presence of the  $\sigma$ -phase with a small portion of a ductile fracture.<sup>15</sup> The ductile fracture is a result of the presence of austenite and the  $\delta$ -ferrite, shown in **Figures 3a** and **3b**.

### 3.3 Mechanical properties

The results of the tensile testing at room temperature are in accordance with the standard ASTM A 276.<sup>11</sup> However, there is no data about the tensile testing at elevated temperature in the ASTM A 276<sup>11</sup> standard. The results at room temperature indicate that an increase in the  $\delta$ -ferrite content from 0.82 % to 10.43 % causes an increase in the tensile strength (TS) from 707 MPa to 821 MPa and an increase in the yield strength (YS) from 356 MPa to 467 MPa, while the reduction (Red.) and elongation (Elo.) are slightly reduced from 73 % to 63 % and from 55.3 % to 42.9 %, respectively, as shown in **Figure 4**.

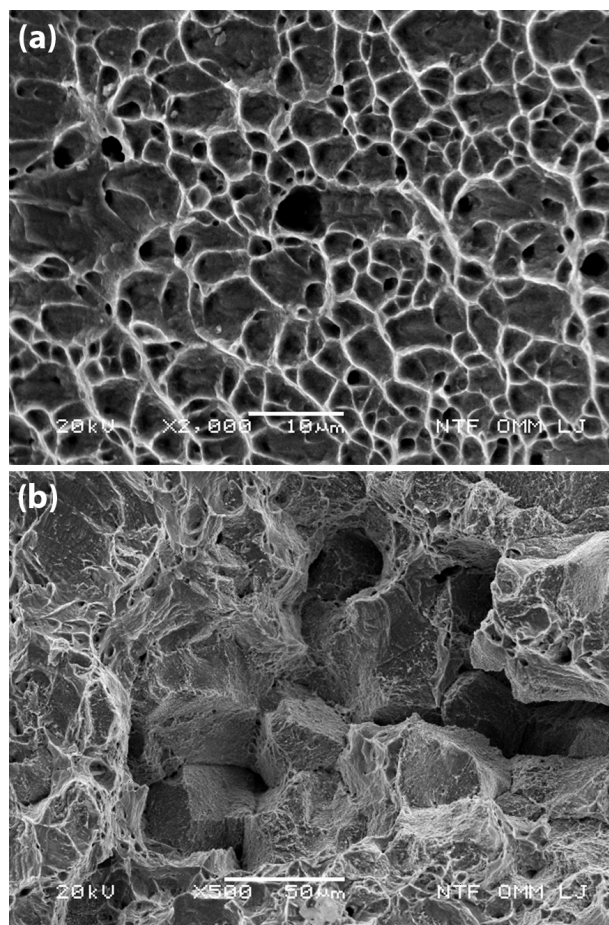


**Figure 3:** Fracture surface – SEM: a) room temperature and b) 750 °C  
**Slika 3:** Površina preloma – SEM: a) sobna temperatura in b) 750 °C



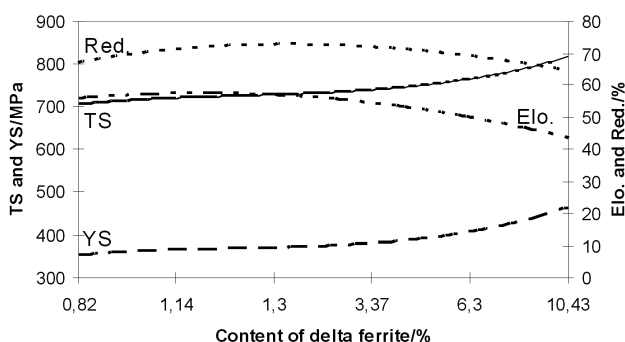


**Figure 4:** Effect of the  $\delta$ -ferrite content on the tensile properties at room temperature

**Slika 4:** Učinek vsebnosti  $\delta$ -ferita na natezne lastnosti pri sobni temperaturi

The highest value of the strength and the lowest value of ductile properties were found for the melt 1 with 10.43 % of the  $\delta$ -ferrite. The values of the strength and ductility are almost constant being up to 3 % of the  $\delta$ -ferrite. With an increase in the  $\delta$ -ferrite content to over 3 %, the strength is increased and the ductility is decreased. The heating of the tested material at 750 °C causes a remarkable decrease in the strength and ductility of the samples in comparison with the test results obtained at room temperature. One of the reasons for this was the transformation of the  $\delta$ -ferrite in the  $\sigma$ -phase. The analysis of the  $\delta$ -ferrite content after the tensile testing at 750 °C shows that the  $\sigma$ -phase content increases with an increase in the  $\delta$ -ferrite content. The content of the transformed  $\delta$ -ferrite was about 60 % for the melts with the  $\delta$ -ferrite content of up to 2 % and about 95 % for the melts with the  $\delta$ -ferrite content of over 6 %. The average content of the transformed  $\delta$ -ferrite for the melts from 2 % to 6 % was about 70 %. **Figure 5** shows that with an increase in the content of the transformed  $\delta$ -ferrite from 77.15 % to 95.01 %, the tensile and yield strengths slightly increase from 245 MPa to 299 MPa and from 180 MPa to 211 MPa, respectively. The yield strength is almost constant, being up to 77 %, while the tensile strength is decreasing. The

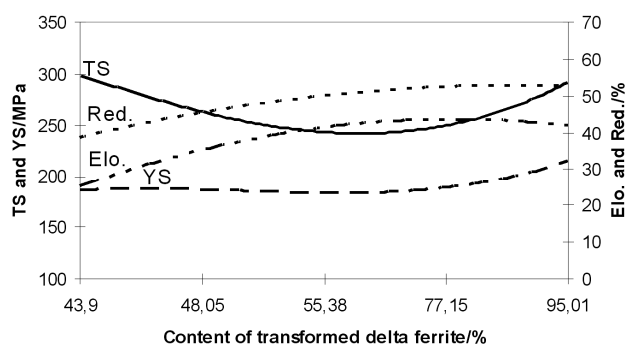


**Figure 5:** Effect of the content of transformed  $\delta$ -ferrite on the tensile properties at 750 °C

**Slika 5:** Učinek vsebnosti pretvorjenega  $\delta$ -ferita na natezne lastnosti pri 750 °C

ductility increases with an increase in the content of the transformed  $\delta$ -ferrite from 43.9 % to 77.15 %. In the range between 77.15 % and 95.01 % the ductility slightly decreases. The value of the reduction is between 40 and 55 %, while the value of the elongation is between 25 and 45 %. The reason for the increase in the tensile strength is the precipitation of the  $\sigma$ -phase because the strength generally grows together with the growth of the precipitated intermetallic phases.<sup>16,17</sup> The intermetallic phases cause an increase in the strength by obstructing, or stopping, the movement of dislocations. It is known from the literature sources<sup>13</sup> that by controlling the distribution and morphology of the  $\sigma$ -phase, it is possible to improve the strength and ductility in the temperature range where the  $\sigma$ -phase precipitates.

Generally, the tensile properties of steel Nitronic 60 depend on the chemical composition of the alloy. By controlling the chemical composition of the alloy we control the  $\delta$ -ferrite content in the steel. The content of the  $\delta$ -ferrite increases with an increased concentration of the ferrite-stabilizing elements, such as Cr and Si, and with a decreased concentration of the austenite-stabilizing elements, such as Mn, Ni and N. The  $\delta$ -ferrite content can become lower than 1 % if the contents of Ni and Mn are increased to the upper allowed limit and the contents of Cr and Si are decreased to the middle of the allowed limit,<sup>18</sup> as seen in **Table 1**. A reduction of the  $\delta$ -ferrite content leads to a decrease in the strength and an increase in the ductility of steel at room temperature. At the elevated temperature (750 °C), the  $\delta$ -ferrite transforms to the  $\sigma$ -phase, having a negative effect on the tensile properties because it is a hard and brittle phase.

## 4 CONCLUSION

In this study, the influence of the  $\delta$ -ferrite on the tensile properties at room temperature and 750 °C was investigated. From the presented results it could be concluded that:

- The microstructure of the solution-annealed steel Nitronic 60 consisted of  $\delta$ -ferrite islands in an austenite matrix at room temperature.
- An increase in the  $\delta$ -ferrite content leads to an increase in the strength and a decrease in the ductility at room temperature, especially for the steel with over 3 %  $\delta$ -ferrite.
- An increase in the content of Si and Cr causes an increase in the strength and a decrease in the ductility of steel due to the increased content of the  $\delta$ -ferrite.
- The EDS analysis shows the presence of the  $\sigma$ -phase at the ferrite/austenite boundaries, which is a result of the  $\delta$ -ferrite transformation at 750 °C. The percentage of the  $\delta$ -ferrite decomposition in the samples was up to 90 %.
- The strength slightly increased and the ductility decreased after the content of the transformed  $\delta$ -ferrite increased above 70 %.

- The SEM analysis also shows the presence of a mixture of the intergranular brittle fracture and ductile fracture at 750 °C, produced as a consequence of the presence of the sigma phase. The fracture surface of the samples tested at room temperature is ductile because of the presence of austenite and the  $\delta$ -ferrite.

## Acknowledgements

A part of the research described in this paper was conducted at the University of Ljubljana (Faculty of Natural Sciences and Engineering) as part of bilateral agreements between the Republic of Slovenia, and Bosnia and Herzegovina within the project "Application of new materials in the automotive industry" No: SLO-BA10-11-011.

## 5 REFERENCES

- <sup>1</sup> J. Janovec, B. Šuštaršič, J. Medved, M. Jenko, *Mater. Tehnol.*, 37 (2003) 6, 307–312
- <sup>2</sup> R. L. Plaut, C. Herrera, D. M. Escriba, P. R. Rios, A. F. Padilha, *Materials Research*, 10 (2007) 4
- <sup>3</sup> A. A. Astafev, L. I. Lepekhina, N. M. Batieva, <https://springerlink.metapress.com/content/106486/?p=3803ac420c9f43dd80ca8a84319a1436&pi=0>, <https://springerlink.metapress.com/content/g625036m8347/?p=3803ac420c9f43dd80ca8a84319a1436&pi=0>
- <sup>4</sup> A. F. Padilha, P. R. Rios, *ISIJ International*, 42 (2002) 4, 325–337
- <sup>5</sup> H. S. Khatak, B. Raj, *Corrosion of Austenitic Stainless Steels Mechanism, Mitigation and Monitoring*, 2002
- <sup>6</sup> F. Tehovnik, F. Vodopivec, L. Kosec, M. Godec, *Mater. Tehnol.*, 40 (2006) 4, 129–137
- <sup>7</sup> J. C. Tverberg, *The Role of Alloying Elements on the Fabricability of Austenitic Stainless Steel*, [cited:1. 4.2009.] Available from: [www.csidesigns.com/tech/fabtech](http://www.csidesigns.com/tech/fabtech)
- <sup>8</sup> J. Pilhagen, *A Literature Review of the Stainless Steel 21-6-9 and its Potential for Sandwich Nozzles*, Master Thesis, Lulea, 2007
- <sup>9</sup> F. Tehovnik, B. Arzenšek, B. Arh, D. Skobir, B. Pirnar, B. Žužek, *Mater. Tehnol.*, 45 (2011) 4, 339–345
- <sup>10</sup> S. Kožuh, M. Gojić, L. Kosec, *RMZ-Materials and Geoenvironment*, 54 (2007) 3, 331–344
- <sup>11</sup> ASTM Standard A276-96, 1997 Annual Book of ASTM Standards, section 1. Iron and steel products, vol.01.03 Steel-Plate, Sheet, Strip, Wire, Stainless Steel Bar, ASTM, 1997
- <sup>12</sup> A. Gigović-Gekić, M. Oruč, I. Vitez, *Metallurgy*, 50 (2011) 1, 21–24
- <sup>13</sup> K. H. Lo, C. H. Shek, J. K. L. Lai, *Materials Science and Engineering, R* 65 (2009), 39–104
- <sup>14</sup> *Metals Handbook: Properties and Selection: Iron, Steels and High-Performance* 10th. Edition, Alloys, vol.1, ASM American Society for Metals, 1990
- <sup>15</sup> A. G. Gekić, M. Oruč, A. Nagode, H. Avdušinović, *RMZ-Materials and Geoenvironment*, 58 (2011) 2, 121–128
- <sup>16</sup> M. Pohl, O. Storz, T. Glogowski, *Materials Characterization*, 58 (2007), 65–71
- <sup>17</sup> S. C. Kim, Z. Zhang, Y. Furuya, C. Y. Kang, J. H. Sung, Q. Q. Ni, Y. Watanabe, I. S. Kim, *Materials Transactions*, 46 (2005) 7, 1656–1662
- <sup>18</sup> M. Oruč, M. Rimac, O. Beganović, S. Muhamedagić, *Mater. Tehnol.*, 45 (2011) 5, 483–487





# PHYSICAL REGULARITIES IN THE CRACKING OF NANOCOATINGS AND A METHOD FOR AN AUTOMATED DETERMINATION OF THE CRACK-NETWORK PARAMETERS

## FIZIKALNE ZAKONITOSTI POKANJA NANOPREVLEK IN METODA ZA AVTOMATSKO DOLOČEVANJE PARAMETROV MREŽE RAZPOK

**Pavlo Maruschak<sup>1</sup>, Vladimir Gliha<sup>2</sup>, Igor Konovalenko<sup>1</sup>, Tomaž Vuherer<sup>2</sup>, Sergey Panin<sup>3</sup>**

<sup>1</sup>Ternopil Ivan Pul'uj National Technical University, 46001 Ternopil, Ukraine

<sup>2</sup>University of Maribor, Faculty of Mechanical Engineering, Smetanova 17, 2000 Maribor, Slovenia

<sup>3</sup>Institute of Strength Physics and Materials Science SB RAS, 634021 Tomsk, Russia  
maruschak.tu.edu@gmail.com

*Prejem rokopisa – received: 2011-10-20; sprejem za objavo – accepted for publication: 2012-04-05*

The regularities and spatial distribution of multiple cracking of a nanocoating are investigated. It is found that in the cracking zones the relaxation of the stresses accumulated in the coating takes place; moreover, the intensity of its failure is determined by the structural level of defect accumulation. A new algorithm for a digital identification of the elements of a crack network in a nanocoating is proposed, and its adequacy is checked.

**Keywords:** multiple cracks, nanocoating, damage, diagnostics, surface, strain

Raziskovali smo zakonitosti in prostorsko porazdelitev več razpok na nanoprevleki. Ugotovili smo, da pride na področjih z razpokami do relaksacije napetosti, nakopičene v prevleki. Intenzivnost njenega propadanja je določena s strukturnim nivojem nakopičenja defektov. Predstavljen je nov algoritem za digitalno identifikacijo elementov mreže razpok na nanoprevleki. Preverili smo ustreznost modela.

**Ključne besede:** več razpok, nanoprevleka, poškodba, diagnoza, površina, raztezek

## 1 INTRODUCTION

The tensile, compressive and shear deformations play key roles in many processes of failure in a nanocoating because they are the results of a mutual influence of multiple defects and blocks of a coating<sup>1,2</sup>. The activation of deformation processes is observed in the sections of maximum coating cracking. Therefore, an important aspect is the quantitative evaluation of multiple cracking needed for the development of optimum algorithms for the identification and calculation of the parameters of a network of detected cracks<sup>2</sup>. However, there are a number of problems, in particular, a significant dispersion of the sizes of the crack-like defects, the shape of the cracks, and the need for determining a degree of their coalescence.

In the previous papers<sup>3,4</sup>, the authors offered a number of algorithms for evaluating the technical condition of the surface of a metallurgical equipment affected by multiple defects. However, the use of these methods for an investigation of a nanocoating requires a combination of material-science approaches, physical and mechanical approaches that will allow an analysis of the hierarchical structure of multiple cracking zones, bringing together the entire volume of information on the processes of initiation, growth and coalescence of

defects into a single system, and identifying the main regularities in this process.

In this paper, the structure of multiple cracking of a zirconium nanocoating, with a network of fatigue cracks, is investigated.

## 2 RESEARCH TECHNIQUE

The main objective of the paper is to find the basic regularities in the cracking of a nanocoating and to analyse the possibility of using a digital processing method for identifying defects. The requirement to determine the main regularities in the formation of the geometrical structure of a multiple cracking of a zirconium nanocoating with a thickness of 100  $\mu\text{m}$  predetermined the need to use the approaches of digital identification. Ion nanostructuring of the surface layer of the specimens made of steel 25Kh1M1F was performed using the high-current, vacuum-arc source of metallic ions on the UVN-0.2 "Quant" setup<sup>5</sup>. After reaching a vacuum of at least  $3 \cdot 10^{-3}$  Pa in the chamber, the specimens were treated with a zirconium-ion flow with the energy of 0.9–2.8 keV and the ion-current density of 0.1–0.3 mA/m<sup>2</sup>. The duration of the treatment was from 5 min to 20 min. The substrate holder with the specimens fixed on the specimen stage is connected directly

to the ion-acceleration schema instead of the traditional extraction of the radial-ion beam from the implanter.

In this case, the acceleration of ions occurs in the dynamic self-organising boundary layer featuring a double electrical layer, which forms around the specimen surface under the negative potential<sup>5</sup>.

Specimens from the ferrite-pearlite steel 25Kh1M1F in mass fractions<sup>6</sup>:  $w(\text{C}) = 0.23 \dots 0.29$ ;  $w(\text{Mn}) = 0.40 \dots 0.70$ ;  $w(\text{Si}) = 0.17 \dots 0.37$ ;  $w(\text{Mo}) = 0.60 \dots 0.80$ ;  $w(\text{Ni}) = 0.30$ ;  $w(\text{Cr}) = 1.50 \dots 1.80$ ;  $w(\text{S}) \delta 0.025$  with applied coatings were loaded, under cyclic tensioning, on the STM-100 test setup at the frequency of  $f = 1 \text{ Hz}$ ,  $\sigma_{\max} = 500 \text{ MPa}$ ,  $\sigma_{\min} = 0.1 \sigma_{\max}$ . After the failure of the specimens the coating condition was investigated at different values of the real transverse necking  $\tilde{\psi}$  of the specimens destroyed by tensioning<sup>7</sup>:

$$\tilde{\psi} = \ln(F_0 / F_k) \quad (1)$$

where  $F_0$  and  $F_k$  are the initial and the current areas of the cross-section, respectively.

Based on the analysis of the photo images, the structural and morphological data about the cracks and the mechanisms of their formation in the zones of localised tensioning and shear were analysed<sup>8</sup>. The measurement of the residual crack opening was determined by using the standard measurement of the Kappa software for TEM. The spatial orientation of the crack-network elements and their relation to the formation of the meso- and macroscale failure zones were determined.

### 3 STAGE-LIKE NATURE OF A NANOCOATING FAILURE

It is known that multiple defects have a multilevel structural organisation. So, any section of a specimen is an aggregate of structural elements separated by cracks of various sizes, which are stress concentrators<sup>9,10</sup>.

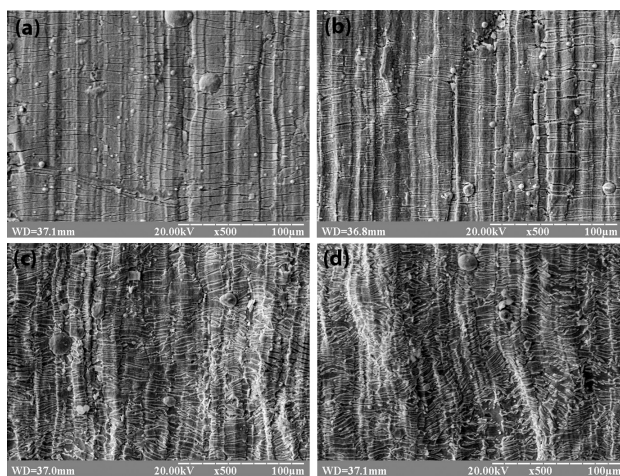


**Figure 1:** Stage-like nature of failure of a zirconium nanocoating at various plastic strains of the coating steel ( $\tilde{\psi} = 0; 0.23; 0.32; 0.35$ , respectively)

**Slika 1:** Stopničasta narava poškodb cirkonijeve nanoprevleke pri različnih plastičnih deformacijah jekla ( $\tilde{\psi} = 0; 0.23; 0.32; 0.35$ )

Failure of the coating material takes place in the vicinity of a number of defects simultaneously, which prevents the peeling of the coating. Fatigue failure of a nanocoating is a step-by-step process, taking place in the following successive steps:

- formation of multiple defects – elastic-plastic deformation of a coating, nucleation of a network of individual cracks, their growth and partial coalescence followed by a gradual accumulation of local plastic strains in the most inhomogeneous sections of the material, **Figure 1a**.
- formation of a longitudinal deformation relief – this phenomenon is connected with the macrolocalisation of the plastic strain in individual sections of a specimen (**Figure 1b**), and shears of the grain conglomerates in the substrate material (steel 25Kh1M1F).
- activation of the transverse shears of the boundaries, formation of local microfragments of a coating – this process is preconditioned by a relative shear of the blocks of a coating due to the attainment of limiting values at the boundaries of the mesostructural elements (blocks), **Figures 1c, d**.

Further plastic deformation of the substrate material causes an intensified accumulation of plastic strains at the boundaries between the newly created blocks and the generation of damage<sup>6</sup>. At this stage, the opening of the crack-like defects is determined by the mutual effect of the elements of the block structure and the adhesive strength of the coating. Upon attainment of the ultimate state failure takes place, as well as the shear with the formation of a rupture, and the shear of the coating fragment.

In **Figure 2** the dependence of the residual crack opening ( $\delta$ ) on the real necking of a specimen is presented. With respect to this dependence, three sections are noticeable and they are reflected in the change of the slope angle of the curve. Within the first section, the

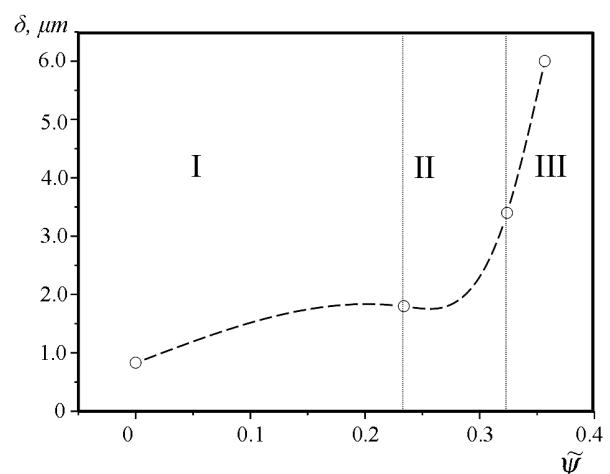


**Figure 2:** Stage-like nature of an increase in the mean value of a crack opening ( $\delta$ ) with an increase in the real necking of the specimen  $\tilde{\psi}$

**Slika 2:** Stopničasta narava srednje vrednosti odpiranja razpoke ( $\delta$ ) z naraščanjem resnične kontrakcije vzorca  $\tilde{\psi}$

newly formed cracks of the fatigue origin are located perpendicularly to the direction of loading; they have an insignificant residual opening ( $\delta = 1.0 \dots 2.0 \mu\text{m}$ ) and are separated from each other. So, the processes of the mutual effect of multiple defects are insignificant.

The second section corresponds to the opening and growth of the already formed network of defects. The coating acquires the properties of a breakup-block medium by dividing itself into separate "islands" of the material surrounded by multiple cracks. The residual crack opening in this section varies within the range of  $\delta = 2.0 \dots 4.0 \mu\text{m}$ .

The third section corresponds to the critical opening of the defects of  $\delta > 4.0 \mu\text{m}$  and a fragmentation of the coating. In this case, individual fragments of the coating are slipping relative to one another. In our opinion, local strains can be determined by using these fragments as the markers of displacements.

#### 4 DISCUSSION OF IDENTIFICATION OF MULTIPLE CRACKS IN NANOCOATING

The algorithm for identifying the crack positions consists of the following main steps: binarisation of the original grayscale image, its filtering, repeated binarisation of the obtained image and its skeletonisation<sup>3,4</sup>. After the completion of the above operations we obtain an array of points that describe the geometrical parameters of the network of cracks in the image. While setting the algorithm, several parameters are used, which are crucial to the correct and precise identification of a crack.

The original image is a colour image obtained with an electron microscope (**Figure 3**). In order to simplify the analysis it is transformed into a black-and-white one by means of an adaptive binarisation, which allows us not only to identify potential objects (cracks), but also to eliminate the effect of inhomogeneous illumination during the image acquisition.

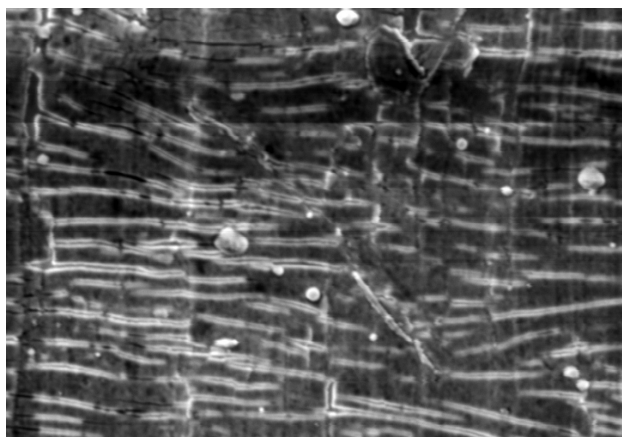


**Figure 3:** Original grayscale image  
**Slika 3:** Originalen sivinski posnetek

The most important parameter of this stage of the algorithm, which has a significant effect on the final result of the identification of the geometrical crack parameters, is the background L edge. A wrong choice of the background edge leads to the situation when a part of an object to be identified is mistaken for the background, or fictitious objects are found that are actually a part of the background. The "correctly chosen parameter" allows a value of the background border, at which the number of the identified crack objects approximates, as much as possible, the number of the cracks available in the image that can be identified by the operator. The range of the optimal values for the said parameter was determined by an experimental method<sup>11</sup>. The crack identification algorithm and the background border effect on the final result are considered in greater detail in our previous papers<sup>8</sup>.

A change in the background edge causes a displacement of the edges of the objects found in the image, due to which the geometrical characteristics of the cracks calculated as a result of the algorithm operation may vary a little.

The result of the transformation is a monochrome image of the surface studied. It contains basic information about the location of potential objects sought; however, it also contains a large amount of noise elements, which complicate the process of identification and, to a certain extent, distort the general view of the cracked surface. In order to reduce the effect of the noise elements (which are present after the binarisation of the original grayscale image) and join the close-set individual fragments of a crack into a solid object, the filtering was performed followed by a repeated binary transformation of the filtered image.

Filtering is carried out in two stages: first, a discrete gauss filter is used, next the obtained image is enhanced by applying the filter to increase the image contrast<sup>12</sup>. The gauss filter is effective in suppressing the noises and smearing the edges of the image objects, as a result of



**Figure 4:** Final image with detected cracks and a network of reference points

**Slika 4:** Končna slika z odkritimi razpokami in mrežo referenčnih točk



which the objects are formed that correspond to the crack positions. The contrast filter allows an increase in the contrast of the image elements.

For the final distinguishing of a crack a repeated binarisation of the filtered image is used. Following all of the above transformations, the final image is obtained, describing the picture of a cracking on the surface analysed (**Figure 4**). In this picture, white pixels correspond to the background and black ones to the cracks.

The most important parameter of the algorithm at this stage is the filter kernel size  $h_F$ . It has an effect on the processes of "screening" the background pixels and coalescence of the separated fragments of the crack, therefore its change may significantly affect the final result of the identification. The image obtained as a result of the above transformations contains information about the shape and the area of the cracks; however, it cannot be used directly for determining the quantitative parameters, such as the number, the length, the slope of the cracks, etc. In order to approximate the aggregate of pixels, which form the detected objects/cracks, a skeletonisation is performed using the simplest array of points<sup>3,4</sup>. The skeletonisation allows us to distinguish the wireframe lines of the cracks by detecting medial lines with the thickness of one pixel in the image. Reference points of the medial lines are the final set of data, on the basis of which a conclusion is made about the crack location, direction of the crack propagation and its length<sup>12</sup>.

Both of the algorithm parameters considered have an immediate effect on the position of the obtained wireframe (medial) lines; therefore, an important issue is an assessment of their influence on the accuracy of determining the identified cracks<sup>13</sup>. The  $L$  parameter is the background border of the binary transformation. The  $h_F$  parameter is the filter kernel size. The corresponding corrections are made to the paper results. The background border of the binary transformation is the generally used parameter, which does not require any special clarification.

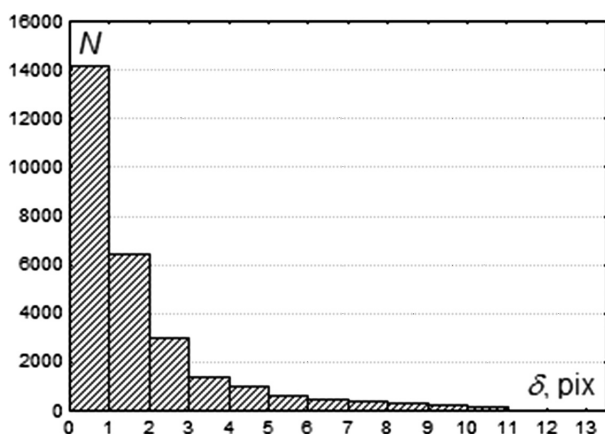


**Figure 5:** Displacement-distribution diagram for the points of the wireframe line

**Slika 5:** Diagram premika točak v liniji mreže

The effect of these parameters was assessed by observing the algorithm operation with the variation of their value within a certain range. To this end, the arrays of the  $P$  point coordinates, which form the wireframe line, were fixed for each group of the parameters ( $h_F$  and  $L$ ). The obtained arrays of  $P$  points were used to determine the displacements of the wireframe line pixels depending on the values of the algorithm parameters studied. It is clear that the other algorithm parameters have insignificant effects on the identification results. Therefore, in general, the total error of determining the position of the crack wireframe line  $\xi$ , caused when setting the algorithm parameters, does not exceed the following value:

$$\xi \leq \xi_L + \xi_h \quad (2)$$

where  $\xi_L$  is the error in setting the background edge;  $\xi_h$  is the error caused by a displacement of the coordinate centre in setting the filter kernel size.

With a view to assessing the effect of the variation of the above algorithm parameters on the displacement of the wireframe line, the relative background edge  $L$  was varied within 10...30 %, and the filter kernel size  $h_F$  varied from 5 to 10 pixels. In this case, the array of  $P^\mu(L, h_F)$  points was fixed for every set of parameter values individually, where  $\mu \in (1...M)$ , and  $M$  is the number of observations. In order to calculate the displacement of the wireframe line, the closest point of the  $P^{\mu 2}(L, h_F)$  array was found for every  $P^{\mu 1}(L, h_F)$  point, and the distance between them was calculated. As a result of the above calculations, the aggregate of sets was obtained, which characterises the displacement of the points of wireframe line  $\delta^\mu(L, h_F)$ . Each  $\delta^\mu_i$  element equals the distance between point  $P^{\mu 1}_i$  and point  $P^{\mu 2}_j$ . To make the sample homogeneous by removing errors from it, the sample was censored using Wright's criterion. In this case, the values, for which the  $|\xi_i - \bar{\xi}| \geq 3S_\xi$  condition was fulfilled (where  $\bar{\xi}$  is the mean value and  $S_\xi$  is the standard deviation of the sample), were removed from the  $\delta^\mu(L, h_F)$  aggregate of values.

A typical view of the  $\delta^\mu(L, h_F)$  displacement-distribution histogram for the image (**Figure 3**) at the variation of the filter kernel size from 5 to 7 pixels and the constant background edge of 20 % is shown in **Figure 5**. It is clear that the majority of the points shift very insignificantly (only by a few pixels).

The investigation of a series of images showed that, at the constant background edge of  $L = 20$  % and the variation of the filter kernel  $h_F$  from 5 to 10 pixels, the standard deviation of the sample varies within the range of 1.7–2.2 pixels.

When recalculated in the units of the real object length, the displacement varies within the range of 0.20...0.26  $\mu\text{m}$ . The maximum displacement fixed for various measurements varied from 0.18  $\mu\text{m}$  to 0.29  $\mu\text{m}$ . Moreover, an increase in the kernel size proportionally influences the displacement of the crack wireframe lines.

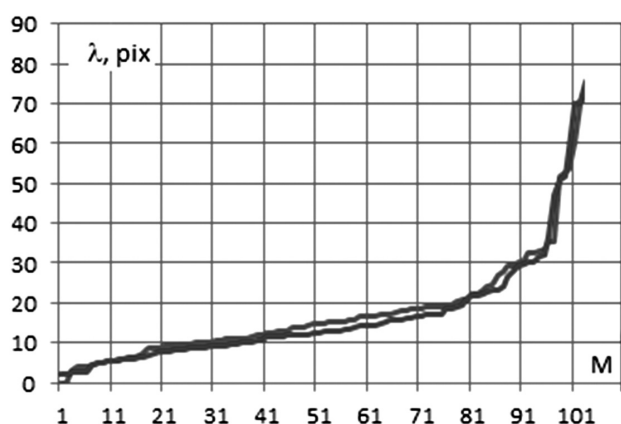


**Figure 6:** Graphs of detected crack lengths  $\lambda$  for the limiting values of the algorithm parameters

**Slika 6:** Graf dolžine odkritih razpok  $\lambda$  za omejene vrednosti parametrov algoritma

At the constant kernel size of  $h_F = 5$  pixels and the variation of  $L$  from 5 % to 20 %, the standard deviation varies within the range of 1.14...1.95 pixels (which corresponds to 0.13...0.23  $\mu\text{m}$  on the test specimen). In order to reveal the effect of the changes of any of the algorithm parameters studied on the final result – the geometrical parameters of the crack network – a number of investigations were carried out, during which the background edge varied within the range of 5...20 %, and the filter kernel size varied from 5 to 10 pixels.

**Figure 6** shows the crack-length-distribution graphs for the image (**Figure 3**) at the limiting values of the background edge and the filter kernel size. The results obtained show that, for different images within the range of the algorithm parameters investigated, the deviation of the length from the mean value is within 0–0.30  $\mu\text{m}$ . With the confidence probability of 95 % this deviation does not exceed 0.26  $\mu\text{m}$ .

## 5 CONCLUSIONS

On the basis of the results of the investigations into the cracking processes in the surface of the heat-resistant steel with a nanocoating, it is established that multiple defects are caused by a plastic deformation of the substrate material. Multiple defects are nucleated in the strain-localisation areas and in the zones of microstructural inhomogeneity.

The new algorithm of digital defectometry has been developed, which is intended for the identification of the

crack-network elements in a nanocoating. The effect of the main algorithm parameters on the measurement results relating to the geometrical characteristics – the coordinates, the lengths and the slope angles of the cracks – is investigated. The results obtained allow a compilation of such a combination of the algorithm parameters, with which the general measurement error of the cracking parameters will be minimal.

It was found that the optimum parameters of the algorithm for identifying the cracks have the following limits:  $h_F = 5...7$  pixels and  $L = 8\text{--}14$  %. With the confidence probability of 95 % the deviation of length is less than 0.30  $\mu\text{m}$ .

## 6 REFERENCES

- <sup>1</sup> V. E. Panin (Ed.), Physical mesomechanics of heterogeneous media and computer-aided design of materials, Cambridge Interscience Publishing, Cambridge 1998, 339
- <sup>2</sup> P. Z. Iordache, R. M. Lungu, G. Epure, et al., J. of Optoelectron. Adv. Mater., 28 (2011), 550
- <sup>3</sup> P. Yasniy, P. Maruschak, I. Konovalenko, V. Gliha, T. Vuherer, R. Bishchak, Multiple cracks on continuous caster rolls surface: A three-dimensional view, Proc. of the 4<sup>th</sup> Int. conf. Processing and Structure of Materials (May 27–29), Palić, Serbia, 2010, 7–12
- <sup>4</sup> P. Yasniy, P. Maruschak, I. Konovalenko, R. Bishchak, Materials Science, 46 (2008), 833
- <sup>5</sup> O. V. Sergeev, M. V. Fedorisheva, V. P. Sergeev, N. A. Popova, E. V. Kozlov, Increase of plasticity of maraging steels by means of ion beam nanostructuring of surface layer, Proc. of the 10<sup>th</sup> Int. Conf. on Modification of Materials with Particle Beams and Plasma Flows, Tomsk, (September 19–24), 2010, 342
- <sup>6</sup> P. Yasniy, P. Maruschak, R. Bishchak, V. Hlado, A. Pylypenko, Theoretical and Applied Fracture Mechanics, 52 (2009), 22
- <sup>7</sup> P. Yasniy, P. Maruschak, V. Hlado, D. Baran, Materials Science, 46 (2008), 144
- <sup>8</sup> I. V. Konovalenko, P. O. Maruschak, Optoelectronics, Instrumentation and Data Processing, 47 (2011), 49
- <sup>9</sup> P. O. Maruschak, S. V. Panin, S. R. Ignatovich et al., Theoretical and Applied Fracture Mechanics, 57 (2012), 43
- <sup>10</sup> P. Yasniy, I. Konovalenko, P. Maruschak, Investigation into the geometrical parameters of a thermal fatigue crack pattern, WSEAS Int. Conference New aspects of engineering mechanics, structures and engineering geology, Heraklion, Crete Island, Greece, 2008, 61–66
- <sup>11</sup> I. Konovalenko, P. Maruschak, Computer analysis of digital images with quasiperiodical structure, Proc. of the Int. conf. TCSET 2012 – Modern Problems of Radio Engineering, Telecommunications and Computer Science, Lviv-Slavske, (February 21–24), 2012, 419
- <sup>12</sup> P. Yasniy, P. Maruschak, I. Konovalenko, R. Bishchak, Mechanika, 17 (2011) 3, 251
- <sup>13</sup> W. K. Pratt, Digital image processing (4<sup>th</sup> Ed.), Wiley, 2007, 807



# LABORATORY ASSESSMENT OF MICRO-ENCAPSULATED PHASE-CHANGE MATERIALS

## LABORATORIJSKA OCENA MIKROENKAPSULIRANIH MATERIALOV S FAZNO PREMENO

**Milan Ostrý<sup>1</sup>, Radek Přikryl<sup>2</sup>, Pavel Charvát<sup>3</sup>, Tomáš Mlčoch<sup>2</sup>, Barbora Bakajová<sup>2</sup>**

<sup>1</sup>Brno University of Technology, Faculty of Civil Engineering, Veveří 95, 602 00 Brno, Czech Republic

<sup>2</sup>Brno University of Technology, Faculty of Chemistry, Purkyňova 464/188, 612 00, Brno, Czech Republic

<sup>3</sup>Brno University of Technology, Faculty of Mechanical Engineering, Technická 2, 616 69, Brno, Czech Republic  
ostrym@fce.vutbr.cz

*Prejem rokopisa – received: 2011-10-20; sprejem za objavo – accepted for publication: 2012-05-07*

The operation of low-energy-consumption and passive houses can be based on the passive or active utilization of renewable energy sources. Thermal energy storage plays a key role in the application of renewable energy sources and it thus contributes to the reduction of global CO<sub>2</sub> emissions. Thermal energy storage is commonly based on the sensible- or latent-heat-storage techniques. Latent-heat thermal storage is based on the absorption or release of heat when a storage material is changing phase. The thermal-storage materials suitable for latent-heat storage are called Phase-Change Materials (PCMs). PCMs have considerably higher thermal-energy-storage densities than the sensible-heat-storage materials and they are able to absorb large quantities of energy in a small range of temperatures during the phase change. Nowadays, micro-encapsulation of phase-change materials is one of the promising approaches in the integration of latent-heat storage in various applications. The most important properties of a latent-heat-storage medium are the heat of the fusion and the temperature range of the phase change. The correct determination of the physical and chemical properties is essential for a practical use of phase-change materials. The paper deals with the results of a laboratory assessment of the selected micro-encapsulated PCMs and shows a practical example of a possible integration in the building structures.

**Keywords:** phase-change materials, latent heat, differential scanning calorimetry, micro-encapsulation

Delovanje nizkoenergijskih pasivnih hiš lahko temelji na uporabi aktivne ali pasivne uporabe obnovljivih energijskih virov. Shranjevanje toplotne energije igra ključno vlogo pri uporabi obnovljivih virov energije in zato vpliva na zmanjšanje globalne emisije CO<sub>2</sub>. Shranjevanje toplotne energije navadno temelji na smiselni tehniki ali tehnikah shranjevanja latentne toplote. Shranjevanje latentne toplote temelji na absorpciji ali sproščanju toplote, ko material za shranjevanje spreminja fazo. Materiale, ki so primerni za shranjevanje latentne toplote, imenujemo Materiali s fazno spremeno (PCM). PCM imajo občutno višjo gostoto shranjenosti toplotne energije v primerjavi z občutljivimi materiali za shranjevanje toplote in so sposobni absorbirati med fazno spremeno večjo količino energije v manjšem temperaturnem intervalu. Dandanes je vgradnja mikroenkapsulacijskih materialov s fazno spremeno obetajoča za številne možnosti uporabe. Najpomembnejši lastnosti medija za shranjevanje latentne toplote sta tališna toplota in temperaturno področje fazne premene. Pravilno določanje fizikalnih in kemijskih lastnosti je bistveno za praktično uporabo materialov s fazno spremeno. Ta članek obravnava laboratorijsko oceno izbranih PCM in kaže praktičen primer možnosti njihove uporabe v gradbeništvu.

**Ključne besede:** materiali s fazno spremeno, latentna toplota, diferenčna dinamična kalorimetrija, mikroenkapsulacija

## 1 INTRODUCTION

Sensible-heat storage utilizes the heat capacity and the change in the temperature of a thermal-storage material during the process of charging and discharging the heat<sup>1</sup>. The amount of stored heat depends on the specific heat of the storage material, the temperature difference and the amount (mass) of the material.

Any building material can generally be used for sensible-heat thermal storage but the materials with high specific heat and high density usually perform the best. The typical representatives of sensible-heat-storage materials are common building materials such as ceramic bricks or blocs, concrete, lime-cement bricks and stone. The indoor environments with the envelopes made of such materials exhibit a much higher degree of thermal stability than the light-weight envelopes (e.g., timber-frame walls). The thermal storage in common building structures has its limits. The first limit is the use of heavy-weight structures. This is a very important con-

straint, especially in modern buildings. For example, glass-building envelopes would need to be supplemented with heavy-weight indoor structures and that is not always possible or desirable. This is where latent-heat storage can be employed.

### 1.1 Latent-heat storage

Latent-heat storage is based on the absorption or release of heat when a storage material undergoes a phase change from solid to liquid<sup>1</sup>. Such thermal-storage materials are called Phase-Change Materials (PCMs). They use chemical bonds to store and release heat<sup>2</sup>. PCMs have a high ability to store thermal energy. PCMs are able to absorb large quantities of heat in a small range of temperatures during a phase change. Latent-heat storage is one of the most efficient ways of storing thermal energy<sup>3</sup>. The selection of a PCM is mainly based on its melting temperature. A PCM's melting temperature should be within the operating temperature range of



the thermal system. With respect to building use, it means within the thermal-comfort temperature range of an occupied space.

### 1.2 Selection of phase-change materials

Phase-change materials can be chosen from both organic and inorganic materials. The organic phase-change materials melt and freeze repeatedly without a phase-change segregation and crystallize with little or no supercooling. The organic phase-change materials, e.g., the paraffins, are compatible with metals without any risk of corrosion. The paraffins have a rather poor thermal conductivity and they are flammable. The melting point of the alkanes increases with an increased number of carbon atoms<sup>1</sup>.

The inorganic PCMs are compatible with plastics and their storage capacity is higher than the capacity of the organic PCMs due to their higher density. The inorganic PCMs, e.g., salt hydrates, are incompatible with uncoated metals. The salt hydrates are important PCMs because of the high heat of fusion and a small volume change during the process of melting and solidification. The main disadvantages of salt hydrates are their poor nucleating properties that result in supercooling.

Suitable PCMs from both organic and inorganic groups are available for applications in the latent-heat-storage technology. Many phase-change materials cannot be used as latent-heat-storage mediums because of the problems with their chemical stability, toxicity, corrosion, volume change and price. The phase-change materials should meet the following thermodynamic, kinetic, chemical and economic criteria<sup>4</sup>.

Thermodynamic criteria:

- high heat of fusion;
- melting range in the desired operating-temperature range;
- high specific heat;
- high thermal conductivity;
- high density and low volume change;
- congruent melting.

Kinetic criteria:

- little or no supercooling during the solidification process;
- sufficient crystallization rate.

Chemical criteria:

- compatibility with the container;
- long-term chemical stability;
- no toxicity;
- no flammability.

Economic criteria:

- availability in the required quantities;
- low cost.

## 2 MATERIALS AND METHODS

The research and development at the Brno University of Technology is focused on the utilization of the latent-heat storage in passive and active solar-heating and cooling technologies. The development of the advanced latent-heat-storage technologies is strongly dependent on the possibility to find suitable phase-change materials that fulfill the above-mentioned requirements. The second problem lies in finding a suitable technology for an integration of latent-heat-storage media in building structures.

Micro-encapsulation is one of the possible approaches to the PCM integration in building structures<sup>5</sup>.

### 2.1 Micro-encapsulated PCMs

Micro-encapsulation is based on enclosing a PCM in a very small capsule. The micro-capsules can be included in the common building materials and structures. Special attention has to be paid to the choice of the material of the capsule to avoid a chemical reaction between the capsules and the building material<sup>5</sup>. Micro-capsules can be added to the composition of lime or gypsum plaster, concrete, fibrous wooden slabs and gypsum wall boards.

A special composition of gypsum plaster and micro-encapsulated PCMs was developed for the application in building structures. The gypsum plaster contains 30 % of micro-capsules Micronal DS 5008 X. The plaster is the final layer of the walls and ceilings in the buildings with a low thermal mass.

### 2.2 Differential scanning calorimetry

Differential Scanning Calorimetry (DSC) is a thermo-analytical technique where a temperature range is scanned. The difference between the amount of the heat required for changing the temperature of a sample and its reference is measured as a function of temperature. Both the sample and the reference are maintained at nearly the same temperature throughout the experiment. The reference is used to determine the heat stored in the sample by considering the difference between the signal of the sample and the reference<sup>6</sup>.

The DSC heat flux has got a Siamese structure<sup>5</sup>. The sample and the reference are connected to the same metal disc. The behavior difference between the sample and the reference submitted to the same temperature excitation leads to a voltage difference between the sample and the reference. The absorbed heat in the PCM sample is deduced from the voltage<sup>5</sup>. The weight of the sample is only a few grams. A calorimeter PYRIS1 Perkin Elmer was used in the tests.

### 3 RESULTS AND DISCUSSION

The experiments focused on determining the thermal properties of a micro-encapsulated PCM and the plaster containing 30 % of a PCM.

**Figure 1** shows the results after two heating/cooling cycles for the micro-capsules with a PCM. The results were obtained with the continuous scanning mode at the rate of 1 °C/min. This rate is rather quick compared to common conditions in rooms. The black and blue curves represent heating, while the red and green curves show the results of the cooling mode. There is some supercooling in the cooling phase that is not really problematic for a practical application in building structures. The presence of supercooling plays a role in discharging the heat stored in the PCM.

As can be seen, the PCM displays two heat-flow peaks. The first peak is well below the comfortable indoor air temperature, thus, it has no implications for the practical use. **Table 1** shows the peak temperatures for both cycles. The difference between the peaks of the cooling and heating phases is about 2 °C. **Table 2** shows the heat of fusions for the heating and cooling phases.

**Table 1:** Peak temperatures for the PCM

**Tabela 1:** Maksimalne temperature za PCM

Cycle	Peak temperature $T/^\circ\text{C}$	
	cooling	heating
I	22.32	24.32
II	22.40	24.20

**Table 2:** Heat of fusions for the PCM

**Tabela 2:** Talilna toplota za PCM

Cycle	Heat of fusion in J/g	
	cooling	heating
I	-84.16	86.83
II	-81.29	86.76

Thermal stability of PCMs was determined with a thermogravimetric apparatus (TGA) Q500 TA Instru-

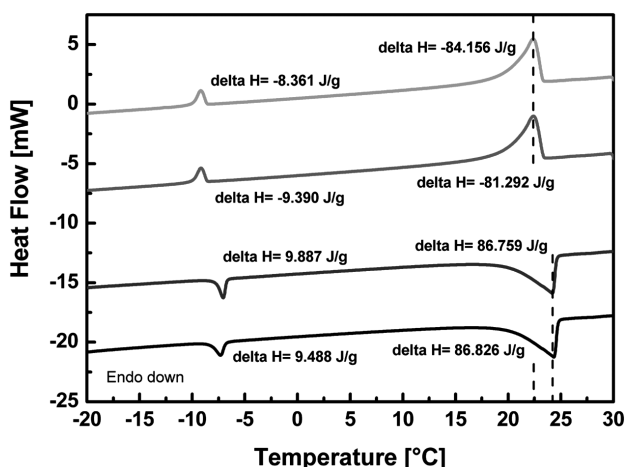


**Figure 1:** DSC results for the PCM

**Slika 1:** Rezultati DSC za PCM

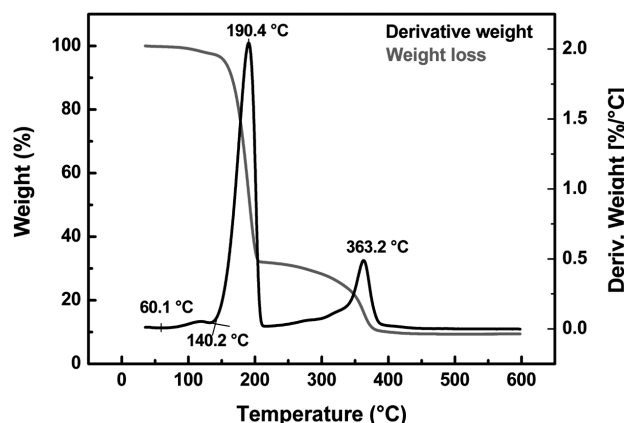


**Figure 2:** Thermal stability of the PCM

**Slika 2:** Toplotna stabilnost PCM

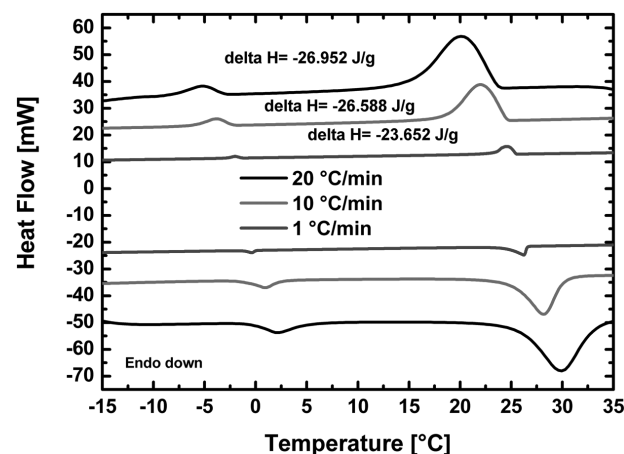


**Figure 3:** DSC results for gypsum plaster

**Slika 3:** Rezultati DSC za mavčni omet

ments. The results from TGA are shown in **Figure 2**. Significant weight losses start at 140 °C, which is above the commonly used temperature range. The temperature range of the indoor climate between 15 °C and 35 °C can be assumed for building applications. **Figure 3** shows DSC results for a gypsum plaster with 30 % of Micronal D5008 X. The chart shows a significant reduction of the latent heat during the heating and cooling processes. Three temperature rates of (1, 10 and 20) °C/min were tested. As can be seen, the onset and the peak temperatures during the heating and cooling strongly depend on the temperature ramp. Melting temperatures rise with an increased heating rate. A shift of the solidification-temperature range follows an increased rate of cooling. The risk of supercooling increases with a faster cooling rate.

### 4 CONCLUSION

The results obtained with DSC confirm suitability of the tested PCMs and the plaster for their integration in building structures. The peak temperature during the

heating is about 24 °C. The micro-encapsulated PCMs have a required melting range for the thermal-energy storage during the summer season. The difference between the peak-melting and solidification temperatures of a PCM is about 2 °C allowing a proper, natural or driven, regeneration of the heat-storage medium at night.

### Acknowledgement

This work was supported by the Czech Science Foundation under contract No. P101/11/1047 and by the Czech Science Foundation under contract No. P104/12/1838 "Utilization of latent heat storage in phase change materials to reduce primary energy consumption in buildings".

### 5 REFERENCES

- <sup>1</sup> A. Sharma, V. V. Tyagi, C. R. Chen, D. Buddhi, Review on thermal energy storage with phase change materials and applications, *Renewable and Sustainable Energy Reviews*, 13 (2009), 318–345
- <sup>2</sup> V. V. Tyagi, D. Buddhi, PCM thermal storage in buildings: A state of art, *Renewable and Sustainable Energy Reviews*, 11 (2007), 1146–1166
- <sup>3</sup> M. M. Farid, A. M. Khudhair, S. A. K. Razack, S. Al-Hallaj, A review on phase change energy storage: materials and applications, *Energy Conversion and Management*, 45 (2004), 1597–1615
- <sup>4</sup> H. P. Garg, S. C. Mullick, A. K. Bhargava, *Solar Thermal Energy Storage*, D. Reidel Publishing Company, 1985, 642
- <sup>5</sup> F. Kuznik, D. David, K. Johannes, J. J. Roux, A review on phase change materials integrated in building walls, *Renewable and Sustainable Energy Reviews*, 15 (2011) 1, 379–391
- <sup>6</sup> H. Mehling, L. F. Cabeza, *Heat and cold storage with PCM. An up to date introduction into basics and applications*, Springer-Verlag, Berlin Heidelberg 2008, 308

## CONTENT OF Cr AND Cr (VI) IN A WELDING FUME BY DIFFERENT Cr CONTENT IN AN EXPERIMENTAL COATING OF A Cr-Ni RUTILE ELECTRODE

### VSEBNOST Cr IN Cr (VI) V VARILNEM DIMU PRI RAZLIČNI VSEBNOSTI Cr V PLAŠČU RUTILNE ELEKTRODE Cr-Ni

Razija Begić<sup>1</sup>, Monika Jenko<sup>2</sup>, Matjaž Godec<sup>2</sup>, Črtomir Donik<sup>2</sup>

<sup>1</sup>Faculty of Engineering, University of Bihać, Irfana Ljubijankića bb., 77000 Bihać, Bosnia and Herzegovina

<sup>2</sup>Institute of Metals and Technology, Lepi pot 11, Ljubljana, Slovenia  
razijabegic@yahoo.co.uk

*Prejem rokopisa – received: 2011-11-17; sprejem za objavo – accepted for publication: 2012-06-01*

In the SMAW welding process welding fumes are generated, harmful to human health and the environment. A welding fume is a mixture of gaseous and solid phases, which are generated during most of the electric-arc-welding processes. This article presents the researches of the particles that constitute the solid-phase-welding fumes. The change in the chemical composition of an electrode and its components (the coating and the core) can affect the chemical composition of the particles in welding fumes. The largest amount of fumes, about 80 %, is generated from electrodes and, accordingly, the focus of research was the influence of the chemical composition of an electrode on the chemical composition of the welding-fume particles. This paper presents the research results obtained for the content of Cr and Cr (VI) oxide particles in welding fumes. The experimental work on six variants of commercial electrodes E 23 12 2 LR 12, a welding chamber collecting fume particles and a chemical analysis of the particles were applied according to the standard EN15011. The aim was to determine an experimental welding electrode that should generate the welding-fume particles with the lowest content of Cr and Cr (VI) oxide.

Keywords: health, welding fumes, particle, coated electrodes, Cr (VI)

Med varilnim procesom SMAW nastaja dim, ki je škodljiv za zdravje in okolje. Dim, ki nastaja pri večini varilnih procesov, je mešanica plinov in trdnih delcev. Ta članek opisuje preiskavo delcev, ki so trdni del dima, ki nastane pri varjenju. Spreminjanje sestave elektrode (stržena in obloge) vpliva na kemijsko sestavo trdnih delcev v dimu. Največji delež dima, okrog 80 %, izvira iz elektrode, zato je bila raziskava osredinjena na učinek kemijske sestave elektrode na kemijsko sestavo delcev v dimu. Ta članek navaja rezultate raziskav vsebnosti oksidnih delcev Cr in Cr (VI) v dimu pri varjenju. Eksperimentalno delo je bilo izvršeno s šestimi različnimi komercialnimi elektrodami E 23 12 2 LR 12. V varilni komori zbrani delci iz dima so bili analizirani skladno s standardom EN15011. Namen je bil ugotoviti eksperimentalno elektrodo, ki proizvaja med varjenjem delce z najmanjšo vsebnostjo Cr v Cr (VI)-oksidu.

Ključne besede: zdravje, varilni dim, delci, opllašene elektrode, Cr (VI)

## 1 INTRODUCTION

No material of any source can be directly compared with the composition and structure of a welding vapour. Chromium is generated in flue gases of welding with coated high-alloyed Cr electrodes and it appears in several phases, of which the six-valent oxide of chromium, Cr (VI), is the most damaging. Epidemiological studies prove the Cr (VI) compounds to be occupational carcinogens. During the MAG stainless-steel welding much less Cr (VI) is generated than during SMAW. Cr (III) compounds are biologically inert because they do not enter the cell, while Cr (VI) causes cell mutation. Chromium has a low threshold limit value (TLV), which is 0.5 mg/m<sup>3</sup>.<sup>1</sup>

## 2 EXPERIMENT

Experimental electrodes were made according to the experimental plan shown in **Table 1**, based on the changes in the chromium content in an electrode and its components (a wire<sup>2</sup> and an electrode coating), marked

with labels A, B, C, D, E and F, representing six varieties of commercial electrodes E 23 12 2 LR 12.

**Table 1:** Change in the contents of Cr in an electrode and its components<sup>4</sup>

**Tabela 1:** Spreminjanje vsebnosti Cr v elektrodi in v plašču elektrode<sup>4</sup>

No	Electrode	Cr content in an electrode wire <sup>2</sup>	Cr content in an electrode coating	Mean Cr content in an electrode
1.	A	18.2 %	20.8 %	19.3 %
2.	E		22.8 %	20.1 %
3.	C		29.4 %	22.8 %
4.	B	19.6 %	18.1 %	19.0 %
5.	F		20.0 %	19.8 %
6.	D		27.4 %	22.7 %

For the tests related to emissions and their qualitative and quantitative chemical analyses it is necessary to have the appropriate equipment, which primarily consists of a collecting chamber, made for the purpose of this research according to the model in the standard EN15011<sup>3</sup>. The chemical composition of the welding-fume particles was obtained with the tests for six experimental electrodes, a



total of 18 probes. The current level was constant,  $I = 95$  A, and the basic material was a low-carbon, unalloyed structural steel S235JRG2.

### 3 RESULTS

The content of chromium in the welding-fume particles is shown in **Table 2**, determined with the AAS method.

**Table 2:** Results of a chemical analysis of the Cr content in the fume particles<sup>4</sup>

**Tabela 2:** Rezultati kemijske analize vsebnosti Cr v delcih dima<sup>4</sup>

No	Electrode	Probe	Cr content in the welding-fume particles, %	
			Cr content	Cr mean value
1	A	A1	5.62	5.91
2		A2	6.00	
3		A3	6.10	
4	B	B1	5.33	5.09
5		B2	5.20	
6		B3	4.73	
7	C	C1	6.00	5.58
8		C2	5.84	
9		C3	4.90	
10	D	D1	5.05	5.18
11		D2	5.40	
12		D3	5.05	
13	E	E1	5.10	5.06
14		E2	4.95	
15		E3	5.10	
16	F	F1	5.30	5.05
17		F2	5.00	
18		F3	4.85	

SEM-EDS and XPS chemical analyses of fume particles were carried out at the Institute of Metal Materials and Technology, Ljubljana. As an addition to the analysis of Cr and Cr (VI) in welding fumes and

particles, the performed chemical analyses also included the contents of Mo, Mn and Ni as the most influential alloying elements and other elements and compounds. The change in the content of Cr particles in welding fumes shown in **Figure 1** depends on the increase in the Cr content in the lining of an experimental electrode.

The functional dependence of the Cr content in the welding fumes and the Cr content in the electrode coating in **Figure 1** corresponds to the exponential equation:

$$Cr_{ZD} = 5.05 + (1.74 \cdot 10^{-8})^{\frac{Cr_{coating}}{1.7}} \quad (1)$$

Reliability of the calculated functional dependence is relatively high with  $R^2 = 0.98$ .

A graphical representation of functional dependencies of the contents of Cr (VI) particles in welding fumes on the Cr content in electrodes and in electrode coatings is shown in **Figure 2**.

**Figure 2** corresponds to the exponential equation:

$$Cr(VI)_{ZD} = 4.74 + (6.2 \cdot 10^{-7})^{\frac{Cr_{coating}}{2.16}} \quad (2)$$

The reliability of functional dependence is relatively high being  $R^2 = 0.97$ .

### 4 DISCUSSION

The test conditions for electrode A were different than for the other electrodes and for this reason electrode A was excluded from the further analysis. The shape of the curve in **Figure 1** shows that a 23–24 % addition of Cr to the electrode coating causes no significant increase in the Cr content in welding fumes. However, if this amount is increased the content of Cr particles in welding fumes has a much stronger growth trend. Similarly, from **Figure 2** it can be concluded that no significant increase in the content of Cr (VI) particles in welding

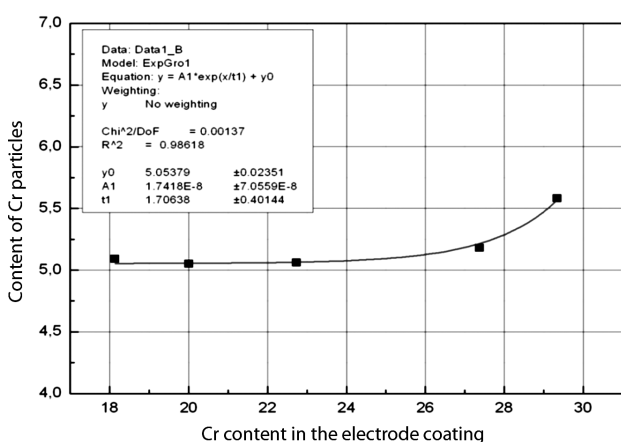


**Figure 1:** Content of Cr particles depending on the Cr content in the electrode coating<sup>4</sup>

**Slika 1:** Vsebnost Cr v delcih v odvisnosti od vsebnosti Cr v plašču elektrode<sup>4</sup>

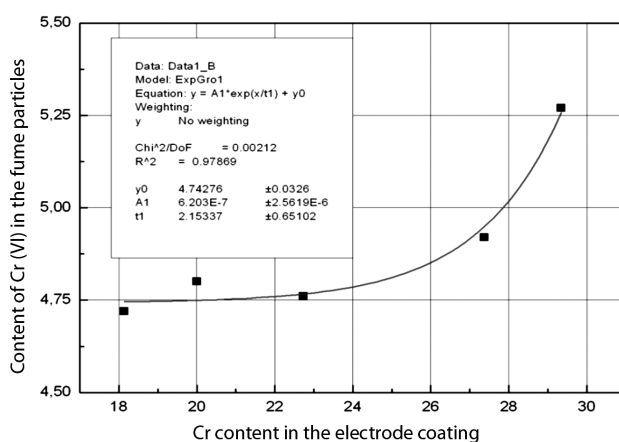


**Figure 2:** Content of Cr (VI) in the fume particles depending on the Cr content in the electrode coating<sup>4</sup>

**Slika 2:** Vsebnost Cr (VI) v delcih dima v odvisnosti od vsebnosti Cr v plašču elektrode<sup>4</sup>

fumes occurs due to a concentration of Cr in the electrodes above 24–25 % Cr.

## 5 CONCLUSION

The problems of welding fumes are becoming associated with harmful emissions that increasingly affect the protection of people and environment. Throughout the world we have seen an increased use of welding needed for joining the structures that are more and more being made of alloyed steel. Therefore, the production of the welding smoke is larger and the increasing use of the high-alloyed electrodes and the resulting chemical compositions of welding fumes are becoming more harmful. Any reduction of the harmful emissions to the atmosphere increases the protection of the people and environment. This paper explores this issue and the results obtained can be applied to the development of the electrodes for SMAW with a lower level of harmful emissions allowing a satisfactory quality of a weld. Two basic requirements needed for a SMAW

process and for the coated electrodes are examined. After qualitative and quantitative analyses of the particles in the welding fumes a feedback loop can be introduced, based on the formation of solid particles, helping us to make decisions on the introduction of a new alloy coating on the electrodes that can lower the amount of harmful components in the welding-fume particles.<sup>4</sup>

## 6 REFERENCES

- <sup>1</sup> V. E. Spiegel-Ciobanu, Von "Schweißbrauche" zu "Schweißtechnische Arbeiten", Die neuen technischen Regeln für Gefahrstoffe, Hannover, TRGS 528 TÜ Bd.50, 2009, Nr. 9
- <sup>2</sup> Rodacciai, Certificato di collaudo, Italia, May 2008
- <sup>3</sup> EN ISO 15011-1, Health and safety in welding and allied processes-Laboratory method for sampling fume and gases generated by arc welding-Part 1: Determination of emission rate and sampling for analysis of particulate fume, April 2002
- <sup>4</sup> R. Begić, Doctoral dissertation, Exploring optimal technological composition of electrode coatings in terms of minimizing welding fumes, September 2011, Faculty of Engineering, University of Bihać



## USE OF A TWO-DIMENSIONAL PSEUDO-HOMOGENEOUS MODEL FOR THE STUDY OF TEMPERATURE AND CONVERSION PROFILES DURING A POLYMERIZATION REACTION IN A TUBULAR CHEMICAL REACTOR

### UPORABA DVODIMENZIONALNEGA PSEVDHOMOGENEGA MODELA ZA ŠTUDIJO TEMPERATURE IN PROFILA PRETVORBE MED REAKCIJO POLIMERIZACIJE V CEVASTEM KEMIJSKEM REAKTORJU

**Mohamed Marghsi, Djafer Benachour**

Laboratory of Preparations, Modifications and Applications of Multiphase Polymeric Materials (LMPMP), Ferhat Abbas University,  
19 000 Setif, Algeria  
mmarghsi@yahoo.fr

*Prejem rokopisa – received: 2012-01-18; sprejem za objavo – accepted for publication: 2012-03-06*

A two-dimensional pseudo-homogeneous model is used to study temperature and conversion profiles during the polymerization reaction of low-density polyethylene (LDPE) in a tubular chemical reactor. This model is integrated with the Runge-Kutta 4<sup>th</sup>-order semi-implicit method, using orthogonal collocation to transform a system of complex equations into the ordinary differential ones, with respect to the heat and mass transfers involved.

Ethylene polymerization has been simulated over a range of temperatures and pressures and according to the mechanisms of radical polymerization. The results of several tests, carried out under the conditions similar to those of an industrial-scale polymerization, are presented. The influences of the initial temperature  $T_0$ , the total pressure  $P_t$  and the ratio  $L/D$  (the main dimensions of the reactor) on the profiles of the temperature and conversion rates are tested and analyzed to predict the behavior and performance of the tubular chemical reactor considered.

The focus was on the effect of an increase in the initial temperature  $T_0$  since such a rise results in a decrease in  $T_c$  (hot spot) appearing at the entrance of the reactor on the one hand, and in an improved conversion on the other hand. An opposite effect is observed for  $P_t$  since a pressure increase will result in a rapid rise in  $T_c$  and a decrease in the conversion. The ranges of pressures and temperatures are thus limited by the system performance: excessive pressures must be avoided and working temperatures must be chosen in the range where the polymerization reaction is very fast; such conditions allow not only a good conversion, but also a resulting polymer with a low crystallinity and, thus, a low density.

In the present work the effect of the  $L/D$  ratio was also studied in order to find the most suitable ratio that permits the best evacuation of the heat released during the polymerization.

**Keywords:** modeling, tubular reactor, simulation, low-density polyethylene, pseudo-homogeneous two-dimensional model

Dvodimenzijski psevdohomogeni model je bil uporabljen za študij temperature in profila pretvorbe med reakcijo polimerizacije polietilena z nizko gostoto (LDPE) v cevastem kemijskem reaktorju. V model je bila vključena Runge-Kuttova semiimplicitna metoda 4. reda z uporabo ortogonalne kolokacije za pretvorbo sistema kompleksnih enačb v navadne diferencialne enačbe glede na vključen prenos toplote in mase.

Simulirana je bila polimerizacija etilena v širšem področju temperature in tlaka skladno z mehanizmom radikalne polimerizacije. Predstavljenih je več preizkusov polimerizacije, izvedenih v razmerah, podobnih industrijskim. Preizkušen in analiziran je bil vpliv začetne temperature  $T_0$ , celotnega tlaka  $P_t$  in razmerja  $L/D$  (glavne dimenzije reaktorja) na profil temperature in hitrost pretvorbe, da bi bilo mogoče napovedati ponašanje in zmogljivost uporabljenega cevastega reaktorja.

Pozornost je bila usmerjena na učinek povišanja začetne temperature  $T_0$ , ker to po eni strani vpliva na znižanje  $T_c$  (vroča točka) na vstopu v reaktor, po drugi pa na izboljšanje pretvorbe. Nasproten učinek je bil opažen za  $P_t$ , ker se narastek tlaka izraža v hitrem povišanju  $T_c$  in zmanjšanju konverzije. Območje tlaka in temperature je torej omejeno z zmogljivostmi sistema: treba se je izogibati prekomernemu tlaku, delovne temperature pa je treba izbrati v območju, kjer je reakcija polimerizacije zelo hitra; take razmere omogočajo dobro konverzijo, in nastali polimer ima majhno kristaliničnost in s tem nizko gostoto.

V tem delu je bilo preučevano tudi razmerje  $L/D$ , da bi dobili najbolj primerno razmerje, ki omogoča najboljši odvod toplote, ki se sprošča med polimerizacijo.

**Ključne besede:** modeliranje, cevast reaktor, simulacija, polietilen nizke gostote, psevdohomogen dvodimenzionalni model



## 1 INTRODUCTION

For many years the production in the chemical industry has been based solely on experience. However, for economic reasons and to avoid extreme conditions of temperature and pressure, the use of simulation methods has become more and more necessary. Indeed, through mathematical models, it is possible to predict relationships between the variations of experimental or production parameters and the practice results.

The polymerization of some unsaturated hydrocarbons, called olefins, is extremely important. The types of polymers obtained consist mainly of low- (LDPE), and high-density polyethylene (HDPE) and polypropylene (PP). LDPE, one of the most frequently produced engineering polymers in the world, is a versatile polymer with a very wide range of applications<sup>1</sup>. Therefore, its polymerization process has been the subject of numerous research works and many studies are still in progress in order to obtain improved LDPE-based materials. In this regard, a better understanding of the polymerization process requires the use of a simulation of the reaction mechanism in order to establish new procedures to reach a better conversion (which is currently 15 % to 35 % in most industrial cases) and to improve the reactor performance based on a model proposed for a tubular chemical reactor. The reactor operating conditions are often difficult to fix. They should ideally be based on the simulation calculations. In other words, an important task is to determine the optimal operating conditions relating to temperature, pressure and conversion for each point of the reactor and this must be done in a rational manner.

Several mathematical models are available for chemical reactors<sup>2-6</sup>. Some researchers and chemists have tried to model and simulate the ethylene polymerization in autoclave reactors<sup>7-9</sup> and in tubular reactors<sup>10,11</sup>. The choice between these models is mostly dictated by the computing resources available and by the knowledge of the values of the parameters required for the simulation.

Tubular chemical reactors have a key role in the chemical industry and they are always part of a larger production system<sup>12</sup>. A tubular reactor for the production of LDPE is usually very long (>1000 m). Despite this reactor length, the conversion is very low (about 15–35 %) and this is due to a high exothermicity of the reaction. Unreacted monomer is separated from the polymer and recycled in the reactor<sup>1,13</sup>. For this reason it is necessary to know the behavior of the reactor, which is contained within the proposal of a set of mathematical models that characterize it<sup>2,5,6,14</sup>. Depending on the precision required, the models can be refined to take into account, in their calculations, the phenomena which are more or less secondary. This will allow presentations that are very close to the real situation.

For this purpose, our present work deals with the use of a two-dimensional pseudo-homogeneous model, based on mass and heat balances<sup>15</sup> in order to study the

behavior of a tubular chemical reactor where a polymerization reaction proceeds. The proposed model, together with its resolution method, allows a better understanding of the reaction kinetics, particularly for the LDPE synthesis reaction, and for obtaining the temperature and conversion profiles. All the steps of this process (via the polymer chemistry as well as polymerization engineering) were based on modeling and simulation.

Through the use of a simulation program taking into account all the parameters, several series of calculations are performed over a wide range of temperatures (60–300 °C) and pressures (800–3000 bar). It was found that it is possible to work at the temperatures that allow a moderate conversion (≈35 %), while avoiding an excessive pressure and producing a resulting polymer that has a low degree of crystallinity.

Considering the exothermicity of this reaction, special attention was paid to the operating conditions to ensure the performances, the functioning and the stability control of the reactor. The idea is to have a better control of the heat exchanges by studying the effect of the  $L/D$  ratio (length or height/diameter of the cylindrical reactor). For such a purpose, it is better to choose a long reactor with a small diameter (i.e., a high  $L/D$  value).

## 2 FORMULATION OF THE MATHEMATICAL MODEL

In an elementary volume of the reactor it will be assumed that the system is treated as a homogeneous one and the proposed model is subjected to the following conditions:

1. the system is stationary  

$$\frac{\partial \psi_i}{\partial t} = \frac{\partial \theta}{\partial t} = 0$$
2. the reactor has a cylindrical shape
3. the effect of the volume variation due to the reaction, or the temperature, is negligible
4. the axial, mass and heat dispersions are assumed negligible  

$$\frac{\partial^2 \psi_i}{\partial z^2} = \frac{\partial^2 \theta}{\partial z^2} = 0$$
5. the diffusion and heat-exchange coefficients in the reactor remain constant
6. the pressure is constant along the reactor
7. the temperature of the reactor wall is constant.

The mass and energy balances in the dimensionless form are presented as follows:

$$\frac{\partial \psi_i}{\partial z} = a_{12} \left[ \frac{\partial^2 \psi_i}{\partial y^2} + \frac{1}{y} \frac{\partial \psi_i}{\partial y} \right] + b_{12} R(\theta_i, \psi_i) \quad (1)$$

$$\frac{\partial \theta}{\partial z} = a_{22} \left[ \frac{\partial^2 \theta}{\partial y^2} + \frac{1}{y} \frac{\partial \theta}{\partial y} \right] + b_{22} R(\theta_i, \psi_i) \quad (2)$$

where:

$$a_{12} = \frac{L^2}{Pe_{mr} \cdot r_0^2} \quad Pe_{mr} = \frac{\bar{v}_z \cdot L}{D_{eff,r}}$$

$$a_{22} = \frac{L^2}{Pe_{hr} \cdot r_0^2} \quad Pe_{mr} = \frac{\bar{v}_z \cdot L \cdot \rho_G \cdot C_{pG}}{D_{eff,r}}$$

$$b_{12} = \frac{L \cdot \rho_s \cdot v_i}{C_i^0 \cdot \bar{v}_z} \left( \frac{1-\varepsilon}{\varepsilon} \right)$$

$$b_{22} = \frac{L \cdot \rho_s \cdot v_i}{T_0 \cdot \bar{v}_z \cdot \rho_G \cdot C_{pG}} (1-\varepsilon) \cdot (-\Delta H_r)$$

with the following boundary conditions:

$$z = 0 \Rightarrow \psi = \psi^0, \quad \theta = \theta^0$$

$$\forall(z, y = 0) \Rightarrow \frac{\partial \psi_i}{\partial t} = \frac{\partial \theta}{\partial t} = 0$$

$$y = \frac{r}{r_0} = 1 \Rightarrow \frac{\partial C_i}{\partial r} = \frac{C_i^0}{r_0} \cdot \frac{\partial \psi_i}{\partial y} = 0 \rightarrow \frac{\partial \psi_i}{\partial y} = 0$$

$$-\lambda_{eff,r} \frac{T_0}{r_0} \cdot \frac{\partial \theta}{\partial y} = -h_w \cdot T_0 (\theta_w - \theta)$$

$$\Rightarrow -\frac{\partial \theta}{\partial y} = -\frac{h_w T_0 r_0}{\lambda_{eff,r} T_0} (\theta_w - \theta) = -B_{i_0} (\theta_w - \theta)$$

with  $\theta_w = \frac{T_w}{T_0}$

Equations (1) and (2) form a system of parabolic partial derivatives, which are very difficult to resolve. Therefore, the use of the orthogonal collocation method, which assumes a simple form for the radial profiles is advantageous.

For each collocation point  $y_j$  we obtain:

$$\frac{\partial \psi_i(z, y_j)}{\partial z} = a_{12} \left[ \sum_{k=1}^N B_{jk} \cdot \psi_{i,k} + \frac{1}{y_j} \sum_{k=1}^N A_{jk} \cdot \psi_{i,k} \right] + b_{12} R(\theta_j, \psi_j) \quad (3)$$

$$\frac{\partial \theta_j}{\partial z} = a_{22} \left[ \sum_{k=1}^N B_{jk} \cdot \theta_k + \frac{1}{y_j} \sum_{k=1}^N A_{jk} \cdot \theta_k \right] + b_{22} R(\theta_j, \psi_j) \quad (4)$$

( $j = 2, 3, \dots, n-1$ )

where  $\psi_{i,k} = \psi_i(z, y_k)$

It is clear that equations (3) and (4) are in the form of two first-order differential systems that can be solved by the Runge-Kutta semi-implicit 4<sup>th</sup>-order method.

By substituting the conversion rate in equations (3) and (4) of the model, we obtain:

$$\frac{\partial X_j}{\partial z} = -a_{12} \left[ \sum_{k=1}^N B_{jk} \cdot (1-x_k) + \frac{1}{y_j} \sum_{k=1}^N A_{jk} \cdot (1-x_k) \right] + b_{12} R(\theta_j, \psi_j) \quad (5)$$

$$\frac{\partial \theta_j}{\partial z} = -a_{22} \left[ \sum_{k=1}^N B_{jk} \cdot \theta_k + \frac{1}{y_j} \sum_{k=1}^N A_{jk} \cdot \theta_k \right] + b_{22} R(\theta_j, \psi_j)$$

( $j = 2, 3, \dots, N-1$ )

After the development of these two equations (5) as a form of two systems, we obtain:

$$F(j) = -a_{12} \sum_{k=1}^N \bar{A}_{jk} \cdot (1-x_k) + b_{12} R(\theta_j, \psi_j) \quad (6)$$

$$F(j+Ncol) = -a_{22} \sum_{k=1}^N \bar{A}_{jk} \cdot \theta_k + b_{22} R(\theta_j, \psi_j)$$

where  $\sum_{k=1}^N \bar{A}_{jk} = \sum_{k=1}^N \left( B_{jk} + \frac{1}{y_j} A_{jk} \right)$

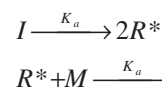
The validation of this model, which takes into account differential terms characteristic of the system behavior, has been particularly considered. In this framework a simulation program was developed to predict the behavior of a tubular reactor, where a polymerization reaction takes place under high pressure. The model can be used for a reaction, whose rate is a function of the temperature and concentrations of the reacting chemicals.

### 3 REACTION KINETICS OF THE ETHYLENE POLYMERIZATION

The reaction system chosen in our work is the radical synthesis of low-density polyethylene (LDPE) in a tubular chemical reactor. LDPE is produced with the radical polymerization of ethylene under high pressure (800–3000 bar) and at the temperatures ranging from 60 °C to 300 °C in the presence of the traces of oxygen and a free radical generator, the azo-bis-isobutyronitrile (AIBN). The reaction is highly exothermic, and one of the first challenges in this process is the removal of the excess heat generated.

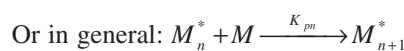
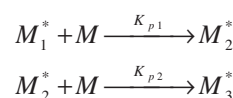
The general mechanism of this polymerization involves three main steps, i.e., initiation, propagation, and termination, as shown below:

**3.1 Initiation:** the step, during which a limited number of active species is created,



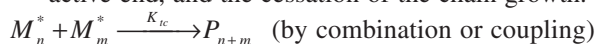
where:  $I$  = initiator,  $R^*$  = initial free radical,  $M_1^*$  = propagating free radical.

**3.2 Propagation:** successive reactions of monomer molecules to one active or activated end, leading to the growth of the macromolecular chain,



where:  $K_{p1}, K_{p2}, \dots, K_{pn}$  are propagation constants.

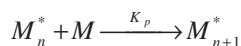
**3.3 Termination:** deactivation of the species or the active end, and the cessation of the chain growth.





The main step of the polymerization is the chain propagation (including several elementary reactions), when the macromolecule is built.

The successive addition of monomer M during the propagation can be generally described as follows:



The expression of the propagation speed is then:

$$V_p = K_p \cdot (M) \sqrt{f \cdot K_d / K_t} \cdot \sqrt{(I)}$$

$V_p$  can also be expressed generally as follows:

$$V_p = K_p \cdot (M) \sqrt{V_i / 2K_t}$$

It is to be noted that the values of various parameters (technology, kinetics, thermodynamics, etc.) are taken from the literature<sup>16–20</sup>. Thus, we have all the data required to calculate the theoretical profiles of the temperature and the conversion in the reactor (**Tables 1 and 2**).

**Table 1:** Operating conditions used for simulation

**Tabela 1:** Delovni pogoji, uporabljeni za simulacijo

$L = 1390 \text{ m}$	$R = 8.3 \text{ J mol}^{-1} \text{ K}^{-1}$
$D = 0.05 \text{ m}$	$T_w = 400 \text{ K}$
$V_{ms} = 0.20 \text{ m s}^{-1}$	$P_t = 2250 \text{ bar}$
$\rho_c = 1900 \text{ kg m}^{-3}$	$D_{eff} = 6 \cdot 10^{-5} \text{ cm}^2 \text{ s}^{-1}$
$\rho_g = 530 \text{ kg m}^{-3}$	$H_w = 81.677 \cdot 10^{-3} \text{ J cm}^{-2} \text{ °C}^{-1} \text{ s}^{-1}$
$C_p = 3.135 \text{ J g}^{-1} \text{ °C}^{-1}$	$\lambda_{eff} = 0.02 \text{ W m}^{-1} \text{ K}^{-1}$
$C_{A0} = 2.47 \cdot 10^{-4} \text{ mol L}^{-1}$	$\Delta H_r = -89.87 \text{ kJ mol}^{-1}$
$C_{M0} = 16.75 \text{ mol L}^{-1}$	$\varepsilon = 0.5$

**Table 2:** Kinetic parameters of the radical polymerization of ethylene (AIBN at 60 °C)<sup>20</sup>

**Tabela 2:** Kinetični parametri radikalne polimerizacije etilena (AIBN pri 60 °C)<sup>20</sup>

$K_d = 0.845 \cdot 10^{-5} \text{ s}^{-1}$	$E_d = 123 \text{ kJ mol}^{-1}$
$K_p = 0.243 \cdot 10^3 \text{ L mol}^{-1} \text{ s}^{-1}$	$E_p = 18.4 \text{ kJ mol}^{-1}$
$K_t = 54 \cdot 10^7 \text{ L mol}^{-1} \text{ s}^{-1}$	$E_t = 1.3 \text{ kJ mol}^{-1}$

## 4 RESULTS AND DISCUSSION

Knowing the great importance of some technoeconomic parameters in the industry using chemical reactors, we propose to study the influence of three parameters – the initial temperature  $T_0$ , the total pressure  $P_t$  and the ratio of the reactor's main dimensions ( $L/D$ ) – on the profiles of the temperature and conversion rates, to establish the optimal working conditions. It is often difficult to control, at the same time, these three parameters and to obtain reproducible results. Therefore, it is necessary to vary one parameter only while maintaining the other two constant.

Some chemical reactors can certainly work at a high temperature or a high pressure, but because of their technology implementation and geometry, it is more difficult to have, simultaneously, a high operating

pressure and an elevated reaction temperature. For this reason, we are mainly interested in obtaining information about the physical state of the reaction mixture.

The purpose is to clarify the influence of physical conditions – mainly temperature  $T_0$  and pressure  $P_t$  as well as the  $L/D$  ratio – on the reactor functioning in order to know its behavior and also to avoid the phenomenon of thermal runaway due to excessive temperature resulting from a bad heat exchange that leads to a thermal instability.

After the simulation treatments of our models, the following results are obtained:

### 4.1 Influence of the initial temperature ( $T_0$ )

In all industrial installations, the temperature measurement is particularly important to ensure the performance and to monitor the smooth running of the operations. The  $T_0$  factor is a basic parameter, from which we deduce most of the other reaction parameters such as pressure, mixture composition and geometry of the reactor (the optimal ratio  $L/D$ )<sup>21</sup>.

Changing the initial temperature  $T_0$ , while maintaining the other two parameters,  $P_t$  and  $L/D$ , constant, affects the dimensionless temperature profiles  $\theta$  and the rate of conversion  $x$ .

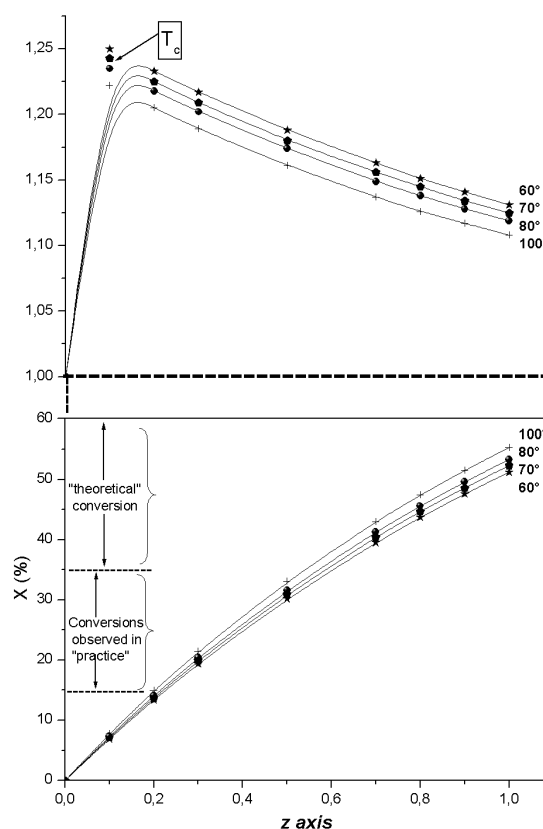


**Figure 1:** Variations of dimensionless temperature  $\theta$  and conversion  $x$  along the  $z$ -axis of the reactor for various values of  $T_0$

**Slika 1:** Spreminjanje brezdimenzijske temperature  $\theta$  in konverzije  $x$  vzdolž  $z$ -osi reaktorja za različne vrednosti  $T_0$

**Figure 1** shows a clear hotspot  $T_c$ , right at the entrance of the reactor ( $z = 0.10$ ), for each value of  $T_0$  considered, where we may have to cope with the problems of thermal instability that most often occur after a failure of the cooling system (placed against the outer wall of the reactor). The value of  $T_c$  decreases with an increase in  $T_0$ , which means that the dimensionless temperature  $\theta$  decreases with an increase in the initial temperature  $T_0$  at any position along the reactor  $z$ -axis. This increase of  $T_0$  has the advantage of increasing the conversion, that is to say, the polymer molecular weight and viscosity. In general, the conversion increases slightly with increasing  $T_0$  for any value of  $z$ . The range of temperature  $T_0$  was limited with the performance of the system that allows both relatively fast reaction rates and relatively good conversions, leading to a polymer having a low crystalline content and a low density.

It is noticeable that the temperature, after reaching the maximum value of  $T_c$  for each  $T_0$ , decreases along the  $z$ -axis, which allows us to conclude that:

- The reaction is greatly accelerated by a rise in the temperature at the entrance of the reactor, where the polymerization rate is maximum. The heat generated is removed through a cooling liquid (usually water) to reduce the occurrence of hot spots,  $T_c$ , and to obtain a uniform distribution of the temperature inside the reactor.

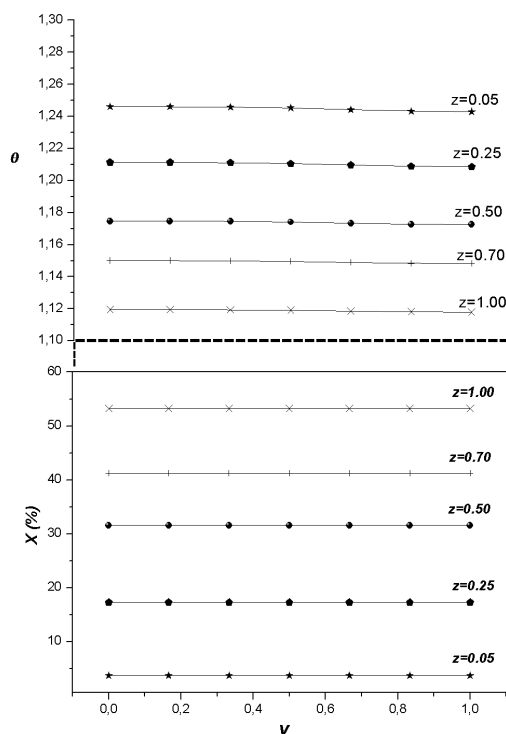


**Figure 2:** Variations of dimensionless temperature  $\theta$  and conversion  $x$  as a function of radial direction  $y$  of the reactor for various positions along the  $z$ -axis

**Slika 2:** Spreminjanje brezdimenzijske temperature  $\theta$  in konverzije  $x$  kot funkcije radialne smeri  $y$  v reaktorju za različne položaje vzdolž  $z$ -osi

- The initiation reaction has a strong thermal energy resulting in the "hot spot" observed during this step. We can say that it is likely that the activation energy of the initiation ( $E_d$ ) is much superior to the other activation energies (propagation ( $E_p$ ) and termination ( $E_t$ )); in our case, the initiation is the result of a thermal decomposition (**Table 2**).

Because the velocity profiles are considered flat, i.e., the flow in our reactor is assumed to be a plug flow, the transit time is the same for each species. For this reason, the radial temperature  $\theta$  and the conversion (**Figure 2**) remain constant.

#### 4.2 Influence of the total pressure ( $P_t$ )

High-pressure polymerization of ethylene in tubular reactors is an important commercial process<sup>22</sup>. The pressure is a factor involved directly in the reaction kinetics through the reaction enthalpy as given by the following expression<sup>19</sup>:

$$\Delta H = 115.3 \cdot [718.6 + (0.05 \cdot T_0) + (0.025 \cdot P_t)] \\ (\text{J} \cdot \text{g}^{-1} \cdot \text{mol}^{-1})$$

To better highlight the effect of the total pressure on the temperature and conversion profiles, the simulations are made assuming that this pressure remains constant along the reactor (an assumption of no charges losses).

The results shown in **Figure 3** (the profiles of dimensionless temperature  $\theta$  and the rate of conversion  $x$  as a

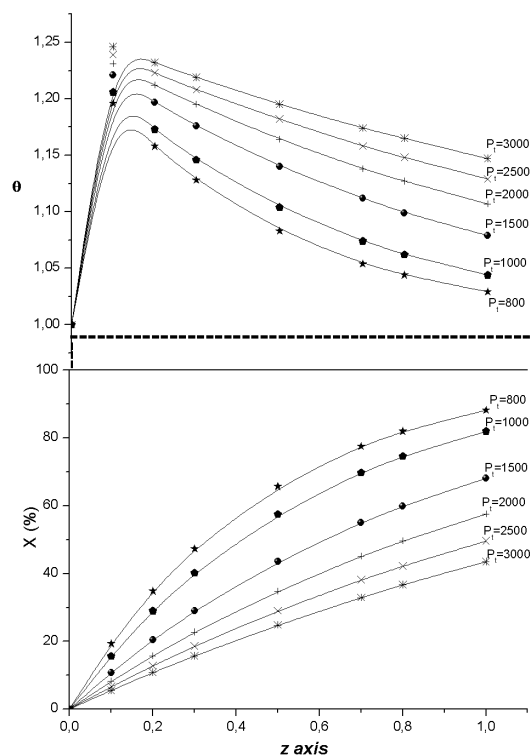


**Figure 3:** Variations of dimensionless temperature  $\theta$  and conversion  $x$  along the  $z$ -axis of the reactor for different values of  $P_t$

**Slika 3:** Spreminjanje brezdimenzijske temperature  $\theta$  in konverzije  $x$  vzdolž  $z$ -osi reaktorja za različne vrednosti  $P_t$



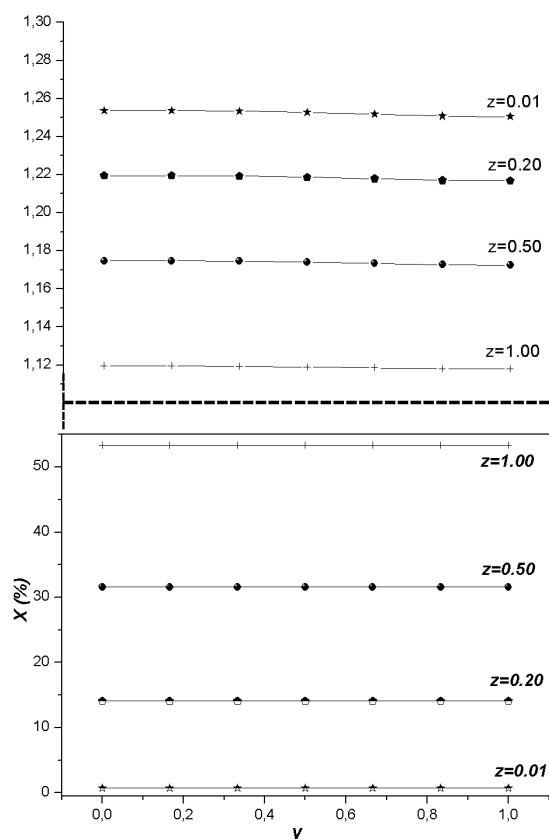


**Figure 4:** Variations of dimensionless temperature  $\theta$  and conversion  $x$  as a function of radial direction  $y$  of the reactor for various positions along the  $z$ -axis

**Slika 4:** Spreminjanje brezdimenzijske temperature  $\theta$  in konverzije  $x$  kot funkcije radialne smeri  $y$  reaktorja za različne pozicije vzdolž  $z$ -osi

function of the pressure along the  $z$ -axis of the reactor) confirm the influence of the pressure on these two parameters. Such results are in agreement with the expectations: when pressure  $P_t$  increases the conveying speeds are highly accelerated and the temperatures are higher, while the conversion rate decreases regardless of the position along the  $z$ -axis of the reactor. This conversion decrease can be explained as follows: a pressure rise increases the conveying speed that, in turn, limits the cross-linking reactions and deposit formation (crust) on the wall (these reactions cause the formation of deposits that prevent adequate heat transfer).

The range of the total pressure  $P_t$  has been limited by the performance of the system in order to avoid excessive pressure ( $\leq 3000$  bar) and prevent an overheating of the system. It may be noticed that, when working at high pressures, hot spots become more consistent, thus potentially leading to a runaway of the reactor. For this reason, the heat must be controlled precisely to prevent such a runaway and to better control the molecular weight distribution of the polymer.

Here we also notice that the radial temperature  $\theta$  and the rate of conversion  $x$  (**Figure 4**) remain practically constant along the radial direction  $y$ . This uniformity of

the temperature and the conversion rate is due to the fact that the velocity profiles are considered flat, i.e., the flow in our reactor is assumed to be a plug flow, therefore, the transit time is the same for each species.

#### 4.3 Influence of the ratio ( $L/D$ )

Equipment geometry and dimensions are very important because, in the industrial production, all the operations are performed in a reactor having certain geometric dimensions. In practice these parameters (characteristics) are designated as "the main dimensions", and can be represented by the length (or height)  $L$  and the diameter  $D$  of the reactor. It is common to use a dimensionless number, characteristic of the device, designated by the ratio ( $L/D$ ). Knowing the value of the  $L/D$  ratio is very important, because, from its value, one can deduce, for example, the type of a flow (i.e., the Reynolds Number) and also the reactor similarity that should then be considered.

If the ratio ( $L/D$ ) increases, the particle motion becomes increasingly ordered, i.e., the axial diffusion is less important. The transition (similarity) between a tubular reactor and a plug-flow reactor can then be characterized with the axial diffusion, i.e., with an increase in the ratio ( $L/D$ ). Indeed, the tubular reactor is used only if the residual heat is moderate. In the opposite case, significant radial temperature differences will appear. These would cause radial gradients of the polymerization rate and the viscosity that would impair the quality of the polymer.

**Figures 5 and 6** show that an increase in the ratio ( $L/D$ ) leads to the reduction of the temperature, which, in turn, causes an increase in the conversion rate, and this can be observed for each  $z$  position along the reactor axis. This allows us to say that a large value of the ratio ( $L/D$ ) greatly influences the homogenization of the reaction medium with molecular diffusion, and that this

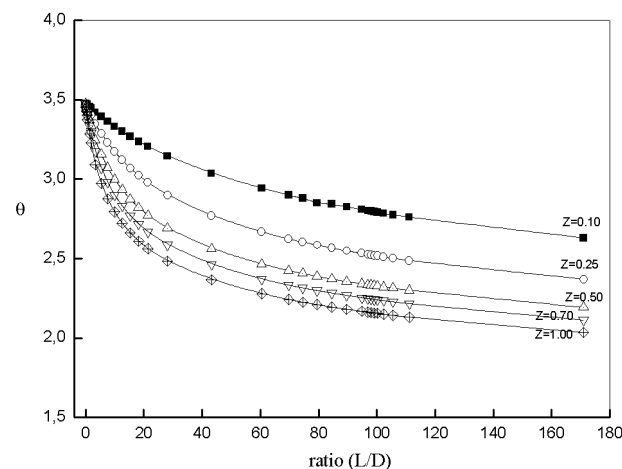


**Figure 5:** Variations of dimensionless temperature versus ratio ( $L/D$ ) for different positions along the  $z$ -axis

**Slika 5:** Spreminjanje brezdimenzijske temperature  $\theta$  z razmerjem  $L/D$  za različne pozicije vzdolž  $z$ -osi

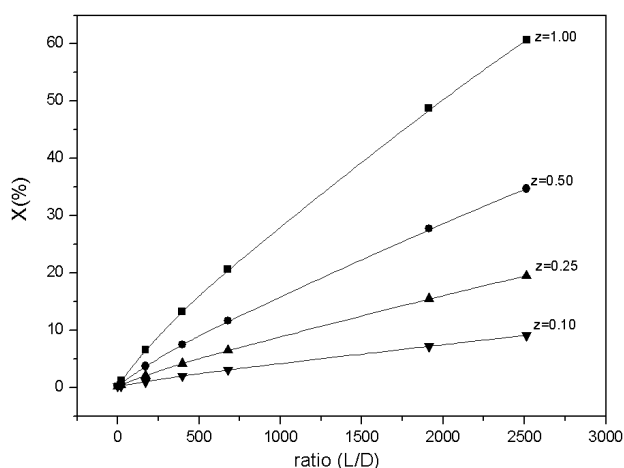


**Figure 6:** Variations of conversion rate  $x$  versus ratio  $(L/D)$  for different positions along the  $z$ -axis

**Slika 6:** Spreminjanje hitrosti konverzije  $x$  z razmerjem  $L/D$  za različne pozicije vzdolž  $z$ -osi

property makes the tubular reactors more adapted to the study and implementation of highly exothermic reactions.

## 5 CONCLUSION

Taking into account all the results obtained, we observe that:

- Measurements of temperatures, pressures and main dimensions of the reactor are particularly important to ensure the performance and monitoring of the functioning of the ongoing operations.
- The two-dimensional model formulation and the development of the appropriate calculation programs led us to a better understanding of the evolution of the temperature and conversion rate during the synthesis reaction of low-density polyethylene in a tubular chemical reactor.
- The proposed model (two dimensional) and the resolution method (Runge-Kutta semi-implicit 4<sup>th</sup>-order method), applied to the process of polymerization of LDPE, allow the obtention and the prediction of the influence of the initial temperature  $T_0$ , the total pressure  $P_t$  and the reactor dimensions (ratio  $L/D$ ) on the temperature and conversion-rate profiles in a tubular chemical reactor in a steady state.

The proposed model as well as the solving method are general enough to be applied to many industrial chemical reactions, with respect to the materials (production of polymers, for instance) and the materials engineering (reactor dimensions and operating conditions). They allow a study and a comparison of the profiles (temperature and conversion) for different operating conditions of the reactor. Thus, they appear to be able to predict, with a reasonable accuracy, the behavior of the reactor in question.

## Nomenclature

$Bi_\theta$	Biot number at the reactor wall
$C_i^0$	initial concentration of the $i$ component [ $\text{mol L}^{-1}$ ]
$C_{P\,G}, C_{P\,S}$	specific heat at a constant pressure of gas, solid [ $\text{J kg}^{-1} \text{K}^{-1}$ ]
$D_{\text{eff}}$	effective diffusivity [ $\text{m}^2 \text{s}^{-1}$ ]
$D_A$	diffusion coefficient of the component A [ $\text{m}^2 \text{s}^{-1}$ ]
$E$	activation energy [ $\text{J mol}^{-1}$ ]
$F$	efficiency factor of the initiator
$h_W$	coefficient of the overall heat transfer to the wall [ $\text{W m}^{-2} \text{K}^{-1}$ ]
$(I)$	initiator concentration [ $\text{mol L}^{-1}$ ]
$K_p$	propagation rate constant [ $\text{L mol}^{-1} \text{s}^{-1}$ ]
$K_d$	rate constant for the initiator dissociation [ $\text{s}^{-1}$ ]
$K_a$	rate constant for the monomer addition [ $\text{s}^{-1}$ ]
$K_t$	termination rate constant [ $\text{L mol}^{-1} \text{s}^{-1}$ ]
$K_{tc}$	termination rate constant by combination [ $\text{L mol}^{-1} \text{s}^{-1}$ ]
$K_{td}$	termination rate constant by disproportionation [ $\text{L mol}^{-1} \text{s}^{-1}$ ]
$L$	reactor length [m]
$M$	monomer
$(M)$	monomer concentration $M$ [ $\text{mol L}^{-1}$ ]
$M^*$	monomer radical
$P_t$	total pressure [bar]
$Pe$	Peclet number
$Pe_{\text{mr}}$	Peclet number on the radial matter
$Pe_{\text{hr}}$	Peclet number of the radial heat
$r$	radial distance [m]
$R_i$	reaction rate [ $\text{mol kg}^{-1} \text{s}^{-1}$ ]
$t$	time [s]
$T$	temperature [K]
$T_0$	initial temperature [K]
$T_W$	temperature of the wall [K]
$V_p$	speed of the propagation (polymerization) [ $\text{mol L}^{-1} \text{s}^{-1}$ ]
$V_i$	initiation rate
$\bar{v}_z$	average axial velocity
$z$	dimensionless axial distance
$Y$	dimensionless radial distance
$Z$	axial distance [m]
$\lambda_{\text{eff}}$	effective thermal conductivity [ $\text{W m}^{-1} \text{K}^{-1}$ ]
$\rho$	density [ $\text{kg m}^{-3}$ ]
$\rho_s$	volume density of the catalyst ( $\rho_s = m/V_s$ ) [ $\text{kg m}^{-3}$ ]
$\rho_G$	volume density of gas
$\rho_a$	bulk density ( $\rho_a = m/V$ ) [ $\text{kg m}^{-3}$ ]
$\varepsilon$	porosity
$\psi_i$	dimensionless concentration ( $\psi_i = C_i/C_{i0}$ )
$\theta$	dimensionless temperature ( $\theta = T/T_0$ )
$\theta_W$	dimensionless temperature of the wall ( $\theta_W = T_W/T_0$ )
$\nu_i$	stoichiometric coefficient
$x$	conversion rate [%]
$\Delta H_r^0$	heat released during the reaction [ $\text{J mol}^{-1}$ ]

## 6 REFERENCES

- <sup>1</sup> M. Hafele, A. Kienle, M. Boll, C. U. Schmidt, Modeling and analysis of a plant for the production of low density polyethylene, *Computers and Chem. Eng.*, 31 (2006), 51
- <sup>2</sup> L. Le Letty, A. Le Pourhiet, J. B. Gros, M. Enjalbert, Modèle Bidimensionnel de Réacteur Catalytique à Lit Fixe, *Chem. Eng. J.*, 8 (1974), 179
- <sup>3</sup> G. Djelveh, J. B. Gros, R. Bugarel, Simulation d'un réacteur catalytique à lit fixe (Oxydation du propène), *Can. J. of Chem. Eng.*, 60 (1982), 146
- <sup>4</sup> J. B. Gros, R. Bugarel, Etude Comparative de Modèles de Réacteurs Catalytiques à Lit Fixe, *Chem. Eng. J.*, 13 (1977), 165
- <sup>5</sup> G. F. Froment, K. B. Bischoff, *Chemical Reactor Analysis and Design*, John Wiley and Sons, New York 1979
- <sup>6</sup> N. Thérien, P. Tessier, Modélisation et Simulation de la décomposition catalytique du méthanol dans un réacteur à lit fixe, *Can. J. of Chem. Eng.*, 65 (1987), 950
- <sup>7</sup> P. Feucht, B. Tilger, G. Luft, Prediction of molar mass distribution, number and Weight overage degree of polymerization and branching of low density polyethylene, *Chem. Eng. Sci.*, 40 (1985) 10, 1935
- <sup>8</sup> P. Lorenzini, M. Pons, J. Villiermaux, Free-radical polymerization engineering, IV: Modelling homogeneous polymerization of ethylene: determination of model parameters and final adjustment of kinetic coefficients, *Chem. Eng. Sci.*, 47 (1992) 15–16, 3981
- <sup>9</sup> R. Dhib, N. Al-Nidawy, Modeling of free radical polymerization of ethylene using difunctional initiators, *Chem. Eng. Sci.*, 57 (2002), 2735
- <sup>10</sup> A. Brandolin, N. J. Capiati, J. N. Farber, E. M. Valles, Mathematical model for high pressure tubular reactor for ethylene polymerization, *Ind. Eng. Chem. Res.*, 27 (1988), 784
- <sup>11</sup> A. Baltas, E. Papadopoulos, C. Kiparissides, Application and validation of the pseudo-kinetic rate constant method to high pressure LDPE tubular reactor, *Comput. Chem. Eng.*, 22(Suppl.1) (1998), S95–S102
- <sup>12</sup> J. R. H. Ross, *Catalyst preparation from Art to Science*, Technische Hogeschool Twente, 1984
- <sup>13</sup> M. Hafele, A. Kienle, M. Boll, C. U. Schmidt, M. Schwibach, Dynamic simulation of a tubular reactor for the production of low-density polyethylene using adaptive method of lines, *J. of Computation and Applied Mathematics*, 183 (2005), 288
- <sup>14</sup> C. R. Barkelew, *Chem. Eng. Prog. Symp.*, Series 55 (1959) 25, 37
- <sup>15</sup> M. Marghsi, Modélisation et simulation d'un réacteur catalytique à lit fixe: Application à la synthèse du SO<sub>3</sub>, Magister's thesis, Université Ferhat-Abbas, Algérie, 1996
- <sup>16</sup> M. Asteasuain, S. M. Tonelli, A. Brandolin, J. A. Bandoni, Dynamic simulation and optimisation of tubular polymerisation reactors in gPROMS, *Comp. and Chem. Eng.*, 25 (2001), 509
- <sup>17</sup> D. M. Kim, P. D. Iedema, Molecular weight distribution in low-density polyethylene polymerization: impact of scission mechanisms in the case of a tubular reactor, *Chem. Eng. Sci.*, 59 (2004), 2039
- <sup>18</sup> D. M. Kim, M. Busch, H. C. J. Hoefsloot, P. D. Iedema, Molecular weight distribution modeling in low-density polyethylene polymerization: impact of scission mechanisms in the case CSTR, *Chem. Eng. Sci.*, 59 (2004), 699
- <sup>19</sup> S. Agrawal, C. D. Han, Analysis of the high pressure polyethylene tubular reactor with axial mixing, *AIChE J.*, 21 (1975), 449
- <sup>20</sup> G. Odian, *Principles of polymerization*, 4<sup>th</sup> ed., Wiley, New York 2004, 206
- <sup>21</sup> J. Horak, J. Pasek, *Conception des réacteurs chimiques industriels sur la base des données de laboratoire*, Eyrolles, Paris 1981
- <sup>22</sup> H. D. Ansporn, Polyethylene. In *Manufacture of Plastic*, Vol. 1, W. M. Smith, ed., Reinhold, New York 1964

## THEORETICAL AND EXPERIMENTAL ESTIMATION OF THE WORKING LIFE OF MACHINE PARTS HARD FACED WITH AUSTENITE-MANGANESE ELECTRODES

### TEORETIČNO IN EKSPERIMENTALNO UGOTAVLJANJE ZDRŽLJIVOSTI STROJNIH DELOV, OPLAŠČENIH S TRDIMI AVSTENITNO-MANGANSKIMI ELEKTRODAMI

**Vukić Lazić<sup>1</sup>, Aleksandar Sedmak<sup>2</sup>, Dragan Milosavljević<sup>1</sup>, Ilija Nikolić<sup>1</sup>, Srbislav Aleksandrović<sup>1</sup>,  
Ružica Nikolić<sup>1</sup>, Milan Mutavdžić<sup>3</sup>**

<sup>1</sup>Faculty of Engineering, S. Janjić 6, 34000 Kragujevac, Serbia

<sup>2</sup>Faculty of Mechanical Engineering, Kraljice Marije 16, 11000 Beograd, Serbia

<sup>3</sup>PD „Kragujevac“, Kragujevac, Tanaska Rajića 16, 34000 Kragujevac, Serbia  
vlazic@kg.ac.rs

*Prejem rokopisa – received: 2012-02-06; sprejem za objavo – accepted for publication: 2012-02-16*

We have investigated the possibility of repairing damaged machine parts by hard facing with austenite-manganese steel electrodes. The subject is a Fe-C-Mn alloy with a microstructure of soft austenite which, after cold deformation, transforms by a shearing mechanism into a hard martensite microstructure. These steels are used mainly for parts exposed to high impact loads and intensive abrasive wear. Depending on the degree of wear, these parts can be replaced by new ones or repaired by hard facing. The selection of the optimal reparation technology for the rotational crusher's impact beams is the subject of this study. Investigations of model samples were conducted first, followed by layers hard faced onto samples with austenite manganese and special electrodes. After this the microstructure and hardness of the welds' characteristic zones were investigated. After reparatory hard facing the impact beams were mounted in the crusher and their behaviour was monitored periodically. Both the new and hard-faced beams' behaviours were monitored and compared under the same working conditions. In this way, the optimal technology for hard facing was established, taking into account not only the technical indicators, but also the economic effects.

**Keywords:** austenite manganese – hadfield steel, mining engineering equipment, hard facing, reparation

Ta članek predstavlja študij možnosti obnove poškodovanih delov z nanašanjem trdih plasti iz avstenitno-manganskih jekel. Predmet raziskave je zlitina Fe-C-Mn z mehko avstenitno mikrostrukturo, ki se med hladno deformacijo s strižnimi mehanizmi pretvori v trdo martenzitno mikrostrukturo. Ta jekla se uporabljajo predvsem za dele, izpostavljene velikim udarnim obremenitvam in močni obrabi. Odvisno od stopnje obrabe se ti deli nadomeščajo z novimi ali pa se obnovijo s trdimi nanosi. V tem delu je preučevana izbira optimalne tehnologije obnove rotacijskih udarnih drobilnikov. Najprej je bila izvršena preiskava na modelnih vzorcih z nanosom trde plasti iz avstenitno-manganske posebne elektrode, nato pa preiskana še mikrostruktura in trdota značilnih varjenih področij. Po obnovi z nanosom trde plasti so bile udarne plošče nameščene v drobilnik in periodično je bilo spremljano njihovo vedenje. Primerjane so bile lastnosti novih in obnovljenih plošč v enakih obratovalnih razmerah. Tako je bila določena optimalna tehnologija obnavljanja delov z upoštevanjem ne samo tehničnih lastnosti, temveč tudi iz ekonomskega stališča.

**Ključne besede:** avstenitno-mangansko – Hadfield jeklo, rudarska strojna opreme, nanašanje trdih prevlek, obnavljanje

## 1 INTRODUCTION

In an investigation of the damage caused to various parts of machines and devices it was established that in more than 50 % of cases the damage occurs due to tribological processes involving more-or-less regular working conditions<sup>1-3</sup>. Accordingly, for the design of the reparation technology for damaged parts, we must first study the possible mechanisms of wear for coupled parts. Here, it should be kept in mind that, besides repairing the parts damaged in normal conditions, hard facing is also used for parts damaged due to failures, as well as for new, flawed cast pieces. Besides, new parts are also hard faced by depositing hard alloys, which can replace the traditional procedures of carburizing and nitriding. All these facts indicate that hard facing is an important advanced technologies.

The key parts of machines, assemblies and devices are frequently produced from very expensive alloys. Thus, by repairing them we are not only shortening the down times due to repairs, but also saving on expensive base materials as well as for the machining of parts. In the majority of cases the economic criterion for applying reparation is that the price of the repair cannot exceed the price of the new part. This is especially important for large-sized parts and batch production, while the reparation of unique machines and devices sometimes has to be performed regardless of the price<sup>4-10</sup>.



## 2 SELECTION AND PROPERTIES OF MATERIALS RESISTANT TO ABRASIVE WEAR

### 2.1 Base metals

The materials used most frequently for manufacturing the working parts of civil-engineering machines exposed to abrasive wear are cast pieces made from manganese steel. When selecting a material for manufacturing the working parts of such machines, i.e., by selecting the filler metals for their repair or hard-facing manufacture, we should pay particular attention to the mechanism of abrasive action, since two very different basic cases are met.

In the first case, at the contact surface of the working parts of civil-engineering machines, abrasive and very high specific pressures and local plastic deformation of those parts appear when the external load forces have an impact character. A typical part exposed to abrasive wear of this type is the impact beam of a stone crusher, where the abrasive element is the compact stone. In the second case, the abrasive is in the dispersed state (e.g., a small aggregate). Thus, on the contact surfaces only smaller specific pressures appear and large plastic deformations do not occur. The characteristic parts exposed to this type of wear are the teeth of loading dredger scoops, the storage crates of the transporters, etc.

Manganese austenite steels, also Hadfield steels<sup>11–15</sup>, exhibit good resistance to the first type of abrasive action. They are usually supplied in the cast, hot- or cold-deformed states. Besides the basic Hadfield steel (ČL3160-JUS, G-X120Mn12-DIN), which contains 1.20

% C, 12 % Mn, 0.50 % Si, 0.35 % P and 0.10 % S, the following multi-alloyed manganese steels are applied steels: (ČL3161-JUS), (ČL3460-JUS), (ČL3462-JUS) and (ČL3463-JUS), which possess good resistance to impact wear because, besides the high contents of manganese ( $w(\text{Mn}) = 12\text{--}17\%$ ) and carbon ( $w(\text{C}) = 1\text{--}1.4\%$ ), they are also alloyed with chromium ( $w(\text{Cr}) = 1\text{--}1.8\%$ ). The hard facing repair of these steels is usually performed by the application of basic manganese electrodes. The good resistance to abrasive wear by dispersed materials is exhibited by heat-treated, low alloyed steels, rapidly cooled cast steels and ledeburite tool steels<sup>12,15,16</sup>.

The chemical composition and instructions for the application of the base metals (ČL3160 and ČL3460) are given in **Table 1**, while the comparative marks by the JUS and DIN Standards, as well as the mechanical properties and microstructure of those materials, are given in **Table 2**<sup>4–6,17</sup>.

### 2.2 Filler metals

In the experimental investigation, various filler metals were applied (E Mn14, E Mn17Cr13, E DUR 600, ABRADUR 58 and INOX B 18/8/6)<sup>17</sup>. In **Table 3** the chemical composition and the comparative Standards' marks are presented, and in **Table 4** are the hardness and applications of tested electrodes.

The most frequently recommended filler metals for the hard facing of the parts for civil-engineering machines subjected to impact abrasive wear and the

**Table 1:** Chemical composition and application of ČL3160 and ČL3460

**Tabela 1:** Kemijska sestava in uporaba ČL3160 in ČL3460

Base metal	Chemical composition, mass fraction, w/%	Application						Suitable for manufacturing the parts exposed to abrasive wear and high impact loads, such as the working parts of mills, crushers, civil engineering machines, for work with raw materials of high hardness, etc.
		C	Si	Mn	Cr	P	S	
ČL3160	Prescribed	1.20	0.50	12.00	–	0.035	0.10	
	Analyzed	1.20	0.48	12.35	–	0.025	0.10	
ČL3460	Prescribed	1.20	0.50	13.00	1.00	0.040	0.10	
	Analyzed	1.20	0.55	13.14	1.12	0.035	0.15	

**Table 2:** Comparative Standard marks, some mechanical properties and microstructure of ČL3160 and ČL3460

**Tabela 2:** Primerjalne oznake po standardih, nekatere mehanske lastnosti in mikrostruktura ČL3160 in ČL3460

Comparative marks		Mechanical properties		Microstructure
JUS	DIN	Tensile strength, $R_m/\text{MPa}$	Hardness, HB	
ČL3160	G-X120Mn12	200	≈ 200 after fast quenching	Austenite
ČL3460	G-X120Mn12	210	≈ 210 after fast quenching	Austenite

**Table 3:** Comparative Standard marks and chemical composition of the tested electrodes

**Tabela 3:** Primerjava oznak po standardih in kemijska sestava preizkušanih elektrod

Comparative marks		Chemical composition, mass fraction, w/%						
SŽ Fiprom Jesenice	DIN8555	C	Mn	Cr	Ni	W	Mo	V
E Mn14	E7-UM-200-KP	1.20	12.50	–	–	–	0.70	–
E Mn17Cr13	–	0.60	16.50	13.50	–	–	–	–
E DUR 600	E 6-UM-60	0.50	–	7.50	–	–	–	–
ABRADUR 58	E 10-UM-60-GR	3.60	–	32.0	–	–	–	–

**Table 4:** Mechanical properties and application of the tested electrodes**Tabela 4:** Mehanske lastnosti in področje uporabe preizkušanih elektrod

Electrode mark SZ Fiprom-Jesenice	Hardness	Application
E Mn14	220 HB – after hard-facing 48 HRC – after forging	For hard-facing of manganese steels of thickness up to 10 mm which are applied for the manufacturing of parts in railroad engineering and parts of the stone crushers
E Mn17Cr13	220 HB – after hard-facing 48 HRC – after forging	For hard-facing of hydraulic presses' mallets, parts of the loading scoops of the civil engineering mechanization, parts of crushers, rails and railway-crossings
E DUR 600	57–62 HRC	For depositing of the hard welds from which the high wear resistance in the hot and cold states is expected, as well as good toughness and impact resistance
ABRADUR 58	57–62 HRC	For hard-facing of tools subjected to intensive abrasive wear in contact with minerals in a cold state
INOX B 18/8/6	-	For welding of the Cr- and Cr-Ni steels, for welding of two different types of steels, for depositing of welds resistant to corrosion and for depositing of the plastic inter-layer.

action of impact loads are austenite manganese electrodes with a large content of manganese and carbon, and the addition of other alloying elements, usually chromium, and then Ni, Mo, V and W<sup>11–13,15,17</sup>.

### 3 ESTIMATION OF THE WELDABILITY OF MANGANESE STEELS

Manganese steels with an austenite structure are prone to overheating and, with the deposition of multi-layer welds, the appearance of cracks is possible. Thus, it is necessary to know the behaviour of those materials when a significant amount of heat is being brought in, which would enable measures preventing the growth of austenite grains and the formation of brittle phases. Depending on the content of manganese and carbon, during a slow enough cooling of a Fe-C-Mn alloy we can obtain the following: perlite, perlite-martensite, martensite-austenite and austenite microstructures. Pearlite and austenite manganese steels have practical applications; however, they have a low plasticity and, due to rapid hardening, they are difficult to machine mechanically. An increase of the plasticity of manganese austenite steels is achieved by the thermal treatment of rapid quenching, which consists of heating up to a temperature of 1093 °C<sup>15</sup>, then heating through that temperature, followed by rapid water cooling. In this way, a pure austenite microstructure and high toughness are obtained. After the cooling, from casting or from the hot-deformation temperature, we obtain an austenite microstructure with particles of complex iron manganese carbides precipitated at the boundaries of the austenite grains. In contrast to this, after slow cooling some martensite will also appear, i.e., a predominantly martensite or austenite-martensite microstructure.

To achieve a satisfactory weldability of these manganese austenite steels it is necessary to prevent the abrupt growth of austenite grains due to the excessive

quantity of heat that is introduced. This is why it is recommended that the hard facing is performed with short welds, the careful selection of hard-facing parameters and forced rapid cooling. In the opposite case, the abrupt growth of austenite grains can occur, which would worsen its weldability and mechanical properties. The tendency of welds that are applied with manganese electrodes to crack is significantly reduced by the addition of a certain quantity of nickel and chromium, usually up to 4 %<sup>13,15</sup>.

## 4 MODEL INVESTIGATIONS

### 4.1 Selection of the hard-facing technology

The tests were conducted on samples made of low-carbon steel (Č0361) with a thickness  $s = 10$  mm for the purpose of selecting the technological parameters of the hard-facing procedure. The samples were welded using the REWL procedure. Depending on the type and the diameter of the used electrode, the hard-facing parameters were within the limits given in **Table 5**<sup>4–6,16</sup>. The method of depositing the weld layers, the order and the number of deposited layers and the appearance of the model are presented in **Figure 1**.

It is necessary to emphasize that, for further metallographic and other investigations, the samples were chosen to be welded using an electrode of diameter  $d_e = 3.25$  mm. Single-pass welds had a width  $b = 6–12$  mm and a height  $h = 3.2–4.6$  mm. The two-layered samples were only welded with the electrodes E Mn14 and E Mn17Cr13 (**Figure 1b**), while the three-layered samples were welded with electrodes E DUR 600 and ABRADUR 58 (**Figure 1c**) with the prior deposition of the inter-layer with the electrode INOX B 18/8/6. For model investigations, neither a prior nor a posterior thermal treatment was applied. After the hard facing the samples were rapidly cooled and then with grinding a

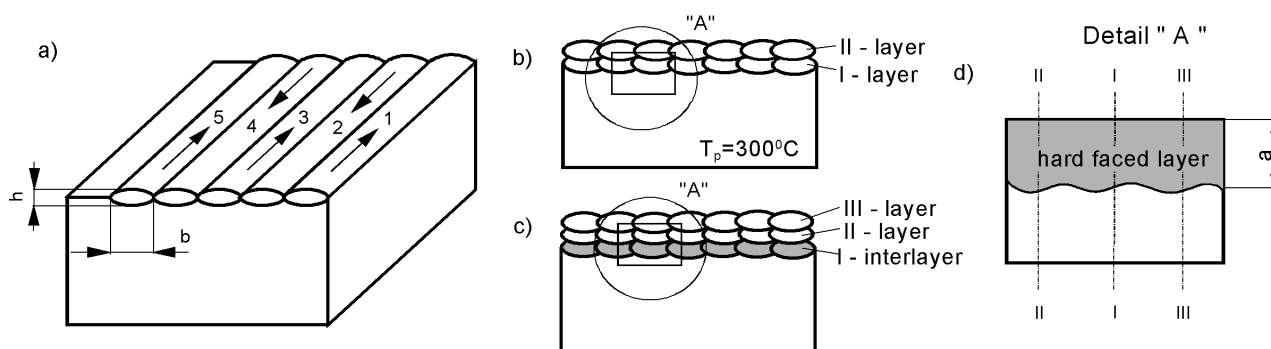


**Figure 1:** Order of weld layers' depositing: a) 1 layer, b) 2 layers (E Mn14, E Mn17Cr13), c) 3 layers (INOX B 18/8/6-E DUR 600, INOX B 18/8/6-ABRADUR 58), d) metallographic ground piece (block)

**Slika 1:** Zaporedje navarjenih slojev: a) 1 sloj, b) 2 sloja (E Mn14, E Mn17Cr13) c) 3 sloji (INOX B 18/8/6-E DUR 600, INOX B 18/8/6-ABRADUR 58), d) kos za metalografske preiskave

**Table 5:** Technological parameters of hard-facing

**Tabela 5:** Tehnološki parametri nanašanja trdih plasti

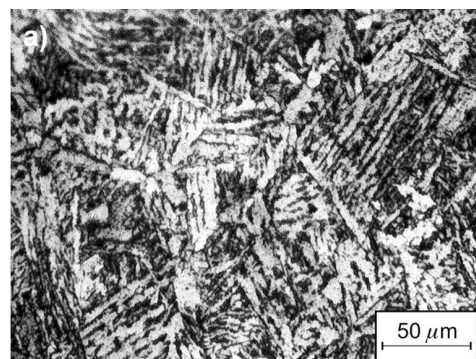
Base metal thickness $s$ , mm	Electrode mark	Electrode core diameter $d_e$ /mm	Current intensity $I$ /A	Working voltage $U$ /V	Welding speed $v_w$ /(cm/s)	Welding driving energy, J/cm
10	E Mn14	3.25	120	25	$\approx 0.148$	16216
	E Mn14	5.00	180	27	$\approx 0.162$	24000
	E Mn17Cr13	3.25	130	25	$\approx 0.152$	17105
	E Mn17Cr13	5.00	200	28	$\approx 0.168$	26667
	INOX B 18/8/6	3.25	100	24	$\approx 0.136$	14118
	INOX B 18/8/6	5.00	160	26	$\approx 0.178$	18697
	E DUR 600	3.25	120	25	$\approx 0.119$	20168
	ABRADUR 58	3.25	130	25	$\approx 0.124$	20968

portion of the material was removed from the back layer<sup>4-6</sup>.

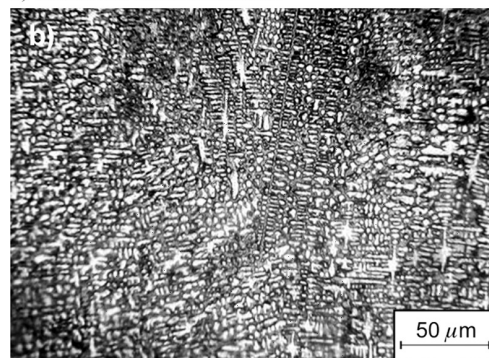
#### 4.2 Metallographic investigations and hardness measurements on models

Manganese austenite steels have a relatively small hardness in the range from 180 HB to 250 HB (usually 200–229 HB). They are highly resistant to abrasive wear only when their working surface layers are intensively plastically cold deformed with effect of strong impact loads or of slow pressure as a result of the pressing load. However, in these steels the hardening of the surface layers is not due to the strain hardening of the austenite, but the plastic deformation initiates the phase transformation of austenite to martensite. After local transformation of the austenite to martensite, a hardness of the surface layers as high as 500–520 HK can be achieved (the usual hardness range is between 330 HK and 480 HK). For this reason, these steels are hard to machine by cutting and are usually treated by hot or cold plastic deformation or by casting.

In some references<sup>4-6,8</sup> the limiting depth was established at which we can still observe an increase in the surface layers' hardness due to the austenite-to-martensite transformation initiated by the plastic cold deformation. The maximum measured hardness was 460 HK, and the width of the transformed zone was 0.50



a) Austenite microstructure



b) Martensite microstructure

**Figure 2:** Microstructure of the Hadfield steel (ČL3160): a) before the plastic deformation and b) after the plastic deformation

**Slika 2:** Mikrostruktura Hadfield jekla (ČL3160): a) pred plastično deformacijom, b) po plastičnoj deformaciji

mm. In **Figure 2** the microstructure of the Hadfield steel (ČL3160), before and after plastic deformation, is presented<sup>4-6</sup>.

In **Figure 2** we can see that the microstructure of the Hadfield steel before the plastic deformation was purely austenite, while after the plastic deformation the needles of martensite can be seen in the austenite matrix.

In some investigations<sup>1-3</sup> it was shown that the austenite-carbide microstructure has the highest wear resistance, rather than the martensite-carbide, as would be expected from their hardness values. The reason lies in the stronger austenite-carbide, grain-boundary bonds due to the smaller difference of the lattices parameters, rather than in the martensite-carbide combination. In other words, abrasive particles are pulling out the carbide particles from the martensite matrix more easily than from the austenite.

Despite the evident difficulties associated with hardness measurements and in determining the hard-faced layers' microstructure, we were able to determine the width of the austenite-to-martensite transformation zone and were also able to record the microstructure of that zone. These data can be of special importance in the hard facing of various working parts of technical systems that operate in such or similar working conditions. In **Figures 3** and **4** are the distributions of the welds before and after

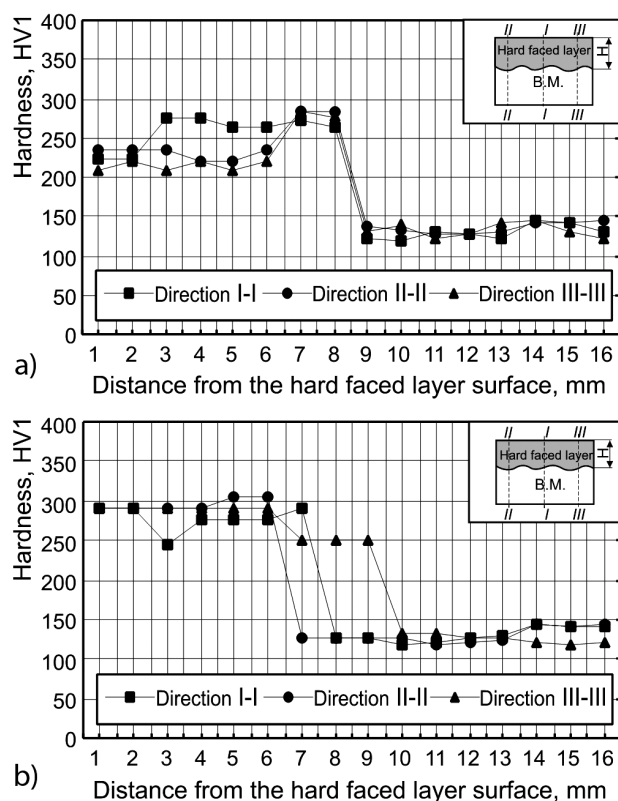


**Figure 3:** Micro hardness distribution along the welds' cross-section before the plastic deformation: a) E Mn14 and b) E Mn17Cr13

**Slika 3:** Rasporeditev mikrotvrdoe v prečni smeri vzdolž zvara pred plastično deformacijo: a) E Mn14 in b) E Mn17Cr13

the plastic deformation. The following filler metals were used: E Mn14 and E Mn17Cr13<sup>4-6,8</sup>.

From **Figures 3** and **4** it is clear that there is an increase in the hardness after the plastic deformation in both tested filler metals. By comparing the results (**Figure 4**) related to the filler metals E Mn14 and E Mn17Cr13, it is clear that a somewhat higher hardness was obtained for the second filler metal. Also, it can be concluded that the width of the transformed austenite-to-martensite zone is larger for the welds deposited by the E Mn17Cr13 electrode. The maximum measured hardness after the cold hardening in the welds deposited by the E Mn14 electrode was about 520 HK, while the width of the transformed zone was 0.60 mm. In the same conditions for welds deposited by the E Mn17Cr13 electrode the maximum obtained hardness was 560 HK and the width of the transformed zone was 1.20 mm<sup>4-6,8</sup>.

The microstructures of the surface layer of the back weld before and after the cold plastic deformation are shown in **Figures 5** and **6**<sup>4-6,8</sup>.

The hardness distributions and the appearance of the formed structures in the characteristic zones of the filler metals E DUR 600 and ABRADUR 58 are presented in<sup>4-6,8</sup>.

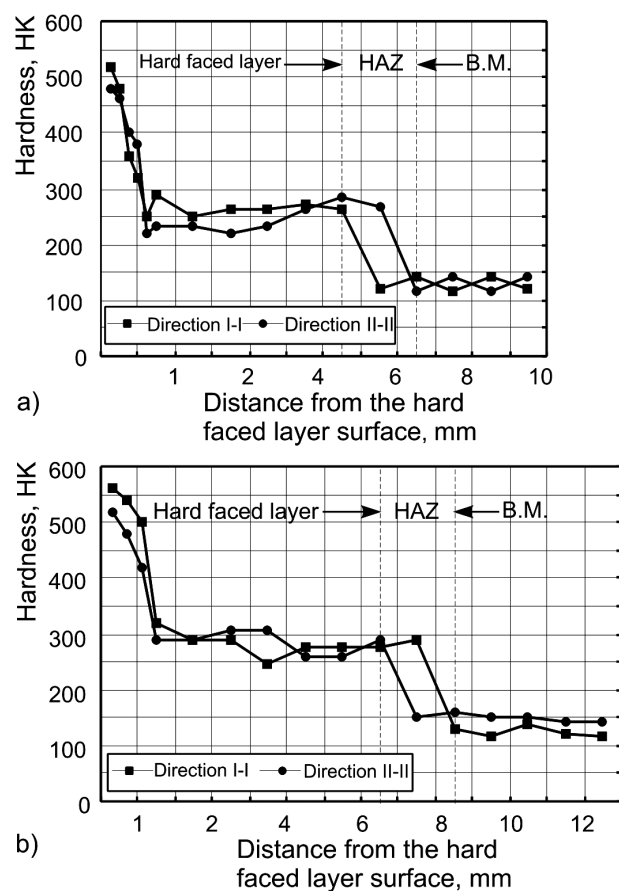


**Figure 4:** Micro hardness distribution along the welds' layer cross-section after the plastic deformation: a) E Mn14 and b) E Mn17Cr13

**Slika 4:** Rasporeditev mikrotvrdoe v prečni smeri vzdolž zvara po plastični deformaciji: a) E Mn14 in b) E Mn17Cr13



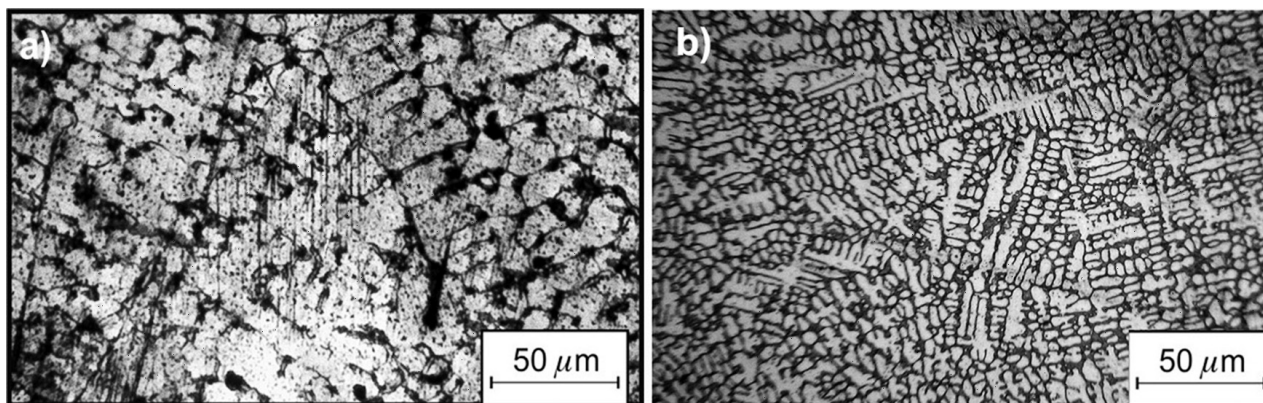


**Figure 5:** Microstructure of the weld's back layer: a) before the plastic deformation and b) after the plastic deformation; Filler metal: E Mn14  
**Slika 5:** Mikrostruktura zvara: a) pred plastično deformacijo in b) po plastični deformaciji; material elektrode: E Mn14

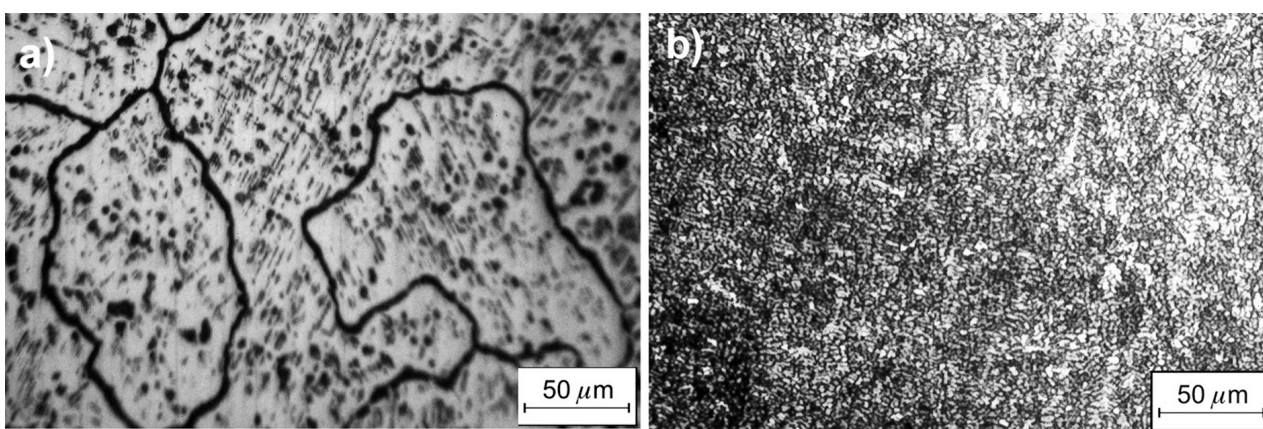


**Figure 6:** Microstructure of the weld's back layer: a) before the plastic deformation and b) after the plastic deformation; Filler metal: E Mn17Cr13  
**Slika 6:** Mikrostruktura zvara: a) pred plastično deformacijo in b) po plastični deformaciji; material elektrode: E Mn17Cr13

## 5 EXPERIMENTAL HARD FACING OF IMPACT BEAMS AND A DETERMINATION OF THEIR WEAR RESISTANCE

### 5.1 Description of the crusher plants' operation

The impact beams of crushers are simultaneously exposed to large impact loads and intensive abrasive wear since they are in working contact with rocks. In fact, the rocks are being crushed, minced and ground in order to obtain various fractions of the granules for direct insertion into roads or buildings. Besides being used for grinding rocks, similar crushing plants are also being used for the mincing of ores and coal.

Impact-beam wear occurs according to the mechanism of abrasive wear of the so-called closed type. The rock is brought into the working space between the beams and the stationary crusher housing where the kinetic energy of the rotational beams is transferred to the work, which is being spent on breaking the cohesive and adhesive bonds of the rock material.

The rock materials for building roads are usually of high hardness, and thus the crushers' working parts must

have high toughness and wear resistance<sup>4-7</sup>. The experimental investigations presented in this paper were conducted on impact beams and segments of the housing forming the crusher's jaw, **Figure 7**. The wear of the beams and the housing was monitored during the crushing of lime stone in a crusher with a capacity of 350 t/h. This is a rotational crusher with four impact beams, which are mounted onto the rotor and are driven by an electric or IC engine, with a pulley and v-belts. Such transmissions enable the belts to slide if overloading occurs, which protects the crusher's vital parts against fracture.

Impact beams have two alternative working surfaces, which allows the beam to be turned over and the second surface used after the first one is worn out. The crusher housing is made of flat spherical segments that are also being worn during the working process.

The crusher impact beams, on which the experimental hard-facing was performed, are made of manganese steel. Their dimensions were 300 mm × 120 mm × 1000 mm and their mass was around 300 kg. The same cast steel sheets were used for manufacturing the housing elements of thickness 30 mm and mass of around 20 kg.

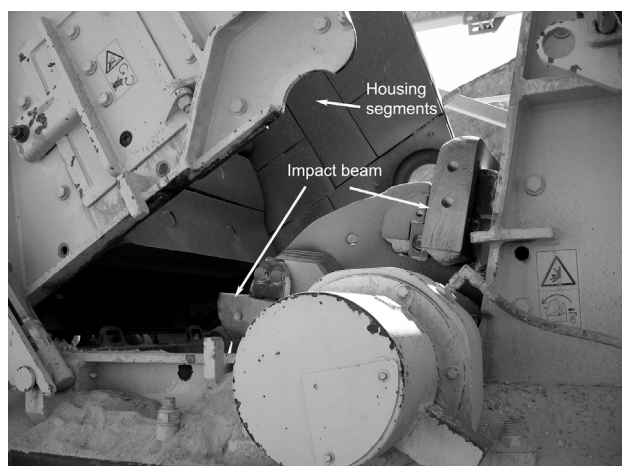


**Figure 7:** Appearance of the impact beams and crusher housing segments

**Slika 7:** Videz udarnih plošč in deli ohišja drobilnika

## 5.2 Experimental hard facing

The hard facing of impact beams was performed by technologies that are similar to the model investigations, but with changed working conditions. The reason for this is the large mass of the impact beams, as the hard facing was done in real working conditions, i.e., in a quarry. This means that the welds were deposited in the most unfavourable conditions, which gives special importance to the obtained results.

In the reparatory hard facing of the damaged impact beams, four beams were hard-faced, each one with a different filler metal (E Mn14, E Mn17Cr13, ABRADUR 58 and E DUR 600). The welds were deposited onto one of the two working surfaces of the impact beams, while the other working surface was brand new and unworn, and in this way a comparison of the working life of new and repaired beams was possible. The welds were deposited longitudinally on the working surface and the necessary weld thickness was achieved by multilayer hard facing with the thickness of each layer ranging from 10 mm at the ends to 35 mm in the middle of the impact beams where the wear was the greatest. The hard facing of the impact beams with electrodes E Mn14 and E Mn17Cr13 was done without the deposition of a plastic inter-layer. On the contrary, the weld layers realized by the ABRADUR 58 and E DUR 600 electrodes were deposited over the pre-

viously deposited plastic inter-layer of INOX B 18/8/6. After the hard facing, no faults of the crack type were spotted during a visual control of the large, hard-faced working surfaces (1200 mm × 100 mm).

In the reparatory hard facing of impact beams, two new beams were hard faced by depositing lateral multi-layers consisting of single-pass welds with the electrodes ABRADUR 58 (one impact beam) and E DUR 60 (the other impact beam). The distance between the deposited layers was about 100 mm, and partial welds were deposited all over the working surface. Two other impact beams were hard faced by depositing partial cross-like (honeycomb) welds over the whole working surface in such way that one impact beam was hard-faced with the E Mn14 electrode while the E Mn17Cr13 electrode was used for the other beam. The maximum weld thickness allowed is up to 10 mm, for construction reasons, since thicker welds would touch the housing during rotation. As in the first case, the hard facing with the ABRADUR 58 and E DUR 600 welds was deposited over the previously deposited plastic layer of INOX B 18/8/6, while the hard-facing welds of the electrodes E Mn14 and E Mn17Cr13 were directly deposited over the base metal. In this way, the second set of impact beams was prepared.

With monitoring of the impact beams' wear it was established that, after continuous work for 72 h, the damage to the working surfaces of the new impact beams was very severe and it was not possible to continue the crushing and adjustment of the crusher and that beams must be turned over to use their second working surface. The material losses of the hard-faced impact beams were obtained by monitoring the manufacturing process during 60 effective working hours so the two could be compared. The results of these examinations are presented in **Table 6** and in **Figure 8**<sup>4,6,16</sup>.

Based on obtained results of the wear-resistance investigations in real working conditions we can conclude that the highest resistance was achieved with the hard faced layer of the E Mn17Cr13 (4.12 %) electrode, followed by the layer deposited with the E DUR 600 (5.73 %) electrode, then the layer deposited with the E Mn14 (7.0 %) electrode, while the layer deposited with the ABRADUR 58 (8.87 %) electrode exhibited wear resistance even lower than that of the base metal – ČL3460 (7.87–8.12 %). Clearly, ABRADUR 58 is not suitable to be used for this type of wear.

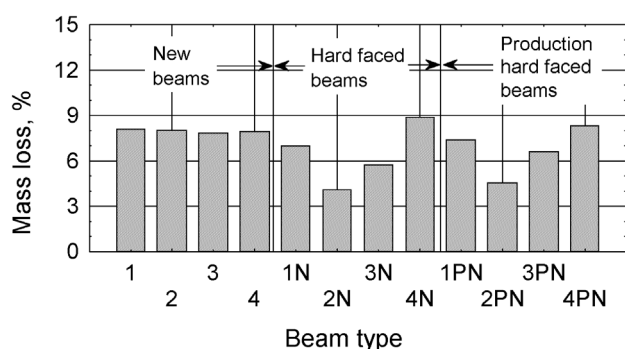
**Table 6:** Material losses of crushers' impact beams in real working conditions after 60 h of operation

**Tabela 6:** Izguba materiala na udarnih ploščah drobilnika po 60-urnem delovanju v realnih razmerah

Tested samples mass (impact beams)	Non hard-faced beams				Reparatory hard-faced beams				Production hard-faced beams			
	1	2	3	4	1*	2*	3*	4*	1*	2*	3*	4*
At the test beginning, kg	300	300	300	300	300	300	300	300	305	305	305	305
At the test end, kg	275.6	276.0	276.4	276.2	279.0	287.6	282.8	273.4	282.2	291.0	284.8	279.5
Mass loss, kg	24.4	24.0	23.6	23.8	21.0	12.4	17.2	26.6	22.5	14.0	20.2	25.5
Mass loss, %	8.12	8.00	7.87	7.93	7.00	4.12	5.73	8.87	7.38	4.59	6.62	8.36

\*Note: 1- E Mn14; 2- E Mn17Cr13, 3- E DUR 600, 4- ABRADUR 58.





1, 2, 3, 4 – New beams; 1N, 2N, 3N, 4N – Reparatory hard-faced beams; 1PN, 2PN, 3PN, 4PN – Production hard-faced beams

**Figure 8:** Graphical representation of the crushers' impact beams material losses after 60 h of operation

**Slika 8:** Grafična predstavitev izgube materiala udarnih plošč drobilnika po 60-urnem delovanju

The whole hard-facing process could have been performed automatically by robots. However, for the crushers' impact beams this is still not possible, especially because the main economic effect of introducing robots into the hard-facing and welding process, increasing the economic efficiency, i.e., lowering the process costs, cannot be achieved on small batch products like beams. For smaller parts and in batch manufacturing, however, the introduction of robots for the hard-facing process would be justified<sup>18–20</sup>.

## 6 CONCLUSION

The extended experimental investigations have shown that the working life of properly hard-faced impact beams significantly exceeds the working life of the original beams. In this way large savings in material costs are realized, the crusher's down-time is reduced, and the range and quantity of the necessary spare parts is smaller. In terms of days, the working life of the new impact beams was about 15 d, while the working life of the repaired beams was reaching about 30 d, on average, depending on the applied filler metal. By analysing the costs of the filler metals and the price of the welders' labour, data were obtained which have shown that the costs of the reparatory hard facing of one impact beam are 25 % lower than the costs of a set of the new beams. This means that by applying the reparatory hard facing, four damaged impact beams (one set) can be renewed for the price of one new beam. By application of reparatory hard facing (primarily with the E Mn17Cr13 electrode) the working life of parts is extended and the down time of the manufacturing process is reduced. All these positive effects came as a result of a complex theoretical model and the investigations of this paper's authors, realized in collaboration with the user company. One of the tasks that remains for future work is how to exploit the advantages of the robotization of the welding and hard-facing process for large parts such as the crusher's impact beams.

## 7 REFERENCES

- <sup>1</sup> P. Blašković, J. Balla, M. Dzimko, Tribology, Vydavatelstvo, ALFA, Bratislava, 1990 (In Slovak)
- <sup>2</sup> K. M. Mashloosh, T. S. Eyer, Abrasive wear and its application to digger teeth, Tribology International, 18 (1985) 5, 257–312
- <sup>3</sup> N. Jost, I. Schmidt, Friction-induced martensite in austenitic Fe-C steels, in: Ludema K. C. (ed): Wear of materials, ASME, N. Y., 1985, 2005–211
- <sup>4</sup> M. Mutavdžić, Reparatory hard-facing of the machine parts and devices in the civil engineering industry mechanization, Master's thesis, Faculty of Mechanical Engineering, Kragujevac, Serbia, 2007 (In Serbian)
- <sup>5</sup> V. Lazić, M. Jovanović, N. Ratković, D. Adamović, R. Vulović, Estimate of the wear resistance of the hard-faced layers deposited by the manganese electrode, Tribology in Industry, 22 (2002) 3/4, 10–17 (In Serbian)
- <sup>6</sup> M. Mutavdžić, V. Lazić, M. Jovanović, D. Josifović, B. Krstić, Selection of the optimum technology of reparatory hard facing of the impact beams of the rotational crushing mills, Welding & welded structures, 2 (2007), 55–67
- <sup>7</sup> G. I. Sil'man, Alloys of the Fe-C-Mn system. Part 4. Special features of structure formation in manganese and high-manganese steels, Metal Science and Heat Treatment, 48 (2006) 1/2, 3–8
- <sup>8</sup> V. Lazić, Optimization of the hard facing procedures from the aspect of tribological characteristics of the hard faced layers and residual stresses, Doctoral Dissertation, The Faculty of Mechanical Engineering, Kragujevac, 2001 (In Serbian)
- <sup>9</sup> V. Lazić, A. Sedmak, S. Aleksandrović, D. Milosavljević, R. Čukić, V. Grabulov, Reparation of damaged mallet for hammer forging by hard facing and weld cladding, Technical Gazette, 16 (2009) 4, 107–113
- <sup>10</sup> B. Nedeljković, M. Babić, M. Mutavdžić, N. Ratković, S. Aleksandrović, R. Nikolić, V. Lazić, Reparatory hard facing of the rotational device knives for terrain leveling, Journal of the Balkan Tribological Association, 16 (2010) 1, 46–75
- <sup>11</sup> G. S. Zhang, J. D. Xing, Y. M. Gao, Impact Wear Resistance of WC/Hadfield Steel Composite and its interfacial characteristics, Wear, 728 (2006), 260
- <sup>12</sup> Engineering handbook – Welding II, WNT, Warszawa, 1983 (In Polish)
- <sup>13</sup> Metals Handbook, Desk Edition, Wear resistant austenitic manganese steel, Edited by J. R. Davis, & Associates, American Society for Metals, Metals Park, Ohio 1998
- <sup>14</sup> Y. N. Dastur, W. C. Leslie, Mechanism of work hardening in Hadfield manganese steel, Metall. Trans. A, 749 (1981), 12A
- <sup>15</sup> R. W. Smith, A. DeMonte, W. B. F. Mackay, Development of high-manganese steels for heavy duty cast-to-shape applications, Journal of Materials Processing Technology, 153–154 (2004), 589–595
- <sup>16</sup> M. Mutavdžić, R. Čukić, M. Jovanović, D. Milosavljević, V. Lazić, Model investigations of the filler materials for regeneration of the damaged parts of the construction mechanization, Tribology in Industry, Journal of Serbian Tribology Society, (2008) 3/4, 3–9
- <sup>17</sup> Catalogues Thyssen Marathon Edelstahl-Vosendorf, FEP-Plužine, Elvaco-Bijeljina, Železarna Jesenice-Fiprom, Böhler-Kapfenberg, Messer Griesheim-Frankfurt am Main, Esab-Göteborg, Lincoln Electric, USA, Atlas zur Wärmebehandlung der Stähle
- <sup>18</sup> K. Kelleghan, Welding Report: Sorting through industry trends, February 12, 2001, <http://www.robot-welding.com>
- <sup>19</sup> R. Miller, Automation and Robots, Postel Newsletter, 3 (2010) 6 <http://www.postle.com>
- <sup>20</sup> J. Berge, Robotic Weld Process Control, Mr. Roboto: Welding fundamentals for managers, February 28, 2002, <http://www.thefabricator.com>